Higgs cross section measurements at $\sqrt{s} = 13$ TeV using the ATLAS detector

Stephen B. Menary

A thesis submitted to
The University of Manchester
for the degree of Doctor of Philosophy
in the Faculty of Science and Engineering

2019

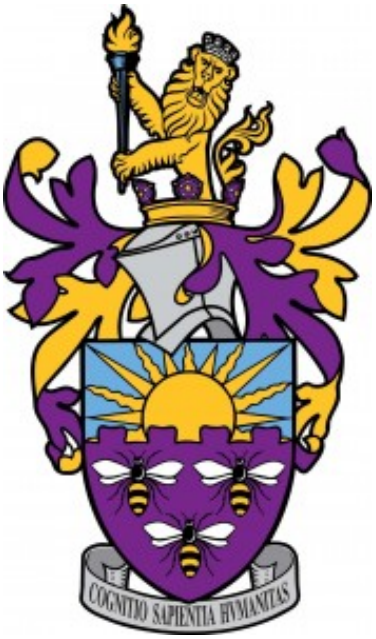

School of Physics and Astronomy
University of Manchester
United Kingdom

Contents

Word count: 45,000

List of Figures

List of Tables

Abstract

A measurement of the Higgs boson fiducial cross section in the diphoton decay channel is presented using 36.1 fb^{-1} data collected by the ATLAS detector with proton-proton collisions provided by the Large Hadron Collider at a centre-of-mass energy of $\sqrt{s} = 13$ TeV. The fiducial volume is defined by kinematic and particle-level isolation requirements applied to the final state photons. A result of 55 ± 9 (stat.) ± 4 (syst.) fb is obtained. The statistical precision is approximately double that of the measurement at $\sqrt{s} = 8$ TeV and probes production at higher partonic centre-of-mass energies. Several differential cross sections are presented in the fiducial phase space. These characterise the properties of Higgs production and decay in a minimally model dependent way.

A measurement of the total Higgs boson cross section is presented using the same dataset and the combination of diphoton and four-lepton decay channels. A result of $57.0\ ^{+6.0}_{-5.9}$ (stat.) $^{+4.0}_{-3.3}$ (syst.) pb is obtained. The fiducial acceptances and branching ratios are assumed to follow the Standard Model expectations. Four differential cross sections are presented using the combination of channels.

The expected sensitivity of a differential cross section measurement in the diphoton channel is presented assuming the phase 2 upgrade of the electromagnetic calorimeter and a dataset of 3 ab^{-1}. This is predicted to significantly improve the measurement of Higgs boson production at high transverse momentum.

A luminosity measurement based on the multiplicity of charged particle tracks is presented. This is used to perform corrections to the stability and scale of the ATLAS luminosity measurement in data collected in 2012, 2015 and 2016. Along with other offline measurements it is used to constrain the calibration transfer and long-term stability which are two of the dominant luminosity uncertainties.

Declaration

No portion of the work referred to in the thesis has been submitted in support of an application for another degree or qualification of this or any other university or other institute of learning

Copyright

Acknowledgements

I would like to thank many people for everything they have done over the last four years.

Firstly I would like to thank Andy and Terry for all of their help and guidance. It has been a priviledge to learn from such accomplished and enthusiastic scientists, and I am grateful for all of the time you have invested in me. Thanks for all the fun science we did, and for giving me so many opportunities to try new things. I would also like to thank the HGam and Lumi groups for welcoming me and for all of your time - through individual help, conversations, meetings, sharing your experience and welcoming me onboard. In particular I thank Florian for all of the time spent explaining things to me, both physics and statistics, and all of the other help. I have come to suspect that there is no answer in life that cannot be found by bootstrapping. To all of the above, thanks for making the work we did such a fun, educational and hopefully productive experience.

Secondly I want to thank the whole of the Manchester group, both past and present. The group has always been so welcoming and given me plenty of support, opportunities and friendship. Thank you to everyone I have ever shared an office with for making work such a fun place to be. Thanks to Abby for letting me win at hangman (sometimes), Rafał for making the move to CERN less lonely, and Fabian for all of the coffee and videogames. Except for Rocket League which I *do not* remember fondly. It's a stupid game anyway and I didn't want to win. Thanks to Johnny for being a great flatmate, to Kevin for being a great friend and to Lorenzo for being a terrible one but still fun to spend time with. In particular, thanks to Rhys who (due to this thesis not being finished as early as I'd hoped) has now spent 8 years listening to my daily crisis reports. I promise that they all felt like the end of the world at the time. Also thanks for all of the other stuff that happened in that time or whatever. Thanks to Sierra Boggess and Ramin Karimloo for keeping me company during all of the late nights in the office.

Thank you to my parents, brother and sister for always being there for me. Thanks for supporting me and letting me know that there is always a place called home to come back to. Finally I would like to thank Thierry Henry.

Preface

The author was born in 1992 and has pursued science for as long as he can remember, eventually joining the University of Manchester in 2010 where he studied for an undergraduate masters degree in physics. Graduating with first class honours in 2014, he remained at the university to study for a PhD in high energy physics having been inspired by undergraduate courses on experimental particle physics and the Standard Model as a quantum field theory, as well as the recent discovery of the Higgs boson. During his doctoral studies he spent 2 years working at CERN whilst living in Meyrin, Switzerland.

Most of his work on the ATLAS experiment has been undertaken within the Luminosity Measurement Task Force (LMTF) and Higgs group. Whilst at CERN he performed many run control shifts in the ATLAS control room which contributed to the real-time operation of the experiment.

He joined the LMTF in October 2014 where he worked on track counting under the supervision of Prof. Terry Wyatt. At this time his main responsibilities were the processing and validation of reprocessed data for the 2012 luminosity measurement, relying on valuable guidance and expertise from Dr. James Robinson. He then studied the relative stability between track counting and other luminometers. In 2015 he was responsible for migrating the track counting framework into the new ATLAS software framework and performing measurements using updated simulation and early 13 TeV collision data. Throughout 2015 and 2016 he was responsible for improving and maintaining the software, timely processing of track counting measurements for the LMTF group, and the study of data quality and dependence on Inner Detector conditions. He was also heavily involved in the study of offline stability including cross-calibration, bunch train dependence, μ-dependence and long-term time-dependence. These contributions drove constraints on two of the dominant sources of uncertainty on the ATLAS luminosity measurement: the long-term stability and the transfer in calibration from low to high pileup conditions. Whilst responsible for processing data to create Run 2 van der Meer (vdM) scan curves for track counting, he was not responsible for the absolute vdM calibration nor the simulation-driven derivation of fake track contributions.

He also joined the Higgs working group in October 2014 where, under the supervision of Dr. Andrew Pilkington, he worked as part of a team measuring fiducial cross sections in the diphoton channel using 13 TeV collision data. Several conference notes and papers

were published to which the author contributed in a variety of ways. Initially he studied the behaviour of truth level observables and object definitions in early 13 TeV simulations with a focus on the truth level photon isolation definition and an alternative method using an overlap between photons and jets. This included studying the correction for detector effects. He co-edited the internal documentation and iterated with the editorial board for the 3 fb^{-1} fiducial cross section measurement presented at the CERN End Of Year Event in December, 2015 [1].

The analysis was updated in August 2016 when it was presented at the International Conference on High Energy Physics (ICHEP) using 13 fb^{-1} data [2]. This included the first differential cross section measurements at 13 TeV. The author was responsible for deriving the optimum signal parameterisation, performing the likelihood-based signal extraction and associated bias tests, optimising the particle level isolation definition, performing cross checks on the correction for detector effects, deriving a reweighting scheme for evaluating unfolding bias, studying pileup dependence and deriving associated pileup modelling and vertex association uncertainties. He also performed general tasks for the $H \to \gamma\gamma$ subgroup including cutflow debugging and the writing of a software package for validation of the common dataset integrity.

The analysis was again updated in February 2017 when it was presented at the European Physical Society Conference on High Energy Physics (EPS) using the full dataset accumulated by ATLAS in 2015 and 2016 with a size of 36 fb^{-1} [3]. As well as improving the statistical precision, a greater number of differential observables were measured along with an effective field theory interpretation. The author was responsible for re-writing and validating the fitting framework, performing the tasks listed for the 2016 analysis, deriving the statistical correlations between distributions using a bootstrap approach and studying a background modelling technique used by the CMS collaboration (the discrete profiling method [4]). The measurement was published as a paper in 2018 [5].

In July and August, 2017 the author studied the expected sensitivity of $H \to \gamma\gamma$ cross section measurements using the proposed High Luminosity upgrade (HL-LHC) for inclusion in the technical design report for the upgraded calorimeter system [6]. The analysis described in this thesis was carried out by the author with guidance from Andy and the Higgs Prospects group. This does not include the HL-LHC simulation nor the reconstruction optimisation, which were provided by other members of the collaboration.

In late 2017 and early 2018 the author was responsible for the production of $H \to \gamma\gamma$ workspaces to be used in the combination of differential cross sections with the $H \to 4l$ channel. This included implementation of workspace unfolding and acceptance corrections, closure testing and the derivation of parton shower and signal composition uncertainties. Whilst not responsible for the initial calculation of acceptance factors, he performed several cross checks to study them. This analysis was presented in March 2018 at the 53$^{\text{rd}}$ Recontres du Moriond [7, 8], at which the author also presented the diphoton paper.

"Sometimes science is more art than science, Morty. A lot of people don't get that."

R. Sanchez

Introduction

The Standard Model (SM) describes the interactions of six quarks and six leptons via the strong nuclear, weak nuclear and electromagnetic forces [9–11]. In this theory, electroweak gauge boson masses appear due to spontaneous breaking of the electroweak gauge symmetry in the early universe through the Higgs mechanism, which predicts the existence of a neutral scalar boson [12–17]. Quarks and leptons can also gain mass through this method if there exists a direct coupling with the Higgs field [9, 18]. For a theory which only describes them in left-handed states, the three flavours of neutrino are the only known particles which require a non-zero mass to be generated through some other mechanism.

Direct production of a particle consistent with a SM Higgs boson was observed in 2012 by the ATLAS [19] and CMS [20] experiments at the Large Hadron Collider (LHC) [21–23] using proton-proton collisions at centre-of-mass energies of $\sqrt{s} = 7$ and 8 TeV (Run 1) [24, 25]. The mass of this particle was measured to be 125.09 ± 0.24 GeV [26] with a spin-parity of 0^+ [27]. The LHC has since been upgraded to deliver $\sqrt{s} = 13$ TeV collisions between 2015 and 2018 (Run 2), providing greater sensitivity to processes with high partonic centre-of-mass energy and more than doubling the rate of Higgs production [28]. The measurements contained within this thesis utilise the 2015-2016 dataset which is approximately twice the size of that obtained in Run 1. Together these effects lead to a factor of 2 improvement in statistical precision. An additional factor of $3 - 4$ increase in dataset size is expected by the end of 2018.

Fermions and gauge bosons are expected to couple directly to the Higgs boson proportionately to their mass. This leads to precise SM predictions for the behaviour of Higgs production and decay. Measuring the rates and properties of such processes is an important test of the Standard Model and a natural area in which to search for new physics such as previously undiscovered massive particles, which may couple strongly to the Higgs and provide observable contributions either through loop processes or direct production. Other examples of possible new physics in the Higgs sector include non-SM-like Lorentz structures with potentially CP-violating behaviour [5, 29–33] in the interactions with other particles, non-SM transition amplitudes, composite Higgs models [34] and mixing with additional scalar particles which may also allow for direct production of dark matter candidates [35]. Indirect sensitivity to the Higgs self-coupling may be achieved in single Higgs production before the direct observation of diHiggs production [36, 37].

This thesis focusses on the measurement of differential cross sections. These represent the rate of Higgs production and decay as a function of observables defined by (i) the kinematic properties of the decay products, (ii) those of objects produced in association with the Higgs and (iii) event topologies. These are measured in a fiducial phase space to minimise dependence on modelling assumptions. This allows one to characterise the Higgs sector in a way that permits after-the-fact constraint of new physics models or Standard Model predictions. This thesis presents fiducial differential cross section measurements in the $H \to \gamma\gamma$ channel. Previous measurements are statistically limited with $\mathcal{O}(50\ \%)$ precision per bin and low granularity in the tails of distributions, and therefore benefit significantly from the increased statistical precision of Run 2. The expected sensitivity of this measurement is also estimated for the High Luminosity (HL-LHC) upgrade. This will significantly improve the measurement of the high energy tail of Higgs production.

In order to maximise the available statistical precision and decouple the effects of production and decay, it is important to measure differential cross sections in as many decay channels as possible. The $H \to \gamma\gamma$ channel has a low branching ratio but the excellent energy resolution and reconstruction efficiency of photons allow for competitive sensitivity. The $H \to ZZ^* \to 4l$ channel has a lower branching ratio and reconstruction efficiency but a very low background rate, also resulting in competitive sensitivity. This thesis presents the combination of several differential distributions using the $H \to \gamma\gamma$ and $H \to ZZ^* \to 4l$ channels. This improves statistical precision whilst introducing some SM dependence. Such a measurement is therefore complementary to the fiducial measurements in the individual channels.

Precise knowledge of the dataset luminosity is required for absolute cross section measurements. It is also used to evaluate background contributions in many analyses. ATLAS uses several offline luminosity measures to derive systematic corrections and uncertainties for the luminosity scale. One important such method is based on the multiplicity of reconstructed tracks. The final track counting analysis of Run 1 data is presented along with the real-time analysis of 2015 and 2016 data.

The thesis is organised as follows: chapter 2 outlines the Standard Model description of particle interactions with a focus on the application to Higgs production and decay, and discusses how processes are modelled; chapter 3 summarises some relevant Higgs sector results from Runs 1 and 2; chapter 4 gives an overview of the ATLAS experiment and the reconstruction of objects such as photons and hadronic jets; chapter 5 discusses the track counting method for constraining the ATLAS luminosity measurement; chapter 6 discusses the measurement of differential cross sections in the $H \to \gamma\gamma$ channel at $\sqrt{s} = 13$ TeV which is the main focus of this thesis; chapter 7 discusses the combination of several differential distributions using the $H \to \gamma\gamma$ and $H \to ZZ^* \to 4l$ channels; chapter 8 estimates the statistical precision of $H \to \gamma\gamma$ differential cross sections using the proposed High Luminosity LHC (HL-LHC) upgrade; finally, chapter 9 provides a summary.

Theory

The dynamics of a classical system are described by the equations of motion. These can be derived using several different formalisms including: application of Newton's second law of motion to each object in the system; application of Hamilton's equations to a function describing the total energy of the system; application of the Euler-Lagrange equation under the principle of least action. Observables are well-defined and evolve deterministically in classical dynamics, meaning that we can exactly infer object positions and momenta at all times if we know them at any one instant.

In a quantum system, observables are not well defined except through measurement. A quantum state represents a linear superposition of all possible physical states, each contributing with a certain amplitude, a. When an observable q_i is measured, the system collapses into the measured state with a probability of $|a|^2$, and now exists in this state with a probability of 1. However, this leads to a corresponding uncertainty in a conjugate observable p_i such that Heisenberg's uncertainty relation $\Delta q_i \Delta p_i \geq \frac{h}{4\pi}$ is always satisfied, where Δ represents the $\sqrt{\text{variance}}$ of a quantity and h is Planck's constant. This can be understood since conjugate observables are related through Fourier transforms, and the transform of a delta function is a plane wave. Examples include position/momentum and time/energy. The dynamics of a quantum system are described as a time-evolution of the state and/or operators through e.g. the Schrödinger equation, and the result of measurement is probabilistic.

This chapter outlines the Standard Model (SM) description of known particles and their interactions in the context of a gauge invariant quantum field theory. The concept of a cross section is introduced as a calculable observable sensitive to possible beyond the Standard Model (BSM) contributions. Details are provided on the Monte Carlo method for modelling physical processes at the LHC. The SM interactions are then used to describe Higgs production at the LHC as well as its subsequent decay with a focus on channels relevant to this thesis.

2.1 Quantum field theory

This section is primarily based on the discussions in Mandl and Shaw [38] and several courses attended at undergraduate degree and graduate summer school level [39–41].

Quantum field theory (QFT) is the framework through which the dynamics of particle interactions are described. The state of a system is a vector on a Fock space which spans all possible particle configurations and momenta; this means that a state, $|\psi; t_0\rangle$, such as $|e_s^-(\vec{p}), \mu_{s'}^+(\vec{q}), \gamma_r(\vec{u}); t_0\rangle$ represents a system consisting of an electron with momentum $\vec{p}$ and spin s, an antimuon with momentum $\vec{q}$ and spin s' and a photon with momentum $\vec{u}$ and polarisation r at time t_0. Creation, $a^\dagger$, and annihilation, a, operators then act on these vectors in order to add and remove particles respectively, for example $a_\gamma^\dagger(\vec{u}, r)\,|0\rangle = |\gamma_r(\vec{u})\rangle$ and $a_\gamma(\vec{u}, r)\,|\gamma_r(\vec{u})\rangle = |0\rangle$. The time coordinate has been left implicit for brevity and $|0\rangle$ is the vacuum state.

One defines the so-called field operator as a function of spacetime co-ordinate, x. This depends on the type of field being considered. For example, the operator describing a real scalar field in free space, $\Phi(x)$, is the solution to the Klein-Gordon equation and is written

$$\Phi(x) = \int \frac{d^3\vec{k}}{(2\pi)^3 2E_k} \left(a(\vec{k})e^{-ik\cdot x} + a^\dagger(\vec{k})e^{ik\cdot x}\right) \tag{2.1}$$

where $k = \left(E_k, \vec{k}\right)$ is the four-momentum. An intuitive example illustrating this operator form is given in Ref. [38] [Chapters 1,5]. An electromagnetic vector potential field is obtained by quantisation of the solutions to Maxwell's equations, whereby an arbitrary vector potential is written as the infinite sum over Fourier modes after the application of periodic boundary conditions. The amplitude of each mode is shown to satisfy the harmonic oscillator equation and is quantised accordingly. This introduces the creation and annihilation operators which increment the occupancy number of the state, interpreted as the addition and removal of quanta. The field operator then has a corresponding canonical conjugate momentum, $\Pi(x)$, defined according to the equal-time commutation relation, $[\Phi(x), \Pi(y)] = i\delta(x-y)$, for spacetime co-ordinates x, y with $[\Phi(x), \Phi(y)] = [\Pi(x), \Pi(y)] = 0\ \forall\ x, y$.

By analogy to classical dynamics, a theory describing a set of fields, $\vec{\Phi}$, is defined by the Lagrangian density, $\mathcal{L}\left(\vec{\Phi}, \partial_\mu\vec{\Phi}\right)$ with $\partial_\mu \equiv \frac{\partial}{\partial x^\mu}$, or equivalently the Hamiltonian density defined as $\mathcal{H} = \vec{\Pi}^T\partial_0\vec{\Phi} - \mathcal{L}$. The Hamiltonian is the generator of time translations and so we define a time-evolution operator, $\hat{U}(t, t_0)$, which describes the evolution of a state ψ as

$$|\psi; t\rangle = \hat{U}(t, t_0)\,|\psi; t_0\rangle = e^{-i(t-t_0)\int \mathcal{H}\mathrm{d}^3\vec{x}}\,|\psi; t_0\rangle \quad [1]. \tag{2.2}$$

Within this formalism, a model is defined by the fields available, the Lagrangian or Hamiltonian density and the scales over which it valid. Transitions may occur between Fock states because the Hamiltonian determines the evolution through time, and is written in terms of the field operators. These contain creation and annihilation operators which allow for occupancy numbers to change.

[1] Using the Schrödinger picture in which time evolution is carried entirely by states.

2.1.1 Perturbative QFT

In general one can write field operators by solving wave equations in the absence of a source. This leads to plane waves with quantised coefficients describing non-interacting particles. However, the presence of interactions in the Hamiltonian means that the wave equations are generally sourced, making them difficult to solve. Instead, one writes the Hamiltonian density, $\mathcal{H} = \mathcal{H}_0 + \mathcal{H}_\mathrm{I}$, as the sum of terms which describe only free fields, $\mathcal{H}_0$, and interactions, $\mathcal{H}_\mathrm{I}$. Provided that the interactions are sufficiently weak and short-lived, one can approximate them as perturbations causing transitions between free initial $|i; t_0 = -\infty\rangle$ and final $|f; t = \infty\rangle$ states. These occur with a probability of $P_{i\to f} = |S_{fi}|^2$ where the transition amplitudes S_{fi} are given by

$$S_{fi} = \langle f; t = \infty | \, U(t, t_0) \, | i; t_0 = -\infty \rangle \tag{2.3}$$

and form the so-called S-matrix. Taking the time-ordered series expansion of Eq. 2.2 one sees that the S-matrix is an infinite sum of terms representing all possible ways in which $|i\rangle$ can evolve into $|f\rangle$ between $t = \pm\infty$. When one uses the Interaction Picture in which the time dependence due to $\mathcal{H}_\mathrm{I}$ is carried by the operators and that due to $\mathcal{H}_0$ is carried by the states, S_{fi} can be written as a sequence of terms of increasing order in α_I, a dimensionless constant representing the interaction strength. If $\alpha_\mathrm{I} \ll 1$ then S_{fi} can be approximated by truncating the perturbation series at a finite order. In electromagnetism, $\alpha_\mathrm{EM} \approx \frac{1}{137}$ at low energy scales and so processes with $n+1$ electron-photon interactions are expected to modify the transition amplitude approximately two orders of magnitude less than processes with n such interactions.

2.1.2 QED

Quantum electrodynamics (QED) is a theory describing spin-$\frac{1}{2}$ particles under the presence of a $U(1)_Q$ gauge symmetry, defined as follows. A symmetry means that one can transform the fields in such a way that the equations of motion remain invariant. Gauge transformations are dependent on x. It will be shown that this necessitates the existence of an interaction with a so-called gauge field which transforms in the adjoint representation. By Noether's theorem, symmetry implies the existence of a conserved scalar quantity. In QED, the gauge boson is the photon and the conserved quantity is electric charge.

Imposing the commutation relations, $[a, a^\dagger] = 1$ and $[a, a] = [a^\dagger, a^\dagger] = 0$, on the harmonic oscillator leads to the existence of creation and annihilation operators which increment the occupancy number of the system, an observable with eigenvalues $0, 1, 2, 3, ..., \infty$. This describes a boson state which follows Bose-Einstein statistics. If the theory is quantised by replacing all commutators with anticommutators then the occupancy number has only the eigenvalues $0, 1$. This describes a fermion state which follows Fermi-Dirac statistics

and obeys the Pauli exclusion principle.

The relativistic fermion equation of motion is the Dirac equation. In units where $\hbar = c = 1$ this is given by

$$\begin{aligned} i\gamma^\mu \partial_\mu \psi(x) - m\psi(x) &= 0 \\ i\gamma^\mu \partial_\mu \bar{\psi}(x) + m\bar{\psi}(x) &= 0 \end{aligned} \tag{2.4}$$

where γ^μ are the 4×4 Pauli matrices, $\psi(x)$ is the four-component spinor representing the fermion wavefunction, $\bar{\psi}(x) = \psi^\dagger(x)\gamma^0$ is the adjoint wavefunction, $\partial_\mu \equiv \frac{\partial}{\partial x^\mu}$ and m is the fermion mass. The spin is a constant of motion with eigenvalues $\pm\frac{1}{2}$ and solutions are plane waves propagating in the positive and negative time directions. The corresponding Lagrangian density is given by

$$\mathcal{L}_{\text{Dirac}} = i\bar{\psi}(x)\partial\!\!\!/\psi(x) - m\bar{\psi}(x)\psi(x) + \text{h.c.} \tag{2.5}$$

where the slash notation, $\phi\!\!\!/ \equiv \gamma_\mu O^\mu$ for operator O^μ, is used and "h.c." denotes the Hermitian conjugate. This will be left implicit from hereon.

Second quantisation promotes the wavefunctions to operators and applies the anti-commutation relations. Plane wave coefficients become creation operators of particles (antiparticles) and annihilation operators of antiparticles (particles), summed over the two spin states. Consider now that one applies a $U(1)_Q$ gauge transformation of extent $\theta(x)$ to the fermion field by making the substitutions

$$\begin{aligned} \psi(x) &\xrightarrow{U(1)_Q} \psi'(x) = e^{iQ_\psi \theta(x)}\psi(x) \qquad & [Q_\psi \equiv +Q = -1] \\ \bar{\psi}(x) &\xrightarrow{U(1)_Q} \bar{\psi}'(x) = \bar{\psi}(x)e^{iQ_{\bar{\psi}}\theta(x)} \qquad & \left[Q_{\bar{\psi}} \equiv -Q = +1\right] \end{aligned} \tag{2.6}$$

where Q is a constant. An extra term is present in the transformed Lagrangian density,

$$\begin{aligned} \mathcal{L}_{\text{Dirac}} \to \mathcal{L}'_{\text{Dirac}} &= i\bar{\psi}'(x)\partial\!\!\!/\psi'(x) - m\bar{\psi}'(x)\psi'(x) \\ &= e^{-i\theta(x)}e^{i\theta(x)}\left[i\bar{\psi}(x)\partial\!\!\!/\psi(x) - Q\bar{\psi}(x)\left(\partial\!\!\!/\theta(x)\right)\psi(x) - m\psi(x)\bar{\psi}(x)\right] \\ &= \mathcal{L}_{\text{Dirac}} - Q\bar{\psi}(x)\left(\partial\!\!\!/\theta(x)\right)\psi(x)\ . \end{aligned} \tag{2.7}$$

This modifies the Euler-Lagrange equations of motion, and so the Dirac Lagrangian does not obey $U(1)_Q$ gauge symmetry. Gauge symmetry is restored if one introduces a new field, A_μ, which transforms in the adjoint representation, i.e.

$$A_\mu(x) \to A'_\mu(x) = A_\mu(x) + \frac{1}{q_e}\partial_\mu\theta(x) \tag{2.8}$$

where q_e is the coupling constant of the theory. The covariant derivative is defined as

$$D_\mu(x)X(x) \equiv \left[\partial_\mu - iq_e Q_X A_\mu(x)\right] X(x) \tag{2.9}$$

for field $X(x)$ such that $D_\mu(x)X(x)$ transforms in the fundamental representation,

$$D_\mu(x)X(x) \to D'_\mu(x)X'(x) = e^{iQ_X\theta(x)} D_\mu(x)X(x) \ . \tag{2.10}$$

The Lagrangian density

$$\begin{aligned} \mathcal{L}_{A\bar{\psi}\psi} &= \bar{\psi}\left[i\partial\!\!\!/ + q_e Q A\!\!\!/ - m\right]\psi \\ &= \bar{\psi}\left[iD\!\!\!/ - m\right]\psi \end{aligned} \tag{2.11}$$

is then $U(1)_Q$ gauge invariant. The dependence of fields and covariant derivatives on x is left implicit. We have found that a change in the $U(1)_Q$ phase at any point must be accompanied by a counter-rotation of the relevant gauge field in the adjoint space, implying both the conservation of a charge *and* the existence of a point interaction of the form $\sim \bar{\psi}(x)A\!\!\!/(x)\psi(x)$.

When applied to electrically charged fermions, Q is the electric charge, q_e is the electric coupling constant and A_μ is the photon field. In order to complete this theory we invoke the field strength tensor from classical electrodynamics with the form

$$F^{\mu\nu} = \partial^\mu A^\nu - \partial^\nu A^\mu \tag{2.12}$$

in order to include the photon kinetic energy. The Lagrangian density of QED is then

$$\mathcal{L}_{QED} = -\frac{1}{4}F_{\mu\nu}F^{\mu\nu} + \bar{\psi}\left[iD\!\!\!/ - m\right]\psi \tag{2.13}$$

No photon mass term has been included since the photon is massless.

Within the QED model, all allowed processes occur due to photons and fermions propagating between spacetime co-ordinates and photon-fermion interactions as shown in Figure 2.1[2]. Bare charged fermions do not exist within QED but continuously generate and interact with a cloud of virtual photons. This has implications for their self-energy which will not be considered here.

[2]In the Feynman gauge, the propagator $i\Delta_{\mu\nu}(x-y)$ for a particle is the vacuum expectation value of the time-ordered product $T[\cdots]$ of the field operators at two different space-time points x, y, e.g. $\langle 0|\, T[A_\mu(x)A_\nu(y)]\, |0\rangle$. The transition amplitude between the vacuum state at two different times therefore takes into account the spontaneous creation and annihilation of the field, even in the absence of initial and final state quanta. The quantum vacuum is therefore not empty but contains an infinity of short-lived virtual particles.

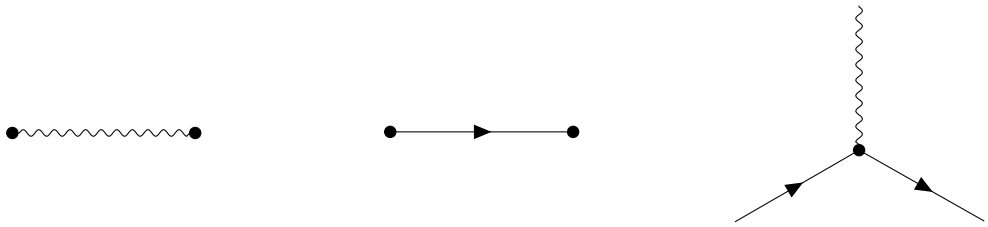

Figure 2.1: QED diagrams for a photon propagating between vertices, a fermion propagating between vertices and a fermion-photon interaction.

2.1.3 QCD

Symmetries are described by group theory. A group is a set of objects, $\mathcal{S} = \{s_1, s_2, ..., s_N\}$, defined with a combination rule $\cdot$ such that the following conditions are satisfied for all i, j, k: closure, $s_i \cdot s_j \in \mathcal{S}$; associativity, $s_i \cdot (s_j \cdot s_k) = (s_i \cdot s_j) \cdot s_k$; existence of an identity $e \in \mathcal{S}$ such that $s_i \cdot e = s_i$; existence of an inverse $s_i^{-1} \in \mathcal{S}$ such that $s_i \cdot s_i^{-1} = e$. A group is *abelian* if $s_i \cdot s_j = s_j \cdot s_i$. An n-dimensional representation of a group is a set of non-singular $n \times n$ matrices which satisfy the group definition with matrix multiplication as the combination law.

We restrict our consideration to groups for which $\mathcal{S}$ consists of continuous elements. Examples include U(N), which describe unitary N-dimensional rotations, and $SU(N)$ which additionally impose the condition of tracelessness. An N-dimensional matrix of complex numbers has $2N^2$ degrees of freedom. Unitarity imposes N^2 constraints and the trace condition imposes an additional 1, leaving a total of N^2 degrees of freedom for $U(N)$ and $N^2 - 1$ for $SU(N)$. An arbitrary $SU(N)$ transformation, u, can therefore be written as a combination of $N^2 - 1$ orthogonal matrices called generators. Call the generators t^a and the associated rotation angles θ^a for $a \in \{1, ..., N^2 - 1\}$, then $u = e^{i\theta^a t^a}$ where repeated indices imply summation.

A $U(1)$ group has only 1 generator, therefore $[t^a, t^b] = 0$ and this is abelian. For $SU(2)$ we find 3 generators which are proportional to the Pauli matrices τ^a such that $t^a = \frac{1}{2}\tau^a$ and $[t^a, t^b] = if^{abc}t^c$ where f is antisymmetric under the exchange of indices. The $SU(2)$ rotation acts on spinor fields and describes a transformation between spin states. Quantum chromodynamics (QCD) describes quarks as Dirac particles which transform under $SU(3)_C$ in the fundamental representation where C labels colour charge. The requirement of $SU(3)_C$ gauge invariance leads to colour conservation and the existence of quark-gluon interactions, and the non-abelian nature causes gluon self-interactions which result in the colour confinement and asymptotic freedom properties of the strong nuclear force.

Small rotations can be written as $\psi' \approx [\mathbb{1} + i\theta^a t^a]\psi$. This contains a sum over 8 QCD generators, therefore $SU(3)_C$ gauge invariance requires the presence of 8 orthogonal gauge fields which transform in the adjoint representation. These are the gluon fields, G^a_μ, with the covariant derivative $D_\mu \equiv \partial_\mu - iq_s t^a G^a_\mu$ where q_s is the strong coupling constant. This

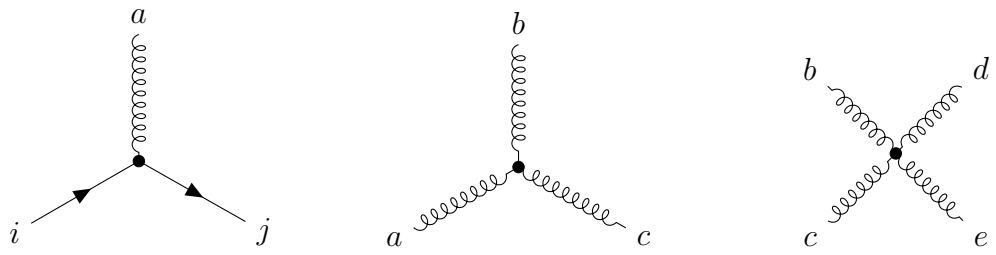

Figure 2.2: QCD diagrams for gluon-quark and gluon self-interaction vertices. Labels i, j and a, b, c, d, e represent quark and gluon colour charges repectively.

can be simplified by writing the gluon octet as $G_\mu = t^a G^a_\mu$. The field strength tensor is given by

$$\begin{aligned} G_{\mu\nu} &= \frac{i}{q_s}[D_\mu, D_\nu] \\ &= t^a \left(\partial_\mu G^a_\nu - \partial_\nu G^a_\mu + q_s f^{abc} G^b_\mu G^c_\nu\right) \\ &\equiv t^a G^a_{\mu\nu} \end{aligned} \tag{2.14}$$

which makes use of the commutation relation $[t^a, t^b] = i f^{abc} t^c$ and the antisymmetry under exchange of indices in f^{abc}. The Lagrangian density describing a fermion with colour charge is then

$$\mathcal{L}_{QCD} = -\frac{1}{4} G^a_{\mu\nu} G^{a,\mu\nu} + \bar{\psi}\left[i\not{D} - m\right]\psi \ . \tag{2.15}$$

Comparing this with the field strength tensor of Eq. 2.14 leads to the interaction vertices shown in Figure 2.2. An important result of QCD is that the gluon itself has colour due to the non-abelian nature of $SU(3)_C$, and so three- and four-point self-coupling vertices exist.

2.1.4 Electroweak interactions

Weak nuclear interactions differ from QED and QCD because they are described by a chiral gauge theory. This is required to reproduce the observation of parity violation. This section describes a unified electroweak theory of electromagnetic and weak interactions assuming zero mass fields. The generation of gauge boson masses will be discussed in section 2.1.5.

For Dirac spinors, ψ, we write the chirality operator as $\gamma_5 = i\gamma^0\gamma^1\gamma^2\gamma^3$ with eigenvalues of ± 1. A basis is formed out of right-handed ψ^R and left-handed ψ^L states defined as the positive and negative chiral eigenstates respectively. The operators $P^L = \frac{1}{2}(1 - \gamma_5)$ and $P^R = \frac{1}{2}(1 + \gamma_5)$ can be used respectively to project the left- and right-handed states from the fermion field. This treatment is summarised by

$$\begin{gathered} \gamma_5\psi^L = (-1)\,\psi^L \quad , \quad \gamma_5\psi^R = (+1)\,\psi^R \\ \psi = \psi^L + \psi^R \\ \frac{1}{2}(1 - \gamma_5)\,\psi = \psi^L \quad , \quad \frac{1}{2}(1 + \gamma_5)\,\psi = \psi^R \quad . \end{gathered} \tag{2.16}$$

The weak interaction is described by the non-abelian $SU(2)_L$ gauge group. This requires 3 generators proportional to the Pauli matrices τ_j satisfying $[\tau_j, \tau_k] = 2if_{jkl}\tau_l$ as described in section 2.1.3. These are written in a common basis as

$$\tau_1 = \begin{pmatrix} 0 & 1 \\ 1 & 0 \end{pmatrix} \qquad \tau_2 = \begin{pmatrix} 0 & -i \\ i & 0 \end{pmatrix} \qquad \tau_3 = \begin{pmatrix} 1 & 0 \\ 0 & -1 \end{pmatrix} \quad . \tag{2.17}$$

The corresponding conserved charges are labelled I_1, I_2, I_3. Only left-handed fields couple to weak gauge fields. This means that ψ^L transform under $SU(2)_L$ whereas ψ^R remain invariant. The left-handed fields are written in doublets Ψ^L containing the up- and down-type quarks or neutrino and charged lepton pairs, i.e.

$$\Psi^L{}_{\text{quark}} = \begin{pmatrix} u^L \\ d^L \end{pmatrix}, \begin{pmatrix} c^L \\ s^L \end{pmatrix}, \begin{pmatrix} t^L \\ b^L \end{pmatrix} \qquad \Psi^L{}_{\text{lepton}} = \begin{pmatrix} \nu_e^L \\ e^L \end{pmatrix}, \begin{pmatrix} \nu_\mu^L \\ \mu^L \end{pmatrix}, \begin{pmatrix} \nu_\tau^L \\ \tau^L \end{pmatrix} \quad . \tag{2.18}$$

The non-interacting right-handed fields are then treated as singlets,

$$\psi^R_{\text{quark}} = u^R, c^R, t^R, d^R, s^R, d^R \qquad \psi^R_{\text{lepton}} = \nu_e^R, \nu_\mu^R, \nu_\tau^R, e^R, \mu^R, \tau^R. \tag{2.19}$$

An $SU(2)_L$ gauge transformation is described by three angles $\theta_j(x)$ such that

$$\begin{aligned} \Psi^L &\xrightarrow{SU(2)_L} \Psi^{L\prime} = e^{i\frac{1}{2}\theta_j\tau_j}\Psi^L \\ \psi^R &\xrightarrow{SU(2)_L} \psi^{R\prime} = \psi^R \end{aligned} \tag{2.20}$$

and one infers that $I_3 = +\frac{1}{2}, -\frac{1}{2}, 0$ for up-type ψ^L, down-type ψ^L and ψ^R respectively.

$SU(2)_L$ gauge invariance requires a triplet of gauge bosons, $W^\mu = \frac{1}{2}\tau_j W^{j,\mu}$, which are analagous to the gluon octet but couple only to left-handed fermions. The off-diagonal terms in τ_1 and τ_2 allow for non-zero transition amplitudes between the upper and lower elements of the doublets. These are flavour changing interactions. When written in the appropriate basis they are interpreted as the emission and absorption of charged $W^{\pm,\mu} = \frac{1}{\sqrt{2}}\left(W^{1,\mu} \mp iW^{2,\mu}\right)$ bosons. The third Pauli matrix is diagonal and necessitates the existence of a neutral gauge boson $W^{3,\mu}$ whose interactions conserve fermion flavour.

The non-abelian nature of $SU(2)_L$ means that the field strength tensor is written with coupling constant q_{EW} as

$$W^i_{\mu\nu} = \partial_\mu W^i_\nu - \partial_\nu W^i_\mu + q_{EW} f^{ijk} W^j_\mu W^k_\nu \ . \tag{2.21}$$

In order to unify the weak nuclear and electromagnetic forces we require that equations of motion are invariant under simultaneous $SU(2)_L$ and $U(1)_Y$ transformations, where $U(1)_Y$ is a chirally independent gauge group associated with the weak hypercharge $Y = Q - I_3$.

Fermion fields then transform through an angle $\theta(x)$ via

$$\begin{aligned} \psi &\xrightarrow{U(1)_Y} \psi' = e^{iY_\psi \theta(x)}\psi \qquad \left[\text{e.g. } Y_{e^L} = -\frac{1}{2}\right] \\ \bar{\psi} &\xrightarrow{U(1)_Y} \bar{\psi}' = \bar{\psi} e^{iY_{\bar{\psi}}\theta(x)} \qquad \left[\text{e.g. } Y_{\bar{e}^L} = +\frac{1}{2}\right] \ . \end{aligned} \tag{2.22}$$

Consider the first generation left-handed leptons described by $\Psi^L = \begin{pmatrix} \nu_e^L \\ e^L \end{pmatrix}$ and $\psi^R \in \{\nu_e^R, e^R\}$. The Dirac Lagrangian density is

$$\begin{aligned} \mathcal{L}_{\text{Massless Dirac}} &= \mathrm{i}\bar{\nu}_e \partial\!\!\!/ \nu_e + \mathrm{i}\bar{e}\partial\!\!\!/ e \\ &= \mathrm{i}\bar{\Psi}^L \partial\!\!\!/ \Psi^L + \mathrm{i}\bar{\nu}_e^R \partial\!\!\!/ \nu_e^R + \mathrm{i}\bar{e}^R \partial\!\!\!/ e^R \end{aligned} \tag{2.23}$$

assuming zero masses. $SU(2)_L \times U(1)_Y$ gauge invariance leads to the covariant derivatives,

$$\begin{aligned} D^\mu \Psi^L &= \left[\partial^\mu - \mathrm{i}\frac{1}{2} q_{EW} \tau_j W^{j,\mu} - \mathrm{i} Y q'_{EW} B^\mu\right] \Psi^L \\ D^\mu e^R &= \left[\partial^\mu - \mathrm{i} Y q'_{EW} B^\mu\right] e^R \\ D^\mu \nu_e^R &= \partial^\mu \nu_e^R \end{aligned} \tag{2.24}$$

with the $U(1)_Y$ coupling constant q'_{EW}, gauge field B_μ and field strength tensor $B_{\mu\nu} = \partial_\mu B_\nu - \partial_\nu B_\mu$. The Lagrangian density is then

$$\mathcal{L}_{\text{Massless EW}} = -\frac{1}{4} B_{\mu\nu} B^{\mu\nu} - \frac{1}{4} W^j_{\mu\nu} W^{j,\mu\nu} + \mathrm{i}\bar{\Psi}^L \not{D} \Psi^L + \mathrm{i}\bar{\nu}_e^R \not{D} \nu_e^R + \mathrm{i}\bar{e}^R \not{D} e^R \tag{2.25}$$

and describes interactions between electrons and electron-neutrinos. This is generalised to all quark and lepton generations by the addition of similar terms for each fermion doublet. The electroweak theory contains two flavour conserving interactions associated with $W^{3,\mu}$ and B^μ. One can change basis using a linear transformation through angle θ_W via

$$\begin{pmatrix} W^{3,\mu} \\ B^\mu \end{pmatrix} = \begin{pmatrix} \cos\theta_W & \sin\theta_W \\ -\sin\theta_W & \cos\theta_W \end{pmatrix} \begin{pmatrix} Z^\mu \\ A^\mu \end{pmatrix} \ . \tag{2.26}$$

θ_W is chosen such that Z^μ couples only to I_3 and A^μ couples only to Q, interpreted as Z bosons and photons respectively. This is satisfied by

$$q_{EW} \sin\theta_W = q'_{EW} \cos\theta_W = q_e \ . \tag{2.27}$$

θ_W therefore determines the relative coupling strengths of the electromagnetic and weak interactions. Experimentally one finds that $\sin^2\theta_W$ is incompatible with the decoupled theory where $\theta_W = 0$ [42, 43]. Electroweak interactions are summarised in Figure 2.3.

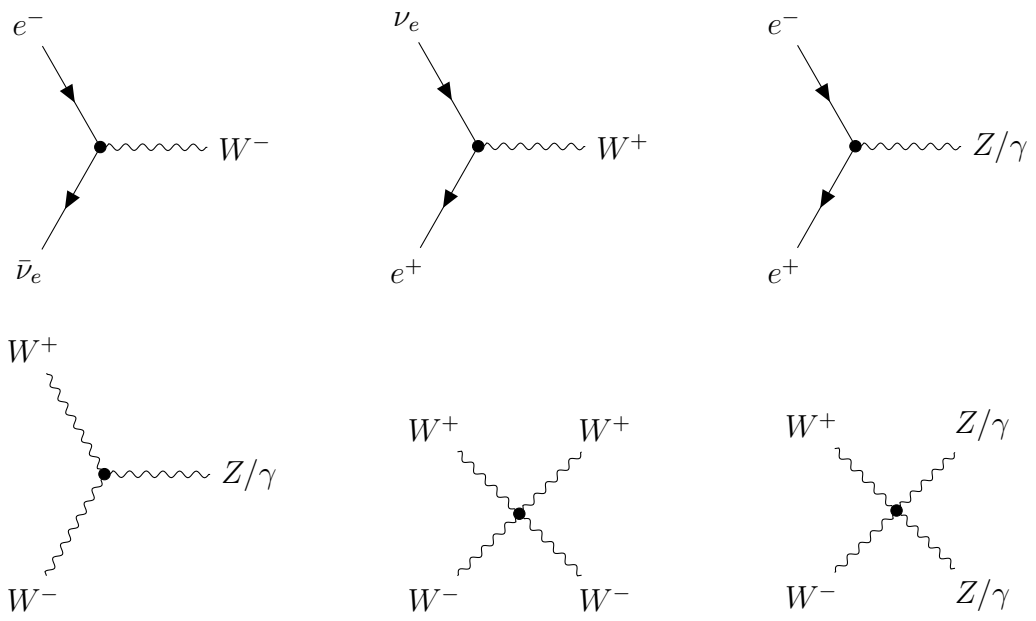

Figure 2.3: Electroweak diagrams for the first lepton generation assuming zero masses. The final diagram represents ZZ, $\gamma\gamma$ and $Z\gamma$ final states.

2.1.5 Mass terms and the Higgs field

Consider a boson, V^μ, which transforms through angle $\theta(x)$ in the adjoint representation of a $U(1)$ group with coupling, g, such that $V^\mu \to V'^\mu = V^\mu + \frac{1}{g}\partial^\mu\theta$. The mass, m_V, of this particle is described by a Lagrangian density of

$$\begin{aligned}\mathcal{L}_{\text{boson mass}} = & -\frac{1}{2}m_V^2 V_\mu V^\mu \\ \xrightarrow{U(1)} & -\frac{1}{2}m_V^2 V_\mu V^\mu - \frac{1}{2g^2}m_V^2\left(\partial_\mu\theta\right)\left(\partial^\mu\theta\right) - \frac{1}{g^2}m_V^2 V_\mu\left(\partial^\mu\theta\right)\end{aligned} \tag{2.28}$$

which breaks the gauge symmetry. In the same way, $W^\pm$ and Z boson mass terms break the $SU(2)_L + U(1)_Y$ electroweak gauge symmetry. One can also see that Dirac fermion mass terms of the form $-m_F\left[\bar{\psi}_F^R\psi_F^L + \bar{\psi}_F^L\psi_F^R\right]$ for some flavour F cannot be gauge invariant since only left-handed fields transform under $SU(2)_L$.

This problem can be resolved by treating $SU(2)_L \times U(1)_Y$ as a spontaneously broken gauge symmetry. Consider a system with a given symmetry. The ground state of this system can follow one of two cases: either it is a unique ground state which exhibits the symmetry; or it is one of a set of degenerate ground states all related by the symmetry transformation. In the latter case, the actual state of the system is not invariant under the symmetry transformation, although applying such a transformation leaves the system in an equivalent energy state. When the system de-excites from a higher energy state it must arbitrarily pick out a ground state to fall into. This is *spontaneous symmetry breaking*. Small perturbations about the ground state may then be insufficient in restoring

a symmetric excited state, and all such states exhibit the same asymmetry.

Spontaneous symmetry breaking occurs in a ferromagnet being cooled down from a high temperature. Initially, thermal motion means that atomic spins are randomly aligned, and so the net magnetic field is $\vec{0}$. As the temperature drops, nearest-neighbour magnetic interactions dominate over thermal motion and spins align causing a non-zero local magnetisation. At zero temperature, the ferromagnet reaches a ground state in which all spins are aligned in an arbitrary direction with a resulting non-zero magnetic field. Although the electromagnetic Hamiltonian is rotationally invariant, this ground state is not. A microscopic observer inside the magnet would observe rotationally invariant laws of physics but find that the equations of motion for charged particles would be affected by interactions with the magnetic field. It is a feature of spontaneous symmetry breaking that some observable quantity must have a non-zero ground state expectation value.

In a quantum field theory, the ground state is the vacuum and states with non-zero field quanta are perturbations. One can generate gauge boson mass terms through spontaneous symmetry breaking by introducing a complex scalar doublet field

$$\phi(x) = \begin{pmatrix} \phi_1(x) + \mathrm{i}\phi_2(x) \\ \phi_3(x) + \mathrm{i}\phi_4(x) \end{pmatrix} \tag{2.29}$$

which transforms through local angles $\theta_j(x), \theta(x)$ in the fundamental representation of $SU(2)_L \times U(1)_Y$ with $I_1, I_2, I_3, Y = \frac{1}{2}$ as

$$\phi(x) \xrightarrow{SU(2)_L \times U(1)_Y} \phi'(x) = e^{\frac{1}{2}\mathrm{i}q'_{EW}\theta(x)} e^{\frac{1}{2}\mathrm{i}q_{EW}\tau^j\theta_j(x)}\phi(x) \quad . \tag{2.30}$$

This value of Y ensures that ϕ_3 is electrically neutral with $I_3 = -\frac{1}{2}$. The dynamics of the field are described by the Lagrangian density,

$$\begin{aligned} \mathcal{L}_{\text{Scalar}} &= (D_\mu\phi)^\dagger (D^\mu\phi) - V(\phi) \\ V(\phi) &= \mu^2\phi^\dagger\phi + \lambda|\phi^\dagger\phi|^2 \end{aligned} \tag{2.31}$$

with the covariant derivative,

$$D^\mu\phi = \left[\partial^\mu - \frac{1}{2}\mathrm{i}q_{EW}\tau_j W^{j,\mu} - \frac{1}{2}\mathrm{i}q'_{EW}B^\mu\right]\phi \tag{2.32}$$

and a potential V determined by the parameters $\mu^2 < 0$ and $\lambda > 0$. This is the simplest form of a potential which is invariant under $SU(2)_L \times U(1)_Y$, tends to infinity as $\phi^\dagger\phi \to \infty$ and has a non-zero ground state satisfied by

$$\left[\phi_1^2 + \phi_2^2 + \phi_3^2 + \phi_4^2\right]^{\text{vacuum}} = -\frac{\mu^2}{2\lambda} \neq 0 \ . \tag{2.33}$$

A continuum of ground states exist, all related by $SU(2)_L \times U(1)_Y$ transformations. An arbitrary vacuum state must be picked out at low energies. The impact on the $W^{\pm}$ and Z boson equations of motion is observed as the existence of mass. One can choose a basis in which only one component of ϕ^{vacuum} is non-zero. Choosing $\phi_3^{\text{vacuum}} \neq 0$ and defining $v \equiv \sqrt{-\frac{\mu^2}{\lambda}}$ gives

$$\langle 0| \phi |0\rangle = \frac{1}{\sqrt{2}} \begin{pmatrix} 0 \\ v \end{pmatrix} . \tag{2.34}$$

Re-writing the doublet in terms of real scalar fields $\eta_1, \eta_2, \eta_3, H$ then gives

$$\phi(x) = \frac{1}{\sqrt{2}} \begin{pmatrix} \eta_1(x) + \mathrm{i}\eta_2(x) \\ v + H(x) + \mathrm{i}\eta_3(x) \end{pmatrix} \tag{2.35}$$

Since these four scalar fields each have a vacuum expectation value of 0, it is possible to quantise them and calculate energy levels perturbatively. It is also possible to perform an $SU(2)_L \times U(1)_Y$ transformation on ϕ which eliminates the η_1, η_2, η_3 fields. This choice is called the *unitary gauge*. The three η are massless Goldstone fields which contribute to transition amplitude calculations in other gauges but cannot be physically observable since they are not present in all gauges. Working in the unitary gauge gives

$$\phi(x) = \frac{1}{\sqrt{2}} \begin{pmatrix} 0 \\ v + H(x) \end{pmatrix} . \tag{2.36}$$

Expanding Eq. 2.31 gives the Lagrangian density

$$\begin{aligned} \mathcal{L}_{\text{Scalar}} = & \frac{1}{2} \left(\partial^\mu H\right) \left(\partial_\mu H\right) - \frac{1}{2} m_H^2 H^2 - 2v\mu^2 H \\ & - m_W^2 W_\mu^+ W^{-\mu} - \frac{1}{2} m_Z^2 Z_\mu Z^\mu \\ & + \frac{1}{4} q_{EW}^2 W_\mu^+ W^{-\mu} HH + \frac{1}{2} v q_{EW}^2 W_\mu^+ W^{-\mu} H \\ & + \frac{1}{8} \left(q_{EW}^2 + q_{EW}'^2\right) Z_\mu Z^\mu HH + \frac{1}{4} v \left(q_{EW}^2 + q_{EW}'^2\right) Z_\mu Z^\mu H \\ & - v\lambda H^3 - \frac{1}{4} \lambda H^4 \\ & + \text{constant} \end{aligned} \tag{2.37}$$

where $m_W = \frac{1}{2} v q_{EW}$ and $m_Z = \frac{1}{2} v \sqrt{q_{EW}^2 + q_{EW}'^2}$. The presence of a non-zero vacuum field has lead to the existence of mass terms for the $V \in \{W^{\pm}, Z\}$ bosons as well as interactions of the form $V\bar{V}H$ and $V\bar{V}HH$. H is a neutral spin-0 field with a mass of $m_H = 2\sqrt{-\mu^2}$ and has self-interaction terms of the form H^3 and H^4. The interactions introduced are summarised in Figure 2.4. Note that the vacuum state is not invariant under any component of $SU(2)_L \times U(1)_Y$ and thus all I_1, I_2, I_3, Y symmetries are spontaneously broken,

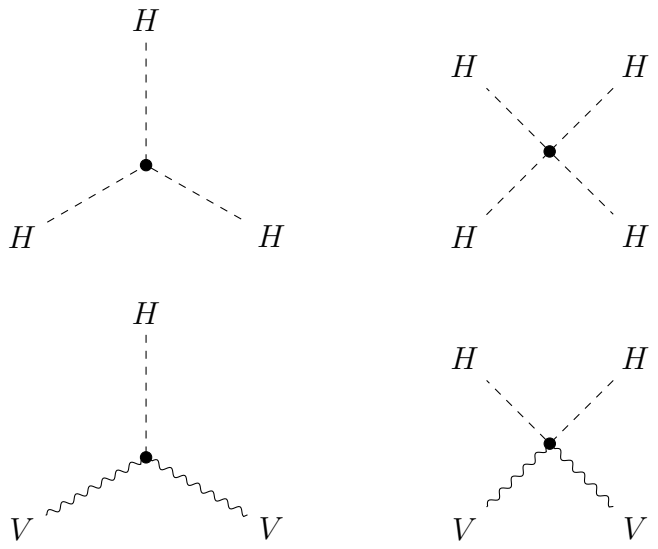

Figure 2.4: Interactions between the Higgs, H, and the weak bosons, $V \in \{W^{\pm}, Z\}$, after spontaneous breaking of $SU(2)_L \times U(1)_Y$ symmetry.

however it is invariant under the $U(1)_Q$ transformation of QED (since ϕ_3 is electrically neutral). This means that the associated gauge field, the photon, does not interact with H and remains massless after spontaneous symmetry breaking.

The spontaneous breaking of $SU(2)_L \times U(1)_Y$ symmetry down to $U(1)_Q$ can also be used to obtain mass terms for fermions assuming the existence of a gauge invariant fermion-ϕ interaction term. In the Standard Model, charged leptons are massive but neutrino masses are zero. For lepton flavour l this is described by a Lagrangian density of the form

$$\begin{aligned}
\mathcal{L}_{\text{Yukawa }(l)} &= -y_l \left[\bar{\Psi}_l^L \phi \psi_l^R + \bar{\psi}_l^R \phi^\dagger \Psi_l^L\right] \\
&= -m_l \left[\bar{\psi}_l^L \psi_l^R + \bar{\psi}_l^R \psi_l^L\right] - \frac{y_l}{\sqrt{2}} H \left[\bar{\psi}_l^L \psi_l^R + \bar{\psi}_l^R \psi_l^L\right] \\
&= -m_l \bar{\psi}_l \psi_l - \frac{y_l}{\sqrt{2}} H \bar{\psi}_l \psi_l
\end{aligned} \tag{2.38}$$

where $m_l = \frac{y_l v}{\sqrt{2}}$. Thus one obtains a charged lepton mass and a chirally independent interaction with the Higgs field. For quarks, both the up- and down-type elements of the doublet are required to have mass. For the first generation, $q \in \{u, d\}$, this can be achieved using a Lagrangian density of the form

$$\begin{aligned}
\mathcal{L}_{\text{Yukawa }(q)} &= -y_d \left[\bar{\Psi}_q^L \phi \psi_d^R + \bar{\psi}_q^R \phi^\dagger \Psi_d^L\right] + -y_u \left[\bar{\Psi}_q^L \phi_C \psi_u^R + \bar{\psi}_u^R \phi_C^\dagger \Psi_q^L\right] \\
&= -m_u \bar{\psi}_u \psi_u - m_d \bar{\psi}_d \psi_d - \frac{y_u}{\sqrt{2}} H \bar{\psi}_u \psi_u - \frac{y_d}{\sqrt{2}} H \bar{\psi}_d \psi_d
\end{aligned} \tag{2.39}$$

where $m_u = \frac{y_u v}{\sqrt{2}}$, $m_d = \frac{y_d v}{\sqrt{2}}$ and $\phi_C = -\mathrm{i}[\phi^\dagger \tau_2]^{\mathrm{T}}$. These terms mean that all fermions except for neutrinos obtain mass and an interaction with the Higgs boson after spontaneous symmetry breaking. This interaction is shown in Figure 2.5.

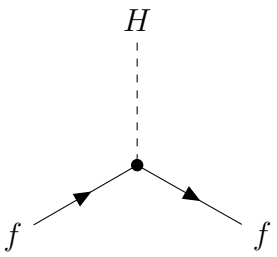

Figure 2.5: Interactions between the Higgs, H, and massive fermions, f.

2.1.6 Flavour and mass states

We have so-far written the fermion fields in such a way that point interactions occur between distinct generations of quarks or leptons. This is important when considering flavour changing weak nuclear interactions. However, all initial, intermediate and final states must propagate between vertices during scattering processes. Such fields are most intuitively written as mass eigenstates, i.e. those which diagonalise the free-field part of the Hamiltonian. These are two distinct bases related by linear transformations.

Quarks are labelled as mass eigenstates. Consider the three generations of down-type mass eigenstates, $i \in \{d, s, b\}$, and flavour states, $j \in \{d_1, d_2, d_3\}$. These are related by a unitary transformation U^d_{ij}. For up-type quarks, call them $k \in \{u, c, t\}$, $j \in \{u_1, u_2, u_3\}$ and U^u_{kj} respectively. The common index j is used in both cases because flavour changing interactions only occur within a single generation of flavour states. The change into the mass basis means that the $u \to W^+ d$ transition amplitude is modifed by a factor $\sum_j U^d_{dj} \left(U^{u\dagger}\right)_{ju}$. In general, any flavour changing transition of the form $k \to i$ is modified by a factor $\left(V^\dagger\right)_{ik} = \sum_j U^d_{ij} \left(U^{u\dagger}\right)_{jk}$. This is a unitary 3×3 matrix with four degrees of freedom after accounting for all Standard Model constraints. It includes one imaginary term which is a source of CP symmetry violation. Off-diagonal terms allow for non-zero transition amplitudes between different quark generations.

By convention we write the effect of V as a modification the down-type field, $\{d, s, b\} \to \{d', s', b'\}$, such that transitions only occur between the same generation of up-type and modified down-type states (e.g. $u \to W^+ d'$, $c \to W^+ s'$ and $t \to W^+ b'$). This is called the Cabibbo-Kobayashi-Maskawa (CKM) matrix [44, 45],

$$\begin{pmatrix} \psi_{d'} \\ \psi_{s'} \\ \psi_{b'} \end{pmatrix} = \begin{bmatrix} V_{ud} & V_{us} & V_{ud} \\ V_{cd} & V_{cs} & V_{cd} \\ V_{td} & V_{ts} & V_{td} \end{bmatrix} \begin{pmatrix} \psi_d \\ \psi_s \\ \psi_b \end{pmatrix} \quad . \tag{2.40}$$

Although the Standard Model treats neutrinos as massless, neutrinos must have non-zero mass to explain the phenomenon of neutrino oscillations. Each neutrino flavour state $\psi_{\nu_e}, \psi_{\nu_\mu}, \psi_{\nu_\tau}$ is written as a linear combination of mass eigenstates $\psi_{\nu 1}, \psi_{\nu 2}, \psi_{\nu 3}$ using the

Pontecorvo-Maki-Nakagawa-Sakata (PMNS) matrix [46, 47], in an analagous way to the rotation between quark mass and flavour states described by U^u. Consider that a beam of neutrinos is created in a pure flavour state. The three different mass states propagate with different momentum (wavelength), and so their relative amplitudes vary as a function of distance from the source. The transition amplitudes at any point in space depend on the amplitudes of the the flavour states. Rotating back into the flavour basis, the neutrino is no longer in a pure flavour state, and so one can observe neutrino interactions in a different flavour to that of the original beam (or a deficit of interactions in the same flavour). These are called oscillations. The existence of non-zero neutrino masses has no observable consequence for the measurements contained within this thesis.

2.1.7 Summary of the Standard Model

The Standard Model has been formulated as a gauge theory describing the interactions of 12 fermion, 12 antifermion and 5 boson fields. Quanta of these fields are observed as discrete particles. The gauge symmetries are described by the $SU(3)_C$ group, corresponding to strong nuclear interactions mediated by gluons, and $SU(2)_L \times U(1)_Y$, corresponding to electroweak interactions mediated by $W^{\pm}/Z$ bosons and photons. The $SU(2)_L \times U(1)_Y$ symmetry is spontaneously broken down to $U(1)_Q$ resulting in a non-zero vacuum expectation value for the field, ϕ_3. This results in mass terms for $W^{\pm}$, Z, quarks and charged leptons. Neutrinos are known to have mass, but this is not taken into account within the Standard Model.

Fermions are separated into *quark* and *lepton* states, of which only quarks have colour charge and interact with gluons. Each category consists of three generations of doublets. Only left-handed doublets interact via $SU(2)_L$. Mixing occurs between different quark generations (mass eigenstates) as described by the CKM matrix. Right-handed neutrinos are not included within the Standard Model.

The field ϕ is an $SU(2)_L \times U(1)_Y$ doublet with four real scalar components. One of these components manifests as a real scalar Higgs field, H, after spontaneous symmetry breaking. Gluons form an octet of massless spin-1 fields associated with the allowed colour transitions of quarks. The photon is a massless spin-1 field associated with the unbroken $U(1)_Q$ symmetry and couples proportionately to electric charge Q. The $W^{\pm}/Z$ fields are massive spin-1 fields associated with the three broken components of $SU(2)_L \times U(1)_Y$ and couple proportionately to I_3.

A summary is shown in Table. 2.1 using Particle Data Group (2017) masses [48]. The top quark mass is defined by direct measurement.

Type	Generation		Field	Mass	Spin	Colour	I_3	Q	Y
Lepton	1	(up)	ν_e^L	0	$1/2$	–	$+1/2$	0	$-1/2$
		(down)	e^L	511 keV	$1/2$	–	$-1/2$	-1	$-1/2$
	2	(up)	ν_μ^L	0	$1/2$	–	$+1/2$	0	$-1/2$
		(down)	μ^L	106 MeV	$1/2$	–	$-1/2$	-1	$-1/2$
	3	(up)	ν_τ^L	0	$1/2$	–	$+1/2$	0	$-1/2$
		(down)	τ^L	1.8 GeV	$1/2$	–	$-1/2$	-1	$-1/2$
			e^R	511 keV	$1/2$	–	0	-1	-1
			μ^R	106 MeV	$1/2$	–	0	-1	-1
			τ^R	1.8 GeV	$1/2$	–	0	-1	-1
Quark	1	(up)	u^L	~ 2.2 MeV	$1/2$	Triplet	$+1/2$	$+2/3$	$+1/6$
		(down)	d^L	~ 4.7 MeV	$1/2$	Triplet	$-1/2$	$-1/3$	$+1/6$
	2	(up)	c^L	~ 1.3 GeV	$1/2$	Triplet	$+1/2$	$+2/3$	$+1/6$
		(down)	s^L	~ 96 MeV	$1/2$	Triplet	$-1/2$	$-1/3$	$+1/6$
	3	(up)	t^L	~ 173 GeV	$1/2$	Triplet	$+1/2$	$+2/3$	$+1/6$
		(down)	b^L	~ 4.2 GeV	$1/2$	Triplet	$-1/2$	$-1/3$	$+1/6$
	1		u^R	~ 2.2 MeV	$1/2$	Triplet	0	$+2/3$	$+2/3$
			d^R	~ 4.7 MeV	$1/2$	Triplet	0	$-1/3$	$-1/3$
	2		c^R	~ 1.3 GeV	$1/2$	Triplet	0	$+2/3$	$+2/3$
			s^R	~ 96 MeV	$1/2$	Triplet	0	$-1/3$	$-1/3$
	3		t^R	~ 173 GeV	$1/2$	Triplet	0	$+2/3$	$+2/3$
			b^R	~ 4.2 GeV	$1/2$	Triplet	0	$-1/3$	$-1/3$
Boson			γ	0	1	–	0	0	0
			$W^\pm$	80 GeV	1	–	± 1	± 1	0
			Z	91 GeV	1	–	0	0	0
			g	0	1	Octet	0	0	0
			H	125 GeV	0	–	$-1/2$	0	$+1/2$

Table 2.1: Summary of Standard Model fields. The convention $Y = Q - I_3$ is used. Masses are quoted from the Particle Data Group (2017) [48].

2.2 Cross sections

In Section 2.1 it was discussed that the transition amplitude, S_{fi}, for a scattering process between free initial $|i\rangle$ and final $|f\rangle$ states at times $t = \pm\infty$ can be inferred at a finite order of perturbation theory using the interaction terms present in the Hamiltonian. The transition probability is then $P_{i\to f} = |S_{fi}|^2$. The initial and final states contain exact momenta, spin, polarisation and colour. In order to relate this to a measurable quantity we define the cross section, σ, as the probability of observing a transition from any available initial state into any of the measured final states per scattering point per unit incident flux per unit time.

The initial states of ATLAS $H \to \gamma\gamma/4l$ measurements are proton constituents at the collision energy. The final states are those containing a diphoton or four-lepton sys-

tem originating from an on-shell Higgs decay. In principle one cannot specify intermediate states such as the Higgs. However, if interference between the $pp \to H \to \gamma\gamma$ and other $pp \to \gamma\gamma$ diagrams is small then the combined cross section can be written as $\sigma(pp \to \gamma\gamma) \approx \sigma(pp \to H \to \gamma\gamma) + \sigma(\text{other})$ where $\sigma(pp \to H \to \gamma\gamma)$ is calculated exclusively from diagrams that contain a Higgs decay and σ (other) is calculated exclusively from those that don't. Fiducial cross sections and bins of differential observables are obtained by applying constraints to the final state four-momenta.

Consider the cross section, $\mathrm{d}\sigma$, of two particles transitioning over volume V and time T into an infinitesimal volume of n final states. The volume of final states is

$$N = \prod_n \frac{V \mathrm{d}^3\vec{p}_n}{(2\pi)^3} \tag{2.41}$$

and the transition probability density per scattering point per unit time is $w = \frac{|S_{fi}|^2}{T}$. If the relative velocity of the initial states is v in then their flux is $f = \frac{V}{v}$ and $\mathrm{d}\sigma$ is given by

$$\mathrm{d}\sigma = \frac{w}{f} \cdot N \ . \tag{2.42}$$

The total cross section is obtained by integration of $\mathrm{d}\sigma$ in the limit of $V, T \to \infty$ such that

$$\sigma \ = \int \mathrm{d}\sigma \ = \lim_{V,T\to\infty} \int \frac{|S_{fi}|^2}{T} \cdot \frac{V}{v} \cdot \prod_n \frac{V \mathrm{d}^3\vec{p}_n}{(2\pi)^3} \ . \tag{2.43}$$

Since transitions with different spin, polarisation or colour states cannot interfere, one can sum or average their cross sections as desired. The dependence of σ with respect to some observable, $\mathcal{O}$, is studied using $\frac{\mathrm{d}\sigma}{\mathrm{d}\mathcal{O}}$ or by comparing to binned measurements by calculating σ over the phase space of each bin. These are differential cross sections.

2.3 Modelling of hadron-hadron physics

It is necessary to predict the behaviour of scattering processes at the LHC, and it is usually not feasible to make analytic predictions due to the challenging nature of the calculations and the complexity of high energy proton collisions. Instead, the *Monte Carlo* method is used in which a large number N of $pp \to X$ scattering events are simulated for any given process, generated and weighted according to their expected probability densities using random phase space sampling. Events are normalised to the best cross section calculation available. One can then study the properties of the simulated events in a variety of contexts. The finite nature of N causes statistical fluctuations on the expected distributions. These are minimised by making N as large as necessary.

This section details the methodology for Monte Carlo event simulation. The following steps are used, each of which is characterised by an energy scale based on the momentum

transfer or mass of particles produced:

1. *Parton distribution functions* (PDFs) are used to parameterise the probability of probing initial state partons with particular momenta when two protons collide.

2. Perturbative QFT calculations and numerical phase space integration provide the probability of transitioning into different final state configurations given a set of allowed processes. This is called the *hard scatter*.

3. Splitting of coloured initial and final state partons via $q \to qg$ and $g \to gg$ is modelled, referred to as the *parton shower*.

4. The non-perturbative evolution of bare quarks and gluons into colour neutral hadrons is modelled, referred to as *hadronisation*.

5. Additional interactions between the proton constituents are modelled. The objects created are overlayed with the hard scatter and called the *underlying event*.

6. The products of additional $p-p$ collisions, called *in-time pileup*, are overlayed. Models are tuned to match experimental observations.

The calculations of hard scatter transition amplitudes (*matrix elements*) are performed at finite order in perturbation theory. The leading order (LO) diagram of a QCD or electroweak process is that which contains the smallest number of couplings. Next to leading order (NLO) calculations include contributions from diagrams with one extra coupling, such as an additional gluon or quark emission. The accuracy of the calculation improves as the number of orders increases to NNLO, N^{3}LO etc. at the cost of computational complexity.

2.3.1 PDFs and matrix elements

A proton is a bound state of *uud* quarks, called valence quarks, which continuously interact via the exchange of gluons. These gluons produce short-lived $q\bar{q}$ pairs of all flavours, called *sea quarks*. All other particles are present at a lower rate due to electroweak interactions. All of these particles, called *partons*, may be initial states for the hard scatter interaction when two protons collide.

Parton distribution functions (PDFs), ρ^i, represent the probability of resolving a parton of type i with momentum $x_i p$ where x_i is the fraction of the proton momentum, p. Cross section calculations are factorised so that the non-perturbative colour confinement behaviour of QCD, defined with momentum transfer below a certain *factorisation scale* μ_f, is absorbed into the PDF. These are constrained experimentally. The hard scatter is then defined as including all interactions at scales above μ_f.

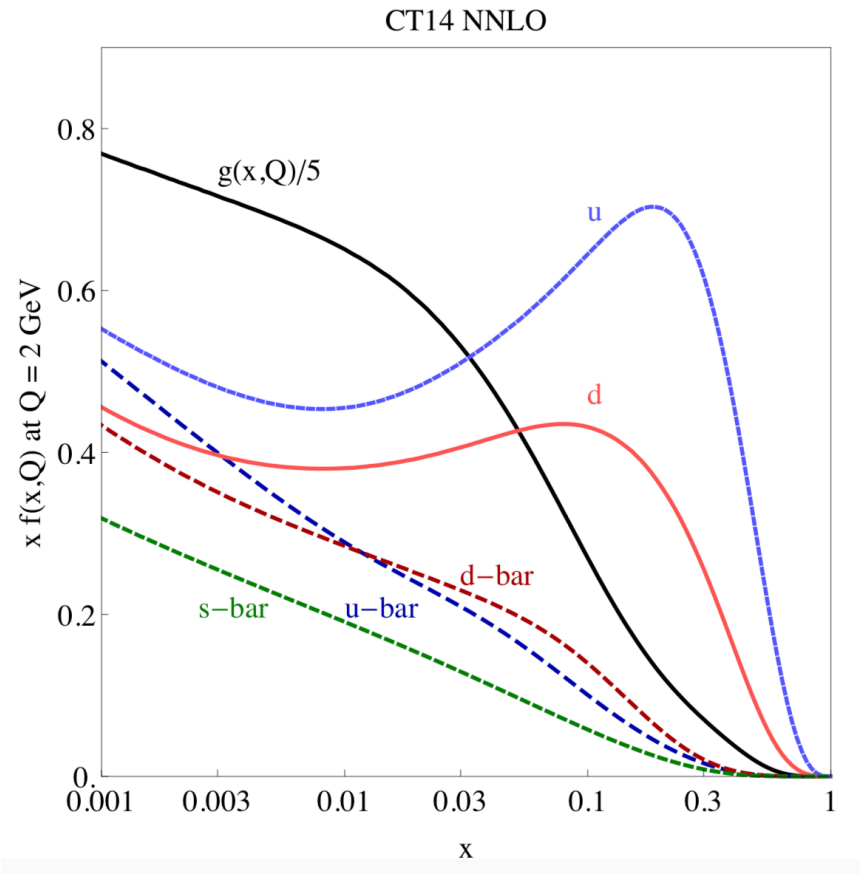

Figure 2.6: CT14 PDF, $f(x, Q)$ at a factorisation scale of $Q = 2$ GeV where x is the faction of the proton momentum carried by the parton. Valence quarks dominate at $x \gtrsim 0.2$. Gluons dominate at low x. This figure is sourced from Ref. [49].

The CT14 PDF set [49] is shown in Figure 2.6 with $Q \equiv \mu_\mathrm{f} = 2$ GeV. Valence quarks dominate at $x \gtrsim 0.2$ whereas gluons dominate at low x. The sea quark contribution also increases at low x. Note that the gluon PDF, $g(x, Q)$, is shown with a scale factor of $1/5$.

Inelastic proton collisions at $\sqrt{s} = 13$ TeV are dominated by $2 \to N$ scattering processes. One initial state parton is taken from each proton and labelled i, j. The matrix element describes the amplitude for obtaining a set of final states, X. It is calculated at finite order in perturbation theory above the factorisation scale using all relevant parameters of the field theory, $\vec{\lambda}$. These include the renormalisation scale up to which the theory is defined. Integrating over the available phase space, one can then derive the hard scatter cross section, $\sigma^{ij\to X}$.

The total cross section for $pp \to X$ is obtained by summing over all incoming partons and integrating over allowed momenta, i.e.

$$\sigma^{pp\to X}\left(\mu_\mathrm{f}, \vec{\lambda}\right) = \sum_{i,j} \int \mathrm{d}x_i \rho^i\left(x_i, \mu_\mathrm{f}\right) \int \mathrm{d}x_j \rho^j\left(x_j, \mu_\mathrm{f}\right) \; \sigma^{ij\to X}\left(x_i p, x_j p, \mu_\mathrm{f}, \vec{\lambda}\right) \; . \quad (2.44)$$

The squared partonic centre-of-mass energy is $\hat{s} = x_1 x_2 s$ when neglecting partonic masses.

2.3.2 Parton shower and hadronisation

The parton shower simulates the splitting of objects in the initial and final states of the hard scatter [50]. For particles with colour, this occurs as a cascade of soft $q \to qg$ and $g \to gg$ emissions which occur iteratively with decreasing scale until an infrared cutoff is reached. Splittings below this scale are considered unresolvable. This removes soft and collinear divergences and so the splitting probabilities can be calculated using perturbation theory. At this stage, colour confinement effects become important and the evolution of partons into colour neutral hadrons is modelled non-perturbatively. This is called hadronisation. The upper scale of the parton shower is defined so as to avoid double counting with emissions already contained within the hard scatter amplitude. The scale evolution of the shower may be expressed as an angular or transverse momentum ordering.

Initial state showers are modelled in the same way as final state showers except that they evolve backwards from the hard scatter process. This is because we require the initial state of the hard scatter to be the result of any splitting. This modifies the flavour and momentum fraction at which the PDF is evaluated. The impact of parton shower is absorbed into $\sigma^{ij\to X}$ in Eq. 2.44.

The most common hadronisation methods follow the Lund string [51, 52] and cluster models. The Lund string model interprets the QCD field lines between quarks as massless strings which store potential energy. A spontaneous $q\bar{q}$ production occurs when a string is sufficiently stretched, breaking it and splitting the system. This process repeats iteratively and hadrons are formed from the resulting quarks without intermediate states. The cluster model enforces the splitting of gluons via $g \to q\bar{q}$ at the shower cutoff scale creating a shower of quarks which form confined colour connected pairs called clusters. These are modelled as excited meson states which decay into hadrons. All implementations are tuned to match data observations.

The parton shower and hadronisation programs used in this thesis are `Pythia 8` [53] (transverse momentum ordering and Lund string hadronisation), `Herwig ++` [54–56] and `Herwig 7` [57, 58] (angular ordering and cluster hadronisation).

2.3.3 Underlying event

A hadron-hadron collision produces many objects in association with the final states resulting from the hard scatter. These are referred to as the underlying event (UE). The dominant sources are (i) the fragmentation of the beam remnants and (ii) scattering between the remaining partons of the protons. The latter are called multiple parton interactions (MPI). The underlying event therefore results from a combination of perturbative splittings, perturbative interactions and non-perturbative hadronic processes. It is complicated by the colour connections between many of the processes occuring in the event.

Underlying event activity creates a high multiplicity pedestal of low-energy objects,

especially at forward rapidities where radiation from, and splitting of, the beam remnants is most probable. By enforcing the condition that the proton collision contained a hard scatter event, we impose a selection bias towards central collisions. These typically have increased underlying event activity and so a higher energy pedestal.

The underlying event is simulated using a variety of perturbative models which are tuned to match the particle multiplicities and energy spectra observed in data. It contributes a background energy density throughout the event. This also impacts the jet reconstruction discussed in section 2.3.4.

2.3.4 Jets

The successive splittings associated with parton shower and hadronisation tend to transform a single parton-level object into a cluster of collimated particles. In particular, a hard scatter may produce a gluon or quark which quickly forms a cluster of hadrons. A jet is a theoretical object defined by recombining these constituents with the aim of reconstructing the original parton. The jet activity of an event is thus intended to match the partonic final states. Various clustering algorithms are available. All jets used in this thesis are defined using the anti-k_T algorithm [59]. This is infra-red and collinear (IRC) safe, meaning that the reconstructed jet four-momenta are not dependent on the low-energy or small-angle splitting of particles. They also have well defined areas which are resilient against change when such splittings occur, or when low energy objects are overlayed throughout the event. This is beneficial in environments with large underlying event or pileup contributions.

The anti-k_T algorithm iteratively re-combines all inputs using measures of momentum and separation. Objects are preferentially clustered if they are nearby and at least one of them is highly energetic. Isolated high momentum objects lead to conical jets with a radius equal to a tunable parameter r in rapidity-azimuth space. They combine into a single non-conical jet if they are separated by less than r and two non-conical intersecting jets if between r and $2r$. Jet clustering algorithms can be applied to any set of topological objects. These include simulated particles before and after the parton shower, energy measurements and reconstructed tracks.

2.4 The Higgs sector

This thesis contains measurements of events in which a Higgs boson decays into diphoton or four lepton final states. This section describes how one expects the Higgs boson to be produced at the Large Hadron Collider, and subsequently decay, within the Standard Model. Observed deviations from this behaviour may indicate the existence of particles or interactions beyond the Standard Model (BSM).

2.4.1 Production of the Higgs at the LHC

When two protons collide with a centre-of-mass energy of $\sqrt{s} = 13$ TeV, gluons, g, and valence quarks, u/d, are the most likely initial states for Higgs production followed by sea quarks, $q/\bar{q}$ (see Section 2.3.1). The four dominant processes are summarised in Figure 2.7 and can be categorised as follows:

(a) Gluon fusion (ggF) in which the Higgs is produced from two gluons via $gg \to H$. Since no direct gluon-Higgs coupling exists within the Standard Model, the process is mediated at leading order by a massive fermion loop as shown in Figure 2.8.

(b) Vector Boson Fusion (VBF) in which the Higgs is produced from a W^+W^- or ZZ pair via $V\bar{V} \to H$. The W and Z bosons originate from initial state quarks which scatter through to the final state (with a change of flavour in the case of $W^\pm$ fusion). These shower and hadronise resulting in two forward jets.

(c) Vector boson associated production (VH) in which the Higgs is radiated from an off-shell vector boson via $V^* \to VH$. There is an additional vector boson in the final state which creates quark jets, charged leptons and/or neutrinos.

(d) Two-quark associated production (qqH) in which the Higgs is produced from a $q\bar{q}$ pair via $q\bar{q} \to H$ with a $q\bar{q}H$ final state. For ttH, the top quarks decay before hadronisation via $t \to bW$ with $W \to l\nu/qq'$ leading to a high multiplicity final state.

Table. 2.2 shows the total cross sections, σ^{tot}, for these production processes as predicted by the SM [28]. Additional sub-dominant contributions exist from $tHX = \{tHq, tHW\}$ associated production. Gluon fusion, VBF and VH are the dominant processes for SM Higgs production, contributing 87 %, 7 % and 4 % respectively.

Process	$\sqrt{s} = 8$ TeV			$\sqrt{s} = 13$ TeV		
	σ^{tot} [pb]	f [%]	$N/20$ fb^{-1}	σ^{tot} [pb]	f [%]	$N/36$ fb^{-1}
ggF	$21.4^{+0.9}_{-1.5}$	87.4	430k	$48.5^{+2.2}_{-3.3}$	87.2	1.8M
VBF	1.60 ± 0.03	6.5	32k	3.78 ± 0.08	6.8	136k
WH	0.70 ± 0.02	2.9	14k	1.37 ± 0.03	2.5	49k
ZH	0.42 ± 0.01	1.7	8k	$0.89^{+0.04}_{-0.03}$	1.6	42k
ttH	0.13 ± 0.01	0.5	3k	$0.51^{+0.03}_{-0.05}$	0.9	18k
bbH	$0.20^{+0.04}_{-0.05}$	0.8	4k	$0.49^{+0.10}_{-0.11}$	0.9	18k
tHX	0.023 ± 0.003	< 0.1	470	0.09 ± 0.01	0.2	3k

Table 2.2: Cross section, σ^{tot}, and fraction, f, of the dominant Higgs boson production mechanisms at the LHC with $\sqrt{s} = 8, 13$ TeV and $m_H = 125.09$ GeV [28]. The expected number of Higgs events, N, is provided for the Run 1 and Run 2 datasets respectively. Gluon fusion is dominant and makes up 87 % of single Higgs events. Interference between ggF and bbH reduces the combined cross section by < 0.1 %. This will be accounted for by an 8 % reduction of the bbH cross section (not applied here).

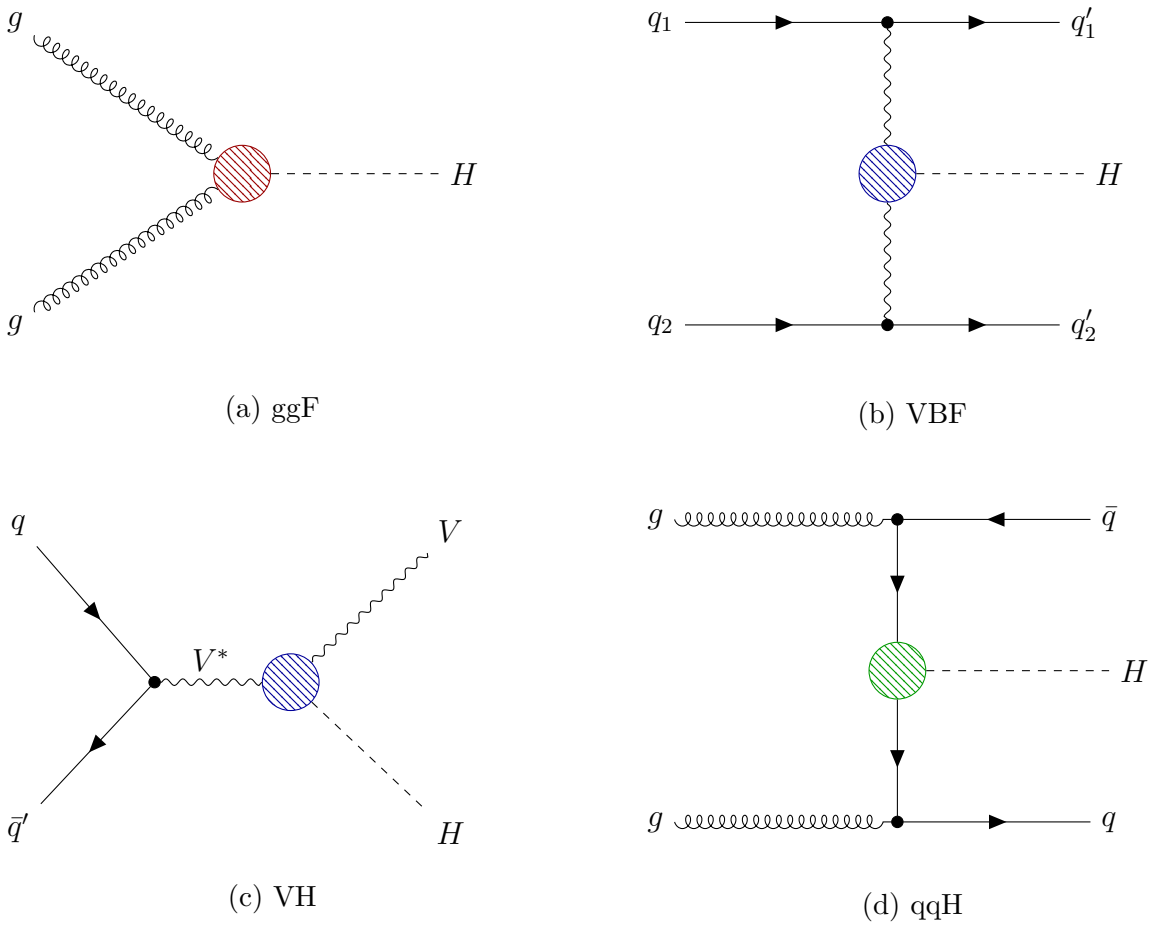

Figure 2.7: Leading order diagrams for the four dominant Higgs production processes. Couplings between the Higgs and SM particles are shown as coloured circles. The leading order Higgs-gluon coupling is shown in Figure 2.8.

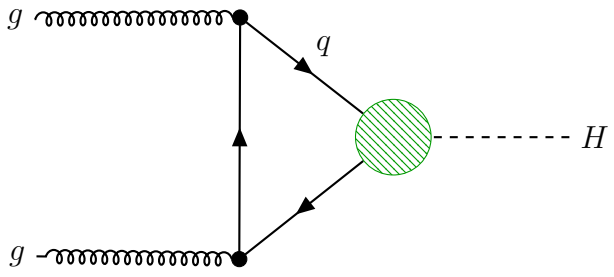

Figure 2.8: Leading order diagram for the Higgs-gluon coupling. It may be sensitive to BSM interactions and heavy coloured BSM particle loops.

Couplings between the Higgs and SM particles are highlighted by the coloured hatched areas in Figure 2.7. The leading order Higgs-gluon coupling (red), as shown in Figure 2.8, occurs through a quark loop at leading order. This is dominated by the top quark since the Yukawa coupling is proportional to the fermion mass. BSM interactions and heavy coloured BSM particles may be indirectly observed through their contribution to this loop. Direct couplings exist between the Higgs and V (blue) or f (green) within the Standard Model. These may also be modified by loop contributions from BSM particles and BSM interactions between the Higgs and SM particles. Modified couplings affect the rate of Higgs production as well as the kinematic distributions of the Higgs and final state particles produced in association with it. These effects may be observable in differential cross section measurements.

2.4.2 Decay of the Higgs

Figure 2.9 [28] shows the dominant branching ratios, $\mathcal{BR}$, for a SM Higgs boson around the measured mass of 125.09 ± 0.36 GeV [26]. Despite a large expected Yukawa coupling, the $H \to t\bar{t}$ decay is disallowed because $m_H < 2m_t$. $H \to b\bar{b}$ is therefore the dominant decay mode. Decay rates to the remaining fermions are ordered by fermion mass. Despite large expected coupling strengths, the $H \to VV^*$ decay modes are suppressed due to the requirement that one vector boson be produced off-shell. The $H \to gg$, $H \to \gamma\gamma$ and $H \to Z\gamma$ decay modes are also suppressed since they occur through loop diagrams at leading order.

The dominant decay diagrams for the $H \to \gamma\gamma$ channel are shown in Figure 2.10. The loop is mediated by charged massive particles and may be indirectly sensitive to contributions from BSM particles and modified interactions. The final state is characterised by two isolated photons with an invariant mass of m_H. The SM branching ratio is $\mathcal{BR}(H \to \gamma\gamma) = 0.227(5)$ % [28]. Destructive interference with the process $gg \to \gamma\gamma$ is estimated to reduce the ggF cross section by approximately 1 % [60–62].

The dominant decay diagram for the $H \to ZZ^* \to 4l$ channel is shown in Figure 2.11 where $l, l' \in \{e, \mu\}$. One of the Z bosons must be produced off-shell because the Higgs boson mass is not sufficient for the production of two on-shell Z-bosons. The final state is characterised by two opposite sign dilepton systems, where the invariant mass of one pair is m_Z and that of the four lepton system is m_H. The SM branching ratio is $\mathcal{BR}(H \to 4l) = 0.0124$ % [63].

2.4.3 Higgs production cross section calculations

The total cross sections of the dominant Higgs boson production processes are modelled following the recommendations of the LHC Higgs Cross Section Working Group [28]. The ggF cross section is calculated with N^{3}LO (QCD) accuracy including NLO electroweak

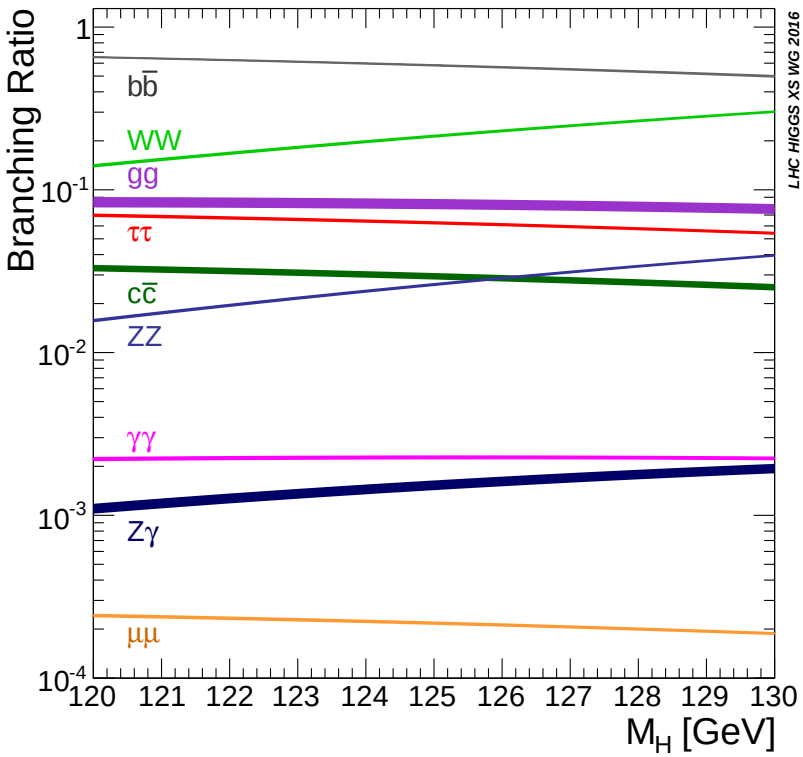

Figure 2.9: Branching ratios of the Higgs provided by Ref. [28]. The Higgs mass is 125.09 ± 0.24 GeV measured by ATLAS and CMS in Run 1 [26].

corrections [64–67]. The VBF, WH and ZH cross sections are calculated with NNLO (QCD) accuracy including NLO electroweak corrections [68–73], except for the $gg \to ZH$ process which follows a resummed calculation at NLO+NLL (QCD). The ttH cross section is calculated with NLO (QCD) accuracy including NLO electroweak corrections [74–77]. The bbH cross section is obtained using a 5-flavour NNLO (QCD) calculation matched to 4-flavour NLO (QCD) using the Santander scheme [78–80].

2.4.4 Event generators

Several event generators are considered when modelling the dominant Higgs boson production and background processes. Those relevant for the work presented in this thesis are described below. Signal generators were chosen through consultation with the analysers of other Higgs boson decay channels within the ATLAS collaboration. They are used consistently in several resulting measurements [5, 63, 81, 82].

The generators are chosen because they provide state-of-the-art accuracy when modelling their relevant processes differentially with respect to energy spectra, rapidities, jet multiplicities and angular separations. They can therefore be used to estimate the signal or background behaviour in all regions of phase space. State-of-the-art modelling of specific Higgs boson production characteristics, such as the shape of the Higgs p_{T} spectrum or the kinematic behaviour of two-jet associated production, may be compared with the relevant

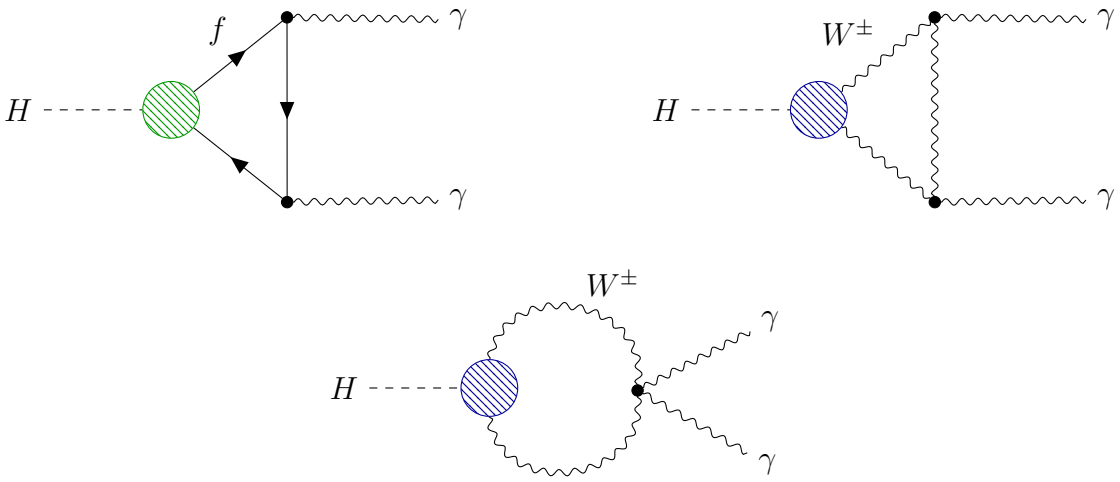

Figure 2.10: Leading order diagrams for Higgs decay into two photons, mediated by fermion and W-boson loops in the SM with $\mathcal{BR}(H \to \gamma\gamma) = 0.227(5)$ % [28]. This may be sensitive to BSM interactions and heavy charged BSM particle loops.

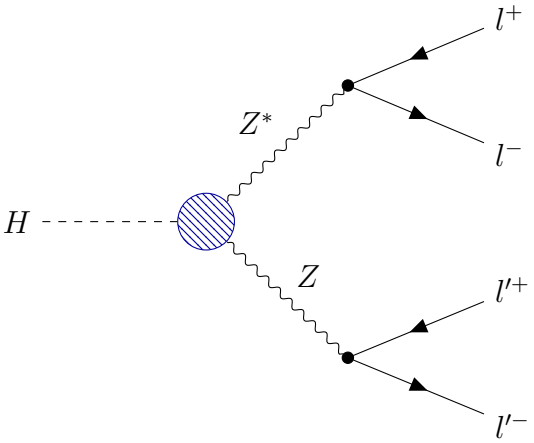

Figure 2.11: Leading order diagram for Higgs decay into $l^+l^-l'^+l'^-$ with $l, l' \in \{e, \mu\}$. One Z is off-shell. The SM branching ratio is $\mathcal{BR}(H \to 4l) = 0.0124$ % [28, 63].

differential measurements when appropriate.

Another important consideration is the method for matching (or merging) the matrix element with the parton shower. This ensures that the matrix element and parton shower combine to describe QCD emissions with the greatest possible accuracy and ensures that the full phase space of final states is modelled without double counting or dead regions. This is of particular importance when modelling observables such as jet multiplicities and jet kinematic distributions.

The `Powheg-Box` program [83–87] is used to generate events for the VBF and VH processes using an NLO (QCD) matrix element calculation with NLO matching performed

using the Powheg method [88]. The MG5_aMC@NLO program [89] can generate events with either leading order or NLO accuracy. It is used to generate NLO events which are matched or merged with NLO accuracy using the MC@NLO [90] and FxFx [91] methods respectively.

The Sherpa program [92, 93] is used to generate events at leading order, allowing for the real emission of additional final state partons, with tree-level matching performed using the MEPS@LO [94] prescription.

Gluon fusion (ggF) events are generated with NNLO (QCD) accuracy using the Powheg NNLOPS program [95]. This is achieved by reweighting the events generated at NLO (QCD) using the Hj-MiNLO program, with NLO matching performed using the Powheg method, to reproduce the Higgs rapidity spectrum from the HNNLO program [96].

Review of Higgs measurements

This chapter summarises a selection of Higgs boson measurements from Run 1 of the LHC. These data were collected with centre-of-mass energies of $\sqrt{s} = 7$ and 8 TeV. The selected results precede the work contained within this thesis. They are presented to provide context for the Run 2 measurements presented in later chapters. Two other Run 2 measurements are also referenced as they represent important milestones in the observation of Higgs boson interactions with other SM particles. An exhaustive list of Higgs boson measurements in Run 2 is not provided.

3.1 Decay channels

During Run 1, the Higgs was observed individually in the $\gamma\gamma$ [60, 97] and $ZZ^* \to 4l$ [98, 99] channels by both the ATLAS and CMS collaborations. Decay through the $WW^* \to l\nu l\nu$ channel was observed by ATLAS [100, 101] and studied by CMS [102] . Observation is defined by a significance of at least 5σ corresponding to a p-value of less than 6×10^{-7}. In the case of a Gaussian probability distribution, this is the number of standard deviations by which the measurement is consistent with the null-signal hypothesis. The $\tau\tau$ [103, 104] , bb [105, 106] and $\mu\mu$ [107, 108] channels were also studied. Table 3.1 shows the measured and expected significances of the five channels with leading sensitivity [109]. The combination of channels in both ATLAS and CMS results in an observed significance of 11σ [109].

Channel	Measured significance [σ]	
	ATLAS	CMS
$H \to \gamma\gamma$	5.0 (4.6)	5.6 (4.1)
$H \to ZZ^* \to 4l$	7.6 (5.6)	7.0 (6.8)
$H \to WW^* \to l\nu l\nu$	6.8 (5.8)	4.8 (5.6)
$H \to \tau\tau$	4.4 (3.3)	3.4 (3.7)
$H \to bb$	1.7 (2.7)	2.0 (2.5)

Table 3.1: Measured (expected) significance of Higgs channels in Run 1 of the LHC, adapted from Table 5 of Ref. [109].

3.2 Mass, spin and parity

During Run 1, the Higgs mass was measured to be

$$m_H = 125.09 \pm 0.21\,(\text{stat.}) \pm 0.11\,(\text{syst.})\ \text{GeV} \tag{3.1}$$

using a statistical combination of the $\gamma\gamma$ and $ZZ^* \to 4l$ channels in both ATLAS and CMS. This represents a precision of 0.2 % dominated by statistical fluctuations.

The Standard Model describes the Higgs with a spin of $S = 0$, a parity of $P = +1$ and symmetry under charge conjugation, $C = +1$. For a state with orbital angular momentum of $L = 0$ and total angular momentum $J = L + S$, we write $J^P = 0^+$. An alternative hypothesis is that of a spin-2 Higgs field with $J^P = 2^+$. Other spin values are disallowed as they cannot describe the observed decays into pairs of electroweak gauge bosons. A third hypothesis is a pseudoscalar field A which has negative parity, $J^P = 0^-$.

ATLAS measurements comparing these three spin/parity hypotheses are presented in Ref. [27] using the combination of the $\gamma\gamma$, $ZZ^* \to 4l$ and $WW^* \to e\nu\mu\nu$ channels. The equivalent CMS analysis is presented in Ref [110] with identical conclusions. A likelihood ratio test statistic is profiled using the measured event yields within several categories defined by observables capable of discriminating between hypotheses. In the diphoton channel these are the transverse momentum of the reconstructed Higgs and the angle between a decay photon and the beam axis as measured in the Collins-Soper reference frame [111][1], both of which are sensitive to spin. In the ZZ^* and WW^* channels, angular information from the decay leptons provides information about the vector boson polarisations and so parity can also be constrained.

The pure 0^- and 2^+ hypotheses are excluded with a probability of greater than 99.9 % and limits are set on possible mixing between SM scalar, BSM scalar and BSM pseudoscalar fields which would violate CP symmetry. Previous $ZZ^* \to 4l$ and $WW^* \to e\nu\mu\nu$ measurements exclude the $1^\pm$ hypotheses with a probability of greater than 99.9 % [112].

3.3 Signal and coupling strengths

The *signal strength*, μ, of a process $A \to B$ is defined as the ratio between the measured cross section, σ^{meas}, and the Standard Model expectation, σ^{SM}, i.e.

$$\mu\,(A \to B) = \frac{\sigma^{\text{meas}}\,(A \to B)}{\sigma^{\text{SM}}\,(A \to B)}\ . \tag{3.2}$$

[1] This is the rest frame of the Higgs, in which the two photons are back-to-back and so have the same polar angle with respect to the beam.

The compatibility with $\mu = 1$ represents the agreement between the measurement and the Standard Model. Event yields are measured in several phase space regions that preferentially enhance or suppress different production processes. A profile likelihood test statistic is used to constrain the global normalisation of each process.

Signal strengths were measured for the various Higgs boson production processes using the combination of all decay channels in both ATLAS and CMS [109]. These are shown in Figure 3.1(a). The ttH measurement deviates above the Standard Model at the level of 2.2σ with all other production mechanisms consistent to within 1σ. Figure 3.1(b) shows the measured signal strengths for the various decay channels (combining all production processes). All measurements are consistent with the Standard Model at the level of approximately 1σ.

The global signal strength combines all production processes and decay channels and is shown at the bottom of Figure 3.1(a). It is consistent with the Standard Model at the level of 1σ with a precision of 10 %. The measured value is

$$\begin{aligned} \mu\,(pp \to H) &= 1.09\ ^{+0.11}_{-0.10} \\ &= 1.09\ \pm 0.07\,(\text{stat.})\ ^{+0.09}_{-0.08}\,(\text{syst.})\ . \end{aligned} \tag{3.3}$$

Ref. [109] also combines the ATLAS and CMS measurements of coupling strengths within the κ-framework. These are factors, κ_X, which scale the tree level Standard Model coupling between the Higgs and particle X. Deviations from $\kappa = 1$ may indicate new physics. Figure 3.2 shows a non-exhaustive example of these measurements which are all consistent with the Standard Model hypothesis of $\kappa = 1$.

3.4 Differential cross sections

Whilst signal and coupling strength measurements are sensitive parameterisations of the agreement between the data and the Standard Model, they are dependent on the accuracy of the Standard Model calculation and are not valid in the presence of BSM interactions that change the kinematic dependence of a production process. This limits their ability to constrain alternative physics models. It is desirable to characterise the behaviour of Higgs events in a minimally model dependent way by measuring differential cross sections in a fiducial phase space. These can be re-interpreted after-the-fact to constrain new physics models or test Standard Model predictions.

The most sensitive differential cross section measurements were performed in the $\gamma\gamma$ and $ZZ^* \to 4l$ decay channels by both ATLAS [113, 114] and CMS [115, 116]. Figure 3.3 shows four observables from the ATLAS $H \to \gamma\gamma$ analysis. These are (a) the Higgs transverse momentum (b) the angle between the photons and beam axis in the Collins-Soper frame [111] (c) the jet multiplicity and (d) the leading jet transverse momentum. These illustrate

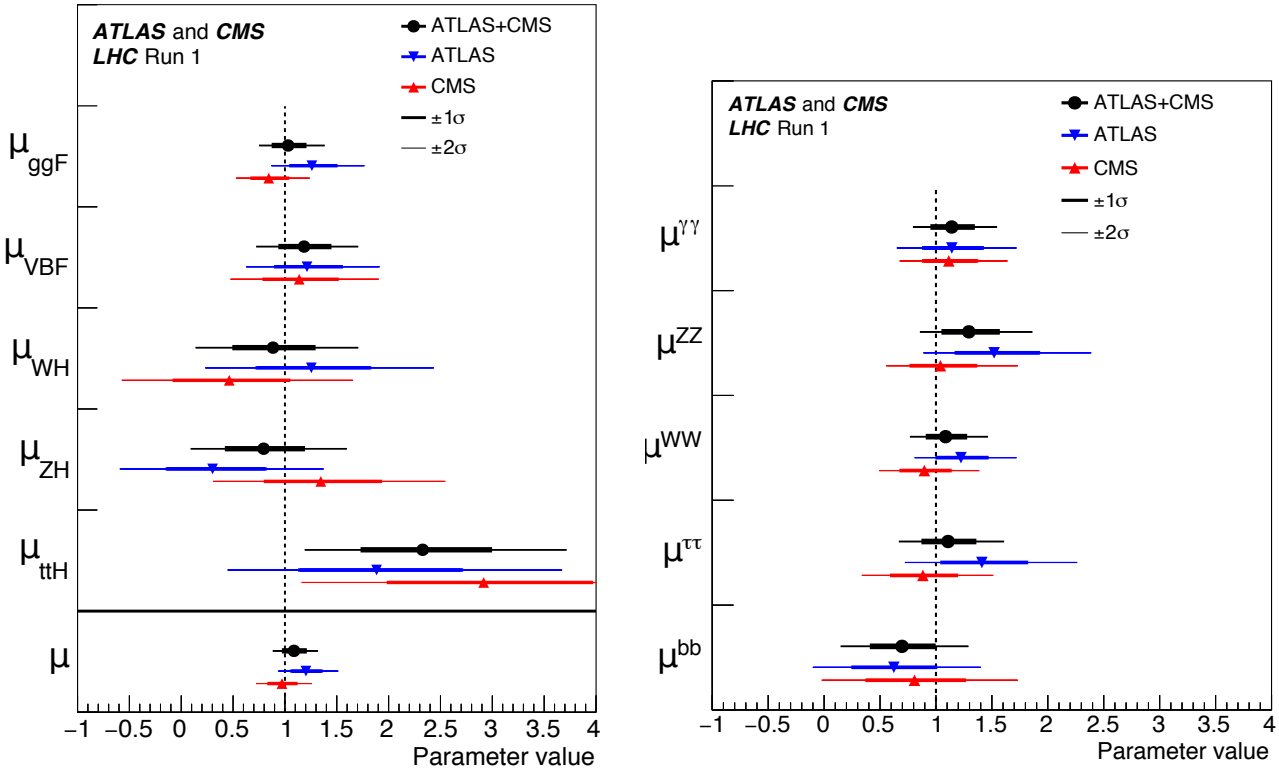

(a) Production process (b) Decay channel

Figure 3.1: Examples of combined ATLAS and CMS signal strength measurements in Run 1. This figure is sourced from Ref. [109].

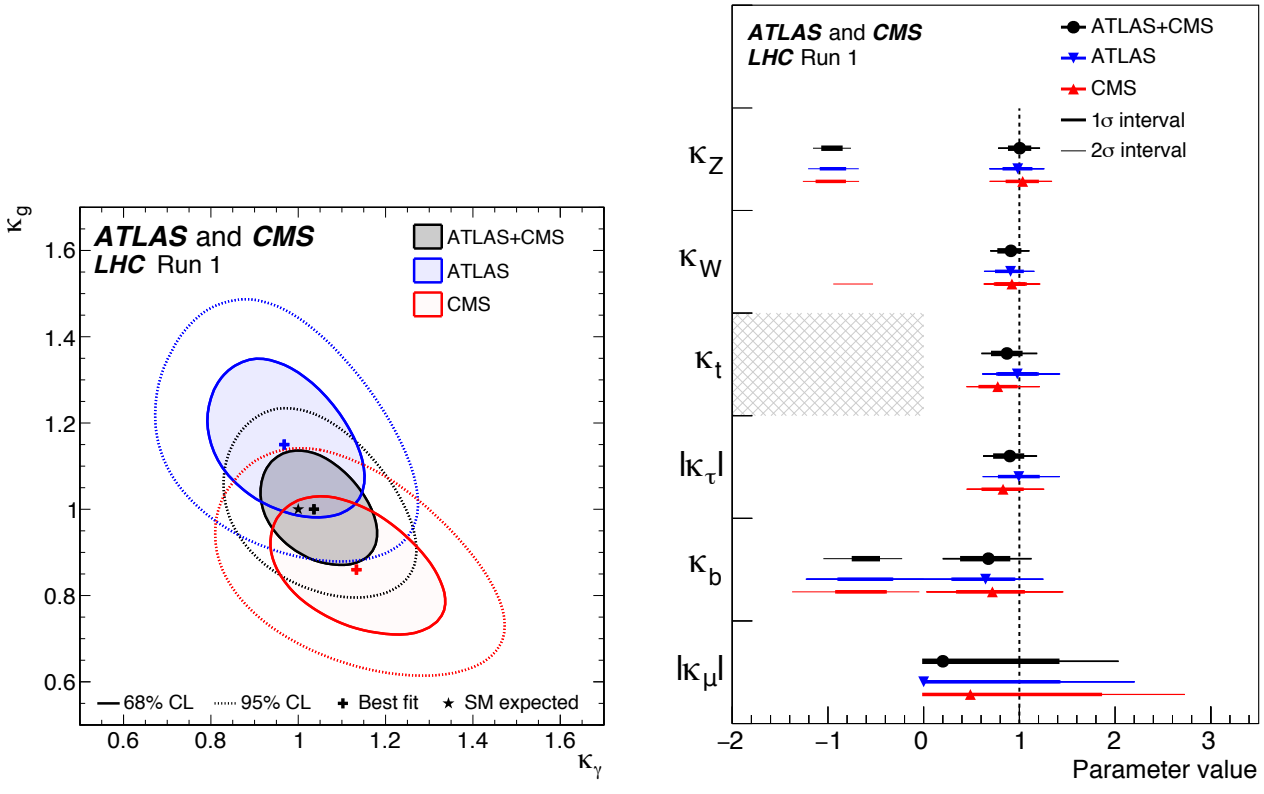

(a) κ_g versus κ_γ (b) κ_V and κ_f

Figure 3.2: Examples of combined ATLAS and CMS coupling strength measurements in Run 1. This figure is sourced from Ref. [109].

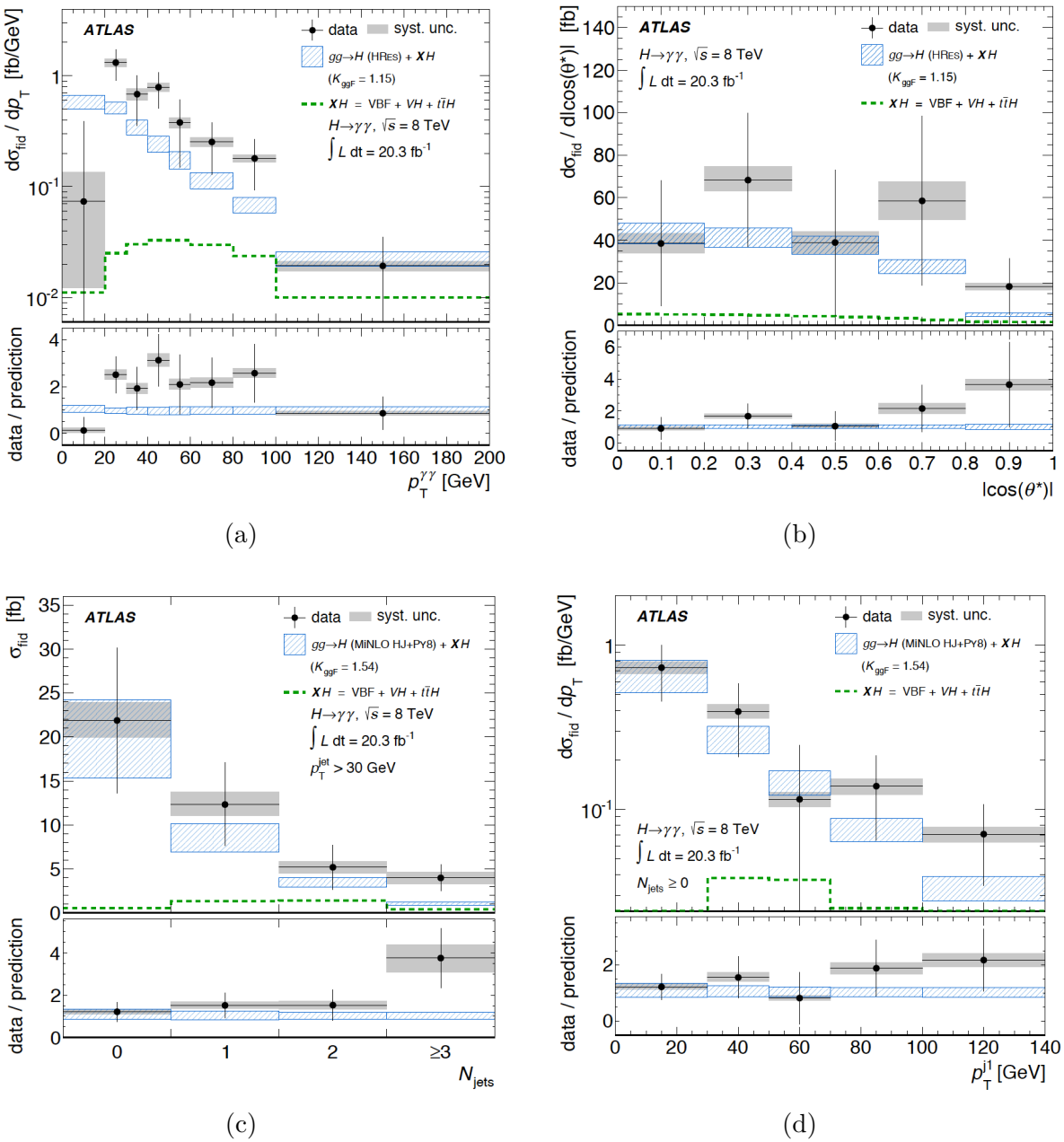

Figure 3.3: Examples of differential cross section measurements in the $H \to \gamma\gamma$ channel with ATLAS at $\sqrt{s} = 8$ TeV. Sourced from Ref. [113]. Observables are (a) the Higgs transverse momentum (b) the photon polar angle in the Collins-Soper frame [111] (c) the jet multiplicity and (d) the leading jet transverse momentum.

observables defined by the properties of the Higgs, its decay products, the topology of the event and additional final state objects. All analyses are dominated by statistical uncertainties.

3.5 Results during Run 2

This section describes two important measurements performed during Run 2 of the LHC. Many other measurements have also been performed with improved sensitivity compared with the Run 1 analyses. These include measurements in the $\tau\tau$ [117, 118] and $WW^* \to e\nu\mu\nu$ [119, 120] decay channels and updated mass measurements [121, 122].

The ttH production process has been observed by both ATLAS [123, 124] and CMS [125–130] using the combination of data collected in Runs 1 and 2. Whilst the ggF process provides indirect sensitivity to the top quark Yukawa coupling, because the top quark is assumed to dominate the loop which mediates the gluon-Higgs interaction, the ttH measurements provide direct sensitivity. This is an important test of the Standard Model in which Yukawa terms are the source of fermion mass. Deviations from the Standard Model may indicate a variety of new physics (see e.g. Ref. [131]). All measurements are consistent with the SM expectation.

The decay of the Higgs boson through the $b\bar{b}$ channel has been observed by both ATLAS [132] and CMS [133] using the combination of data collected in Runs 1 and 2. The analyses of both experiments are dominated by VH production. They provide direct sensitivity to the bottom quark Yukawa coupling, motivated in the same way as the top quark Yukawa coupling above. All measurements are consistent with the SM expectation. The interactions of the Higgs with the two heaviest quarks have therefore been directly observed.

Note that the Higgs decay into lepton pairs was observed in the $H \to \tau\tau$ channel using the combination of ATLAS and CMS data in Run 1 [109]. This means that interactions with both quarks and leptons have now been observed.

The ATLAS experiment

ATLAS is one of the two general purpose detectors at the Large Hadron Collider (LHC) at CERN, the European Organisation for Nuclear Research. This chapter provides a technical overview of the LHC and the ATLAS experiment. It then describes the reconstruction of final state objects, which correspond to particles interacting with the detector.

4.1 The Large Hadron Collider

The LHC is the highest energy particle accelerator in the world [21–23, 134]. It is designed to collide beams of protons at centre-of-mass energies of up to $\sqrt{s} = 14$ TeV and with a peak instantaneous luminosity of $\mathcal{L} \sim 10^{34}$ cm^{-2}s^{-1}, or beams of heavy ions with $\sqrt{s} =$ 5.02 TeV/nucleon and $\mathcal{L} \sim 10^{27}$ cm^{-2}s^{-1}.

The LHC is located in the 26.7 km tunnel originally built for the Large Electron-Positron (LEP) collider [135–138]. Particle-antiparticle colliders such as LEP and Tevatron [139] can accelerate both counter-rotating beams using the same magnetic field, however this is not possible for a proton collider. The tunnel has an internal diameter of 3.7 m and is arranged into 8 arc and 8 straight sections. These contain 4 interaction points (IPs) where beam collisions occur, as well as collimation, radio frequency (RF) cavity and beam dump systems among others. It is not possible to contain two separate magnet systems within the diameter of the tunnel, therefore a twin bore approach is used in which a single magnet system produces two coupled magnetic fields with opposite polarity.

The LHC injection chain makes use of several staged accelerator systems [134, 140]. Protons are obtained from ionised hydrogen gas and linearly accelerated to momenta of 50 MeV by LINAC-2. This will be replaced by LINAC-4 after Run 2 [141, 142]. These are sequentially accelerated up to 1.4 GeV by the booster ring, to 25 GeV by the Proton Synchrotron (PS) and to 450 GeV by the Super Proton Synchrotron (SPS). They are then fed into the LHC by two 2 km-long tunnels. Finally, the LHC uses the RF cavity to accelerate the protons to 6.5 TeV (Run 2). The arcs contain 8 T dipole magnets to guide the beams around the ring and a combination of dipole, quadrupole, sextupole and octopole magnets to control the beam optics. Up to 2556 proton bunches are circulated with a spacing of 25 ns in each beam [143].

The following seven experiments are located at the interaction points:

ATLAS [19, 144] is a general purpose detector designed for sensitivity to a range of final state objects and topologies typical of SM electroweak interactions, Higgs boson production, soft QCD and possible signatures of BSM physics on the $\mathcal{O}(10-1000)$ GeV scale. Acceptance is maximised by full azimuthal coverage and longitudinal coverage at angles not prohibited by the beam pipe.

CMS [20] is a general purpose detector with a single magnetic field provided by a compact superconducting solenoid. It has similar acceptance, resolution and physics goals to ATLAS. Measurements of physical processes are expected to be compatible between the ATLAS and CMS experiments to ensure their reproducibility.

LHCb [145] is a single arm forward spectrometer designed with excellent particle identification and vertex resolution. It targets sensitivity to flavour physics including rare B-meson decays, mixing and the formation of (possibly exotic) bound states. A key goal is the constraint of CKM matrix parameters including the CP-violating phase and unitarity triangles in which BSM contributions may be indirectly observed.

ALICE [146] is a general purpose detector designed to study the behaviour of QCD at high energy densities, in particular the formation of a non-confined state called the quark-gluon plasma, the energy of which is expected to be achievable at the LHC. It primarily studies heavy nucleus collisions in which $\mathcal{O}(8000)$ charged particles are expected to be produced.

TOTEM [147] combines telescopes in the CMS forward region with Roman pot detectors located $147-220$ m from the IP. These are used for precision measurements of the total, elastic and diffractive $p-p$ cross sections.

LHCf [148] uses sampling and imaging calorimeters at $z = \pm 140$ m from the ATLAS interaction point to measure the spectra of very forward photons and pions. These are used to constrain electromagnetic shower models, describing interactions of cosmic rays with nuclei in the upper atmosphere, at a centre-of-mass equivalent of $\sim 10^{17}$ eV cosmic protons [149].

MoEDAL [150] is integrated around the LHCb Vertex Locator. It is designed to track and trap highly ionising BSM particles such as magnetic monopoles, up to masses of several TeV, and massive stable charged particles.

Approximately 48.1 pb^{-1} data was delivered to ATLAS at a centre-of-mass energy of 7 TeV in 2010 followed by 5.5 fb^{-1} in 2011 and 22.8 fb^{-1} of 8 TeV data in 2012. Run 2 of the LHC delivers 13 TeV proton collisions with 4.2 fb^{-1} delivered in 2015, 38.5 fb^{-1} in 2016, 50.2 fb^{-1} in 2017 and further collisions being delivered in 2018.

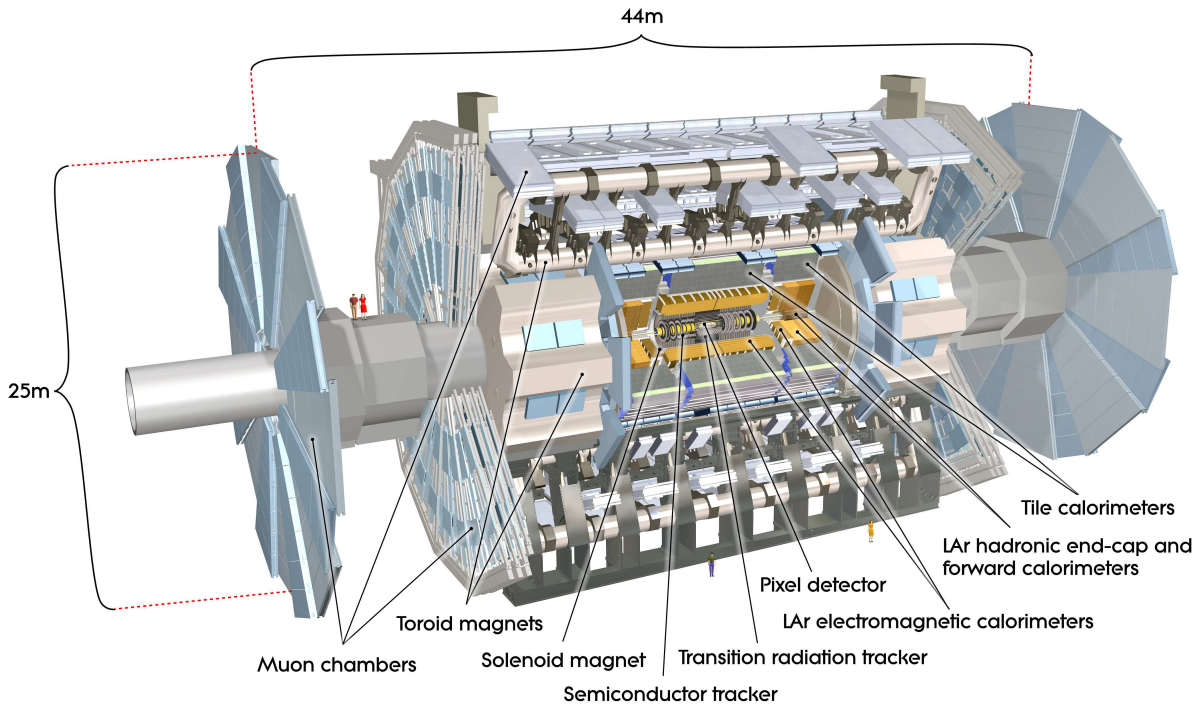

Figure 4.1: Layout and dimensions of the ATLAS detector. This figure is sourced from Ref. [144].

4.2 The ATLAS detector

The measurements and searches targeted by ATLAS are characterised by a variety of final state particles and topologies. These must all be identified and reconstructed with sufficient efficiency, granularity, acceptance and resolution. This is achieved by nesting several detector subsystems, each of which are optimised for the measurement of different particles and spanning a hermetic region around the interaction point.

Figure 4.1 shows the layout of the ATLAS detector. Particles are produced at the IP in the centre and progress through the various detector subsystems. These will be described in the following sections. The dimensions of ATLAS are driven by the size of the toroid magnets leading to a height of 25 m, a length of 44 m and a mass of 7000 T.

Detector subsystems are designed to tolerate the high intensity radiation doses experienced over several years of running and use fast shielded or radiation-hard electronics capable of providing a distinct readout efficiently associated with a 25 ns bunch crossing. Full or partial detector readouts are saved to disk for events which exhibit characteristic signatures of the physical processes of interest, such as the presence of isolated photons or leptons. This fast decision-making process is controlled by the trigger system.

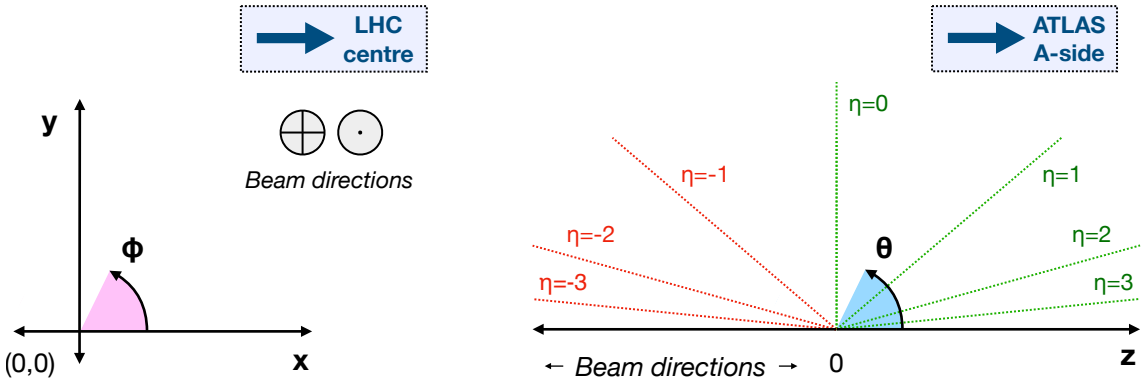

(a) Transverse to beam

(b) Parallel to beam

Figure 4.2: ATLAS coordinate system. The x, y-plane is transverse to the beamline which runs parallel to the z axis. Beams collide at the interaction point at $(x, y, z) = (0, 0, 0)$. Solid angles are defined by the coordinates, (η, ϕ).

4.2.1 Coordinate system

The ATLAS coordinate system is defined as right-handed with the origin $(x, y, z) = (0, 0, 0)$ at the interaction point. The x-axis points towards the centre of the LHC ring and the y-axis points upwards. These describe a plane transverse to the beamline. The azimuthal angle in the transverse plane is labelled ϕ and is measured anticlockwise from the x-axis. The z-axis runs parallel to the beamline. The positive z-direction is labelled as the A-side and the negative z-direction is the C-side. The angle with respect to the beamline is labelled θ.

The momentum in a direction i is labelled p_i and the total energy is E. The momentum of an object in the transverse plane is labelled p_T with a transverse energy defined as $E_T = E \sin\theta$. The rapidity y of an object is defined as

$$y = \frac{1}{2} \ln \frac{E + p_Z}{E - p_Z} \tag{4.1}$$

and is a mass-dependent measure of longitudinal boost. The massless limit of rapidity is called the pseudorapidity, η, and is related to θ by

$$\eta = -\ln \tan \frac{\theta}{2} \,. \tag{4.2}$$

Figure 4.2 summarises the ATLAS coordinate system. Solid angles are labelled as points in the η, ϕ-plane. If two objects are separated by $\Delta\phi$, $\Delta\eta$ and Δy then their separation is quantified by the measures

$$\begin{aligned} \Delta R &= \sqrt{\Delta\eta^2 + \Delta\phi^2} \\ \Delta R^y &= \sqrt{\Delta y^2 + \Delta\phi^2} \,. \end{aligned} \tag{4.3}$$

4.2.2 Inner detector

The Inner Detector (ID) [144, 151] is designed to measure charged particles close to the IP. Their charge, vertex of origin and transverse momentum are determined using the direction and radius of curvature within a 2 T axial magnetic field provided by a thin superconducting solenoid magnet. Three subsystems are used with increasing radius from the IP. These are the Pixel (including the Insertable B-layer, IBL), semiconductor tracker (SCT) and transition radiation tracker (TRT). All three systems register hits when traversed by a charged particle. The particle track is reconstructed using pattern recognition algorithms as described in Section 4.3. Other than the IBL, each subsystem is divided into barrel and end-cap regions. These are optimised for resolution over a wide acceptance in $|\eta|$. Figure 4.3 shows the layout and dimensions of the ID. The design transverse momentum resolution is

$$\frac{\Delta p_{\mathrm{T}}}{p_{\mathrm{T}}} = 0.05\ \% \times \frac{p_{\mathrm{T}}}{\mathrm{GeV}} \bigoplus 1\ \% \ . \tag{4.4}$$

The impact parameters d_0 and z_0 are respectively the transverse and longitudinal displacements of a track at the point at which it is closest to the beamline. This is called the perigee. The design d_0 resolution is 10 μm for central high-p_T tracks.

The Pixel [152, 153] and SCT [154] detectors span a range of $|\eta| < 2.5$ using silicon pixels and strips, respectively, which respond with hits as charged particles pass through and excite electrons to the conduction band (leaving holes in the valence band). A bias voltage causes these charges to drift towards electrodes and provide a readout current. The use of pixels at $33 - 150$ mm radius from the IP improves track resolution within an environment where $\mathcal{O}\,(1000)$ charged particles are expected to be produced per proton bunch crossing and provides sensitivity to secondary interaction vertices created from heavy flavour hadron and τ decays. The barrel layers are organised into three concentric 4 m long cylinders. The end-cap disks are transverse to the beamline with three layers on each side of the IP. The pixel size is $50 \times (400 - 600)$ μm^2 with 47 thousand pixels located on each of the 1744 sensors and a total of approximately 80 million readout channels. The bias voltage varies between 150 V and $\lesssim$ 600 V, the largest being expected at the end of Run 2 to counteract the impact of radiation damage. The IBL is an additional pixel layer placed in the barrel at a radius of 33 mm with a pixel size of 50×250 μm^2. This system was introduced at the start of Run 2 with the aim of further improving impact parameter and vertex resolution. One IBL and three other Pixel hits are expected from each charged particle originating from the primary interaction vertex.

The SCT consists of 4 layers of stereo sensors in the barrel cylinders and axial sensors on 9 perpendicular end-cap disks located at a radius of $299 - 560$ mm from the IP. Each sensor is double layered, and each layer consists of two 6 cm long silicon strips of approximately 80 μm pitch. The layers are angled at 207/162 μrad in order to provide hits on a 2-dimensional plane. There are 15912 such sensors operating with a bias voltage

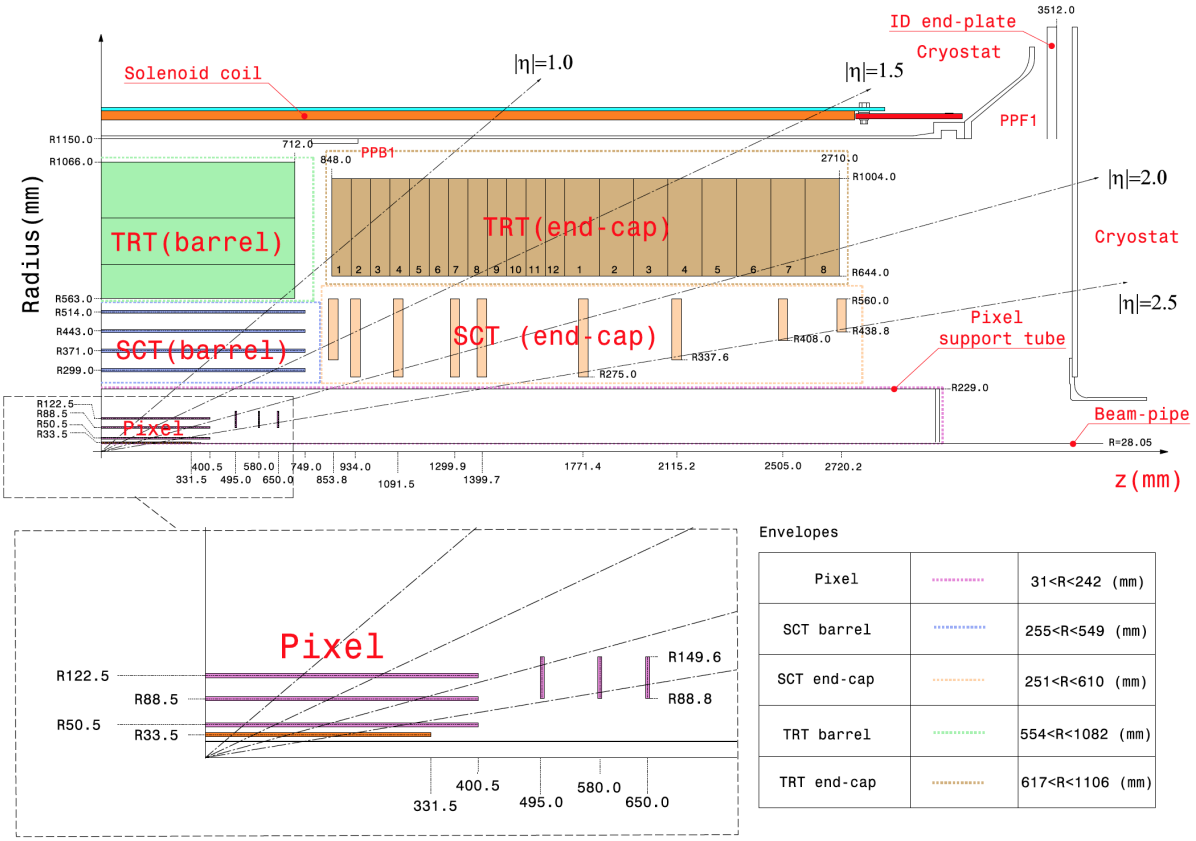

Figure 4.3: Schematic diagram of the ATLAS Inner Detector on the A-side sourced from Ref. [155]. The IBL is shown as the filled red Pixel module.

of 150− $\lesssim$ 350 V and 768 active strips per sensor with approximately 6 million readout channels. Both the Pixel and SCT silicon modules are cooled to ~ -10 °C to reduce noise from thermal excitations. Four SCT hits are expected from each charged particle.

The TRT [156] uses 4 mm diameter drift tubes (polyimide straws) containing a mixture of gaseous Xe (70 %), CO_2 (27 %) and O_2 (3 %) interleaved with polypropylene fibres in order to detect transition radiation generated by charged particles as they move between the materials. This ionises gas molecules causing a drift of charges towards electrodes separated by a potential of 1530 V. The resulting hits have a resolution of 130 μm and provide discrimination between electrons and charged hadrons. There are a total of 351 thousand readout channels over 160 planes, providing 35 expected hits per primary track. As well as particle identification, the TRT improves momentum resolution as track curvature can be constrained over a larger path length.

4.2.3 Calorimetry

Several calorimeter systems are used to detect, identify and measure the energies of electromagnetically interacting and/or hadronic particles based on the shape of, and energy deposited by, showers which are initiated as they pass through layers of absorber material

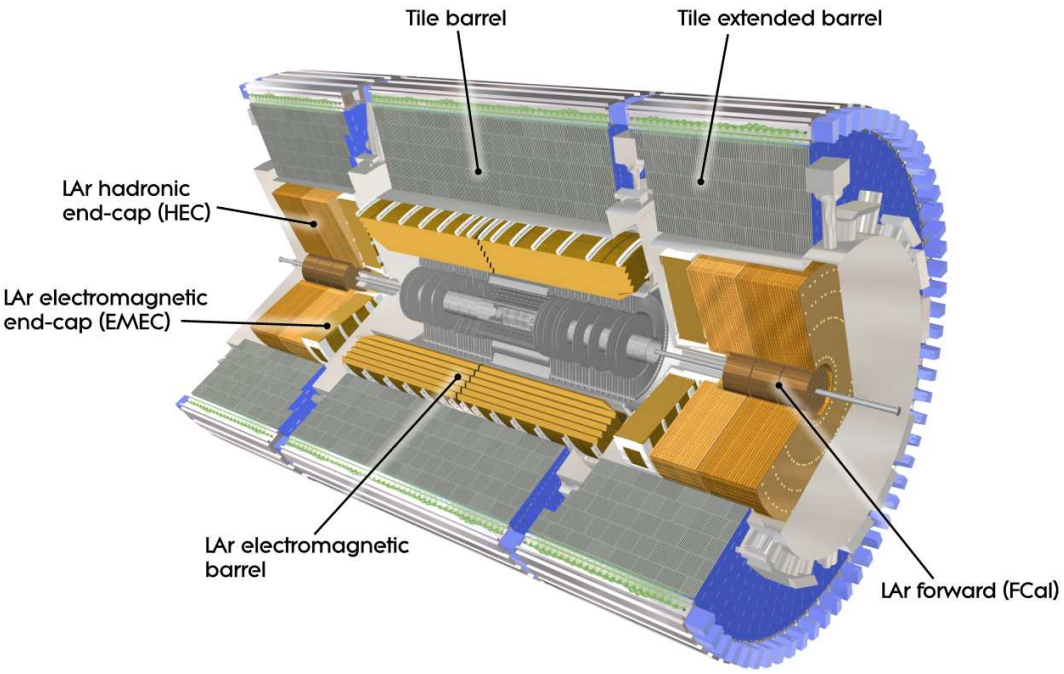

Figure 4.4: Diagram of the ATLAS calorimeter systems. This figure is sourced from Ref. [144].

surrounded by an active detector medium. This is the operating principle of a sampling calorimeter. The ATLAS calorimeters are nested around the ID in barrel and end-cap modules covering central and forward rapidities, respectively, as shown in Figure 4.4. The systems shown in brown are contained within one central and two forward cryostat bores and operate at a potential of $1000 - 2500$ V. Charges drift in this electric field and are collected at electrodes within a time of approximately 450 ns.

The EM barrel and end-cap (EMEC) calorimeters [157] are positioned closest to the ID and use liquid Argon (LAr) as the active medium due to its linear response, long-term stability and radiation resilience. The barrel module covers $|\eta| < 1.475$ and is arranged into three layers with lead (Pb) absorbers arranged in an accordion-like folding pattern in order to cover the full azimuth without gaps in acceptance. The first layer is finely segmented in $|\eta|$ in order to precisely determine the direction of propagation with a central resolution of $\Delta\eta \times \Delta\phi = 0.003 \times 0.1$. The second layer has a thickness of at least 16 radiation lengths and absorbs the majority of the shower energy with a central resolution of $\Delta\eta \times \Delta\phi = 0.025 \times 0.025$. A thinner and coarser third layer is used to estimate leakage beyond the calorimeter. A LAr presampler in front of the calorimeter provides an estimate of energy losses before the calorimeter over the range $|\eta| < 1.8$. The EMEC consists of four wheels (one inner and one outer on each side of the IP). These are each divided into eight wedge shaped modules and cover the range $1.375 < |\eta| < 3.2$ with a three-layer Pb-LAr system as in the barrel.

Hadronic calorimetry is performed in the barrel by the Tile calorimeter (TileCal) [158] and in the forward region by hadronic end-cap (HEC) [157] covering $|\eta| < 1.7$ and $1.5 < |\eta| < 3.2$ respectively. TileCal is divided into a central 5.8 m barrel with two extended 2.6 m barrels which use steel as the absorber and polystyrene-based scintillation tiles as the active medium. As they pass through, charged particles generate UV light which is reflected into wavelength-shifting fibres connected to PMTs which gather the signal in three layers with a cell size of $\Delta\eta \times \Delta\phi = 0.1 \times 0.1$. HEC is arranged into two wheels of 32 wedge modules with a copper absorber and LAr medium under a bias of 1800 V for which the drift time is ~ 430 ns. The cell size is $\Delta\eta \times \Delta\phi = 0.1 \times 0.1$ for $|\eta| < 2.5$ and $\Delta\eta \times \Delta\phi = 0.2 \times 0.2$ up to $|\eta| = 3.2$.

FCal [157] is a three-layer system providing both EM (FCal1) and hadronic (FCal2 and FCal3) calorimetry in the range $3.1 < |\eta| < 4.9$. Both cases use LAr as the active medium with copper and tungsten absorbers, respectively. This forward coverage is important when measuring forward jet production and evaluating the total transverse momentum of all objects created from a hard scatter event.

4.2.4 Muon spectrometer

Muon chambers [159] are positioned between toroidal magnets which cause charged particles to bend (in the η direction) in a $0.5 - 1$ T magnetic field after exiting the calorimeters. Precision tracking chambers are designed to identify their charge and momentum with a resolution $\frac{\Delta p}{p}$ of approximately 3 % for muons with a transverse momentum of 10 GeV, rising to approximately 10 % at 1 TeV. Fast trigger chambers allow decisions to be made on the $12 - 25$ ns timescale with a bunch crossing identification (BCID) efficiency of at least 99 %. The layout is shown in Figure 4.5. Additional chambers were placed in the transition region between barrel and end-cap at $1.0 < |\eta| < 1.4$ for Run 2.

The precision tracking chambers are predominantly monitored drift tubes (MDTs) with coverage of $|\eta| < 2.7$ in three barrel layers and $3 - 4$ end-cap wheels (η-dependent). These consist of 30 mm tubes containing Argon (93 %) and CO_2 (7 %) at a pressure of 3 bar with charge collection at central electrodes with a potential of 3080 V. In the innermost end-cap wheel the MDTs are replaced by cathode-strip chambers (CSCs) in the range $2.0 < |\eta| < 2.7$ due to their improved performance at the higher rates experienced in the forward region. These drift chambers consist of orthogonal cathode strips which operate at a potential of 1900 V and with a gas mixture of 80 % Argon and 20 % CO_2. All chambers are arranged into octants consistent with the 8-fold symmetry of the toroid magnets and provide full azimuthal coverage. A gap in acceptance exists at $|\eta| \lesssim 0.08$ (ϕ-dependent) which allows service access to the ID and calorimeters. Each MDT chamber provides 3-8 tube layers with a combined hit resolution of 35 μm, compared with 40 μm $\times$ 5 mm in the CSCs.

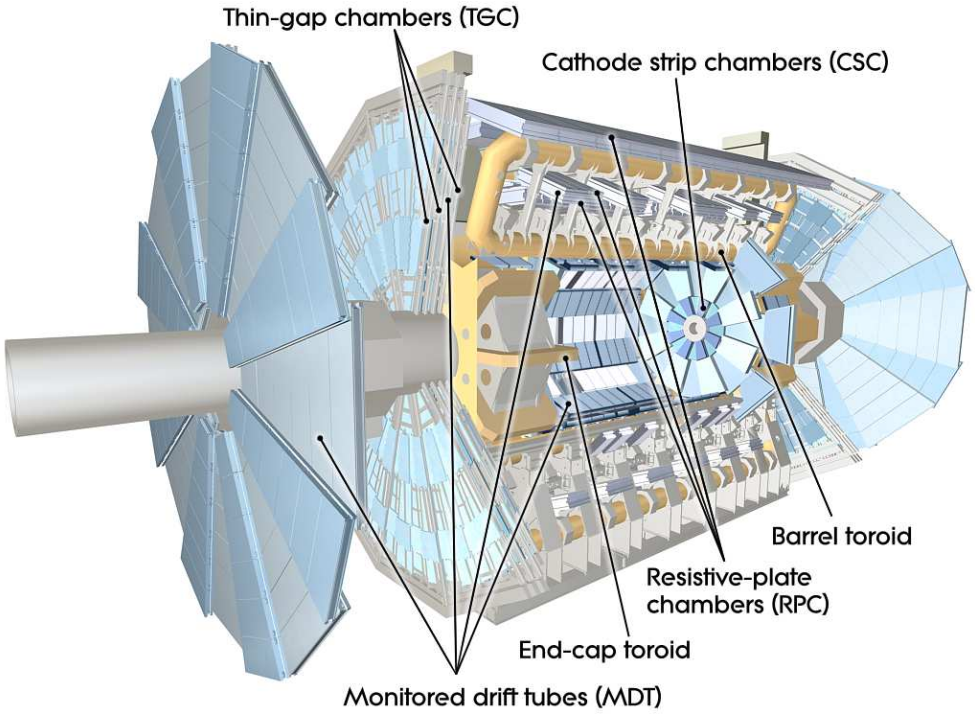

Figure 4.5: Diagram of the ATLAS muon systems. This figure is sourced from Ref. [144].

The trigger chambers are a combination of resistive-plate chambers (RPCs) at $|\eta| < 1.05$ and thin-gap chambers (TGCs) at $1.05 < |\eta| < 2.4$. As well as fast readout and efficient BCID properties, they provide coarse momentum resolution for use in the trigger and robustness against n/γ backgrounds.

4.2.5 Trigger and data acquisition

Collisions at design luminosity occur at a rate of 1 GHz, however it is not possible to process and store this amount of information. For each bunch crossing, the trigger system [160] uses a combination of fast electronics and algorithms based on partial event information to decide whether or not to save an event to disk for offline analysis. Events were recorded at a rate of 1 kHz in 2016 [161]. The decision is performed in three steps called the level-1 (L1), level-2 (L2) and event filter (EF). L2 and EF are collectively referred to as the high level trigger (HLT).

The L1 trigger operates using fast front-end electronics which can trigger on high momentum objects or missing energy based on low granularity inputs from all calorimeters (L1Calo) and the dedicated muon chambers (RPCs and TGCs). Isolation requirements can be applied in the selection of events with candidate electrons or photons based on the energies of nearby calorimeter clusters. Additional information is provided by minimum bias scintillation counters and beam-pickup monitors for triggering on filled and unpaired bunches. The L1 trigger accept decision is made by the central trigger processor (CTP)

which takes the L1 inputs and compares them with a menu of up to 256 pre-programmed combinations of objects and thresholds. The CTP allows for prescaling which reduces the number of L1 accepts by a constant factor for a given trigger. It also assigns deadtime in which no further triggers can be made and defines the transition between luminosity blocks (LBs). An LB is a nominally 60 s interval considered as a unit of data taking for which a mean luminosity value is assigned.

If a L1 trigger is accepted, the regions of interest (RoIs) are passed on to the HLT. This operates using software run on farms of commercially available hardware. It builds events based on the RoIs and uses higher granularity detector readout to make individual trigger decisions. Triggers are organised into data streams and passed on to output nodes which store the (full or partial) detector readout on a local file system, finally to be transferred to permanent storage.

4.2.6 Luminometers

Many detector components and subsystems exist for purposes such as structural support, shielding, monitoring, electronics and subsidiary measurements. This section describes those subsystems that can be exploited due to their sensitivity to the instantaneous luminosity being delivered to ATLAS.

The LUCID (LUminosity measurement using Cherenkov Integrating Detector) is the primary device for luminosity measurement (luminometer). It consists of 16 aluminium tubes originally filled with C_4F_{10} at a pressure of $1.2 - 1.4$ bar which are positioned at 17 m on either side of the IP at $|\eta| \approx 5.8$. Charged particles produced from inelastic proton collisions generate Cherenkov radiation which is reflected through quartz windows into photomultiplier tubes (PMTs). These generate a signal hit for activations above a given threshold. The gas was removed during 2012 to reduce the chance of saturation. In this case photons are generated only through interaction with the quartz window. Four of the PMTs have a smaller aperture acceptance to further reduce saturation. An additional four quartz fibre bundles generate Cherenkov photons which are directed into shielded PMTs at a distance of 2m. Fast electronics allow readout within the 25 ns window of each LHC bunch crossing. Once calibrated, this provides the online ATLAS luminosity measurement in Run 2.

LUCID was upgraded for Run 2 in order to prevent saturation and improve component lifetime in an evironment with increased instantaneous luminosity [162]. The PMTs were upgraded with smaller apertures and new front-end electronics were installed capable of charge integration of digitised PMT signals in 25 ns windows. A new high voltage gain calibration system utilises three different technologies. Photons are supplied to 16 tubes on each side by light emitting diodes (LEDs) and the TileCal laser calibration system. The remaining four tubes are calibrated using ^{207}Bi sources which emit monoenergetic electrons

above the threshold for Cherenkov radiation within the quartz. A periodic automated gain calibration is performed to countaract the effect of PMT aging.

The BCM (Beam Conditions Monitor) is comprised of two groups of four diamond sensors, arranged into a cross pattern on either side of the IP, located at $z = \pm 184$ cm and $R = 5.5$ cm. It is primarily used to detect rare events in which proton bunches collide with the collimators protecting the innermost subsystems of ATLAS, as well as monitor the rate of beam-gas interactions, and trigger beam aborts if needed to protect ATLAS instruments from excessively high instantaneous particle fluxes [163]. Fast sub-nanosecond readout electronics and sensitivity to the flux of co-incident forward radiation from collisions at the interaction point allow this to be used as a bunch-by-bunch luminometer.

Cell activations within the TileCal, EMEC and FCAL calorimeter systems are used as an offline luminosity measure. The multiplicities of ID objects such as tracks, vertices and pixel clusters are also used. As of the early 2017 analysis of Run 2 data collected in 2015 and 2016, the track counting method is the only ID method used to measure luminosity corrections and uncertainties. This is discussed in Chapter 5.

4.3 Object reconstruction

This section describes the offline reconstruction of physical objects. This is the process by which physical objects are interpreted from raw detector readouts. Such objects include charged particle tracks, photons, electrons, muons, hadronic jets and missing transverse momentum. These form the basic elements of offline analyses.

4.3.1 Tracks and vertices

Charged particle tracks and interaction vertices are reconstructed by applying pattern recognition algorithms to clusters present in the Pixel, SCT and TRT modules [164–166]. These are interpreted as charged particles originating from primary and secondary interaction points and are used as input into higher level object reconstruction. The tracking of muons is discussed in Section 4.3.3.

A track is defined by five degrees of freedom at any given point in space; one charge, two position co-ordinates and two momenta [167]. The perigee is written as $\vec{q_0} = \left(d_0, z_0, \phi, \theta, \frac{q}{p}\right)$ where q is the charge. Other points on the track are obtained by iteratively applying transport and mapping functions which describe the extrapolation onto the next active surface and take into account the quasi-helical motion within the inhomogeneous magnetic field as well as interactions with detector material, which cause scattering and energy loss due to ionisation, bremsstrahlung, Compton scattering and hadronic interactions with atomic nuclei. The total path, defined by $x(z)$ and $y(z)$, is obtained by numerical integration.

A particle may activate several modules within the same detector layer and provide

multiple adjacent hits[1]. These collectively define a cluster at a single point in space. Tracks are defined using a seed-and-follow approach, and track quality is determined using $\vec{q}_0$ parameter uncertainties, the minimised χ^2 as well as cluster information such as the numbers of layers traversed, holes (layers with no associated cluster), shared clusters and outliers. Quality criteria reduce contamination from fake tracks formed from spurious combinatoric association of unrelated clusters. Tracking inefficiency is mostly driven by material interactions. The track sagitta represents the degree of transverse curvature and provides a p_{T} measurement.

Track reconstruction is seeded by associating clusters in the innermost pixel layers with loose impact parameter constraints. These are iteratively built outwards through ID layers using a combinatorial filter approach in which a range of possible next steps are constrained by the measured clusters. Various track building algorithms are applied for use in different contexts. Performance is improved by the use of smoothed Kalman filters [168] which progressively constrain material scattering points and Gaussian sum filters [169] for the description of energy loss due to bremsstrahlung. Energy losses due to ionisation are corrected for deterministically. Vertices are defined by associating track origins with individual points which are optimised using a χ^2 function. The dominant fake source is spurious track association, and inefficiency is driven by merged and split vertices. The primary vertex (PV) of an event is defined as having the largest $\sum p_T^2$ of all associated tracks [170].

These algorithms use cluster position measurements which require precise knowledge of module alignments. These are periodically calibrated based on track χ^2 optimisation as well as cosmic ray and "field-off" data [171]. Loose track working points achieve 91 % efficiency at $|\eta| \leq 0.1$ reducing to 73 % at $2.3 \leq |\eta| \leq 2.5$, with tight working points achieving $62 - 86$ % [172]. Performance studies do not typically present the measured transverse momentum resolution, since tracks are used as inputs to higher-level objects which are calibrated individually [173, 174]. These will be discussed in later sections. The measured d_0 resolution is less than 10 μm for central high-p_{T} tracks and rises to approximately 100 μm for those with $p_{\mathrm{T}} \sim 1$ GeV and $|\eta| \sim 2.5$ [174].

4.3.2 Photons and electrons

Photons and electrons are reconstructed from electromagnetic (EM) calorimeter energy deposits within $|\eta| < 2.5$. The Run 2 calibration uses the Run 1 data-driven corrections and intercalibration, but introduces a re-optimised simulation accounting for updated pileup and detector conditions [175–177]. Notably, extra scintillation modules have been introduced into the transition region between the barrel and end-cap modules, the TRT gas mixture was modified at the start of 2016 (shown to have small impact) and the introduc-

[1] See, for example, Section 3.1 and Figure 2 of Ref. [166].

tion of the IBL has introduced a layer of inactive material and affected track reconstruction.

The signal from each EM cell is filtered, amplified, digitised and sampled over intervals of 25 ns. The samples are weighted according to the expected pulse shape after subtraction of the electronic pedestal, and summed. A calibration factor then relates this to the energy deposited in the cell. The space is divided into a grid of $\Delta\eta \times \Delta\phi = 0.025 \times 0.025$ towers which combine all calorimeter layers. Clusters are formed by combining 3×5 towers using a sliding window seeded by individual towers with $E_T > 2.5$ GeV [178]. Clusters are labelled as electron candidates if they are matched with a primary Inner Detector track or unconverted photon candidates if no suitable track exists. Converted photons are those for which the process $\gamma \to e^+e^-$ occurs before reaching the calorimeter. These candidates are identified by matching the cluster to a single track with no innermost pixel hit or two tracks originating from a conversion vertex and with TRT hits consistent with the electron hypothesis. Reclustering into groups of 3×7 (barrel) and 5×5 (end-cap) towers is performed.

Not all energy is contained within the cluster due to interactions with upstream material and absorber layers as well as leakage outside of the cluster and beyond the EM calorimeter. The particle energy is obtained from the cluster energy using a simulation-based multivariate analysis (MVA) which combines information from transverse and longitudinal shower shape observables, location and track/cluster kinematic relations where appropriate. This calibration is performed separately in the barrel and end-cap modules for each of the three classes of object. Measured energy deposits in the first two calorimeter layers allow a precise mapping of inactive material in front of the calorimeter and are used to correct the simulation. A series of further data-driven corrections account for known instrumental effects, and a data-driven intercalibration allows the responses of different detector regions to be related to a global energy scale. This is calibrated at the $Z \to e^+e^-$ resonance peak and validated in $J/\psi \to e^+e^-$ and $Z \to l^+l^-\gamma$ events. The fractional resolution of the momentum measurement varies between 2 % (3.5 %) for photons (electrons) with transverse momenta of 25 (15) GeV and 1 % at high momentum [176, 177].

Further identification criteria are applied to the electron, converted photon and unconverted photon candidates in order to define their quality. These apply cuts to shower shape observables, track-cluster matching, track properties including kinematics, TRT and inner pixel layer hits and conversion vertex association. Loose, medium and tight requirements progressively cut more aggressively on these observables in order to reject fake objects at the expense of reduced efficiency.

The tight photon identification requirements are detailed in Ref. [179]. The observable R_{had} (R_{had1}) measures the energy deposited in the (first layer of the) hadronic calorimeter divided by the energy deposited in the EM calorimeter. The observable f_1 measures the ratio between the first layer of the EM calorimeter and its total. These characterise the longitudinal spread of the shower and provide discrimination against hadrons incorrectly

reconstructed as photons. The fine segmentation of the first layer of the EM calorimeter provides discrimination against neutral hadrons (particularly π^0 mesons) which have decayed into pairs of photons. These deposit energy in two distinct pulses which are quantified by ΔE, the difference between the first and second energy maxima E_1 and E_2, as well as $E_{\text{ratio}} = {}^{\Delta E}/_{E_1+E_2}$. Further observables characterise the transverse spread of the shower using the ratios between central and outer cell depositions in various calorimeter layers as well as energy-weighted measures of shower width. These are all required to be consistent with a single-photon hypothesis. Tight identification has an efficiency of $84-94$ % ($87-98$ %) for unconverted (converted) photons in the range $25 < E_T < 200$ GeV [5, 180].

4.3.3 Muons

Muons are reconstructed from tracks in the Inner Detector (ID) and Muon Spectrometer (MS) with additional information from the calorimeters [181, 182]. ID tracks are reconstructed as described in Section. 4.3.1. MS tracks are reconstructed by building track segments from hit patterns in the various muon chambers using a Hough transform [183] in the MDT and combinatorial search algorithms in the CSC. These are combined using a combinatorial search seeded in the middle chambers where the most trigger hits are present and optimised using a global χ^2 fit. Hits are added and outliers removed based on the χ^2 impact. Quality requirements on MS tracks are applied based on the number of segments combined, number of layers traversed and optimised χ^2.

Four methods are used to reconstruct full muon tracks: combined (CB) tracks match MS tracks with those in the ID and are re-fit for optimisation, valid for muons within the ID acceptance of $|\eta| < 2.5$; segment-tagged (ST) tracks match ID tracks with individual segments in the MS and are useful at low p_{T} or in low acceptance regions of the MS; calorimeter-tagged (CT) tracks match ID tracks with calorimeter deposits consistent with the low-ionisation expected from muons, useful in the MS acceptance gap at $|\eta| < 0.1$; extrapolated (ME) tracks apply impact parameter requirements to MS-only tracks, useful beyond the ID acceptance at $|\eta| > 2.5$. Overlapping muon tracks are prioritised according to CB > ST > CT and the comparison with ME tracks is based on track quality.

Muons are identified using hit/hole requirements as well as cuts on χ^2 and the consitency between the momentum and ${}^{q}/_{p}$ measured in the ID and MS. This reduces the large background from muons originating from hadron decays when searching for exclusively prompt muons. Loose, medium and tight cut levels are used with increasing purity and decreasing efficiency, with an additional high-p_T category optimised for heavy resonance searches. Efficiencies are measured to be > 98 % for the loose/medium and $90-98$ % for tight selections using tag-and-probe analysis of $Z \to \mu\mu$ and $J/\psi \to \mu\mu$ decays [181, 182]. The fractional momentum resolution is measured to be approximately 2 % at small $|\eta|$ rising to 3 % in the endcaps for muons originating in $Z \to \mu\mu$ decays [184].

4.3.4 Jets

Final state objects which undergo parton shower and hadronisation lead to jets of collimated objects. The analyses presented in this thesis use jets reconstructed by the anti-k_T algorithm [59] from topologically clustered electromagnetic and hadronic calorimeter cells (topo-clusters) [185] calibrated at the EM scale.

Topo-clusters are seeded by calorimeter cells with $E/\sigma \geq 4$ where E is the measured energy deposit and σ is the expected noise. Adjacent cells with $E/\sigma \geq 2$ are iteratively included in three dimensions until none remain. A final layer of positive energy cells is included and the cluster centre is defined as the energy-weighted sum of all constituents. The calibrated topo-clusters are combined into jets using the anti-k_T algorithm [59]. Track-jets are clustered from Inner Detector tracks associated with the selected primary vertex. These allow for improved pileup resilience at the cost of acceptance limited to $|\eta| < 2.5$.

Several steps are used to convert the combined cluster energy into a calibrated jet [186, 187]. The jet direction is origin-corrected to the identified primary vertex. The expected pileup contribution is subtracted using event-by-event estimation of the median energy density and the jet area evaluated using ghost association as well as a residual constant dependent on the mean number of proton collisions per bunch crossing [188]. Jet energies are corrected for calorimeter response using a p_T, η-dependent calibration derived from simulation. This step includes a correction for bias in the measured η resulting from the combination of calorimeter technologies [189]. A series of corrections are applied which account for observed dependence of the jet energy scale on the shower shape and utilise additional information from ID and MS tracking, referred to as global sequential calibration. Final data-driven "in-situ" corrections account for differences between jet response in data and simulation.

The jet energy resolution is measured to be approximately 15 % at $p_{\mathrm{T}} = 30$ GeV reducing to below 5 % at $p_{\mathrm{T}} > 1000$ GeV [190, 191]. The relative uncertainty on this quantity is estimated to be between 1 % and 4 % depending on the jet p_{T} and η, and the uncertainty on the jet energy scale is $1 - 6$ % [192]. Pileup jets within $|\eta| < 2.4$ and $30 < P_T < 60$ GeV are suppressed using a multivariate discriminant (JVT) [193]. This is a 2-dimensional likelihood defined as a function of (i) the summed p_{T} of jet-associated-tracks which originate from the selected primary vertex divided by the total, corrected for pileup, and (ii) the summed p_{T} of jet-associated-tracks divided by the calibrated jet p_{T}. This is designed to maintain a roughly constant efficiency as a function of the number of primary vertices. A *medium* working point yields an efficiency of 92 %.

Multivariate discriminants based on track and secondary vertex observables are used to tag jets from b- and c-hadron decays with varying efficiencies [194–196]. A 70 % efficient b-tag working point yields a factor 380 (12) reduction in light-quark (c-quark) jets.

4.3.5 Missing transverse momentum

The transverse momentum of an event is defined as the vector sum of calibrated photons, electrons, muons, jets and a soft term comprised of the remaining low energy track or calorimeter objects [197]. Tracks passing basic quality requirements and associated with the correct primary vertex are most commonly used. The missing transverse momentum, E_T^{miss} is the length of (the negative of) this vector and represents the sum of long-lived final states such as neutrinos or dark matter candidates which do not interact with ATLAS as well as out-of-acceptance objects such as those at high η. This approach is summarised as follows:

$$\vec{p}_{x,y} = \sum_{\gamma} \vec{p}^{\,\gamma}_{x,y} + \sum_{e} \vec{p}^{\,e}_{x,y} + \sum_{\mu} \vec{p}^{\,\mu}_{x,y} + \sum_{\text{jet}} \vec{p}^{\,\text{jet}}_{x,y} + \sum_{\text{soft}} \vec{p}^{\,\text{soft}}_{x,y} \tag{4.5}$$

$$E_T^{\text{miss}} = \sqrt{p_x^2 + p_y^2}\ . \tag{4.6}$$

The E_T^{miss} resolution is estimated to be between 5 GeV and 30 GeV depending on conditions such as the number of jets, true E_T^{miss} and number of primary vertices [186, 198].

4.4 Detector simulation

In the MC simulation of physical processes, the detector response is modelled using a detailed simulation of particle-detector interactions. This is performed using the `Geant4` program [199]. Objects are reconstructed using the same procedures applied to the measured data. These are called **detector** or **reconstructed level** objects and are affected by detector inefficiency and resolution. By contrast, **truth level** objects are those without the application of detector effects. These have perfect efficiency and resolution up to the level of quantum fluctuations. Object scale factors are used to account for residual differences between the simulated and measured efficiencies of detector level selection criteria. Table 4.1 summarises the measured resolutions which are applicable to later chapters.

Object	Quantity	Approx. resolution	Reference
Track	d_0	$10 - 100$ μm (p_{T}, η dependent)	[174]
γ (converted)	E	$0.5 - 8$ % (p_{T}, η dependent)	[176, 177]
γ (unconverted)	E	$0.5 - 4$ % (p_{T}, η dependent)	[176, 177]
e	E	$0.5 - 10$ % (p_{T}, η dependent)	[176, 177]
μ	p_{T}	$2 - 3$ % ($Z \to \mu\mu$ decays)	[184]
Jet	p_{T}	$3 - 15$ % (p_{T}, η dependent)	[190, 191]
E_T^{miss}		$5 - 30$ GeV	[186, 198]

Table 4.1: Representative resolutions measured in data for various objects.

Luminosity determination using track counting

The *online luminosity* is the primary measurement of the instantaneous luminosity delivered to ATLAS in each luminosity block. It must be published in real time, independently for every BCID, using a method which is statistically precise and systematically well behaved over a wide range of luminosity and beamspot conditions. The online luminosity is provided by `BCM` in Run 1 and `LUCID` in Run 2. These detector subsystems utilise fast front-end electronics independent of the ATLAS data acquisition system and so are unaffected by trigger prescales or dead-time imposed by the CTP.

The response of the online luminosity is tested throughout the data taking period by comparing it with several *offline luminosity* measurements. These are used to derive systematic corrections to the calibration and stability of the online luminosity, as well as to constrain related systematic uncertainties. Redundancy is exploited, meaning that several offline luminosity measurements are performed using different techniques so that any disagreement can be associated with the instability of an individual method. This chapter describes the measurement of offline luminosity using the multiplicity of tracks reconstructed in the Inner Detector (ID). This method is independent from the online luminometers both instrumentally and in technique, making it an important comparison. Furthermore, studies of simulated data in Runs 1 and 2 predict the track counting method to have a linear response over a wide range of luminosity values. It is not suitable as an online luminometer because it relies on events recorded at a finite trigger rate, and so the measurement is statistically limited for individual BCIDs and/or luminosity blocks.

Before offline luminosity measurements can be used to apply systematic corrections to online luminometers, they must be shown to provide self-consistent results. This chapter focusses on the implementation and continuing development of the track counting measurement (initiated in Run 1 prior to the work contained within this thesis), the internal stability of the method over time, the comparison with the `TileCal` offline luminosity measurement, the comparison with the online luminosity, and finally the resulting systematic corrections and uncertainties derived for the online measurement. It is shown that the use of track counting as an offline luminometer significantly constrains two of the dominant systematic uncertainties: the calibration transfer and long-term time stability.

Section 5.1 introduces the topic of luminosity measurement. Section 5.2 summarises the other luminometer algorithms. Section 5.3 provides technical details of the track counting method. Section 5.4 details the data quality requirements. Section 5.5 presents studies relating to the final analysis of data collected during 2012 [200]. Sections 5.6 and 5.7 present the track counting measurements in 2015 and 2016 data taking, respectively.

5.1 Introduction

The instantaneous luminosity $\mathcal{L}_b$ delivered to ATLAS by a pair of colliding bunches can be related to beam parameters using

$$\mathcal{L}_b = \frac{f_r n_1 n_2}{2\pi \Sigma_x \Sigma_y} = \frac{f_r \mu_b}{\sigma_{\text{inel}}} \tag{5.1}$$

where $f_r = 11,245.5$ Hz is the LHC revolution frequency and $n_{1,2}$ are the numbers of protons in the two bunches. The quantity Σ_j is equal to $1/\sqrt{2\pi}$ times the convolution of the beam profiles in direction j divided by their product at $x = y = 0$, assuming zero crossing angle and beam profiles which factorise between orthogonal directions in the transverse plane [201]. If these assumptions are violated then the product $\Sigma_x \Sigma_y$ is replaced with a 2-dimensional convolution. It can also be related to the mean number of inelastic proton collisions per bunch crossing for the bunch pair, μ_b, and inelastic proton cross section σ_{inel} as shown. Measured values of σ_{inel} are shown in Table 5.1. The total instantaneous luminosity $\mathcal{L}$ is the sum over all n_b bunch pairs. Defining μ as the mean of μ_b gives

$$\mathcal{L} = \sum_{b=1}^{n_b} \mathcal{L}_b = \frac{n_b f_r \mu}{\sigma_{\text{inel}}} \,. \tag{5.2}$$

The integrated luminosity, $\mathcal{L}_{\text{int}} = \int \mathcal{L} \mathrm{d}t$, is defined as the integral over time. Its precise measurement is required for a given dataset in order to perform cross section measurements such as those presented within this thesis. It is often a dominant source of systematic uncertainty when measuring high rate processes [202], and is also used to estimate background contributions in e.g. the $H \to ZZ^* \to 4l$ channel [63]. Luminosity is measured by defining a *visible interaction rate*, μ_{vis}, as the mean rate of some observable process per bunch crossing. This is related to the inelastic collision rate through

$$\mu = \frac{\sigma_{\text{inel}}}{\sigma_{\text{vis}}} \cdot \mu_{\text{vis}} \tag{5.3}$$

such that

$$\mathcal{L} = \frac{n_b f_r \mu_{\text{vis}}}{\sigma_{\text{vis}}} \tag{5.4}$$

where σ_{vis} is the visible cross section. This acts as a calibration factor and is derived using

one of two methods:

- the van der Meer (vdM) method [203] in which Σ_x and Σ_y are measured and related to σ_{vis} by scanning the beams in perpendicular directions and measuring μ_{vis} at each scan point. Systematic uncertainties are minimised by the use of low intensity bunches, few and widely spaced colliding bunch pairs and (in several scan periods) beams with wide transverse profiles which are tailored using custom injector settings to promote factorisation in the transverse plane.

- cross-calibration in which the integrated luminosity measured over some data taking period is normalised to that measured by a second luminometer.

The following definitions are used:

Run : a period of data-taking typically characterised by a single pair of beams which "burn-off" over a period of several hours leading to a falling instantaneous luminosity curve (except in special runs such as van der Meer scans).

Luminosity block (LB) : a unit of data-taking within a run over which detector conditions and instantaneous luminosity are assumed to be constant and typically of 60 s duration. Luminosity measurements are performed on a per-LB basis and whole LBs are vetoed for offline analysis if detector defects are identified.

Bunch crossing identifier (BCID) : an index labelling the successive 25 ns windows in which bunch pairs collide. A BCID corresponds to the collisions of the same bunch pair throughout a run.

Offline luminometers are primarily used to study the following concerns:

Calibration transfer : a change in σ_{vis} when transferring between the μ-ranges and beamspot conditions of vdM scan and high luminosity conditions. Track counting is the primary offline luminometer for studying this because the linearity between μ_{vis} and μ is assumed down to arbitrarily low μ whereas calorimeter based methods are affected by a background pedastal which is significant in vdM conditions. Calibration transfer is studied by comparing the ratio between the luminosities measured by different luminometers in both the vdM period and high luminosity runs.

Long-term stability : run-to-run instabilities caused by e.g. changes in detector conditions or aging of components over the course of a year. This is studied by comparing the run integrated luminosity ratios between runs.

μ-dependence : nonlinear corrections to the relation between μ and μ_{vis}. This is studied by comparing the per-LB luminosity ratios within individual runs.

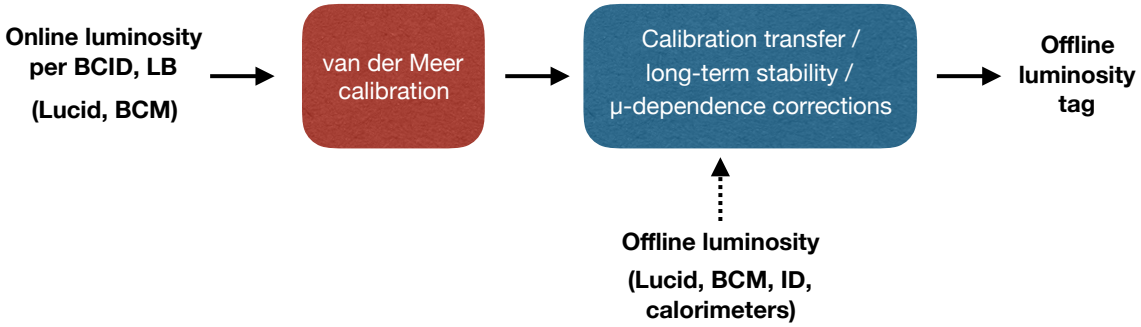

Figure 5.1: Luminosity measurement strategy.

$\sqrt{s}$	σ_{inel} [mb]	Reference
7 TeV	73.7 ± 3.4	[204]
8 TeV	74.7 ± 1.7	[205]
13 TeV	78.1 ± 2.9	[206]

Table 5.1: Inelastic proton-proton cross sections.

Train dependence : dependence of σ_{vis} on the position of the BCID in the bunch train. This is typically studied by comparing luminosity ratios on a BCID-aware basis.

It is important to perform these comparisons using several apparently stable luminometers in order to identify the source of any observed disagreement. The strategy is summarised in Figure 5.1. Luminosity tags represent iterations of the measurement with well defined systematic uncertainties.

The track counting method was developed during Run 1. It provides a BCID-aware measurement which is expected to be stable over time and linear over a wide range of μ. Track counting is independent of the other luminometers in both hardware and methodology with a primary dependence on Inner Detector conditions and track reconstruction effects. These features make it an important offline luminosity measure. Unlike other luminometers, it is statistically-limited due to the use of prescaled triggers. This imposes a particular challenge when studying train dependence due to the limited precision of per-BCID measurements. However, the BCID-averaged measurement is made with typically $\mathcal{O}(0.5\ \%)$ statistical precision per-LB and $\mathcal{O}(< 0.1\ \%)$ when integrated over a run and is therefore well suited for deriving percent-level corrections and systematic uncertainties.

5.2 Other luminometers

`LUCID` is the only system purpose-built for luminosity measurement, as described in section 4.2.6. The PMTs, electronics and calibration system have been upgraded for Run 2. The luminosity can be measured through hit counting, event counting or charge integration.

The most common `LUCID` algorithms use event counting and consider the A and C sides as independent detectors. An `EventOR` algorithm relates μ_{vis} logarithmically to the

fraction f_{evt} of events which registered a hit above threshold in any PMT during the LB. Sensitivity is reduced when $f_{\text{evt}} \lesssim 1$ and saturation occurs when $f_{\text{evt}} = 1$ as the algorithm is no longer responsive to a further increase in luminosity. Saturation is reduced by limiting the probability of an event registering a hit, for example by considering only a subset of PMTs. Alternatively, one can use hit counting or charge integration algorithms for which μ_{vis} scales linearly with the number of hits or total charge recorded. Up to 124 pre-programmed algorithms are performed in real-time by the A and C side electronics. `EventAND` algorithms require coincident hits in multiple PMTs. Further algorithms combine hits in both the A and C sides, although these tend to saturate quickly.

`BCM` algorithms use event counting based on activations above threshold in the four diamond sensors on each side of the IP. The horizontal and vertical sensors are treated as independent luminometers and labelled as `H` and `V` respectively. `BCM` event counting algorithms saturate at higher luminosity than for `LUCID` due to a lower acceptance.

The integrated luminosity is measured using the current drawn by the PMTs of individual `TileCal` cells. This is expected to scale linearly with particle flux after subtraction of an electronic pedastal and single beam backgrounds. The current is integrated over times of several milliseconds and so the measured luminosity represents the sum of all BCIDs. The pedastal subtraction, current response and abnormal timestamps associated with van der Meer scans forbid a reliable absolute calibration of `TileCal`, and so it is typically cross-calibrated with other luminometers. `EMEC` and `FCal` are also used to measure integrated luminosity. These calorimeters use a cryostatically cooled active LAr medium at high voltage. This voltage is modulated in order to maintain a constant electric field within individual cells, drawing additional current proportional to the incident particle flux.

5.3 Technical overview of track counting

5.3.1 Operating principle

Define λ as the mean number of charged particle tracks expected to be observed per inelastic $p-p$ collision. This includes those produced in primary and secondary interactions and convolves the effect of reconstruction efficiency over the observable phase space. The number n_{t} of tracks measured in a randomly chosen event is expected to follow a Poisson distribution with a mean of $\lambda\nu_{\text{b}}$,

$$P\left(n_{\text{t}}|\nu_{\text{b}}\right) = e^{-\lambda\nu_{\text{b}}}\frac{\left(\lambda\nu_{\text{b}}\right)^{n_{\text{t}}}}{n_{\text{t}}!} \tag{5.5}$$

where ν_{b} is the true number of inelastic collisions during that bunch crossing.

The true number of collisions, ν_{b}, is expected to be drawn from a Poisson distribution with mean μ_{b}. The μ measured for any given LB is the average over all n_{b} colliding BCIDs.

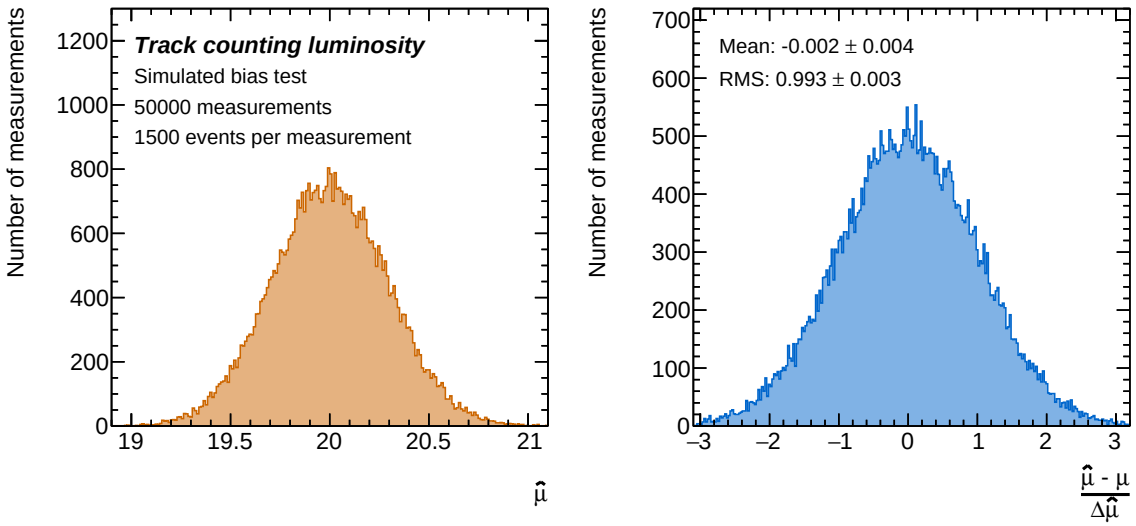

Figure 5.2: Results of a simulated bias test with two BCIDs and $\mu_{\mathrm{b}} = 10, 30$.

The visible interaction rate is defined as the mean number of tracks produced per event, $\mu_{\mathrm{vis}} = \lambda\mu$. This is estimated using the test statistic,

$$\begin{aligned} \hat{\mu}_{\mathrm{vis}} &= \frac{1}{n_{\mathrm{e}}} \sum_i n_{\mathrm{t}}^i \qquad\qquad i = 1, ..., n_{\mathrm{e}} \\ \Delta\hat{\mu}_{\mathrm{vis}} &= \frac{1}{\sqrt{n_{\mathrm{e}}}} \sqrt{\frac{1}{n_{\mathrm{e}}} \sum_i n_t^{i\,2} - \left(\frac{1}{n_{\mathrm{e}}} \sum_i n_t^i \right)^2} \end{aligned} \tag{5.6}$$

where n_{e} is the number of sampled events and each event i is a single bunch crossing. The statistical uncertainty $\Delta\hat{\mu}_{\mathrm{vis}}$ is estimated using the standard error on the mean. The estimator for a given BCID is constructed by summing only over events associated with that BCID.

A bias test is performed as follows. Two BCIDs are defined with $\mu_{\mathrm{b}} = 10, 30$ and so $\mu = 20$. A value of $\lambda = 3$ is chosen. 50 k measurements are simulated, each consisting of 1.5 k events. For each event, a value of μ_{b} is randomly chosen from the two options with a uniform probability. A value of ν_{b} is drawn from a Poisson distribution with a mean of μ_{b}. The measured number of tracks is then drawn from a Poisson distribution with a mean of $\lambda\nu_{\mathrm{b}}$. The test statistic is constructed for each measurement and scaled by $1/\lambda$ in order to form the estimator, $\hat{\mu}$. The distribution of $\hat{\mu}$ is shown in Figure 5.2(left). The pulls, defined as the residual divided by the estimated uncertainty, are shown in Figure 5.2(right). This is consistent with a mean of 0 indicating an unbiased measurement and an RMS of 1 indicating correctly estimated uncertainties.

Name	Description
L1-RD0-Filled	Random sampling of events from all filled BCIDs
L1-RD0-BGRP9	Random sampling of events from a pre-determined subset of filled BCIDs, labelled BGRP9
L1-MBTS2-BGRP9	Events from BGRP9 for which co-incident hits were measured in both sides of the Minimum Bias Trigger Scintillator system [207]

Table 5.2: Description of triggers used for track counting measurements.

5.3.2 Data acquisition and track reconstruction

In normal data-taking conditions, the PixelBeam data stream is used to provide a partial detector read-out consisting of only Pixel and SCT modules for events accepted by a prescaled L1-RD0-Filled trigger. This randomly accepts events from filled BCIDs, those which contain proton bunches in both beams, providing an unbiased sampling. Track and vertex reconstruction is performed using the vtxLumi settings which are designed to minimise CPU usage whilst providing a small fake track efficiency and a real track efficiency resilient against changes in ID conditions, particularly the disabling and re-enabling of individual Pixel modules over the course of a year. Tracks are required to have $p_T > 900$ MeV and are reconstructed using hits recorded within 600 mm of the beamline, excluding TRT information which is not recorded.

Figure 5.3 shows the median event rates recorded per-LB during normal data-taking runs along with the median per-LB statistical precision of the track counting luminosity measurement. One in every four run labels are shown. A recording rate of at least 175 Hz is achieved throughout the year. The vdM data stream is used in special runs such as vdM scans. Depending on the beam conditions either a L1-RD0-Filled, L1-RD0-BGRP9 or L1-MBTS2-BGRP9 [207] trigger is used. These are summarised in Table 5.2. The BGRP9 suffix indicates that only a specific set of BCIDs are triggered, thus maximising the statistical sensitivity of their measurement. The MBTS-2 trigger is not random but instead requires co-incident hits to be registered on either side of the Minimum Bias Trigger Scintillator system. This provides improved statistical precision when $\mu \ll 1$, such as in the tails of a vdM scan, where most bunch crossings do not contain any inelastic collisions. The test statistic $\hat{\mu}_{\text{vis}}$ must be re-defined in this case because the trigger provides a biased sampling of events. Although an absolute vdM calibration was performed in Run 2 by another member of the analysis team, it is not relevant for the stability analyses considered in this thesis and so will not be described.

5.3.3 Track properties

Tracks are selected by applying cuts on several quantities. The number of clusters associated with a track is defined as the sum of hits and all disabled ("dead") sensors extrapolated

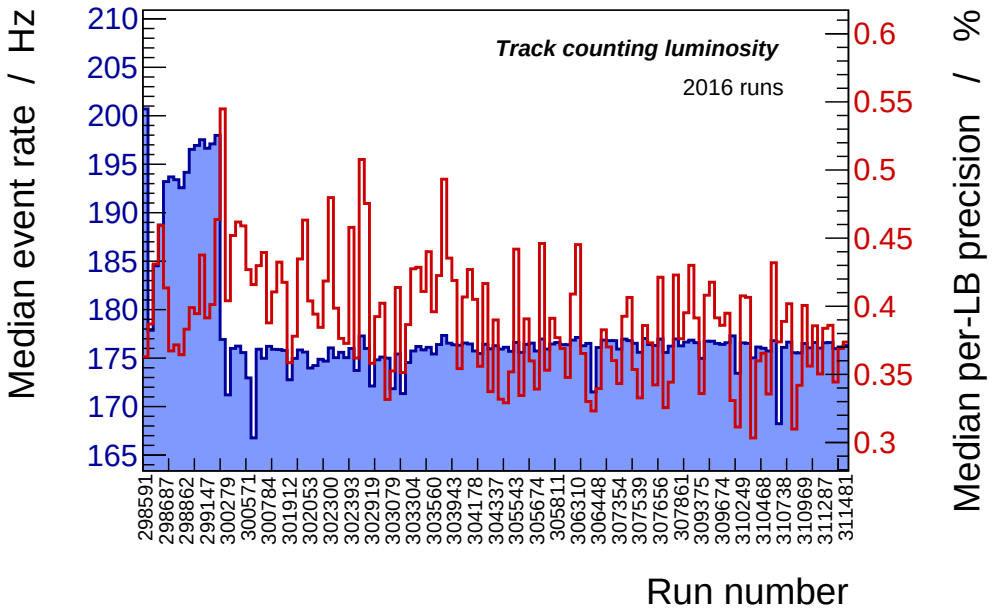

Figure 5.3: Median event rates and track counting statistical precision in 2016 runs.

over by the track trajectory,

$$\text{Num. clusters} = \text{Num. hits} + \text{Num. dead sensors} . \tag{5.7}$$

It is assumed that these would have registered a hit if they were operational. This reduces the dependence of reconstuction efficiency on the disabling of silicon modules. The total number of clusters is the sum of clusters in the Pixel and SCT. A hole is defined as an operational module along the trajectory of a track which did not register a hit. Maximum hole requirements reduce the fake track contribution. The d_0-significance,

$$s\left(d_0\right) = \frac{d_0}{\Delta d_0} \tag{5.8}$$

is the ratio between the measured impact parameter d_0 and its uncertainty, Δd_0.

Various track selection working points are defined in Runs 1 and 2 targeting the rejection of fake tracks, linearity of μ_{vis} with μ and resilience against changes in Inner Detector conditions. Figure 5.4 shows the measured μ_{vis} as a function of LB using the `tight` working point for a representative run in 2015. The number of tracks per event as well as track p_{T}, η, $s\left(d_0\right)$, hole and cluster multiplicites are shown in Figure 5.5. Drops in instantaneous luminosity at LB $\sim 360, 1020, 1080$ occur due to LHC beam scans used for beam size estimation [208] and cause an excess of events with 0 reconstructed tracks. Figure 5.6 shows the track occupancy in this run along with the mean numbers of Pixel and SCT hits and dead sensors. Local variations represent a residual dependence on detector conditions. This is acceptable provided that such conditions remain stable over time.

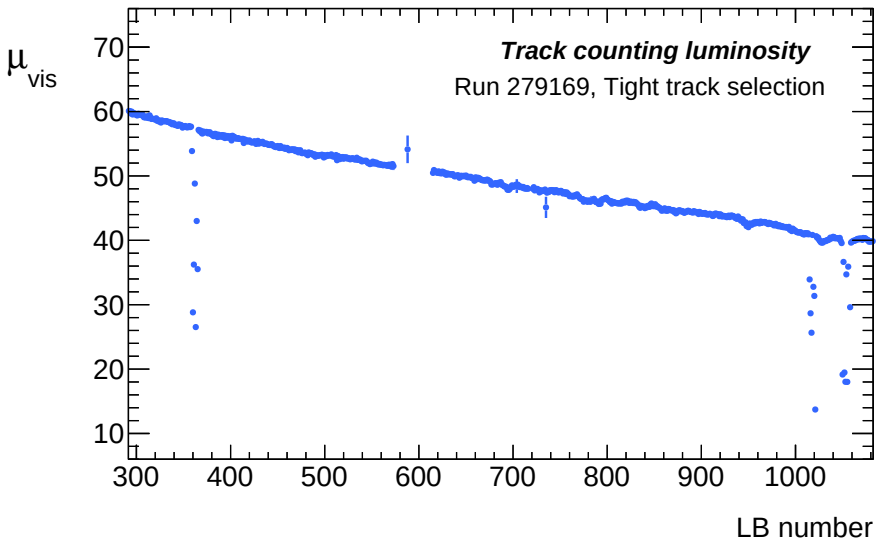

Figure 5.4: μ_{vis} as a function of luminosity block (LB) measured in run 279169.

5.4 Data quality

Data quality requirements are designed to promote a constant track reconstruction efficiency as a function of time. Data are required to pass the `Physics-AllGood` good runs list (GRL) during normal data-taking. This rejects LBs during which defects were registered in the ATLAS subsystems and is also used for offline physics analyses, thus ensuring a consistent LB selection.

Several additional data quality checks are performed. The track properties shown in Figures 5.5 and 5.6 are checked for consistency between runs. In particular, the track occupancy in the η, ϕ-plane has been found to show visible changes due to the enabling and disabling of Pixel modules or problems in the offline reconstruction. An example is shown in Figure 5.7 where run 280673 is seen to contain an (η, ϕ) region with reduced occupancy compared with other nearby runs. This is highlighted by the dotted red box. When ~ 0.1 % luminosity precision is required in the comparison between two runs, the impact of (η, ϕ) anomalies is estimated by comparing the total number of tracks reconstructed in the two runs with and without the suspect region of η, ϕ-space. The track efficiency change in Figure 5.7 is found to be -0.22 ± 0.02 %.

Fluctuations in tracking efficiency which occur over a short period of time may not be identified using the GRL or run-integrated property comparisons. The instantaneous luminosity measured by track counting is compared with other luminometers on an LB-by-LB basis. Outliers which are present in the ratio with respect to multiple different luminometers are removed by hand. This is shown using `LUCID` (red) and `TileCal` (blue) in Figure 5.8 for run 299147 in 2016. Beam scan periods are also removed because they cause a rapid change in instantaneous luminosity which violates the approximation of constant luminosity within any given LB.

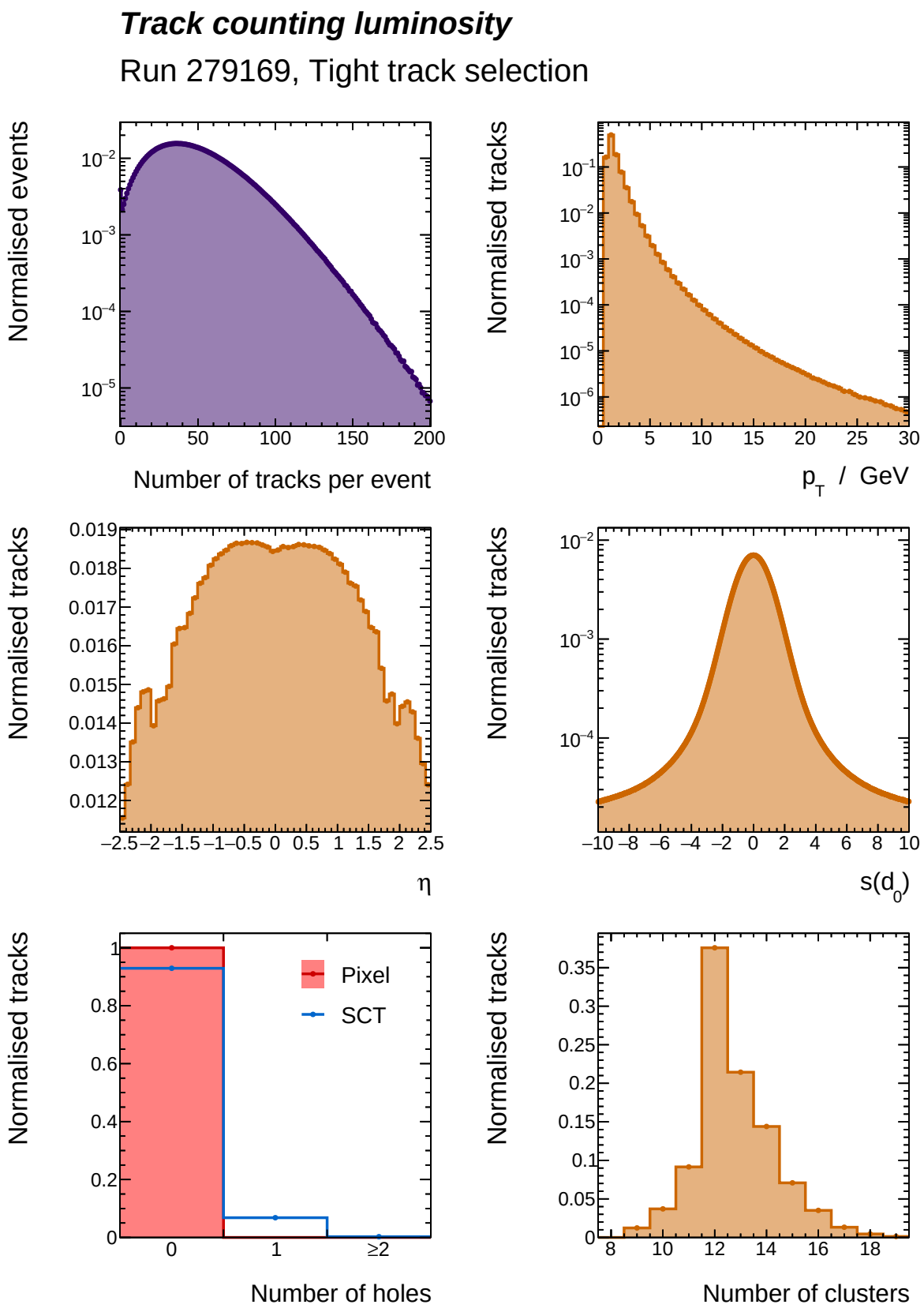

Figure 5.5: Properties of tracks selected in run 279169.

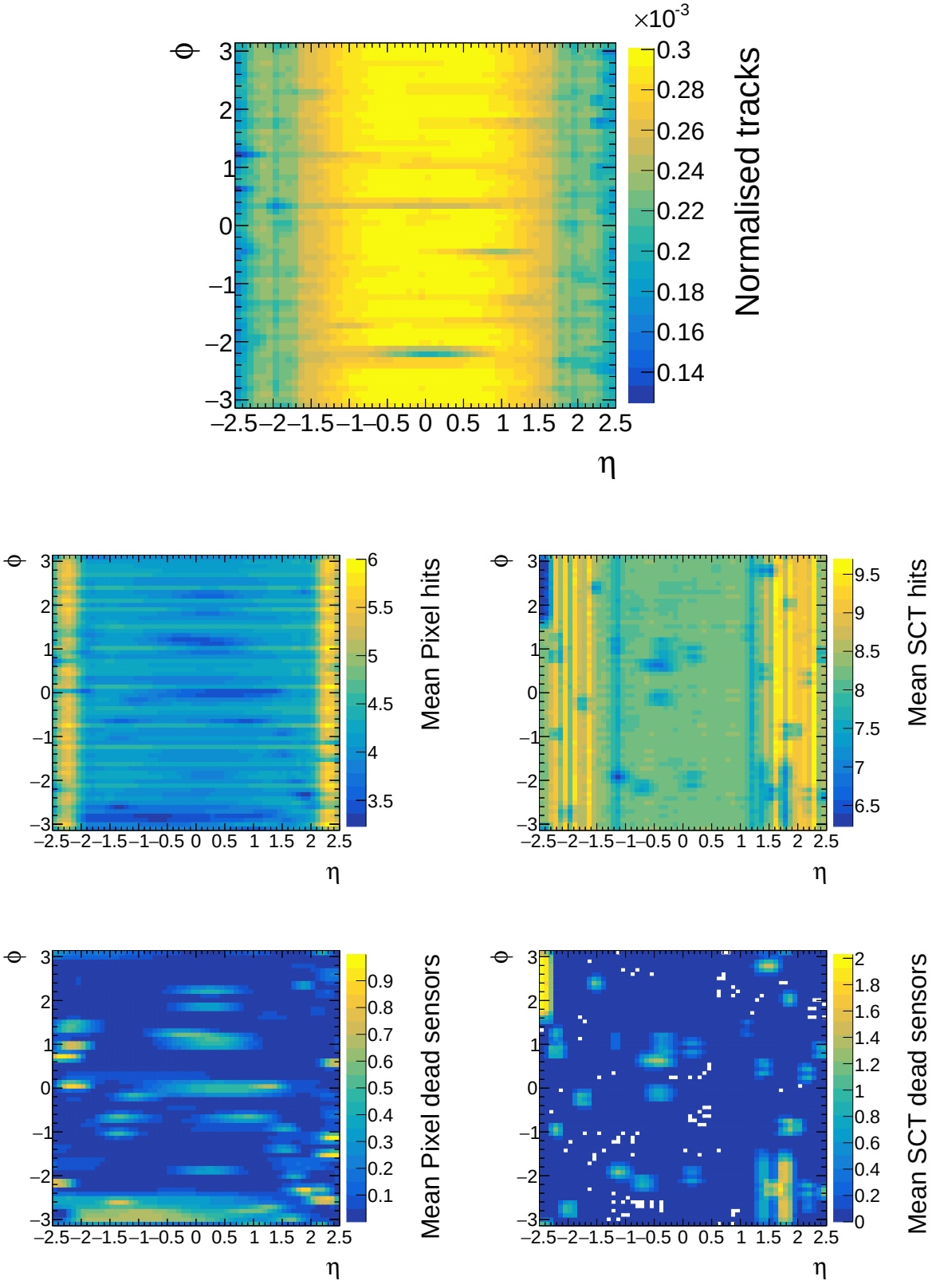

Figure 5.6: Track occupancy in the η, ϕ-plane as well as the mean numbers of Pixel and SCT hits and dead sensors measured using *tight* tracks in run 279169.

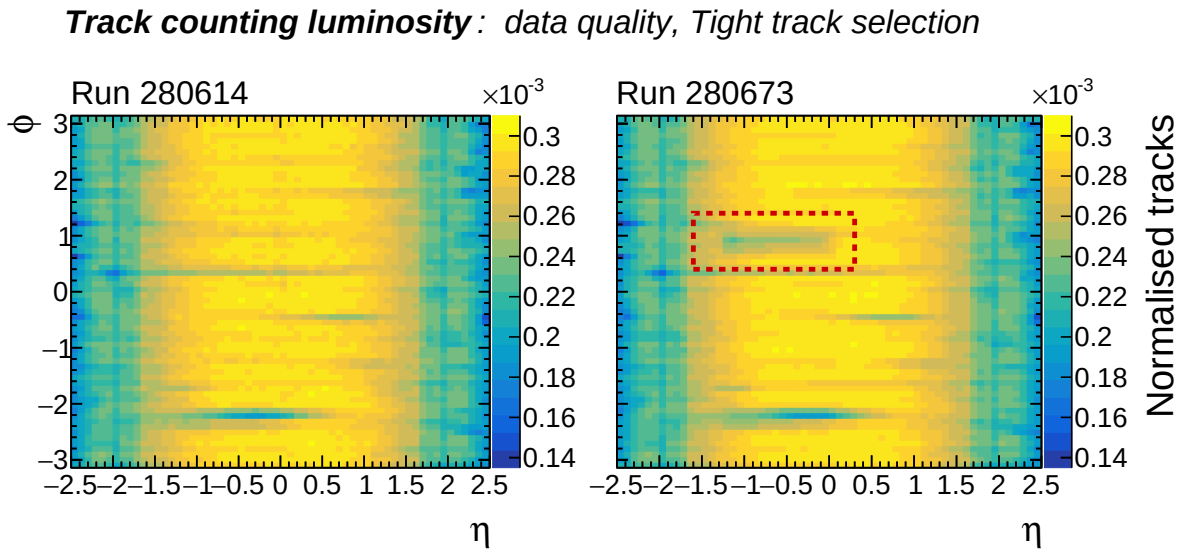

Figure 5.7: Data quality comparison using (η, ϕ) track occupancy

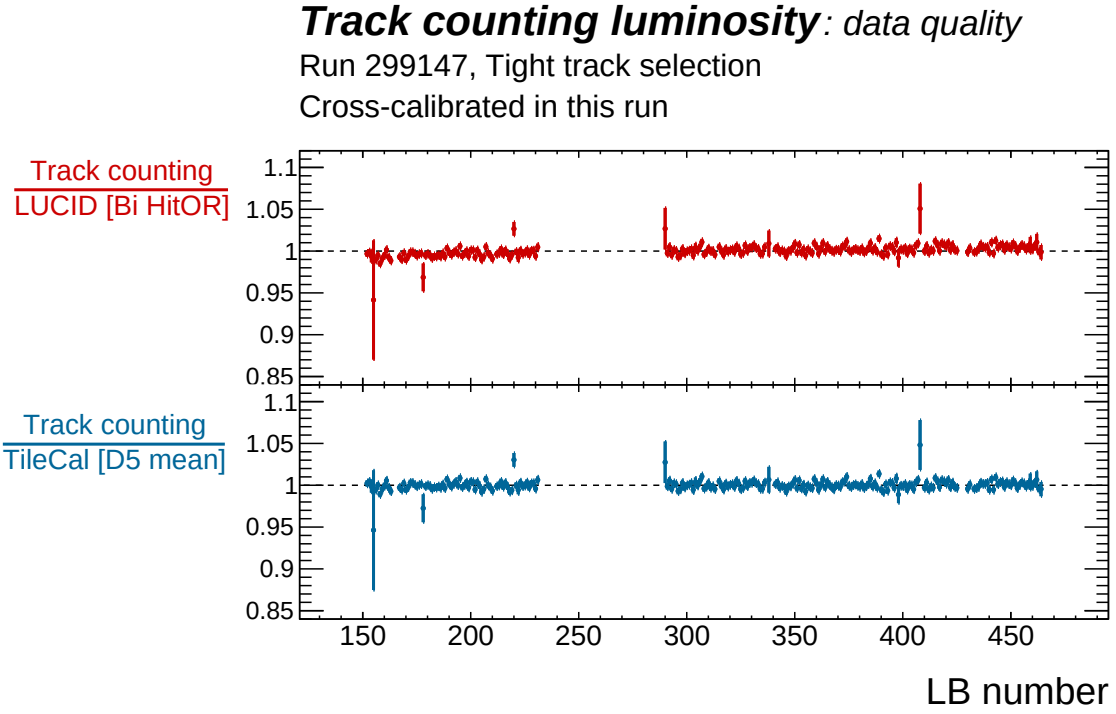

Figure 5.8: Track counting ratio to `LUCID` and `TileCal` in run 299147.

5.5 2012 data

The `vtxLumi` reconstruction settings require a minimum of 7 silicon clusters, maximum of 1 hole in the Pixel detector and 2 in total with a maximum gap of 1 layer between holes. The minimum track p_{T} is 900 MeV. Three working points are defined using the following additional selections:

Fake removal requiring a minimum of 9 silicon clusters, no Pixel holes and $|s(d_0)| < 7$.

Middle ground requiring a minimum of 9 silicon clusters, ≤ 1 Pixel hole and $|s(d_0)| < 7$.

Associated tracks requiring a minimum of 9 silicon clusters, no Pixel holes and that the track is associated with a reconstructed primary vertex.

Several values of the $s(d_0)$ cut were studied by another member of the analysis team. The requirement of $|s(d_0)| < 7$ was chosen because, combined with the other track selection cuts, it achieves a typically small estimated fake track contribution. Furthermore, it is a relatively loose cut (see Section 5.6.1) which reduces any sensitivity to possible systematic variations in the $s(d_0)$ distribution.

Fake tracks are reconstructed due to the spurious association of silicon clusters not generated by a single charged particle. The fake track contribution is derived by another member of the analysis team using Monte Carlo simulation. A track is defined as real if at least 50 % of its hits are associated with a truth level particle produced either before (primary) or during (secondary) the `GEANT` simulation of detector interactions. The mean fake contribution is parameterised as a function of μ using a sum of linear and nonlinear terms. It is subtracted on an LB-by-LB basis using the `BCM-H-OR` measurement as a seed. The fake subtraction at $\mu = 0$ is zero by definition, rising to 0.16 %, 0.22 % and 0.43 % at $\mu = 20$ for the `fake removal`, `middle ground` and `associated tracks` working points respectively. By contrast, a working point defined with no cuts in addition to the `vtxLumi` preselection has an estimated fake track contribution of 5.30 % at $\mu = 20$. An uncertainty of 50 % is assigned to the fake subtraction.

`BCM-H-OR` was chosen as the baseline 2012 luminometer due to the reproducibility of separate van der Meer calibrations performed in April, July and November as well as its internal stability throughout the year. It defines the ATLAS luminosity measurement for each BCID in each LB, subject to offline corrections. Figure 5.9 shows the μ-profile of the 21.7 fb^{-1} data recorded in 2012. The majority of data lie in the range $10 < \mu < 35$ with a mean of $\langle\mu\rangle = 20.7$.

5.5.1 Stability vs. TileCal

Offline luminometers must provide consistent measurements if they are to be used to derive reliable corrections for `BCM-H-OR`. `TileCal` was found to exhibit good internal stability

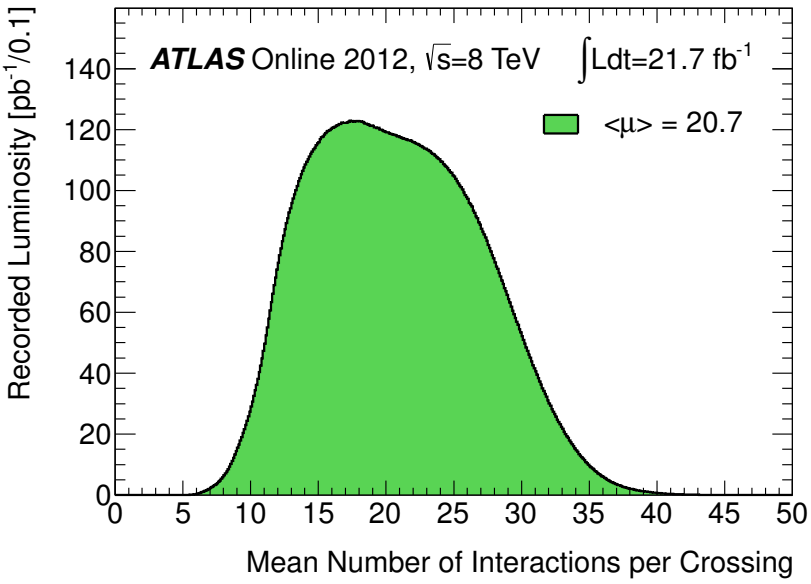

Figure 5.9: μ profile of data recorded in 2012.

(consistency between different cell measurements) and have well understood pedastal and background subtractions. It is treated as the most reliable of the calorimeter measurements and is used as a benchmark for comparison with track counting. The relative stability between track counting, μ(Tracks) and `TileCal`, μ(TileCal) is tested in two ways.

- The *relative μ-dependence* is tested by plotting the ratio $^{\mu(\text{Tracks})}/_{\mu(\text{TileCal})}$ as a function of $\mu \equiv \mu(\text{TileCal})$ for all LBs in a given run. The gradient of a linear fit is extracted in units of $\%/\mu$. This process is repeated for each run.

- The *long-term stability* is tested by plotting the ratio of the integrated luminosities measured by the two luminometers.

The three track counting working points are calibrated using the van der Meer method with a trigger rate of 5 kHz per BCID. Multiple BCIDs and scans curves are measured in each of the three scan periods to test the calibration consistency. `Fake removal` is chosen as the default working point due to its small estimated fake fraction and independence of vertex reconstruction. In order to decouple the effects of μ-dependence and long-term stability, the luminosity integration is performed only over LBs within the range $20 < \mu < 25$. Of 330 possible runs, 46 contain both track counting and `TileCal` luminosity measurements and fully span this range.

The relative μ-dependence between track counting and `TileCal` is shown in Figure 5.10 (top). It is found to be approximately 0.01 ± 0.02 $\%/\mu$ where the uncertainty covers the scatter of most runs. The track counting and `TileCal` measurements are therefore expected to drift by 0.25 ± 0.50 % between $\mu = 10$ and $\mu = 35$, which are the typical limits of normal data-taking conditions.

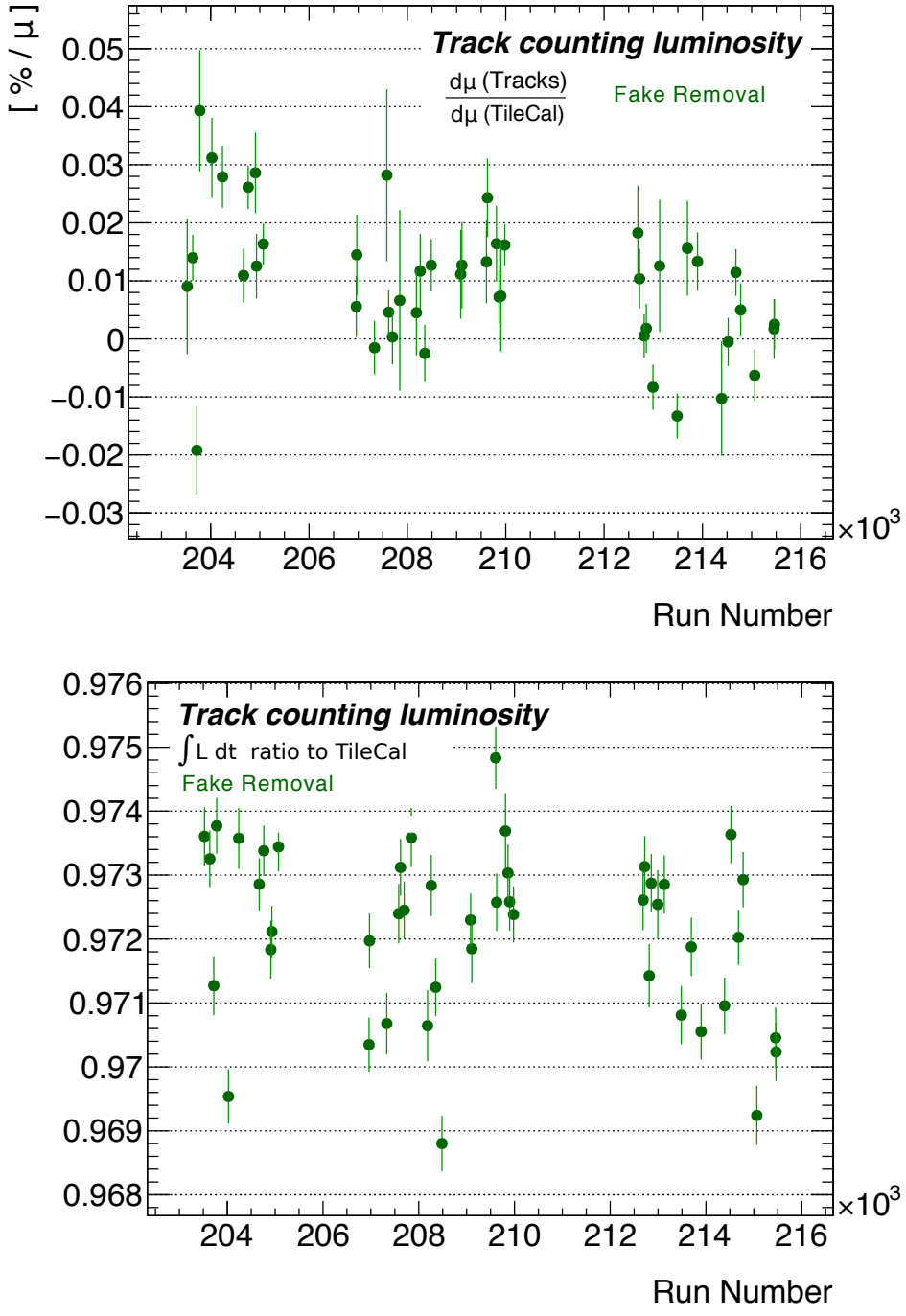

Figure 5.10: Relative μ-gradient and ratio of luminosity integrated over LBs with $20 < \mu < 25$ between the `fake removal` working point and `TileCal` in 2012 runs.

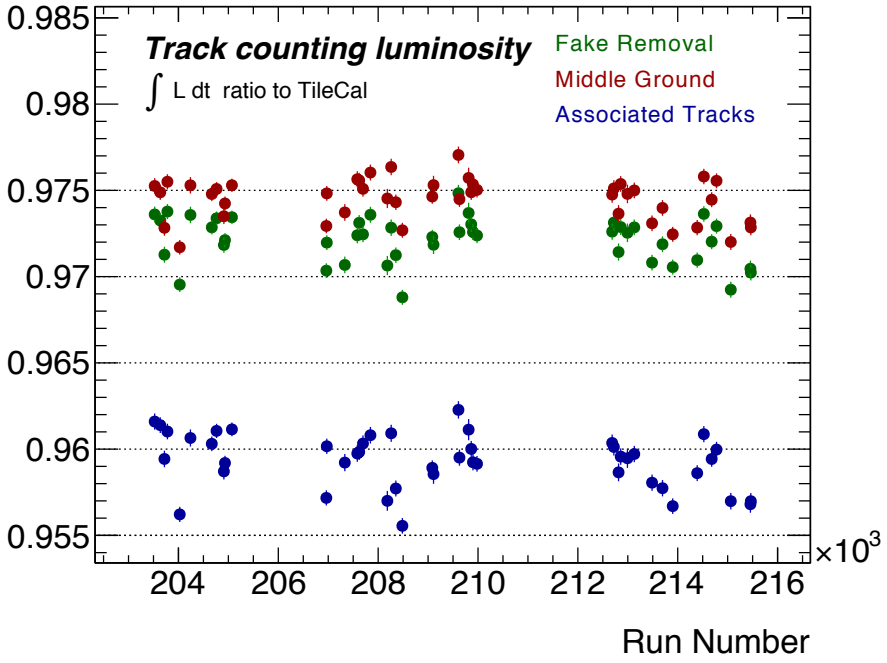

Figure 5.11: Ratio of luminosity integrated over LBs with $20 < \mu < 25$ between track counting and `TileCal` in 2012 runs.

Working point	μ-gradient vs. TileCal [$\%/\mu$]	
	Before fake subtraction	After subtraction
Fake removal	0.016(11)	0.008(11)
Middle ground	0.026(13)	0.015(13)
Associated tracks	0.032(14)	0.012(14)

Table 5.3: Weighted average of the relative μ-dependences measured per-run between track counting and `TileCal`. Standard deviations are shown in parentheses.

The long-term stability is shown in Figure 5.10 (bottom). At high luminosity, the preliminary calibrations used for the two luminometers disagree by approximately 2.5 – 3.0 %. This is not important in the study of relative stability and can be rectified by appropriate cross-calibration. An envelope between 0.970 and 0.974 captures all runs except for 4 outliers. The estimated long-term relative stability is therefore ±0.2 %.

Table 5.3 shows the average μ-dependence of all three working points relative to `TileCal`. It also shows the values obtained when the simulation driven fake subtraction is not applied. The correction is shown to improve the stability with respect to `TileCal`. A small residual slope of $\lesssim 0.02$ $\%/\mu$ is observed for all working points with a standard deviation of a similar magnitude.

Figure 5.11 shows the long-term stability of each working point relative to `TileCal`. The scatter is within ±0.3 % in all cases. However, since the three working points were calibrated to give consistent results during van der Meer conditions, their relative offset in Figure 5.11 indicates an internal track counting calibration transfer of 1.3 %.

The studies in this section indicate that track counting and TileCal are relatively stable at the level of $\mathcal{O}\,(< 0.5\ \%)$ in data-taking runs throughout the year. Either measurement may therefore be used to derive stability corrections for the online luminosity. However, an internal calibration transfer between the track counting working points is observed. The cause of this is not understood.

5.5.2 Corrections to online luminosity

The track counting, BCM and LUCID algorithms are all calibrated using the vdM method. Their calibrations are estimated to be consistent to within 0.5 % by comparing luminosity measurements in the quiescent beam period of the November scan set. This is the data collected during stable beam collisions occuring before and after the scan periods.

A significant relative μ-dependence is observed when comparing BCM and LUCID to track counting and calorimeter-based luminometers. A calibration transfer correction is used to extrapolate the vdM calibration to high luminosity conditions. A second correction for long-term drift is applied to account for instrumental effects and the varying μ-ranges between runs. Any residual μ-dependent effects are covered by the systematic uncertainties.

The absolute calibrations, and the online luminosity corrections described below, were performed by other members of the analysis team. The corrections are derived based on the track counting measurements and stability studies already presented.

Calibration transfer

The calibration transfer correction is calculated using the following procedure:

1. The run-integrated luminosity ratio between track counting and {LUCID, BCM} is plotted as a function of the annual cumulative integrated luminosity fraction, as shown in Figure 5.12. Run-to-run fluctuations are smoothed using a linear parameterisation.

2. The parameterisation is evaluated in LHC fill 3323, which occurs soon after the November vdM scan in fill 3316. This is equal to (but the opposite sign of) the calibration transfer correction. The `fake removal` working point is used to define the central value and the difference to `associated tracks` is assigned as a symmetric systematic uncertainty of ±1.3 %.

The BCM and LUCID calibration transfer corrections are summarised in Table 5.4 with an absolute uncertainty of ±1.4 % dominated by track counting internal consistency. Additional contributions come from the trigger dead-time estimation which affects the track counting calibration (±0.2 %), calibration consistency (±0.5 %) and track counting statistic fluctuations (±0.1 %). Approximately half of this correction can be accounted for by the observed relative μ-dependences with the remainder not fully understood.

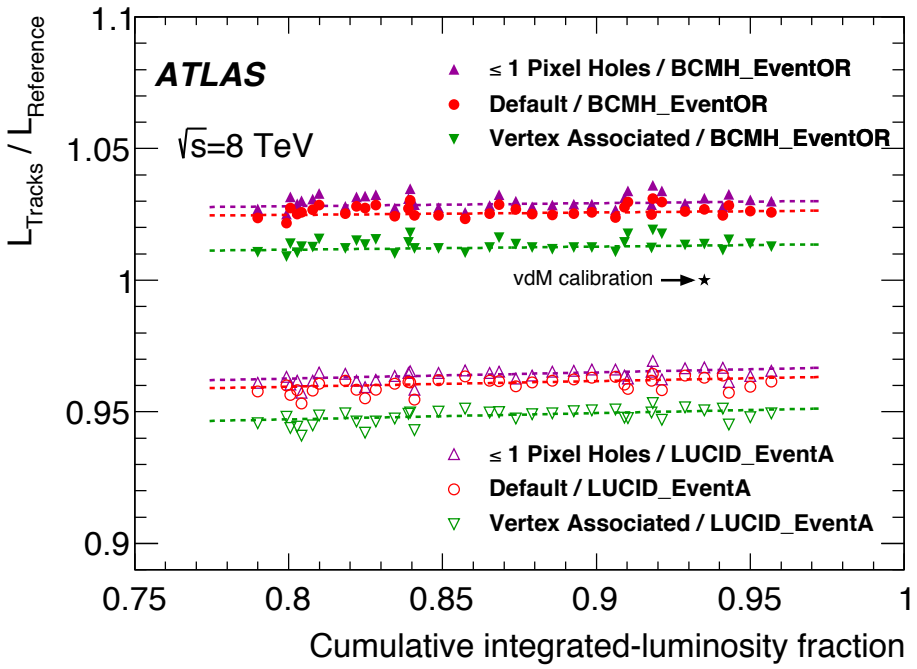

Figure 5.12: Calibration transfer calculation for BCM and LUCID using the three track counting working points, shown in different colours. Figure sourced from Ref. [200].

Algorithm	Correction to σ_{vis} [%]
BCM-H-OR	-2.5 ± 1.4
BCM-V-OR	-2.9 ± 1.4
LUCID-OR-A	$+3.5 \pm 1.4$
LUCID-OR-C	$+3.9 \pm 1.4$

Table 5.4: Calibration transfer corrections applied to LUCID and BCM in 2012 data.

Long-term stability

Figure 5.13(a) shows the integrated luminosity ratio between {track counting, BCM} and TileCal in all 2012 runs. The y-axis represents the percentage deviation from unity. All luminometers are cross-calibrated in fill 3323 as this is where the calibration transfer correction was applied. This is indicated by the vertical arrow. A significant BCM drift is observed throughout the year. An internal comparison of BCM algorithms also reveals a shift of 0.6 % in the H/V ratio extending over a one-month period in October and November. This is visible in the comparison with TileCal. It is correlated with an increase in electronic noise over this period.

The long-term stability correction is derived using two linear parameterisations per algorithm: one during the BCM noise period and one covering all runs before and after. The resulting long-term relative stability is shown in Figure 5.13(b) after applying this correction. The EMEC and FCal measurements are also shown. A systematic uncertainty of ±0.5 % is assigned to cover residual run-to-run fluctuations.

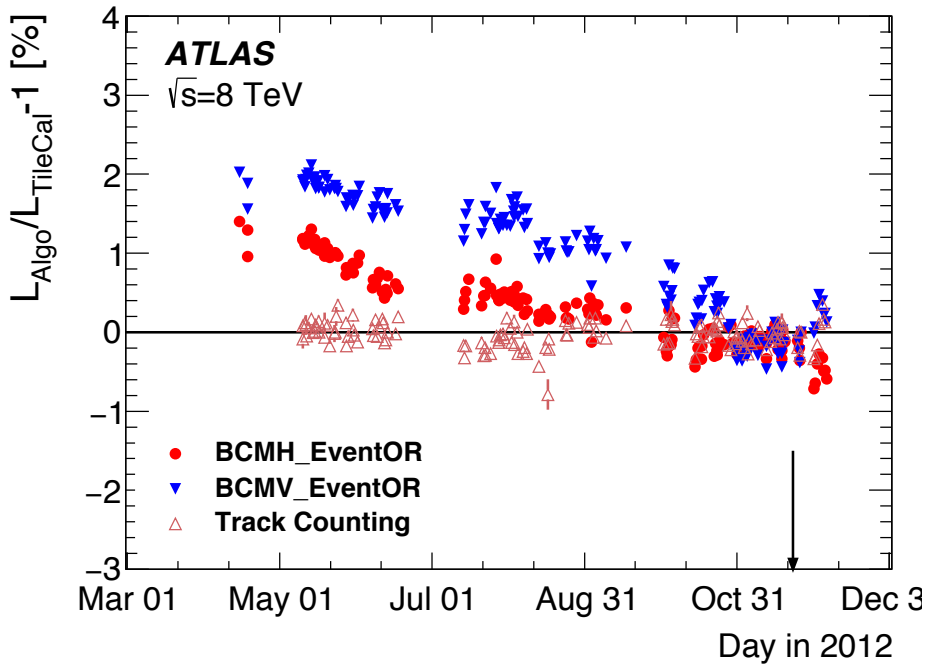

(a) Before BCM stability correction

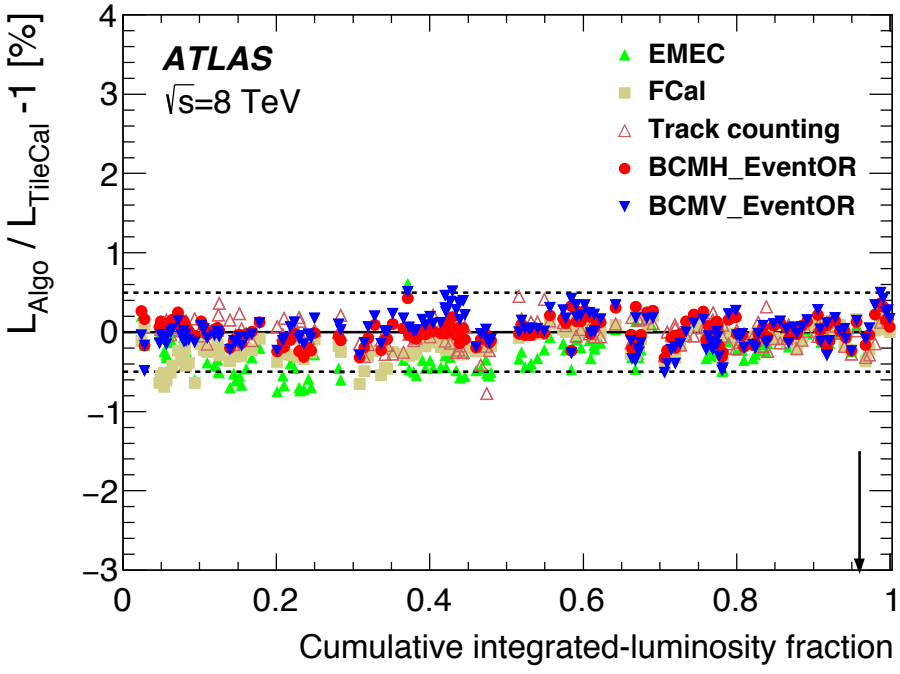

(b) After BCM stability correction

Figure 5.13: Run-integrated luminosity comparison throughout 2012 runs cross-calibrated in fill 3323 indicated by the arrow. Figures sourced from Ref. [200].

5.5.3 Summary of 2012

In high luminosity conditions, track counting and TileCal are shown be relatively stable in both run integrated luminosity and μ-dependence. Track counting is used to perform a correction to transfer the calibrations of LUCID and BCM to high luminosity conditions. An internal relative calibration transfer between track working points introduces an uncertainty of ± 1.3 %. A long-term stability correction is applied to BCM which accounts for drift over the course of 2012 as well a one-month noise period. Comparisons between BCM and offline luminometers results in a ± 0.5 % stability uncertainty. These corrections and uncertainties account in part for a known relative μ-dependence between BCM and offline luminometers. The van der Meer calibration of BCM has an uncertainty of ± 1.2 % driven by instrumental effects, knowledge of beam conditions and fit assumptions. The total luminosity uncertainty for 2012 is ± 1.9 %.

5.6 2015 data

LUCID-Bi-Or-A is chosen to be the baseline luminometer in 2015. This is an EventOr algorithm which uses only the Bismuth calibrated PMTs on the A-side of the upgraded LUCID detector. Online high voltage calibration as well as offline calibration tuning, transit time and luminosity scan corrections are applied. It is chosen due to its stability over time and small transit time sensitivity. It does not saturate in the range of μ delivered in 2015. This is shown in Figure 5.14. The majority of data is collected in the range $10 < \mu < 20$. As well as the increase in centre-of-mass energy, an important change is the spacing between adjacent filled BCIDs which has a minimum of 50 ns in 2012 and 25 ns in 2015. A significant train dependence was observed when comparing the per-BCID luminosity measured by BCM both internally and with respect to LUCID and track counting in 25 ns conditions, and so BCM is not used as an online luminometer in 2015. The introduction of the IBL means that at least one extra Pixel hit is expected per primary track, effectively increasing the acceptance of fixed silicon cluster requirements.

Track counting measurements are performed for the runs summarised in Table 5.5. After an early commissioning period, several low-μ runs were performed using isolated BCIDs providing 191 nb^{-1} data for the LHCf experiment [209]. Several runs were then performed using 50 ns trains from which 85 pb^{-1} data was collected and used to perform inclusive W, Z and $t\bar{t}$ cross section measurements [210, 211]. Collisions were then delivered using the design target of 25 ns trains with increasing intensity throughout the remainder of the year with the following exceptions:

- Run 276731 using 50 ns trains was performed in between 25 ns runs.
- A vdM scan period was performed using two separate LHC fills. These are runs

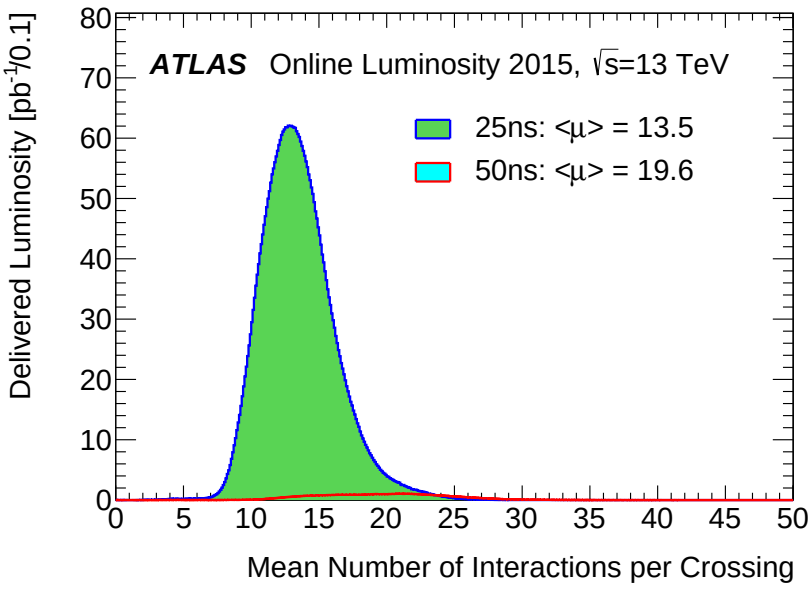

Figure 5.14: μ profile of data recorded in 2015.

277025 and 277089 and contain both scans and quiescent beams.

- A μ-scan was performed in run 280520. This used beam displacement to deliver a range of $0.1 \lesssim \mu \lesssim 18$ with bunch trains typical of high luminosity running.

- Several runs were performed with low-μ, isolated BCIDs and wide beam profiles for the ALFA experiment. Runs 281662 and 281712 have track counting data.

5.6.1 Updates

This section summarises several updates to the track counting measurement in 2015.

Pixel enhanced working points

In early 2015 data it was observed that track counting was inconsistent with other luminometers at the $\mathcal{O}(10\ \%)$ level when comparing runs with isolated BCIDs and those with 25 ns trains. It was found that the `vtxLumi` reconstruction suffered from out-of-time pileup caused by SCT pulses extending into the 25 ns window following the collision which produced the track. Since track reconstruction is seeded up to a radius of 600 mm which covers the whole of the SCT, it was possible to reconstruct a track based only on these pileup SCT hits. These are called *ghost tracks* and are characterised by two properties:

- an excess of tracks at high $|\eta|$.

- an excess of tracks with 0 associated Pixel hits.

Run	BCID spacing	Num. BCIDs	Median μ	$\int \mathcal{L}dt$ [pb^{-1}]	Details
266904 ... 267167	Isolated, 50ns	$2-6$	$10-20$	–	
267358 ... 267599	Isolated	$11-37$	$0.002-0.03$	–	LHCf
267638 ... 271744	50ns trains	$38-414$	$14-22$	85	$W/Z/t\bar{t}$
276262 ... 276689	25ns trains	$141-303$	$13-19$	40	
276731	50ns trains	254	19	25	
276778 ... 276954	25ns trains	$446-447$	$13-15$	10	
277025	vdM	5	0.7	–	
277081	Isolated	8	0.05	–	vdM
277089	vdM	8	0.7	–	
278727 ... 280500	25ns trains	$49-1309$	$11-16$	800	
280520	25ns trains	881	18	24	μ-scan
280614 ... 281411	25ns trains	$1309-1813$	$12-16$	800	
281662	Isolated	3	0.07	–	ALFA
281712		3	0.08	–	
282625 ... 284484	25ns trains	$517-2232$	$3-17$	1300	

Table 5.5: Summary of runs with track counting measurements in 2015.

These observations are demonstrated in Figure 5.15. Ghost tracks exclusively affect BCIDs which are neither isolated nor the first in a train as there must be a filled BCID in the preceeding 25 ns window. This is a track counting train dependence. The impact of ghost tracks was initially mitigated by defining `pixel enhanced (N)` working points which are equivalent to `fake removal` with the additional requirement that tracks be reconstructed using at least 1 (N) Pixel cluster(s). Data were subsequently reprocessed using a `01x` requirement. This only allows an SCT hit to be registered provided that a hit was not present in the previous BCID. The reprocessing was found to remove all observable impact of ghost track contributions. All further results presented use reprocessed data.

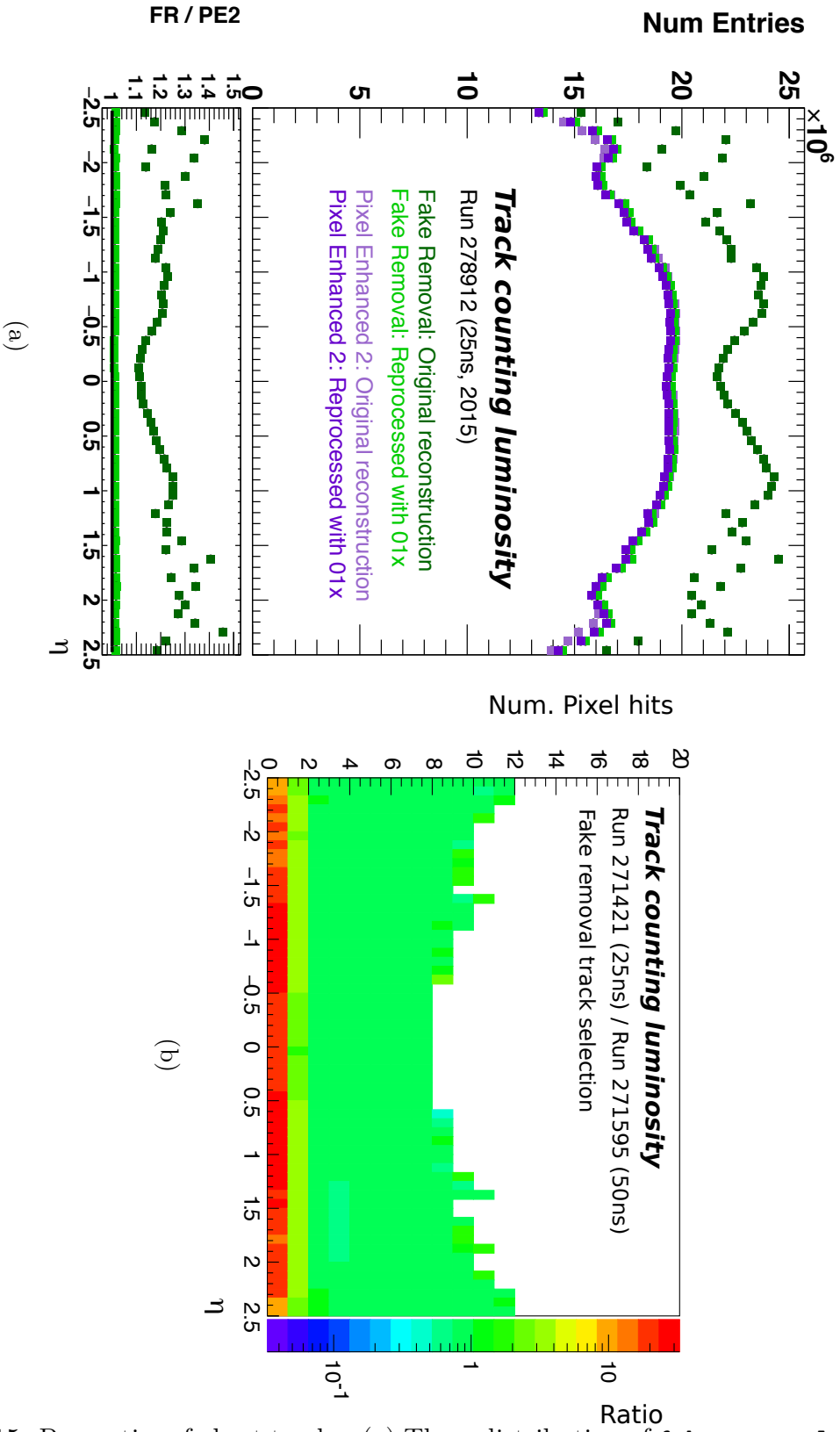

Figure 5.15: Properties of ghost tracks. (a) The η distribution of `fake removal` and `pixel enhanced 2` tracks before and after reprocessing with the `01x` requirement. (b) The ratio between the number of pixel hits per track observed in 25 ns and 50 ns trains before reprocessing with the `01x` requirement.

Other working points

Vertex associated tracks were not used in 2015 because vertex reconstruction is known to be impacted by the significant μ-dependent effects of split and merged vertices. An additional working point is introduced which utilises the `tight` track definition recommended for physics analyses. This is shown to be fairly well described by simulation [212], although is intended for use with TRT information. Tracks are required to have at least 9 silicon clusters for $|\eta| \leq 1.65$ and 11 for $|\eta| > 1.65$, at least one hit in the IBL or next-to-innermost Pixel layer, no Pixel holes, a maximum of 2 SCT holes and a maximum of 1 module shared with another reconstructed track.

Calculation of $s(d_0)$

It was discovered that the distribution of $s(d_0)$ was dependent on the width of the beamspot. This is because d_0 is calculated from the IP at $(x, y) = (0, 0)$ whereas the true origin of a track is from any point within the beamspot. A larger beamspot will therefore cause a typically larger measured d_0 and so the calculation shown in Eq. 5.8 will provide a wider distribution of $s(d_0)$. This is shown in Figure 5.16(a), which compares data collected in four typical high luminosity runs (labelled "Physics" and shown in red/orange) with the wider beam profiles delivered in the two ALFA (blue) and two vdM (green) runs.

This inconsistency is rectified by a redefinition of $s(d_0)$ in which the denominator is the quadrature sum of Δd_0 and the measured beamspot width, σ_{beamspot}, i.e.

$$s\left(d_0\right) = \frac{d_0}{\sqrt{\left(\Delta d_0\right)^2 + \left(\sigma_{\text{beamspot}}\right)^2}} \,. \tag{5.9}$$

Figure 5.16(b) shows the same comparison of runs. The redefinition is shown to be significantly more consistent and is therefore used for all further results within this chapter.

Fake fraction

The fraction of non-primary tracks is evaluated for Run 2 working points using events simulated with Run 2 conditions including $\sqrt{s} = 13$ TeV and the presence of the IBL in the range $0 < \mu < 60$. This work was performed by another member of the analysis team. A track is defined as non-primary if the matching probability with a truth-level charged particle is estimated to be less than 70 % or if the particle was produced by the `GEANT` simulation. The non-primary fraction f_{NP} is parameterised as a cubic function of the number of tracks n_{t} with the requirement that $f_{\text{NP}}(n_{\text{t}} = 0) = 0$. This is shown in Table 5.6 evaluated at $\mu = 20$ for three working points using an approximate calibration factor of $\mu = 3.8 \times n_{\text{t}}$. The non-primary fraction is less than 5 % in all cases. The linear component of this function does not need to be subtracted. Only the second and

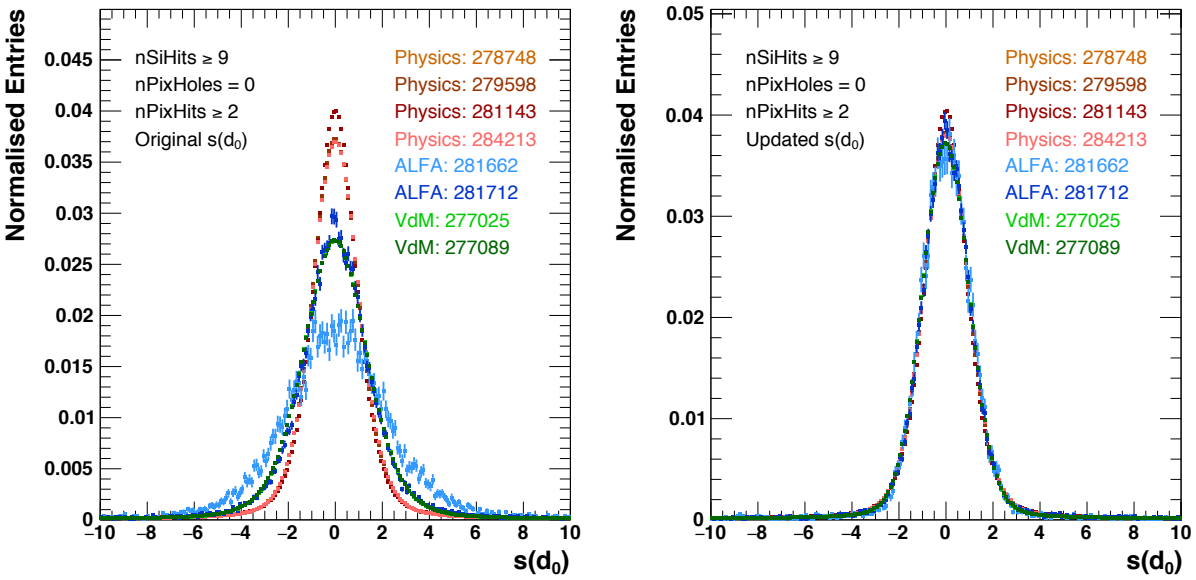

(a) before $s(d_0)$ update.

(b) after $s(d_0)$ update.

Figure 5.16: Consistency of the measured $s(d_0)$ in a variety of conditions.

Working point	$f_{\mathrm{NP}}(\mu = 20)$	$f_{\mathrm{CT}}(\mu = 20)$	$f_{\mathrm{CT}}(\mu = 40)$	$f_{\mathrm{CT}}(\mu = 60)$
Tight	4.7 %	0.05 %	0.2 %	0.4 %
Fake removal	4.5 %	0.05 %	0.2 %	0.5 %
Pixel enhanced 2	3.7 %	0.05 %	0.2 %	0.5 %

Table 5.6: Estimated fraction of non-primary tracks, f_{NP}, and track counting calibration transfers, f_{CT}, using Run 2 simulation.

third order terms are the source of a μ-dependence which would lead to a track counting calibration transfer. The non-linear contribution is evaluated at various values of μ and labelled $f_{\mathrm{CT}}(\mu)$ as shown in Table 5.6. A contribution of 0.05 % at $\mu = 20$ is considered negligible and so no fake subtraction is applied to 2015 data. Such a subtraction may be considered if a significant fraction of collisions are delivered at $\mu = 60$ due to an estimated 0.5 % track counting calibration transfer.

5.6.2 Internal stability

It was noticed that the mean of the measured $s(d_0)$ within a run has a significant drift between 0 and -1 towards the end of 2015 as shown by the blue curve in Figure 5.17. This is possibly due to a displacement of the beamspot centre from the nominal IP at $(x, y) = (0, 0)$. It is expected that such a drift would impact the acceptance of the $|s(d_0)| < 7$ requirement imposed by `fake removal` and `pixel enhanced (N)` working points. Since the `tight` working point does not impose such a requirement, it is used to measure the fraction of tracks for which $|s(d_0)| > 7$. This is shown by the red points where runs are distinguished by their bunch structure and vdM quiescent beams are shown as stars. Other

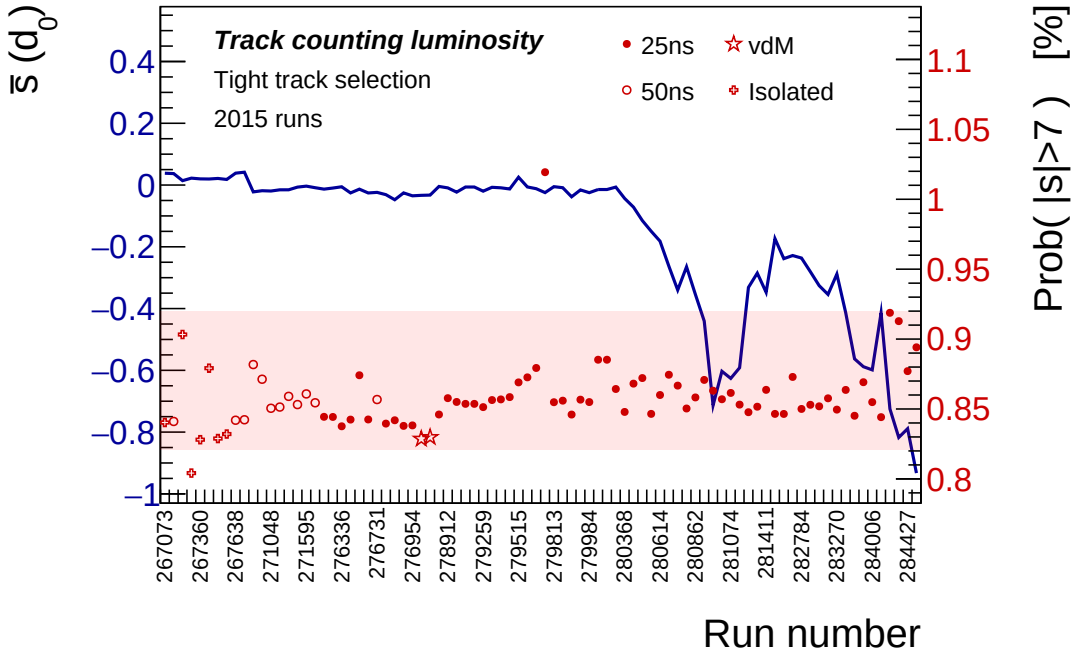

Figure 5.17: Drift of the mean $s(d_0)$ in 2015 runs (blue curve) and the estimated impact on the acceptance of the $s(d_0)$ requirement (red points).

than two outliers, all runs are covered by an envelope of 0.87 ± 0.05 % indicated by the red box. This suggests that other working points likely suffer from a maximum instability of ± 0.05 % due to the $s(d_0)$ drift.

The internal stability of track counting is evaluated by comparing the run-integrated luminosity measurements of different track working points. This is shown in Figure 5.18 where the y-axis represents the percentage difference with respect to `pixel enhanced`. All working points are cross-calibrated in run 276952. Comparisons with `fake removal` (red), `pixel enhanced 2` (blue) and `tight` (green) are shown with markers indicating bunch structure. The vdM quiescent beams are shown as stars. The GRL is used for all runs except for vdM quiescent beams and run 277081 directly in between them. Grey boxes indicate periods with $\mu < 1$ and isolated colliding BCIDs.

All runs with $\mu > 1$, shown outside of the grey boxes, are internally consistent to within ± 0.2 %. This covers runs using 50 ns and 25 ns trains, shown as open and filled dots respectively, as well as run 267073 which uses isolated BCIDs. This imples either a small absolute train dependence or one which is highly correlated between working points. The consistency of `fake removal` and `pixel enhanced (N)` working points implies that there is no significant contribution from ghost tracks. The consistency between `tight` and other working points implies that the measurement is stable with respect to variations of $s(d_0)$, number of silicon and IBL hits and number of shared silicon modules. The overall consistency implies a stability of Inner Detector conditions throughout the year.

Comparison with runs for which $\mu < 1$ reveals a shift of 0.6 % in the ratio between

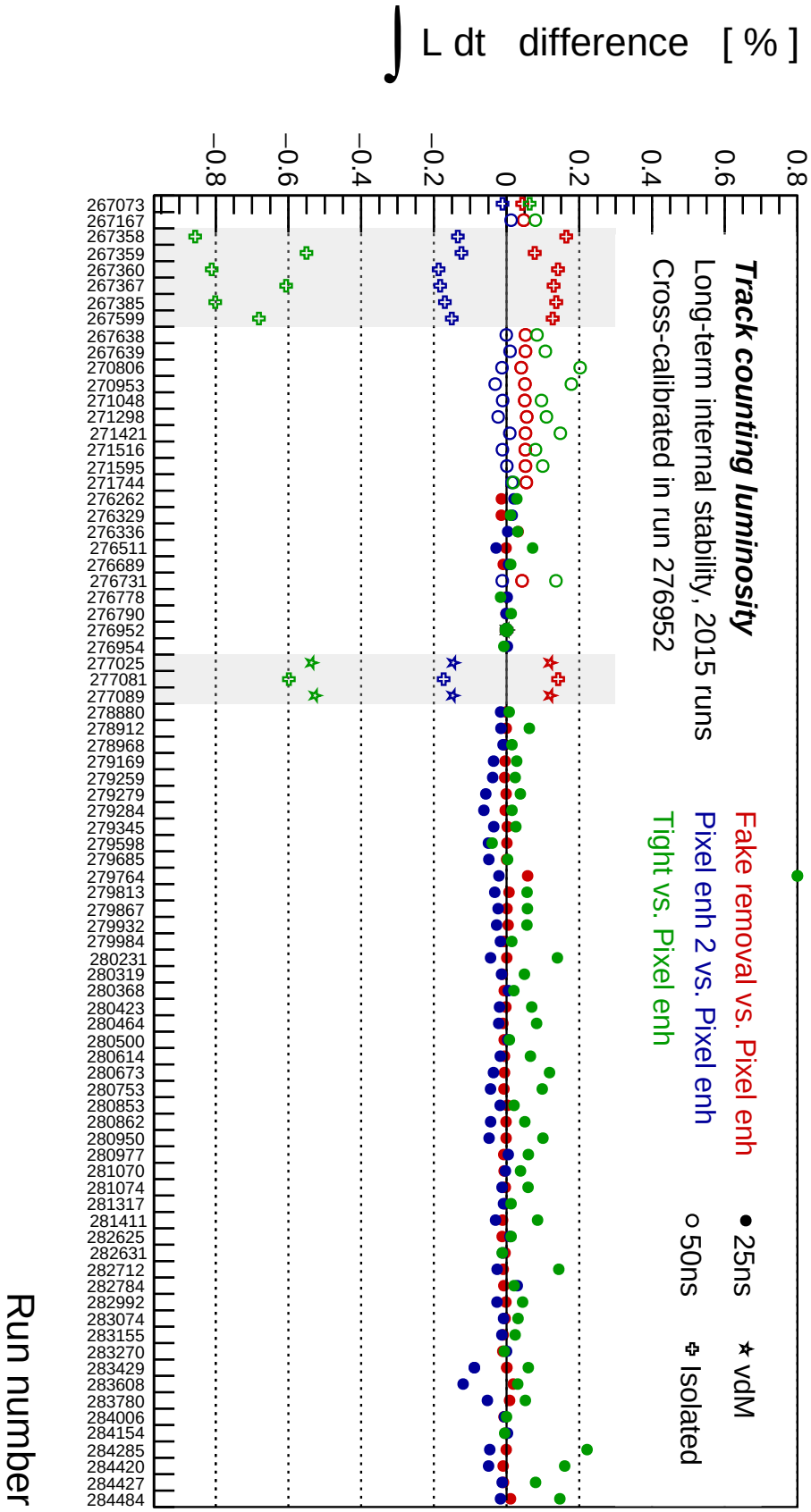

Figure 5.18: Relative stability of track counting working points in 2015. Grey boxes indicate runs with $\mu < 1$ and isolated colliding BCIDs.

the `tight` and `pixel enhanced` working points. Whilst the cause is not known, this likely indicates an uncorrected relative μ-dependence of the tracking efficiency or a dependence on the beamspot conditions of low-μ runs. This internal inconsistency means that the uncertainty on the calibration transfer relative to `LUCID` must be at least ± 0.6 %.

5.6.3 Corrections to online luminosity

The following strategy is used for 2015 data. A calibration transfer correction is applied to the `LUCID-Bi-Or-A` measurement. This is evaluated separately for runs with 25 ns and 50 ns trains. A long-term stability correction is not applied. Systematic uncertainties on the calibration transfer and long-term stability are derived. Special treatment is applied to the LHCf dataset due to the use of low-μ conditions and isolated bunches.

Calibration transfer

The relative calibration transfer between track counting and `LUCID` is estimated by cross-calibrating the luminosity measurements in the vdM quiescent beam period of run 277025 and calculating the average disagreement in integrated luminosity measured is several high luminosity runs. Use of cross-calibration eliminates systematic uncertainties associated with absolute calibration. This procedure is performed separately for 50 ns and 25 ns trains using the following runs:

$$\begin{aligned} 50 \text{ ns } &\in \{267639, 270806, 271048, 271421, 271516, 271595, 271744, 276731\} \\ 25 \text{ ns } &\in \{276262, 276329, 276511, 276689, 276790, 276952, 276954\} \ . \end{aligned} \tag{5.10}$$

These are chosen due to their proximity (in time) to the vdM scan session and the availability of offline luminosity measurements.

The cross-calibration obtained in vdM run 277025 is validated and checked for consistency with vdM run 277089. Figure 5.19 shows the absolute track counting measurements and the comparison with `LUCID-Bi-Or-A`. After cross calibrating in run 277025, the ratio in run 277089 is consistent with unity at the level of 0.1 % and within a 2 σ statistical fluctuation. No individual LB outliers are observed. The `L1-RD0-BGRP9` trigger was used in run 277025 which sampled only 5 of the 8 colliding BCIDs. The `LUCID` measurement is therefore calculated using a consistent BCID selection in this run.

The calibration factors obtained using the two vdM quiescent beam runs are shown in Table 5.7. All four working points observe $\lambda = 3.7 - 3.8$ tracks per inelastic collision and are stable at the level of 0.1 % between runs.

Figure 5.20 shows the run integrated luminosity ratio between track counting and `LUCID` for the runs specified in Eq. 5.10 with 50 ns (open points) and 25 ns (closed points) bunch spacing. Clear evidence for a relative calibration transfer is observed. This is larger in

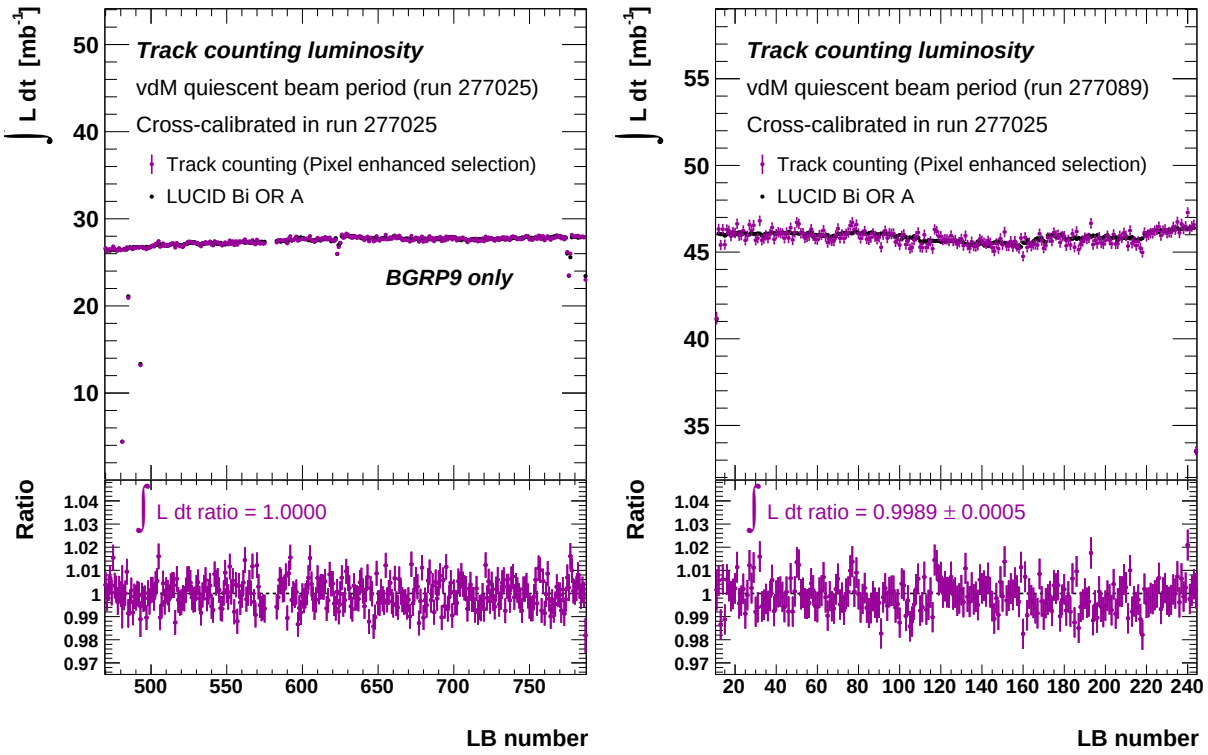

Figure 5.19: Consistency between runs with vdM quiescent beams in 2015.

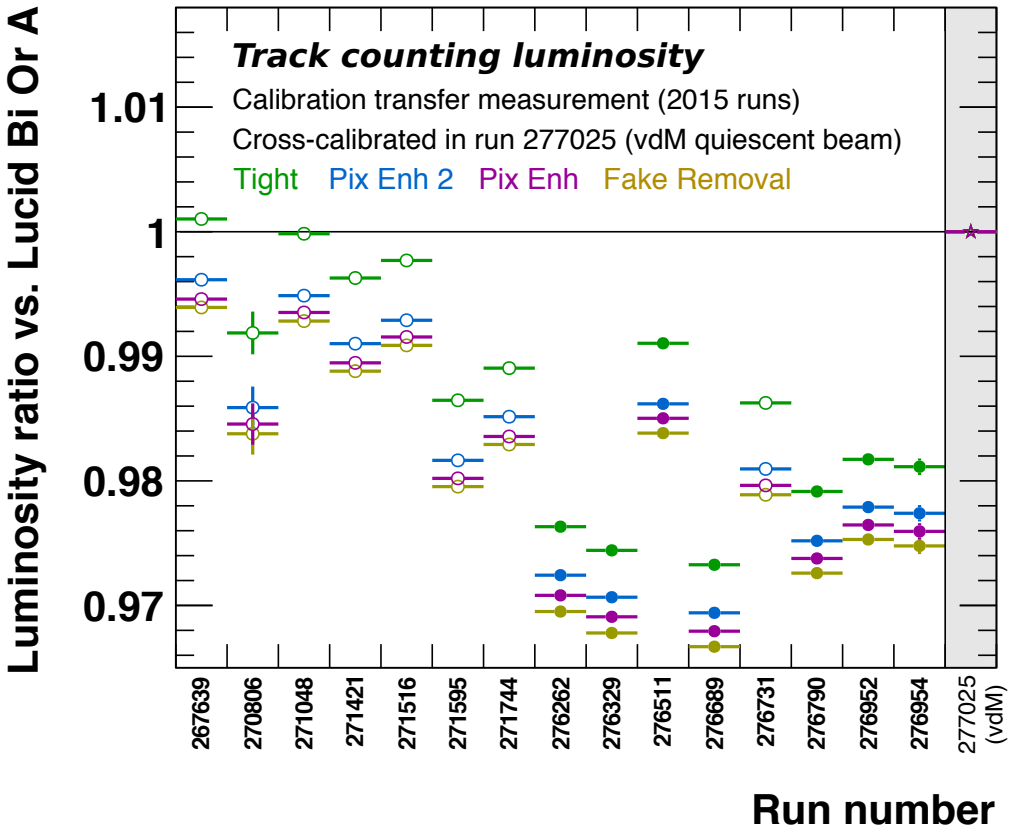

Figure 5.20: Relative calibration transfer between track counting and LUCID in 2015. Closed and open points represent runs with 25 ns and 50 ns trains respectively.

Working point	λ		
	Run 277025	Run 277089	Run 276952
Tight	3.842	3.838	3.778
Fake removal	3.792	3.788	3.706
Pixel enhanced	3.766	3.762	3.684
Pixel enhanced 2	3.739	3.735	3.663

Table 5.7: Average number of tracks per inelastic *pp* collision after cross-calibration with `LUCID-Bi-Or-A` in various runs.

Luminometer	Algorithm	μ_{vis} (`LUCID-Bi-Or-A`) correction [%]	
		50 ns trains	25 ns trains
Track counting	Tight	−0.6	−2.0
	Fake removal	−1.4	−2.7
	Pixel enhanced	−1.3	−2.6
	Pixel enhanced 2	−1.1	−2.4
TileCal	E3 (mean)	0.0	−1.4
	E4 (mean)	0.0	−1.2
	D5 (mean)	−1.4	−2.6
	Average	−0.5	−1.7

Table 5.8: `LUCID` calibration transfer estimates using track counting and `TileCal`.

runs with 25 ns trains. The run-to-run scatter is larger than statistical fluctuations and motivates an average correction. The relative calibration transfer is observed to vary when using different track working points. This suggests an internal track counting calibration transfer consistent with the observations of Figure 5.18. The ordering of working points is consistent between all runs.

The `TileCal` measurement can be cross-calibrated in the vdM quiescent beam period provided that the pedestal and background subtractions are well understood. It is used as an independent measure of calibration transfer. Three cell measurements are provided by another member of the collaboration after averaging between the A- and C-sides. These are `E3`, `E4` and `D5`. The `TileCal` recommendation is to take the average of these measurements as the central value of the estimate. A track counting average is not favourable due to the significant correlation between working points. `Pixel enhanced` is chosen as the central value due to its moderate Pixel cluster requirement and removal of $s(d_0)$ outliers.

Table 5.8 shows the calibration transfer measurements for all `TileCal` and track counting algorithms. The recommended central values are highlighted in green. The disagreement between `tight` and `pixel enhanced` working points is 0.7 % for 50 ns trains and 0.6 % for 25 ns trains. The `D5` measurement of `TileCal` is consistent with the `pixel enhanced` working point, however the `E3` and `E4` cells disagree by $1.2 - 1.4$ %.

The calibration transfer correction is defined using the `pixel enhanced` measurement because track counting shows greater internal consistency and does not require a significant background subtraction. The difference with respect to the `TileCal` average is defined as

a symmetric systematic uncertainty. This covers all track working points within a 1 σ window and the most outlying TileCal cell measurements within 2 σ. The correction to μ_{vis} (LUCID-Bi-Or-A) is -1.3 ± 0.8 % for 50 ns trains and -2.6 ± 0.9 % for 25 ns trains. This is comparable with the correction derived using 2012 data. Note that a negative correction applied to μ_{vis} has the same effect as a positive correction applied to σ_{vis}.

Long-term stability at high μ

Figure 5.21 shows the run integrated luminosity comparison between track counting, TileCal, EMEC and LUCID-Bi-Or-A for runs with trains of filled bunches. Only LBs with track counting data are considered. The calibration transfer correction is applied to LUCID-Bi-Or-A which is used as the reference algorithm. The comparison with the vdM runs is shown. All luminometers are cross-calibrated in run 276952. A long-term stability correction is not required because no systematic deviation from 0 is observed consistently by all offline luminometers. An envelope of ± 1 % covers the majority of run-to-run scatter as shown by the grey filled area. This is assigned as a systematic uncertainty.

LHCf dataset

Figure 5.22 shows the run integrated luminosity comparison between track counting, BCM and LUCID for LHCf runs after cross-calibration in the vdM quiescent beam period of run 277025. These runs are characterised by isolated BCIDs and μ ranges comparable with vdM scans, therefore no calibration transfer correction is necessary. This is confirmed by the comparison with vdM runs (track counting only). Calorimeter measurements are not applicable due to the low μ range, however BCM may be used because no bunch trains are present. The LUCID Bismuth EventOr measurement from the C-side is used as a measure of internal stability. Track counting statistical uncertainties are large because many of the events sampled by the L1-RD0-FILLED trigger contain no inelastic collisions when $\mu \ll 1$. Only LBs with track counting data are considered in this plot. An envelope of ± 1 % is assigned as the systematic uncertainty based on the LUCID-to-BCM ratio considering all LBs. This plot demonstrates that such an uncertainty is not ruled out by track counting.

5.6.4 Summary of 2015

The track counting measurement is performed in 2015 data-taking. Key changes compared with 2012 are the use of $\sqrt{s} = 13$ TeV, 25 ns bunch spacing and the introduction of the IBL. The μ_{vis} of LUCID-Bi-Or-A is corrected for calibration transfer at the level of -1.3 ± 0.8 % (50 ns bunch spacing) and -2.6 ± 0.9 % (25 ns bunch spacing), derived using track counting as the central value and TileCal to define the uncertainty. A long-term stability uncertainty of ± 1.0 % is derived using track counting, TileCal and EMEC. No calibration transfer is applied to LHCf runs and a long-term stability uncertainty of ± 1.0 % is assigned

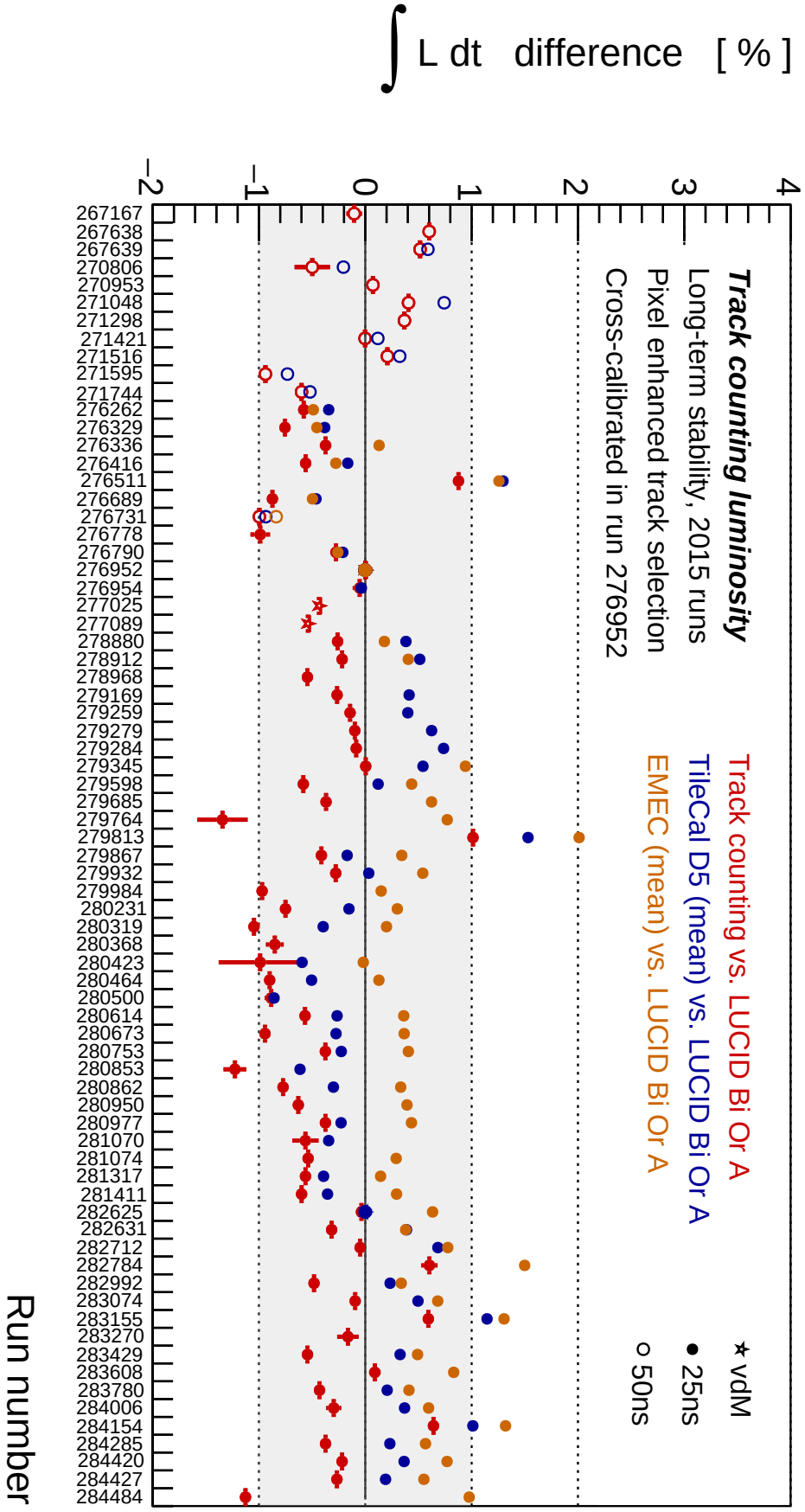

Figure 5.21: Comparison between run-integrated luminosities measured by LUCID and offline luminometers for 2015 runs after a LUCID calibration transfer correction.

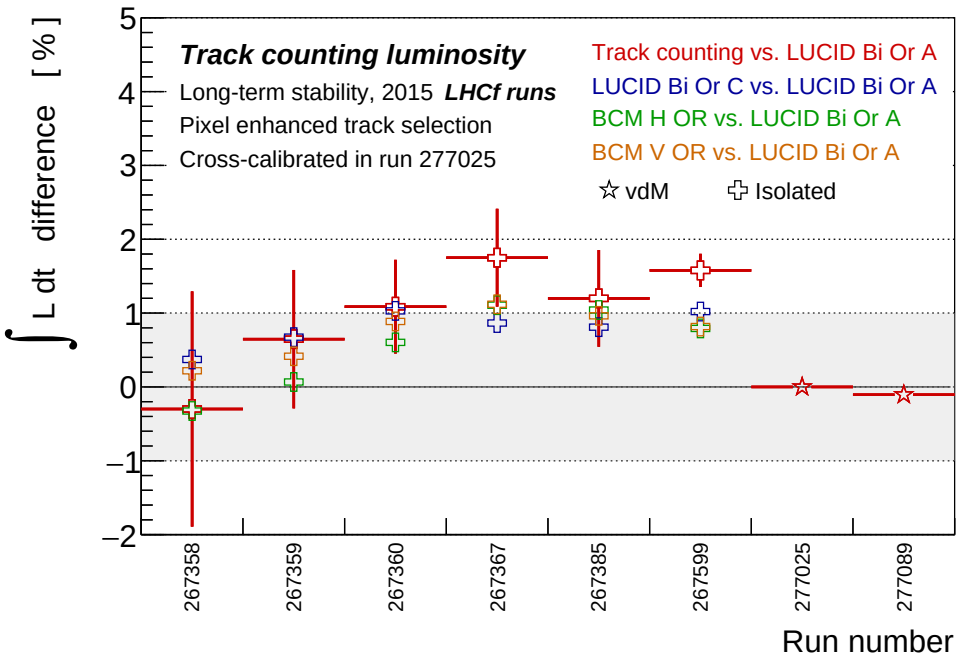

Figure 5.22: Comparison between run-integrated luminosities measured by LUCID and offline luminometers for 2015 LHCf runs.

based on the comparison of BCM and LUCID and validated using track counting. The LUCID-Bi-Or-A vdM calibration uncertainty is ±1.7 %. The total luminosity uncertainties for 2015 data are ±1.9 % (LHCf) and ±2.1 % (25 ns and 50 ns trains). These results correspond to luminosity tag OflLumi-13TeV-004 delivered in May 2016.

5.7 2016 data

LUCID-Bi-HitOr is defined as the baseline luminometer in 2016. This is a HitOr algorithm using only Bismuth calibrated PMTs and is chosen due to its apparent stability over time and because of possible saturation in EventOr algorithms. Figure 5.23 shows the μ-profile of 2016 data. The mean is $\langle\mu\rangle = 25$ and a majority of data are delivered in the range $10 < \mu < 45$. A total of 38.5 fb^{-1} data was delivered to ATLAS in 2016.

All data applicable to physics analyses were collected using trains with 25 ns bunch spacing. Several special runs were performed. These are summarised in Table 5.9. Two van der Meer scans were performed in runs 299390 and 300287. Several beam separation and crossing angle scans were performed in runs 309311, 309375 and 310781 with the aim of measuring the $\Sigma_x\Sigma_y$ ratio between ATLAS and CMS using both isolated BCIDs and the 25 ns trains typical of normal data taking. Eq. 5.2 shows that this is equal to the reciprocal of the ratio of delivered luminosities and was studied to test whether equal luminosities were being delivered to both experiments.

Run 299584 is a long run spanning a range of $8 < \mu < 22$ over a time of 12 hours with an integrated luminosity of approximately 250 pb^{-1}. Whilst not atypical compared with

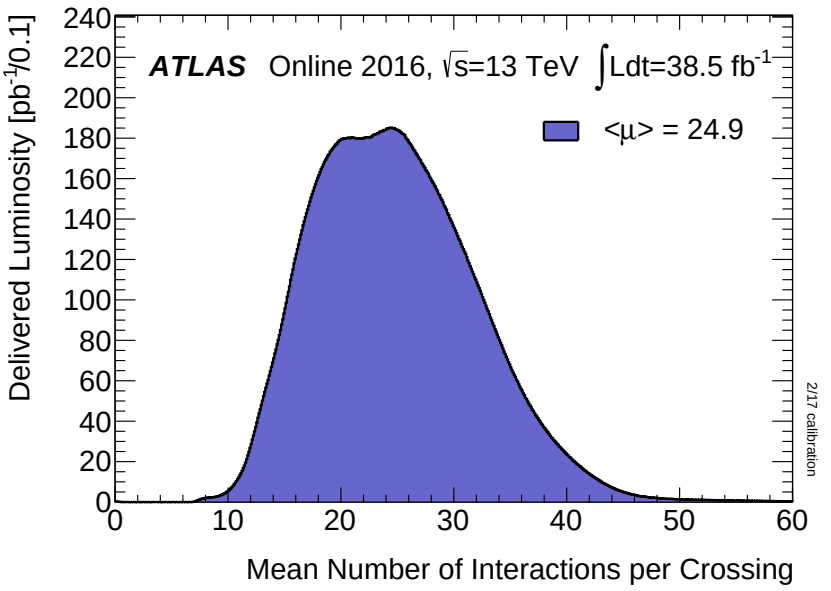

Figure 5.23: μ profile of data delivered in 2016.

Run number	Bunch conditions	Details
299390 300287	vdM	vdM
309311 309375	Isolated 25 ns trains	Beam separation scans
310781	Isolated	Crossing angle scans
299584	25 ns trains	Long run
310574	25 ns trains	High intensity run

Table 5.9: Summary of special runs in 2016.

later data taking, this run was performed in between the two vdM fills and is therefore a good candidate for the study of calibration transfer. Run 310574 is atypical due to the use of high intensity bunches with isolated (train) BCIDs spanning a range of $80 < \mu < 140$ ($30 < \mu < 60$) and a median of approximately $\mu = 40$. Performed on October 14$^{\text{th}}$, only 99 colliding BCIDs were present compared with the $2028 - 2208$ typical of 2016 data.

5.7.1 Internal stability

The default track selection is chosen to be `tight lumi` in 2016. This is equivalent to the `tight` working point of 2015 with the additional requirement of $|s(d_0)| < 7$. To assess the stability of this cut, `tight lumi 5 (9)` working points are defined with requirements of $|s(d_0)| < 5$ (9) instead. `Tight lumi A (C)` working points use only tracks on the A-side (C-side) of ATLAS in order to create statistically independent track selections. Systematic variation in the `A` vs. `C` comparison would indicate local changes in tracking efficiency driven by detector conditions. The `fake removal` and `pixel enhanced (N)` working points are

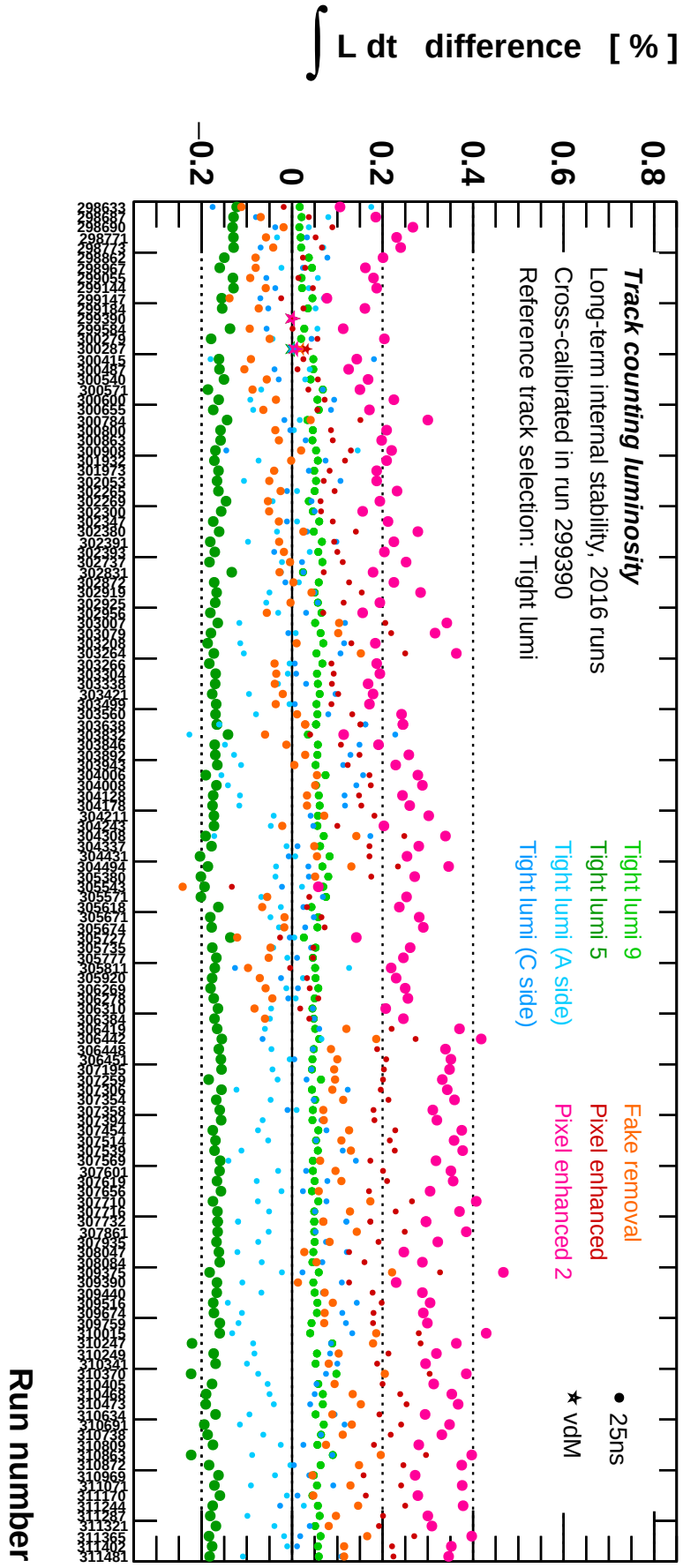

Figure 5.24: Relative stability of track counting working points in 2016.

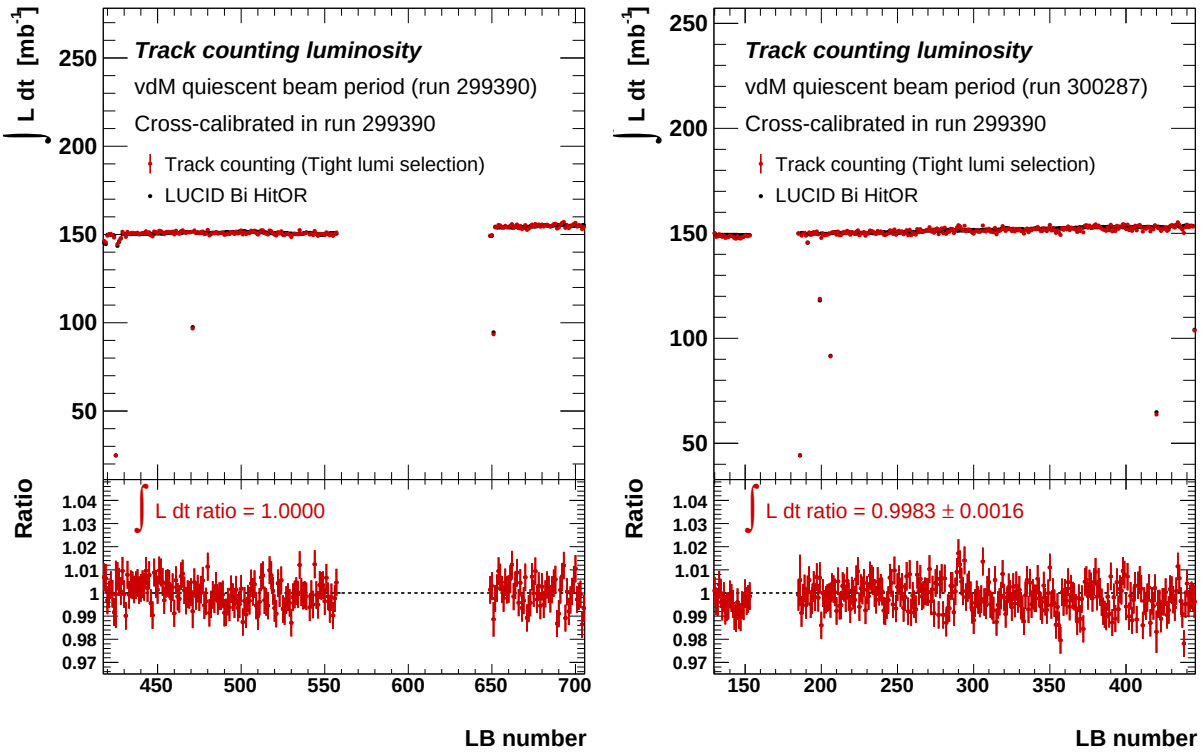

Figure 5.25: Consistency between runs with vdM quiescent beams in 2016.

unchanged with respect to the 2015 analysis.

Figure 5.24 shows the comparison of run integrated luminosities measured by the different working points in 2016 runs. All working points are cross-calibrated in the quiescent beam period of vdM run 299390. The two vdM quiescent beam periods are shown as stars. All other runs use 25 ns trains. The `tight lumi 5` and `9` working points are shown in green and systematically deviate on either side of `tight lumi` throughout the year. This indicates a small calibration transfer inconsistency due to the choice of $|s(d_0)|$ requirement. The `tight lumi A` and `C` working points also systematically deviate symmetrically around `tight lumi` as shown in blue. The working point with the largest deviation is `pixel enhanced 2` indicating a track counting calibration transfer working point inconsistency of up to ± 0.4 %. No significant systematic changes are observed throughout the year.

5.7.2 Comparison with LUCID

Using the same procedure as in 2015, now applied to 2016 data taking, track counting is cross-calibrated to `LUCID` in the vdM quiescent beam period of run 299390. This is shown in Figure 5.25(left) using the `tight lumi` working point. Figure 5.25(right) shows the resulting luminosity comparison in the second vdM quiescent beam which occured in run 300287. The cross-calibration consistency is measured to be 0.2 ± 0.2 %.

The calibrated number of tracks per inelastic collision, λ, obtained from cross-calibration to `LUCID` in the 2016 vdM quiscent beam periods are shown in Table 5.10. They differ by

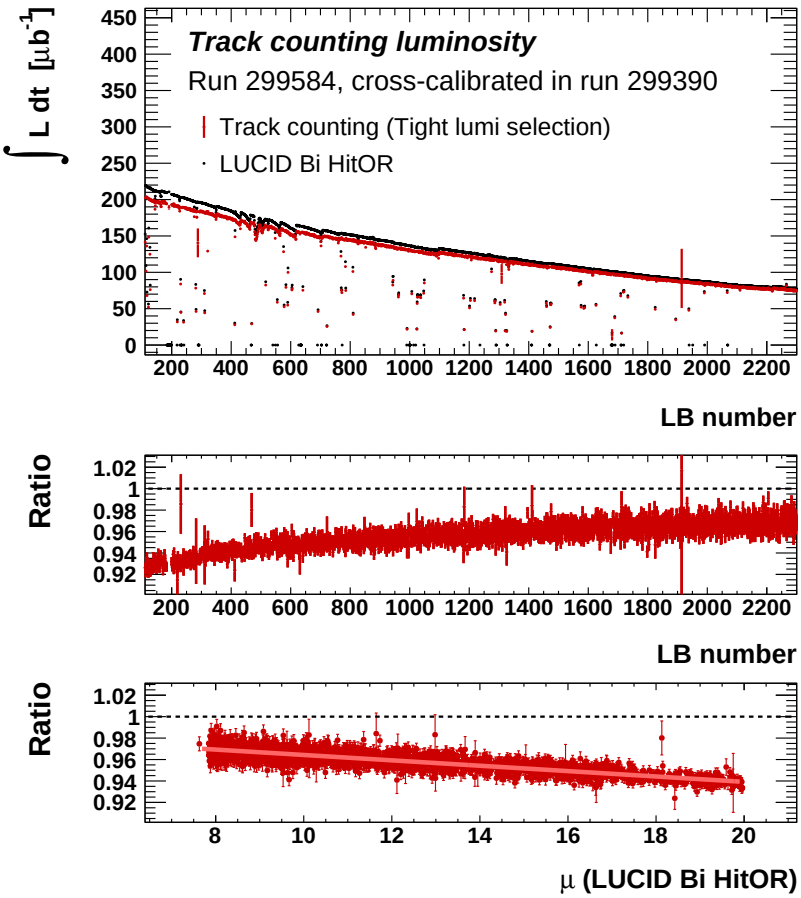

Figure 5.26: Comparison between track counting and LUCID in run 299584 as a function of LB number and μ as measured by LUCID.

Working point	λ	
	Run 299390	Run 300287
Tight	3.898	3.891
Fake removal	3.847	3.842
Pixel enhanced	3.819	3.814
Pixel enhanced 2	3.794	3.788

Table 5.10: Average number of tracks per inelastic pp collision after cross-calibration with LUCID-Bi-HitOr in vdM quiescent beams.

1.4 % compared with the 2015 cross-calibration shown in Table. 5.7. This change is smaller than the LUCID absolute calibration uncertainties of ± 1.7 % in both 2015 and 2016.

Figure 5.26 shows the track counting and LUCID luminosity measurements in run 299584 as a function of LB number (top) as well as the ratio (middle). The ratio differs from unity by up to 8 % at the beginning of the run falling to 3 % at the end. The bottom plot shows the ratio as a function of μ as measured by LUCID. This is fit with a linear parameterisation using a χ^2 optimisation. The negative gradient suggests that the track counting response falls with increasing μ, the LUCID response rises, or both. The limits of the parameterisation are defined by the minimum and maximum μ values measured.

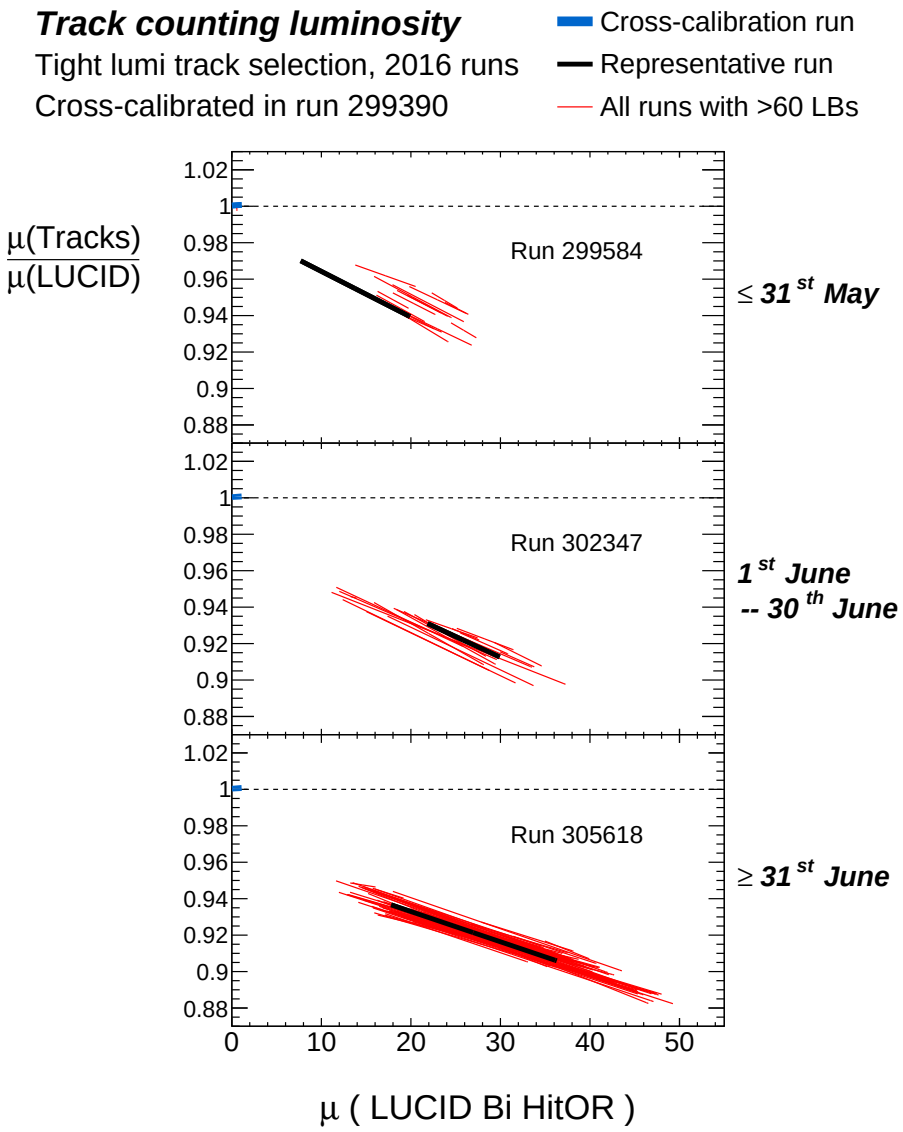

Figure 5.27: Linear parameterisations of the ratio between track counting and LUCID in 2016 runs as a function of μ as measured by LUCID.

Figure 5.27 shows the linear fits obtained individually from all runs with greater than 60 LBs. The year is split into three periods separated at 31$^{\text{st}}$ May and 30$^{\text{th}}$ June. The cross-calibration in the vdM run is shown in blue. A representative run is selected from each period and shown in black. The relative μ-dependence between track counting and LUCID is observed in all runs. A relative calibration transfer of $4-12$ % is observed. Much of this is explained by the relative μ-dependence.

Each fit is defined by a gradient and a constant term. Figure 5.28(left) shows the gradient as a function of run number. The relative μ-dependence is measured to be -0.25 %/μ at the start of the year with a systematic drift to approximately -0.15 %/μ at the end. The transitions between the three periods are indicated by the alternating grey and white backgrounds and the representative runs are shown in black. In order to separate the ef-

fects of μ-dependence and long-term instability, the constant term is evaluated at a value of $\mu = 20$ as shown in Figure 5.28(right). This value was chosen as it is consistently measured by runs throughout the year and so the linear parameterisations do not need to be extrapolated. A systematic drift between -5 % and -7 % is observed in addition to the relative μ-dependence. The overall disagreement between the two luminometers is the combination of these two effects.

5.7.3 Comparison with TileCal

Following a treatment analagous to the comparisons with `LUCID` presented in the previous section, the measured luminosity ratio with respect to `TileCal` is parameterised as a linear function of μ for all runs with over 60 LBs. The cross-calibration is performed in run 299584 rather than the vdM quiescent beam and so no relative calibration transfer conclusions can be drawn.

Figure 5.29(left) shows the relative μ-dependence as a function of run number. Values of up to -0.05 %/μ are typical at the start of the year with a systematic drift towards $0 - 0.05$ %/μ by the end. This is significantly smaller in magnitude than the relative μ-dependence between track counting and `LUCID` suggesting that this is driven by a change in `LUCID` response. However, the consistent systematic drifts in the `LUCID` and `TileCal` comparisons suggest an observable contribution from track counting. Figure 5.29(right) shows the luminometer comparison at $\mu = 20$. No clear systematic trend is observed and the overall agreement is better than ± 1 %.

5.7.4 Train dependence in run 310574

Since run 310574 contains only 99 colliding BCIDs, the statistical precision of the per-BCID track counting measurement is better than in typical 2016 runs which contain > 2000. Three of the BCIDs are isolated and numbered 11, 1247 and 2430. The remaining BCIDs are arranged into two trains occupying slots $714 - 761$ inclusive and $1875 - 1922$ inclusive. BCIDs 714 and 1875 are the first to collide in their respective trains and so are not affected by out-of-time pileup. In this respect they are expected to behave similarly to isolated BCIDs. This run was performed at high luminosity with a peak of $\mu \sim 140$ (isolated) and $\mu \sim 60$ (trains). Figure 5.30 shows the measured μ of isolated, 1^{st}-in-train and $2^{\text{nd}} - 4^{\text{th}}$-in-train BCIDs as a function of LB.

Figure 5.31(left) shows the ratio between track counting and `LUCID` measurements separately for isolated, 1^{st}-in-train and $\geq 2^{\text{nd}}$-in-train BCIDs. BCIDs within each category are combined to improve the statistical precision. Coloured boxes represent the total spread of data within each category. For isolated BCIDs, shown in red, the ratio between track counting and `LUCID` is approximately constant within an envelope of 0.925 ± 0.005 indicating a spread of ± 0.5 %. The ratio also appears constant for first-in-train BCIDs within

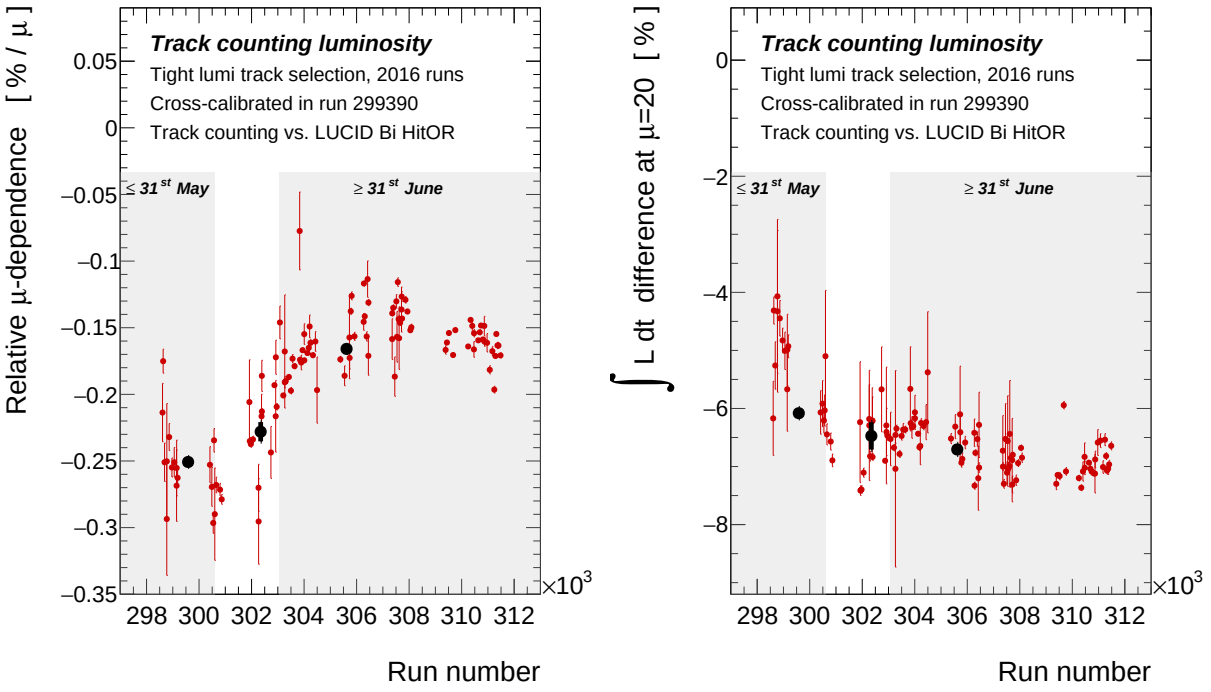

Figure 5.28: Relative μ-dependence and long term stability between track counting and LUCID in 2016 runs.

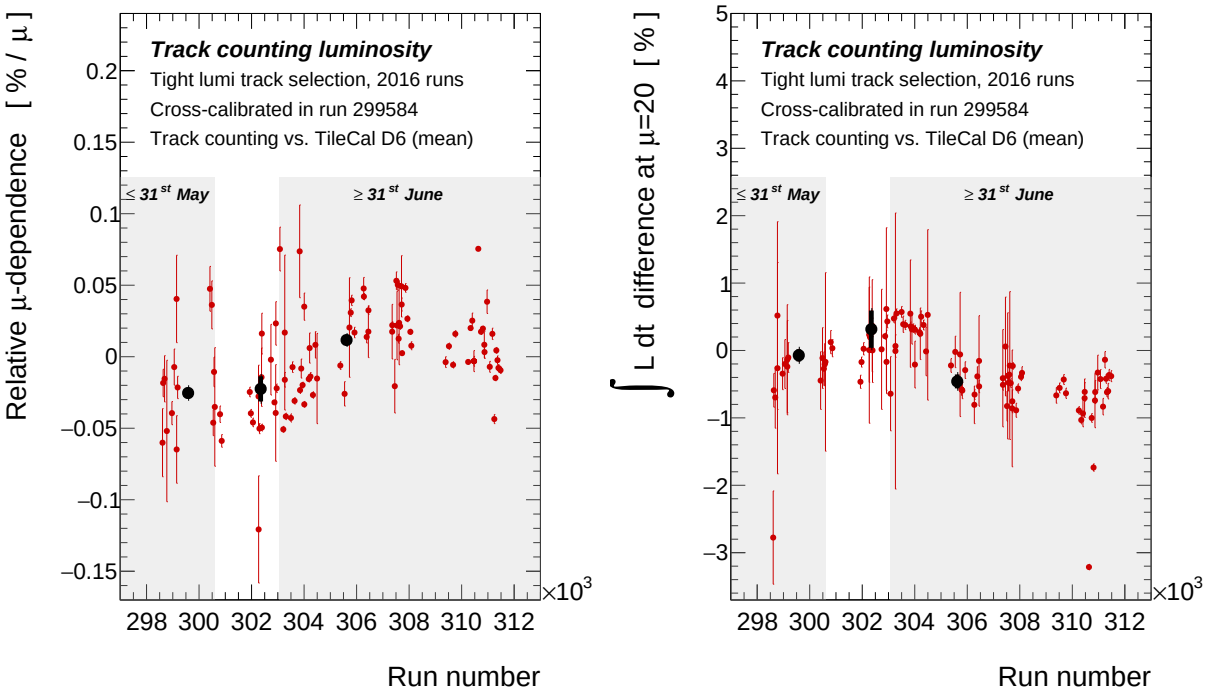

Figure 5.29: Relative μ-dependence and long term stability between track counting and TileCal in 2016 runs.

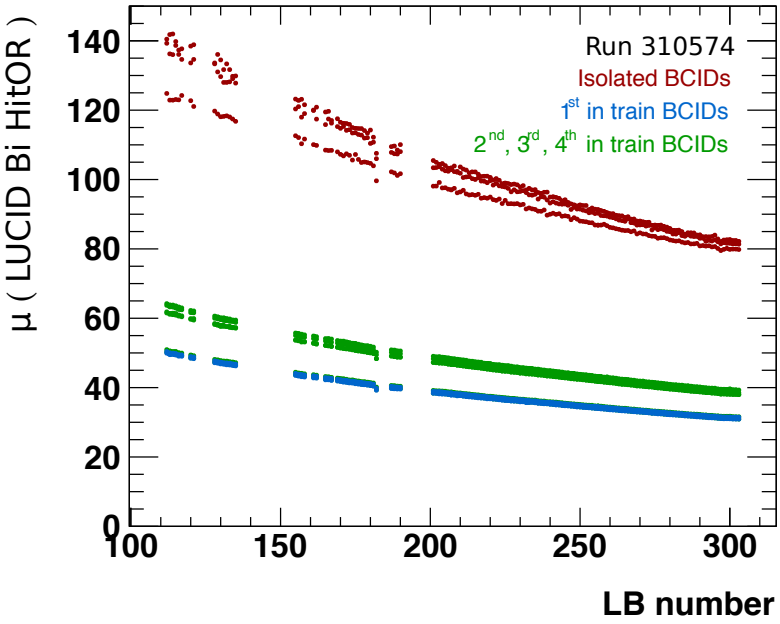

Figure 5.30: μ range spanned by isolated and in-train BCIDs in run 310574.

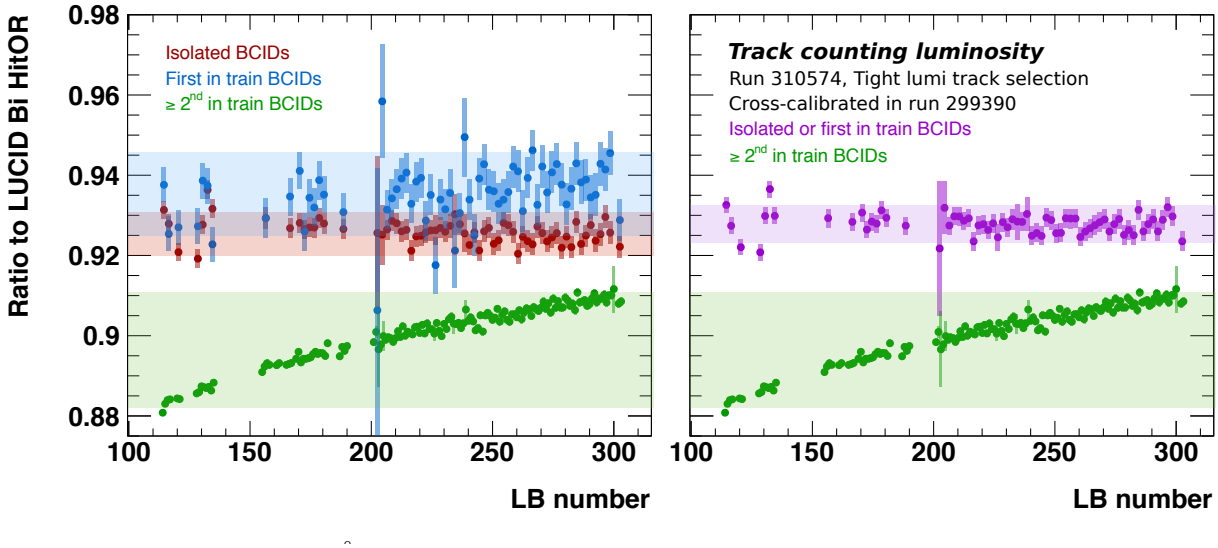

Figure 5.31: BCID-aware ratio between track counting and LUCID in run 310574 showing (left) isolated and first-in-train BCIDs separately and (right) combined.

an envelope of 0.935 ± 0.010 shown in blue. The disagreement in central value suggests a sensitivity to the different μ-ranges or bunch conditions probed by isolated and 1st-in-train BCIDs. Figure 5.31(right) shows the average of these in purple with an envelope of 0.928 ± 0.005. This indicates that track counting and LUCID luminosity measurements performed without a filled BCID in the previous 25 ns window are stable at the level of ± 0.5 % over the large μ-range spanned by this run.

By contrast, BCIDs which are $\geq 2^{\text{nd}}$-in-train show a clear systematic trend. The ratio

varies from 0.88 to 0.91 over an interval of $60 \gtrsim \mu \gtrsim 20$. This is consistent with the relative μ-dependence of approximately -0.15 %/μ observed between track counting and LUCID using BCID-blind measurement. This indicates that such a μ-dependence is driven primarily by in-train BCIDs.

5.7.5 Corrections to online luminosity

Studies in this chapter have shown that there exists a significant relative μ-dependence between track counting and LUCID in 2016 driven by in-train BCIDs. An additional long-term drift is observed which is not μ-dependent. Track counting is shown to be comparatively stable with respect to TileCal. The following strategy, developed and performed by other members of the analysis team, is used. A time-dependent μ-dependent correction to LUCID is applied. This accounts for calibration transfer (both from μ-dependence and any additional sources) and long-term stability. Calorimeter measurements are used to measure systematic uncertainties because the agreement between track counting and LUCID is enforced by the correction. This ensures that any unknown track counting instabilities are accounted for in the final luminosity uncertainty.

μ-dependent correction

Track counting is cross-calibrated to LUCID-Bi-HitOr in the vdM quiescent beam period of run 299390. The LUCID-Bi-HitOr measurement is then corrected using a linear parameterisation of the tight lumi-to-LUCID ratio as a function of μ. This is done separately in the three periods shown in Figure 5.28. In each period, the correction is defined using the individual reference runs shown in black. Run 299584 is used for the period up to run 300600, run 302347 for the period up to run 303059, and run 305618 thereafter. The resulting corrections are shown in Table 5.11 and evaluated at values of $\mu = 14$ corresponding to the average delivered in 2015, $\mu = 25$ which is the average in 2016 and $\mu = 40$ which represents the upper tail of the μ-profile in 2016.

At the beginning of the year, a correction of -2.4 % to μ_{vis} (LUCID-Bi-HitOr) at $\mu = 14$ is consistent with the 2015 calibration transfer correction of -2.6 % applied for 25 ns train running. At $\mu = 25$ the correction varies from -5.3 % to -8.2 % throughout the year. At $\mu \sim 40$ the correction is typically between -9 % and -11 %.

Reference run	Correction [%]	Applied to runs	Size of correction at $\mu = 14$	$\mu = 25$	$\mu = 40$
299584	$+1.304 - 0.263 * \mu$	≤ 300600	-2.4 %	-5.3 %	-9.2 %
302347	$-1.400 - 0.222 * \mu$	$300601 - 303059$	-4.5 %	-6.9 %	-10.3 %
305618	$-4.020 - 0.166 * \mu$	≥ 303060	-6.3 %	-8.2 %	-10.7 %

Table 5.11: μ-dependent corrections applied to μ_{vis} (LUCID-Bi-HitOr) in 2016.

Long-term stability uncertainty

The systematic uncertainty associated with long-term stability is evaluated by cross calibrating track counting, LUCID, TileCal, EMEC and FCal in run 299584 and evaluating the spread in relative luminosity measurements throughout all other physics runs using LUCID-Bi-HitOr as the baseline for comparison. Using this procedure, the annual integrated luminosities measured by TileCal, EMEC and FCal are observed to be 0.4 %, 1.3 % and 2.6 % higher than that measured by track counting. Since no offline luminometer is known to be more reliable than any other in high luminosity 2016 runs, the absolute luminosity scale of LUCID is corrected upwards by 1.3 %, i.e. half the distance between the two extremes. Figure 5.32 shows the resulting long-term stability comparison using only LBs for which track counting data is present. Two LUCID EventOr algorithms using Bismuth calibrated PMTs on the A-side and C-side are also shown. At the start of the year there is a systematic deviation of EMEC not replicated by any other offline luminometer. This is is not a LUCID instability and so does not contribute to the systematic uncertainty which is estimated to be ±2.5 %. This is represented by the grey shaded area.

Calibration transfer uncertainty

The μ-dependent correction was derived after cross calibrating track counting to LUCID in the vdM quiescent beam period of run 299390. The long-term stability uncertainty was evaluated after cross-calibrating all luminometers in run 299584. The systematic uncertainty associated with calibration transfer is evaluated by cross-calibrating track counting and TileCal in run 299390 and comparing their relative run-integrated luminosity measurements in run 299584. Four different TileCal cell measurements result in a range of values between 0.6 and 1.6 %. The maximum disagreement is used to define a calibration transfer uncertainty of ±1.6 %.

5.7.6 Summary of 2016

Track counting is used to derive three different μ-dependent corrections, corresponding to three different periods in 2016, applied to the LUCID-Bi-HitOr luminosity measurement. This results in a $5-8$ % reduction in measured luminosity at $\mu \sim 25$. The luminosity scale is additionally corrected upwards by 1.3 % to account for a relative disagreement between track counting and EMEC. A long-term stability uncertainty of ±2.5 % is derived using the offline comparison with EMEC, FCal and TileCal. A calibration transfer uncertainty of ±1.6 % is derived using TileCal.

The systematic uncertainty on the 2016 van der Meer calibration is ±1.7 %. The total luminosity uncertainty is ±3.4 %. These results correspond to luminosity tag OflLumi-13TeV-008 delivered in February 2017.

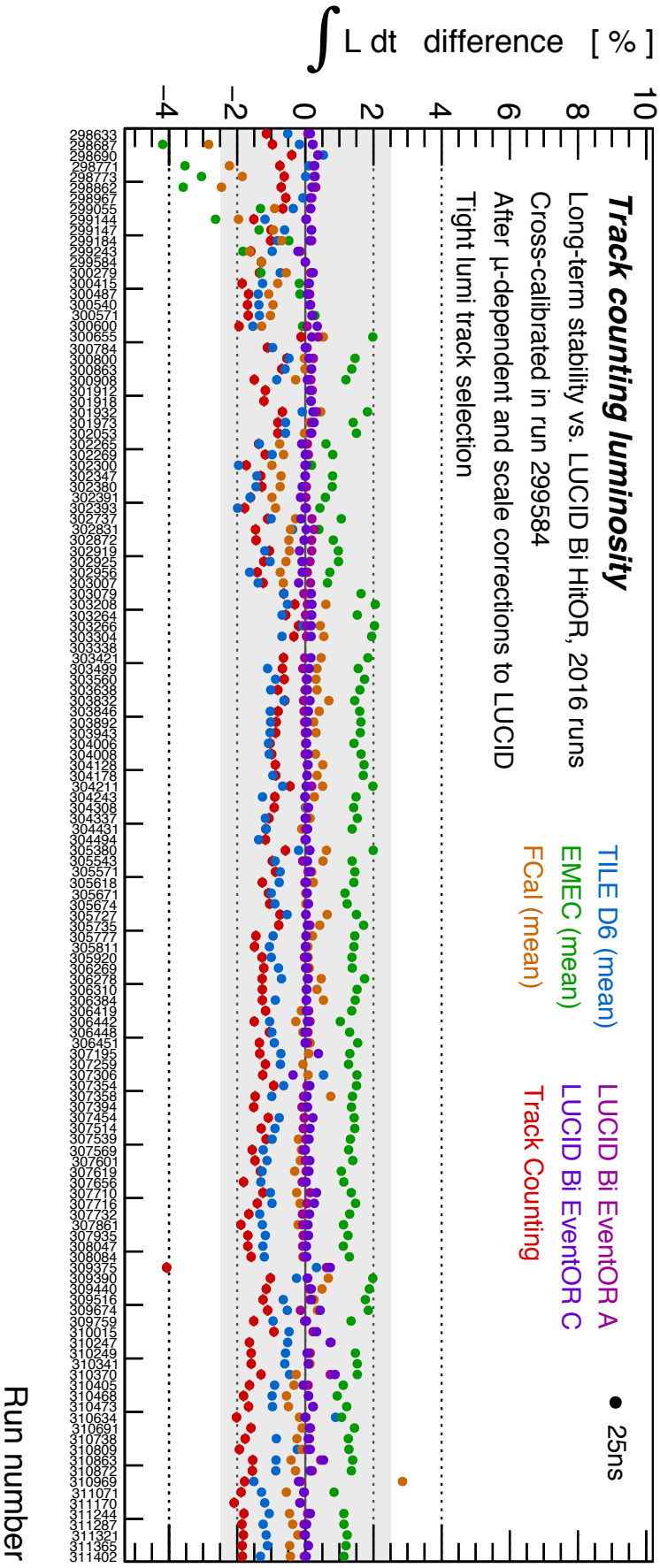

Figure 5.32: Run-integrated luminosity comparison between LUCID and offline luminometers after LUCID μ-dependent and scale corrections in 2016.

Fiducial cross sections in the $H \to \gamma\gamma$ channel at $\sqrt{s} = 13$ TeV

This chapter describes the measurement of fiducial and differential cross sections of the process $pp \to H \to \gamma\gamma$ using 36.1 fb^{-1} data collected by the ATLAS detector at $\sqrt{s} = 13$ TeV [5]. Unless stated otherwise, all presented results are applicable to the analysis of combined $2015 - 2016$ data which supersedes several preliminary publications [1–3]. Section 6.1 introduces the measurement. The studied dataset and Monte Carlo samples are described in section 6.2, followed by the main analysis components in sections 6.3 - 6.5. Sections 6.6 and 6.7 summarise the results. As part of this analysis, an alternative method for modelling the background contribution was studied. This is presented in section 6.8.

6.1 Introduction

The cross section of the process $pp \to H \to X$ is sensitive to the nature of Higgs boson interactions with Standard Model (SM) particles. Such interactions are described by the SM but may contain contributions from beyond-the-SM (BSM) interactions or mediator particles. The quantity X represents the Higgs decay products which are measurable within ATLAS. A variety of decay channels should be measured to maximise statistical sensitivity and exploit the sensitivity of different channels to different interactions. This ensures that each possible interaction is constrained to its maximum extent and breaks degeneracies between contributions to Higgs production (affecting all channels equally) and decay (specific to individual channels). Differential cross sections provide further sensitivity by combining knowledge of the total rate with information about its shape with respect to well-chosen observable quantities. Such observables are based on kinematic properties of the decay products as well as objects produced in association with the Higgs.

This analysis complements the measurement of signal strengths and simplified template cross sections (STXS) [5, 28, 213]. STXS and signal strengths assume SM templates to describe how the various Higgs boson production processes (ggF, VBF, WH, ZH, ttH, bbH, tHW and tHq) are distributed throughout measurable regions of phase space. Such approaches effectively characterise the measured Higgs events and highlight where statistically significant deviations from the Standard Model may have been observed. They

provide well-optimised sensitivity towards BSM models which modify the *rates* of production processes without (i) significantly affecting the assumed templates or (ii) introducing new processes which were not accounted for in the measurement. They are not well-suited for the constraint of BSM models which violate these assumptions. It is desirable to also measure Higgs events in a way which allows the constraint of BSM models *in general*. This goal is achieved by measuring differential cross sections in a fiducial phase space using a method designed to minimise model assumptions.

A fiducial phase space is defined by selection criteria applied to the final state objects. The cross section into this region of phase space, $\sigma^{\text{fid}}(pp \to H \to X)$, is related to the total Higgs production rate, $\sigma^{\text{tot}}(pp \to H)$, by

$$\sigma^{\text{fid}}(pp \to H \to X) = \mathcal{A} \cdot \mathcal{BR}(H \to X) \cdot \sigma^{\text{tot}}(pp \to H) \tag{6.1}$$

where $\mathcal{BR}(H \to X)$ is the decay channel branching ratio and $\mathcal{A}$ is the fiducial acceptance factor. This equation also holds for individual bins i of a differential distribution. We can then write

$$\sigma_i^{\text{fid}} = \mathcal{A}_i \cdot \mathcal{BR} \cdot \sigma_i^{\text{tot}} \tag{6.2}$$

where the dependence on channel is left implicit for brevity. The number of measured signal events ν_i^{sig} in bin i is then related to the fiducial cross section according to

$$\sigma_i^{\text{fid}} \cdot L_{\text{int}} = \frac{1}{C_i} \cdot \nu_i^{\text{sig}} \tag{6.3}$$

where the factor C_i accounts for the detector inefficiency and resolution and L_{int} is the integrated luminosity of the dataset.

The quantities σ_i^{tot}, $\mathcal{A}_i$ and $\mathcal{BR}$ are calculable within any given model. Fiducial cross section measurements are therefore suitable for *re-interpretation* in order to constrain current and future models. The effects contained within C_i are experimental and accounted for within the measurement of σ_i^{fid}. The fiducial selection criteria are designed to closely match the selection requirements applied to the events measured by ATLAS. This means that the C_i do not account for any significant model dependent acceptance corrections of their own.

The diphoton channel $X = \gamma\gamma$ has a small SM branching ratio of 0.227(5) % [28]. However, the excellent photon reconstruction efficiency and energy resolution obtained by ATLAS allow the reconstruction of a statistically significant invariant mass peak from which to measure the Higgs signal yield. Sensitivity is limited by the statistical fluctuations of a large background contribution, primarily irreducible in origin. The total phase space measurable by ATLAS is dominated by ggF production, thus providing sensitivity to the ggH effective coupling. This loop-induced process is sensitive to contributions from massive colourful BSM particles or BSM interactions of known particles. Measurable sub-regions of

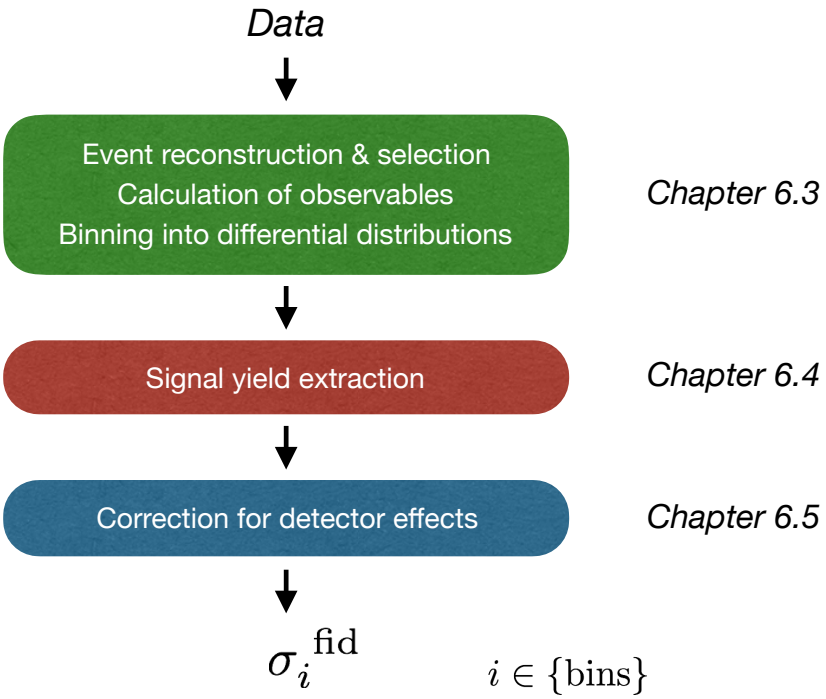

Figure 6.1: Differential cross section measurement method.

phase space contain significant contributions from VBF and VH production, thus providing sensitivity to VVH direct or effective couplings which may be mediated by massive BSM particles with weak isospin. The diphoton channel requires decay via the $H\gamma\gamma$ effective coupling which is dominated by charged fermion and vector boson loops, thus providing indirect sensitivity to massive charged BSM particles or BSM interactions.

The measurement method is summarised in Figure 6.1. Diphoton events are reconstructed, selected and binned as a function of various differential observables as described in section 6.3. The Higgs signal yields are extracted simultaneously for each bin of a differential distribution (but separately for different distributions) using an extended maximum likelihood fit to the diphoton invariant mass spectra as described in section 6.4. These are corrected for detector effects as described in section 6.5.

6.2 Data and Monte Carlo samples

The dataset consists of 3.2 fb^{-1} data collected with $\langle\mu\rangle = 14$ during 2015 following the profile shown in Figure 5.14 and 32.9 fb^{-1} collected with $\langle\mu\rangle = 25$ during 2016 as shown in Figure 5.23 for a total of 36.1 fb^{-1}. This is lower than the total delivered luminosity due to (i) the efficiency of data-taking which is typically above 90 % after taking into account trigger dead-time and the warm-start procedure of the Inner Detector subsystems and (ii) the requirement that all detector subsystems be operating normally.

Monte Carlo simulations are used to study the dominant signal processes as well as $\gamma\gamma$ and $V\gamma\gamma$ backgrounds. The event generators are summarised in Table 6.1. Signal samples are produced using $m_{\mathrm{H}} = 125$ GeV, consistent with the Run 1 LHC measured value of 125.09 ± 0.24 GeV [26], and $\Gamma_{\mathrm{H}} = 4.07$ MeV following the SM prediction [28]. A branching ratio of 0.227 % is calculated using `HDecay` [214] and `Prophecy4F` [215–217]. After generation, events are reweighted to the most precise total cross section calculation available assuming $m_{\mathrm{H}} = 125.09$ GeV. Simulation of detector effects is provided by `Geant4` [199] for signal and $V\gamma\gamma$ background samples. In order to reduce the computation time required to process the large number of events in the background $\gamma\gamma$ sample, the calorimeter cell response is simulated parametrically [218–220]. Events in all samples are reweighted to match the μ profile observed in data in a process called *pileup reweighting* (PRW).

Gluon fusion (ggF) events are generated with NNLO (QCD) precision using the `Powheg NNLOPS` program [95, 221] with the `PDF4LHC15` PDF set [222]. This weights events to reproduce the Higgs rapidity spectrum of the `HNNLO` program [96]. Parton shower, hadronisation and underlying event are provided by `Pythia8` [53] using the `AZNLO` tuning to data [223]. Events are normalised to a calculation performed at N^{3}LO (QCD) with NLO electroweak corrections [64–67].

VBF, W$^+$H, W$^-$H, $q\bar{q} \to ZH$ and $gg \to ZH$ events are generated with NLO (QCD) precision using the `Powheg-Box` program [83–87] with the `PDF4LHC15` PDF set and showered with `Pythia8` using the `AZNLO` tune. The $gg \to ZH$ process is dominated by box and loop diagrams and is normalised with NLO+NLL (QCD) precision. All other samples are normalised to NNLO (QCD) precision with NLO electroweak corrections [68–73].

ttH events are generated with NLO (QCD) precision using the `MG5_aMC@NLO` [89] program with the `NNPDF3.0` PDF set [224] and showered using `Pythia8` using the `A14` tune [225]. The normalised calculation is performed at NLO (QCD) with NLO electroweak corrections [74–77]. `MG5_aMC@NLO` is also used to generate events for bbH, including the effect of interference with gluon-fusion, using the `CT10` PDF set [226] and `Pythia8` for showering. It is normalised using a 5-flavour NNLO (QCD) calculation matched to 4-flavour NLO (QCD) [78–80].

tHW and tHq associated production processes are generated respectively with NLO and LO precision using `MG5_aMC@NLO`. The ttH contribution to tHW is subtracted and events are showered with `Herwig++` [54–56] using the 5-flavour CT10 PDF set and UEEE5 tune [227] for underlying event. The `A14` tune of `Pythia8` is used to shower tHq events using the 4-flavour `CT10` PDF set. Both samples are normalised with NLO (QCD) precision [228].

Background $\gamma\gamma$ and $V\gamma\gamma$ events are generated, allowing for up to three additional real emissions, with LO precision using the `Sherpa` program [92] with the `CT10` PDF set and showered using `Sherpa` [93, 94]. Underlying event is provided by `Pythia8` using the `A2` tune [229] and `MSTW2008LO` PDF set [230].

Process	Generator	PDF set	Showering	Num. events
Signal				
ggF	Powheg NNLOPS	PDF4LHC15	Pythia8	1.98M
VBF	Powheg-Box	PDF4LHC15	Pythia8	921k
W^+H	Powheg-Box	PDF4LHC15	Pythia8	247k
W^-H	Powheg-Box	PDF4LHC15	Pythia8	248k
$q\bar{q} \to ZH$	Powheg-Box	PDF4LHC15	Pythia8	471k
$gg \to ZH$	Powheg-Box	PDF4LHC15	Pythia8	49k
ttH	MG5_aMC@NLO	NNPDF3.0	Pythia8	1.94M
bbH	MG5_aMC@NLO	CT10	Pythia8	199k
tHq	MG5_aMC@NLO	CT10	Pythia8	99k
tHW	MG5_aMC@NLO	CT10	Herwig++	49k
Background				
$\gamma\gamma$	Sherpa	CT10	Sherpa	
$V\gamma\gamma$	Sherpa	CT10	Sherpa	

Table 6.1: Details of the event simulation.

6.3 Event measurement

6.3.1 Diphoton reconstruction and selection

The principles behind event and object reconstruction were described in section 4.3. Events are triggered when two clusters of at least 35 GeV and 25 GeV transverse energy are identified in the EM barrel or end-cap calorimeters. Loose shower shape requirements are imposed. The trigger efficiency is greater than 99 % for events which pass the full event selection. Offline photon reconstruction is performed as described in section 4.3.2.

Offline selection requires two reconstructed photons with $E_{\mathrm{T}} > 25$ GeV and either $0 < |\eta| < 1.37$ or $1.52 < |\eta| < 2.37$. This excludes the barrel/end-cap transition region which suffers from reduced efficiency and increased inactive material. The highest and second-highest E_{T} photons are defined as the *leading* and *subleading* photons respectively and together define the diphoton system.

A neural network is used to reselect the primary vertex by augmenting Inner Detector information with the directions of the two selected photons as measured by the EM calorimeter [113]. The PV selection is precise to greater than 3 mm in 79 % of gluon fusion events rising to 97 % in processes with several tracks and jets created by the hard scatter. The photon η and ϕ directions are corrected to this vertex of origin. A primary vertex is required to have been identified.

Event preselection requires two photons to pass the *loose* identification criteria [231] defined using the shower shape in the second layer of the EM calorimeter and leakage into the hadronic calorimeters. The contamination from electrons faking converted photons is reduced using an ambiguity resolver based on ID tracks, and both photons are required to

Selection stage	Event yield			Cut efficiency [%]		
	2015	2016	Total	2015	2016	Total
Preselection	2.6 M	28 M	31 M	-	-	-
Tight ID	410 k	4.1 M	4.5 M	16	15	15
Isolation	160 k	1.5 M	1.7 M	38	37	37
$E_{\mathrm{T}}/m_{\gamma\gamma} > 0.35$ (0.25)	140 k	1.3 M	1.5 M	87	87	87
$m_{\gamma\gamma} \in [105, 160]$ GeV	31 k	300 k	330 k	23	23	23

Table 6.2: Selected events in data at various stages of event selection.

match with the trigger-level objects.

Photon showers are then required to pass the *tight* identification criteria to suppress the neutral hadron background as described in section 4.3.2. They must be isolated in the calorimeter by requiring $E_{\mathrm{iso}}^{\mathrm{calo}} < 0.065 \times E_{\mathrm{T}}^{\gamma}$ where E_{T}^{γ} is the photon transverse energy and $E_{\mathrm{iso}}^{\mathrm{calo}}$ is computed as the sum of all positive energy topo-clusters within a cone of $\Delta R = 0.2$. The expected contribution from pileup and the underlying event, referred to as the *ambient energy* $E_{\mathrm{T}}^{\mathrm{amb}}$, is computed from the median energy density of the event, ρ, and subtracted along with E_{T}^{γ} [180]. They must also be isolated in the Inner Detector by requiring $E_{\mathrm{iso}}^{\mathrm{trk}} < 0.05 \times E_{\mathrm{T}}^{\gamma}$ where $E_{\mathrm{iso}}^{\mathrm{trk}}$ is computed as the sum of all tracks with $p_{\mathrm{T}} > 1$ GeV originating from the selected primary vertex and passing loose quality criteria within a cone of $\Delta R = 0.2$. Tracks associated with $\gamma \to e^+e^-$ conversions are not considered. This treatment is summarised in Eq. 6.4.

$$\begin{aligned} E_{\mathrm{iso}}^{\mathrm{calo}} &= \left(\sum_{\Delta R<0.2} E_{\mathrm{T}}^{\text{+ve topo-cluster}} \right) - E_{\mathrm{T}}^{\gamma} - E_{T}^{\mathrm{amb}}(\rho) \\ E_{\mathrm{iso}}^{\mathrm{trk}} &= \sum_{\Delta R<0.2} p_{\mathrm{T}}^{\text{loose track, } p_{\mathrm{T}} > 1 \text{ GeV}} \end{aligned} \tag{6.4}$$

The diphoton system is required to be well balanced using requirements of $E_{\mathrm{T}}/m_{\gamma\gamma} > 0.35$ (0.25) for the leading (subleading) photons, where $m_{\gamma\gamma}$ is the diphoton invariant mass. This is required to fall within a window of $105 < m_{\gamma\gamma} < 160$ GeV.

A total of 332,030 events are selected in data. Table 6.2 shows the measured event yields and relative selection efficiencies at various stages in the cutflow. The selection efficiency for signal events is expected to be 42 %.

6.3.2 Additional object reconstruction and selection

Several measurements are performed using observables or selection criteria defined using objects produced in associated with the diphoton system and reconstructed as described in section 4.3. Electrons are reconstructed from matching tracks with calorimeter clusters and required to satisfy $p_{\mathrm{T}} > 15$ GeV and either $0 < |\eta| < 1.37$ or $1.52 < |\eta| < 2.47$.

Medium identification criteria are applied [232] and electrons are discarded if they fall within $\Delta R < 0.4$ of a selected photon. *Loose* calorimeter and track isolation criteria are applied with an expected signal efficiency of approximately 99 % [5, 232]. Pileup objects are suppressed by applying requirements of $|z_0 \sin\theta| < 0.5$ and $|s\,(d_0)\,| < 5$.

Muons are reconstructed from tracks in the Inner Detector and Muon Spectrometer and required to satisfy $p_{\mathrm{T}} > 15$ GeV and $|\eta| < 2.7$. *Medium* identification criteria are applied [5, 181, 182]. *Loose* calorimeter and track isolation criteria are applied with a signal efficiency of approximately $95 - 99$ % depending on p_{T}. Muons are required to satisfy $|z_0 \sin\theta| < 0.5$ and $|s\,(d_0)\,| < 3$.

Jets are reconstructed from calorimeter clusters using the anti-k_{T} algorithm with a radius parameter of $r = 0.4$ implemented within the `FastJet` package [233, 234] and required to satisfy $p_{\mathrm{T}} > 30$ GeV and $|y| < 4.4$ unless stated otherwise. A pedestal from pileup and underlying event is subtracted using estimates of the median ambient energy density and jet area [235]. A medium JVT requirement calculated from the selected primary vertex suppresses pileup jets within $|\eta| < 2.4$ and $p_{\mathrm{T}} < 60$ GeV (see section 4.3.4). Jets are discarded if they fall within $\Delta R < 0.4$ of a selected photon or $\Delta R < 0.2$ of a selected electron. Jets originating from b-hadron decays are identifed using a 70 % efficient working point.

When multiple jets are reconstructed, the two highest p_{T} jets are used to define a dijet system. The missing transverse momentum is reconstructed as described in section 4.3.5.

6.3.3 Data validation

Within each run, data are validated by comparing the rate of event preselection with the measured instantaneous luminosity as a function of LB as shown in Figure 6.2. An LB is flagged if it contains a published luminosity value but no selected events. Non-statistical deviations in the comparison may highlight a data quality or processing problem. Figures 6.3(a) and (b) show the luminosity-normalised preselection and selection rates for all runs, expressed as a cross section. A time evolution of $\mathcal{O}\,(\lesssim 10\ \%)$ is observed in the preselection rate. There are no systematic outliers in the selection rate which may indicate data quality or processing problems within individual runs.

Figure 6.3(c) shows the stability of each of the four post-preselection cutflow steps as a function of run number, presented as a fraction of the preselected event yield. Figure 6.4 shows how the relative efficiency of each cutflow step varies as a function of μ. Note that Poisson uncertainties are used as an approximation leading to an overestimate when the efficiency is ~ 90 %. Negative systematic trends are observed for the tight identification and isolation requirements. This is consistent with the intended removal of pileup events but may also indicate a loss of signal efficiency at increasing μ. A modest positive systematic trend is observed in the mass window requirement with a total impact of approximately 7 % over the measured range. The source of this is not currently understood.

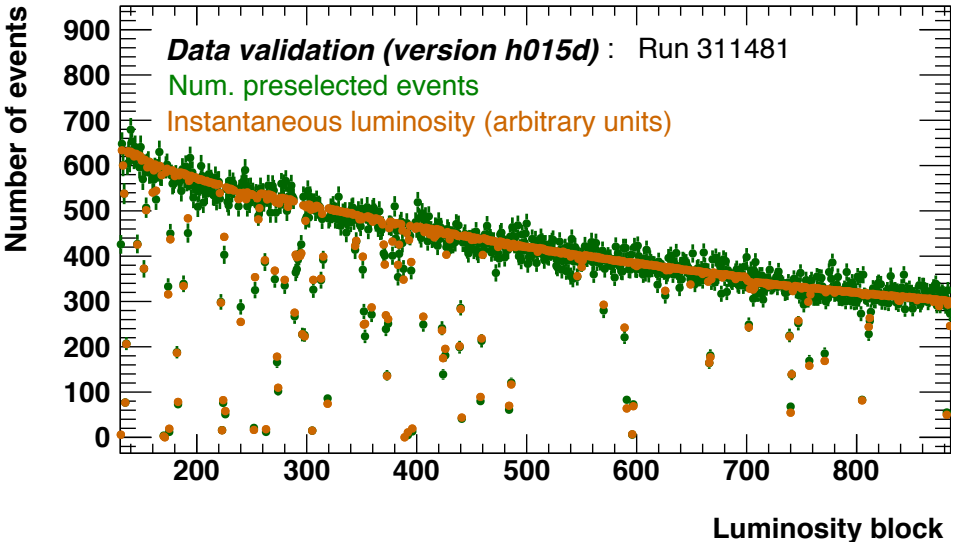

Figure 6.2: Preselection rate as a function of LB in run 311481.

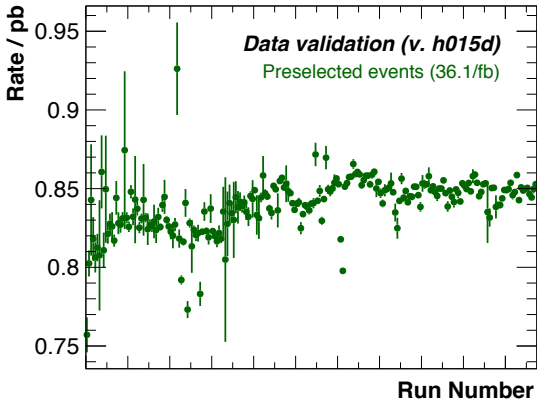

(a) Preselection (absolute rate)

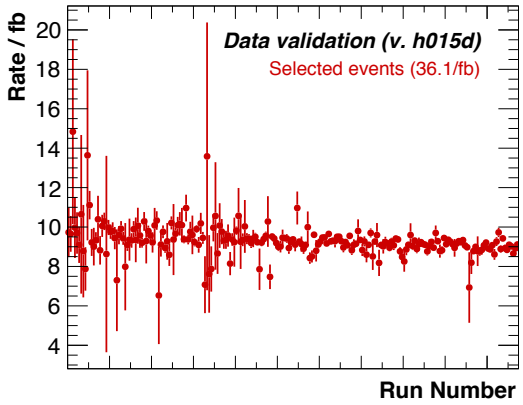

(b) Full selection (absolute rate)

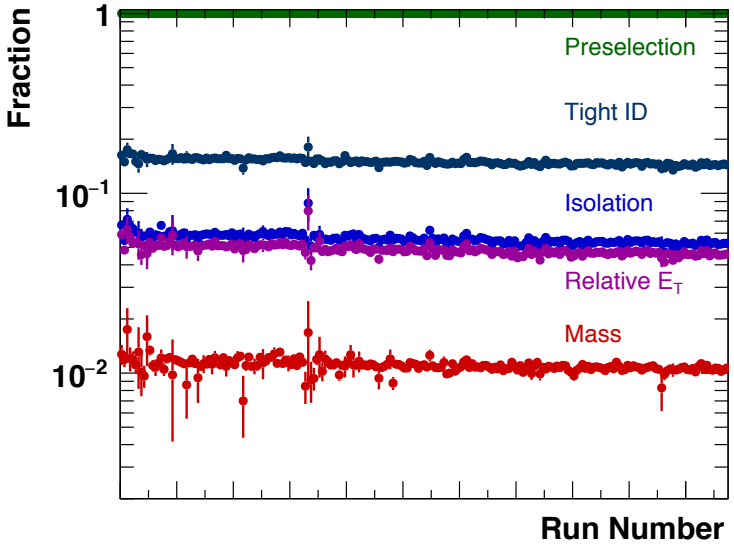

(c) Event selection efficiency relative to preselection.

Figure 6.3: Run-to-run stability of the event rates at various selection stages.

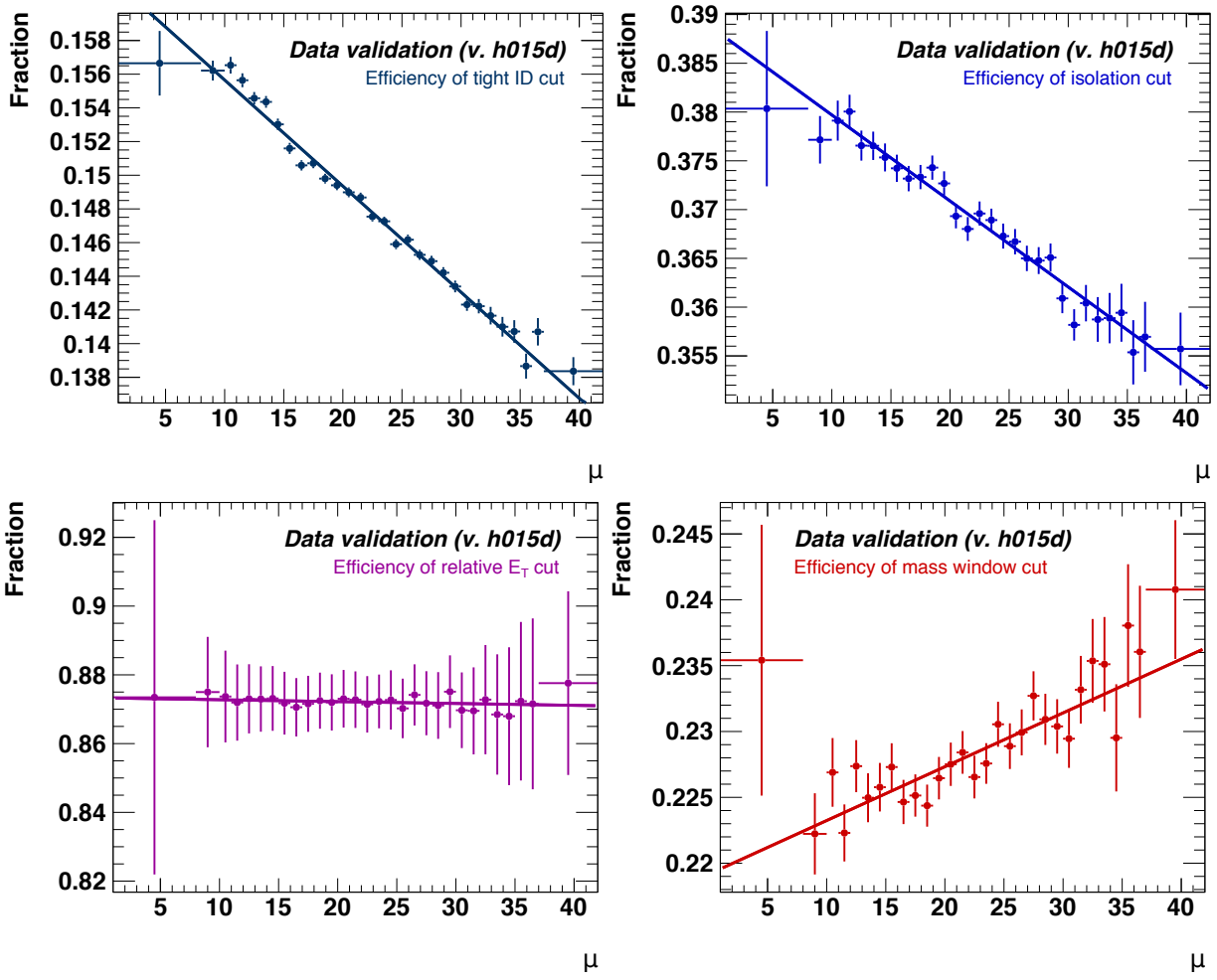

Figure 6.4: Cut efficiency variation as a function of μ in data.

6.3.4 Observable definitions

Two types of measurement are performed. Fiducial cross sections are measured in several regions of phase space targeting sensitivity towards individual production processes. Differential cross sections are measured as a function of observable quantities within the most inclusive fiducial region. The statistical precision of future measurements should be sufficient for the measurement of differential cross sections within production process enriched regions of phase space.

Regions

Fiducial measurements are performed in the following regions, chosen by balancing the expected statistical sensitivity with the purity of rare processes. Figure 6.5 shows the fraction of detector level events expected from each production process. This demonstrates that each measurement provides different relative sensitivity to the modelling of the various processes or interactions with different particles.

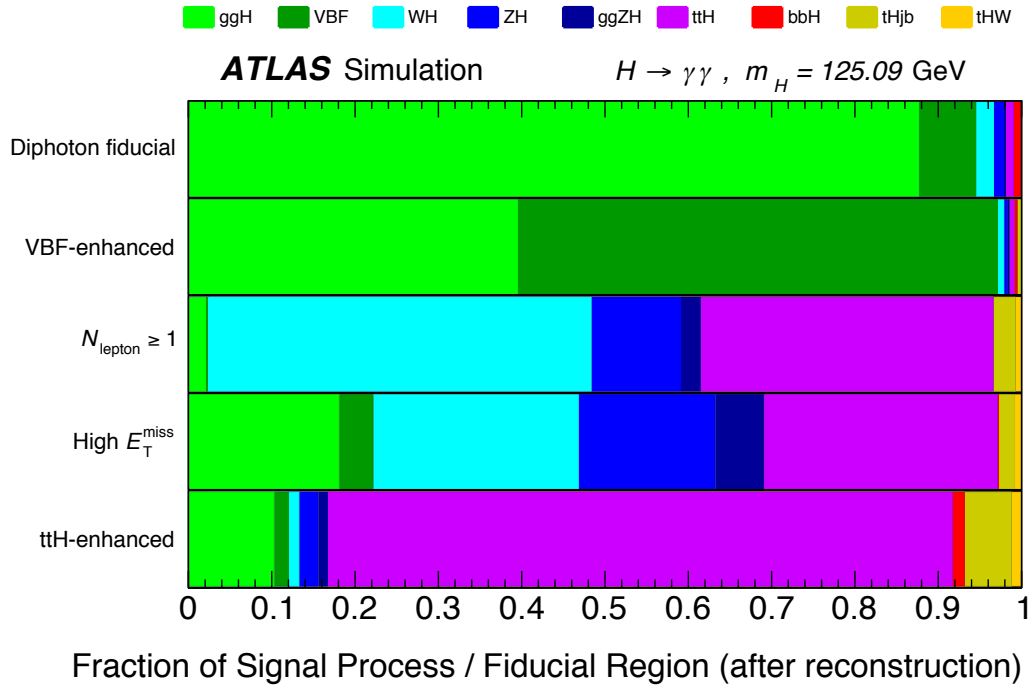

Figure 6.5: Expected fraction of each production process per measured region.

Diphoton fiducial contains all diphoton events measured in section 6.3.1. The expected SM signal yield is 1730 events of which 88 % originate from ggF and 7 % from VBF.

VBF enhanced contains *diphoton fiducial* events for which a dijet system was also selected. The minimum jet p_{T} requirement is relaxed to 25 GeV. The dijet mass is required to be at least 400 GeV and the two jets must be separated by $|\Delta y| > 2.8$. The azimuthal separation between the diphoton system and the dijet system is required to be $|\Delta\phi| > 2.6$. The expected SM signal yield is 74 events of which 39 % originate from ggF and 58 % from VBF.

$N_{\mathbf{lepton}} \geq 1$ contains all *diphoton fiducial* events for which an electron or muon was also selected. The expected SM signal yield is 13 events of which 46 % originate from WH, 13 % from ZH and 35 % from ttH.

High $E_{\mathbf{T}}^{\mathbf{miss}}$ contains all *diphoton fiducial* events with $E_{\mathrm{T}}^{\mathrm{miss}} > 80$ GeV and $p_{\mathrm{T}}^{\gamma\gamma} > 80$ GeV. The expected SM signal yield is 12 events of which 18 % originate from ggF, 25 % from WH, 22 % from ZH and 28 % from ttH. The cross section in this region may be enhanced by Higgs production in association with dark matter particles.

ttH enhanced contains all *diphoton fiducial* events with (i) three selected jets and a selected electron or muon or (ii) four selected jets. In both cases at least one jet must pass the b-hadron identification. The expected SM signal yield is 14 events of which 10 % originate from ggF and 75 % from ttH.

Differential observables

Differential cross sections are measured as a function of the observables described in this section. The bin boundaries are manually chosen to be as fine as possible whilst satisfying the following criteria: each bin should have an expected statistical significance of 2 σ; the expected purity should be at least 50 % in each bin, although this is not achieved in several jet-based observables due to pileup contributions and imperfect jet energy resolution; boundaries are defined using intuitive units, such as 5 GeV intervals for an energy distribution or units of π for an angular one; where it can be accomodated without limiting either analysis, common bin boundaries are agreed with the $H \to ZZ \to 4l$ analysis to facilitate the combination of channels later on. The purity is defined as the probability that a measured signal event originated from the same bin at truth level. All distributions are measured within the *diphoton fiducial* region.

The Higgs transverse momentum, $p_{\mathrm{T}}^{\gamma\gamma}$, is measured. This is sensitive to perturbative QCD modelling of the gluon-Higgs effective coupling though the ggF production process. This is indirectly sensitive to heavy quark Yukawa couplings [236]. The tail of the distribution is sensitive to processes with high partonic centre-of-mass energy. The absolute rapidity, $|y_{\gamma\gamma}|$, of the Higgs is measured with sensitivity to parton density functions and the modelling of ggF. The rapidity separation between the two photons, $\Delta y_{\gamma\gamma}$, is sensitive to the decay of the Higgs. The polar angle between the photons and the beam axis is measured in the Collins-Soper frame [111], equivalent to the rest frame of the Higgs, through the $|\cos\theta^*|$ observable. This is sensitive to the Higgs boson spin[1] and is calculated as

$$|\cos\theta^*| = \frac{|(E_{\gamma 1} + p_z^{\gamma 1}) \cdot (E_{\gamma 2} - p_z^{\gamma 2}) - (E_{\gamma 1} - p_z^{\gamma 1}) \cdot (E_{\gamma 2} + p_z^{\gamma 2})|}{m_{\gamma\gamma}\sqrt{m_{\gamma\gamma}^2 + (p_{\mathrm{T}}^{\gamma\gamma})^2}} \tag{6.5}$$

where $\gamma 1$ and $\gamma 2$ label the leading and subleading photons respectively. The observable $p_{\mathrm{Tt}}^{\gamma\gamma}$ is defined as the component of the diphoton transverse momentum which is transverse to the diphoton thrust axis [239, 240]. It is calculated as

$$p_{\mathrm{Tt}}^{\gamma\gamma} = |\vec{p}_{\mathrm{T}}^{\,\gamma\gamma} \times \vec{t}| \qquad \vec{t} = \frac{\vec{p}_{\mathrm{T}}^{\,\gamma 1} - \vec{p}_{\mathrm{T}}^{\,\gamma 2}}{|\vec{p}_{\mathrm{T}}^{\,\gamma 1} - \vec{p}_{\mathrm{T}}^{\,\gamma 2}|} \tag{6.6}$$

[1] This can be understood by considering the gluon fusion production of an on-shell Higgs boson created at rest in the lab frame, $gg \to H\,(\vec{p}_{\mathrm{lab}} = 0) \to \gamma\gamma$. Assume that the gluons collide collinearly with the beamline. In the case of a spin-0 resonance, there is no preferred axis for the decay into photons (which must be back-to-back to satisfy momentum conservation). The decay is therefore isotropic, and the distribution of θ^* is nominally flat, before being sculpted by selection citeria such as the lack of detector acceptance at $\theta^* \sim 0, \pi$. Since the initial gluons cannot be longitudinally polarised, a spin-2 resonance must be created in a spin-state which is polarised transverse to the beamline (along which the spin projection is $S_z = 0$). In this case, the decay photons must be collinearly polarised transverse to the beamline. They also cannot be polarised longitudinally with respect to their own momentum. These conditions enforce $|\cos\theta^*| = 1$. Including all $\vec{p}_{\mathrm{lab}} \neq 0$ causes a distribution which is suppressed at $|\cos\theta^*| = 0$. This behaviour is demonstrated in Ref. [27] (Figure 1), Ref. [237] (Figure 5) and Ref. [238] (Figure 88).

and is also sensitive to QCD modelling with higher resolution than $p_{\mathrm{T}}^{\gamma\gamma}$ in parts of the spectrum. The jet multiplicity, N_{jet}, is measured using minimum jet p_{T} requirements of 30 GeV and 50 GeV. This is sensitive to perturbative QCD modelling and the relative production process fractions. Raising the p_{T} threshold leads to an increased fraction of rare production processes in high multiplicity bins and reduces detector level pileup jet contamination, however also reduces the statistical sensitivity.

The following observables are sensitive to perturbative QCD modelling and the relative production process fractions. For events with at least one selected jet, the leading jet transverse momentum, p_{T}^{j1}, and rapidity, $|y_{j1}|$, are measured along with the scalar sum of all jet transverse momenta, $H_{\mathrm{T}} = \sum_j p_{\mathrm{T}}^{j}$. Two event shape observables characterise the emission of quarks and gluons [241]. For each jet, the thrust-like quantity, τ_j, is computed as

$$\tau_j = \frac{\sqrt{m_j^2 + \left(p_{\mathrm{T}}^{j}\right)^2}}{2\cosh\left(y^j - y_{\gamma\gamma}\right)} \ . \tag{6.7}$$

The observable τ_1 represents the highest measured τ_j in the event whilst $\sum_j \tau_j$ is the sum of all jets with $\tau_j > 8$ GeV.

Dijet observables are particularly sensitive to the modelling of the VBF process and so the properties of the VVH coupling. In VBF events, the dijet system tends to have a high invariant mass, large rapidity separation and opposite transverse momentum compared with the Higgs. For events with a selected dijet system, the subleading jet transverse momentum p_{T}^{j2} and rapidity $|y_{j2}|$ are measured along with the invariant mass of the dijet system, m_{jj}. The absolute value of the dijet rapidity separation, $|\Delta y_{jj}|$, is measured along with the azimuthal separation, $|\Delta\phi_{jj}|$. This is sensitive to the CP nature of interactions between the Higgs and vector bosons [5, 29–33]. A signed azimuthal spread is defined as $\Delta\phi_{jj} = \phi_{j1} - \phi_{j2}$. This is sensitive to potential CP-violating effects originating from the interference between CP-even and CP-odd Lorentz structures. The transverse momentum, $p_{\mathrm{T}}^{\gamma\gamma jj}$, of the combined Higgs-plus-dijet system is measured along with the absolute azimuthal separation between the diphoton and dijet systems, $|\Delta\phi\left(\gamma\gamma, jj\right)|$.

The bin boundaries of all 1-dimensional distributions are shown in Table 6.3. Underflow bins are labelled in green. Overflow bins are labelled in red and are not presented as they typically have low expected significance. Figure 6.6 shows the fraction of measured events expected from each production process in bins of $p_{\mathrm{T}}^{\gamma\gamma}$ and N_{jet} (30 GeV). The expected VBF, VH and ttH contributions increase as a function of $p_{\mathrm{T}}^{\gamma\gamma}$. The highest fraction of VBF is expected in the $N_{\mathrm{jet}} = 2$ bin.

Variable	Binning	Units
Observables requiring no jets		
$p_{\mathrm{T}}^{\gamma\gamma}$	$\{0 \leftrightarrow 20 \leftrightarrow 30 \leftrightarrow 45 \leftrightarrow 60 \leftrightarrow 80 \leftrightarrow 120 \leftrightarrow 170 \leftrightarrow 220 \leftrightarrow 350$, overflow$\}$	GeV
$p_{\mathrm{Tt}}^{\gamma\gamma}$	$\{0 \leftrightarrow 5 \leftrightarrow 10 \leftrightarrow 15 \leftrightarrow 22 \leftrightarrow 30 \leftrightarrow 40 \leftrightarrow 50 \leftrightarrow 65 \leftrightarrow 80 \leftrightarrow 100 \leftrightarrow 125 \leftrightarrow 160 \leftrightarrow 250$, overflow$\}$	GeV
$\Delta y_{\gamma\gamma}$	$\{0 \leftrightarrow 0.1 \leftrightarrow 0.2 \leftrightarrow 0.3 \leftrightarrow 0.4 \leftrightarrow 0.5 \leftrightarrow 0.65 \leftrightarrow 0.8 \leftrightarrow 1.0 \leftrightarrow 1.25 \leftrightarrow 2$, overflow$\}$	
$\lvert y_{\gamma\gamma}\rvert$	$\{0 \leftrightarrow 0.15 \leftrightarrow 0.3 \leftrightarrow 0.45 \leftrightarrow 0.6 \leftrightarrow 0.75 \leftrightarrow 0.9 \leftrightarrow 1.2 \leftrightarrow 1.6 \leftrightarrow 2.4\}$	
$\cos\theta^*$	$\{0 \leftrightarrow {}^1/_{16} \leftrightarrow {}^1/_8 \leftrightarrow {}^3/_{16} \leftrightarrow {}^1/_4 \leftrightarrow {}^5/_{16} \leftrightarrow {}^3/_8 \leftrightarrow {}^1/_2 \leftrightarrow {}^3/_4 \leftrightarrow 1\}$	
N_{jet}(30 GeV)	$\{= 0$, $= 1$, $= 2$, $\geq 3\}$	
N_{jet}(50 GeV)	$\{= 0$, $= 1$, $\geq 2\}$	
Observables requiring ≥ 1 jet		
p_{T}^{j1}	$\{0$ jets , $30 \leftrightarrow 55 \leftrightarrow 75 \leftrightarrow 120 \leftrightarrow 350$, overflow$\}$	GeV
$\lvert y_{j1}\rvert$	$\{0$ jets , $0 \leftrightarrow 0.5 \leftrightarrow 1.0 \leftrightarrow 1.5 \leftrightarrow 1.9 \leftrightarrow 2.3 \leftrightarrow 2.5 \leftrightarrow 4.4\}$	
H_{T}	$\{0$ jets , $30 \leftrightarrow 70 \leftrightarrow 140 \leftrightarrow 200 \leftrightarrow 500$, overflow$\}$	GeV
τ_1	$\{0$ jets , $0 \leftrightarrow 10 \leftrightarrow 20 \leftrightarrow 30 \leftrightarrow 40 \leftrightarrow 150$, overflow$\}$	GeV
τ	$\{0$ jets , $8 \leftrightarrow 17 \leftrightarrow 25 \leftrightarrow 40 \leftrightarrow 80 \leftrightarrow 150$, overflow$\}$	GeV
Observables requiring ≥ 2 jets		
p_{T}^{j2}	$\{0$ jets , 1 jet , $30 \leftrightarrow 70 \leftrightarrow 120$, overflow$\}$	GeV
$\lvert y_{j2}\rvert$	$\{\leq 1$ jet , $0 \leftrightarrow 1.2 \leftrightarrow 2.0 \leftrightarrow 4.4\}$	
$\lvert\Delta\phi_{jj}\rvert$	$\{\leq 1$ jet , $0 \leftrightarrow 1.047 \leftrightarrow 2.094 \leftrightarrow 3.15\}$	
$\Delta\phi_{jj}$	$\{\leq 1$ jet , $-\pi \leftrightarrow -{}^\pi/_2 \leftrightarrow 0 \leftrightarrow {}^\pi/_2 \leftrightarrow \pi\}$	
$\lvert\Delta\phi(\gamma\gamma, jj)\rvert$	$\{\leq 1$ jet , $0 \leftrightarrow 3.01 \leftrightarrow 3.10 \leftrightarrow 3.15\}$	
$\lvert\Delta y_{jj}\rvert$	$\{\leq 1$ jet , $0 \leftrightarrow 2 \leftrightarrow 4 \leftrightarrow 8.8\}$	
m_{jj}	$\{\leq 1$ jet , $0 \leftrightarrow 170 \leftrightarrow 500 \leftrightarrow 1500$, overflow$\}$	GeV
$p_{\mathrm{T}}^{\gamma\gamma jj}$	$\{\leq 1$ jet , $0 \leftrightarrow 15 \leftrightarrow 200$, overflow$\}$	GeV

Table 6.3: Binning of 1-dimensional differential distributions. Underflow bins are shown in green. Overflow bins, shown in red, are not presented.

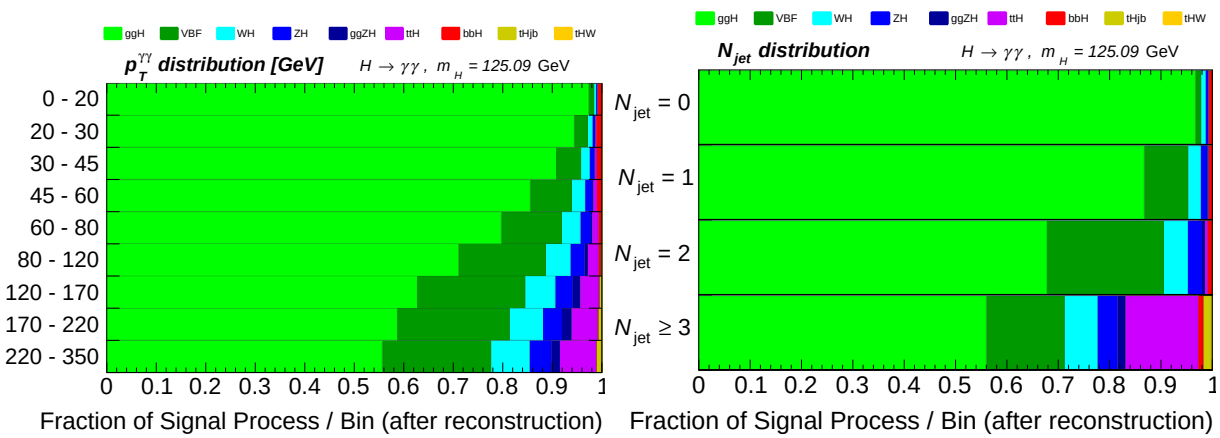

Figure 6.6: Expected fraction of each production process in bins of $p_{\mathrm{T}}^{\gamma\gamma}$ and N_{jet}.

Double differential distributions define bin boundaries according to two observables. This measures their respective correlation in signal events. Two distributions are measured. The $p_{\mathrm{T}}^{\gamma\gamma}$ vs. $|\cos\theta^*|$ distribution is sensitive to the spin and CP properties of the Higgs and is defined using bin boundaries which factorise into $p_{\mathrm{T}}^{\gamma\gamma} \in \{ 0 \leftrightarrow 30 \leftrightarrow 120 \leftrightarrow 350 \}$ GeV and $|\cos\theta^*| \in \{ 0 \leftrightarrow 0.5 \leftrightarrow 1 \}$. The $N_{\mathrm{jet}}(30\ \mathrm{GeV})$ vs. $p_{\mathrm{T}}^{\gamma\gamma}$ distribution is sensitive to QCD modelling and is defined using bin boundaries which do not factorise. These are $p_{\mathrm{T}}^{\gamma\gamma} \in \{ 0 \leftrightarrow 15 \leftrightarrow 30 \leftrightarrow 75 \leftrightarrow 350 \}$ GeV for $N_{\mathrm{jet}} = 0$, $\{ 0 \leftrightarrow 40 \leftrightarrow 60 \leftrightarrow 100 \leftrightarrow 350 \}$ GeV for $N_{\mathrm{jet}} = 1$, $\{ 0 \leftrightarrow 100 \leftrightarrow 200 \leftrightarrow 350 \}$ GeV for $N_{\mathrm{jet}} = 2$ and $\{ 0 \leftrightarrow 200 \leftrightarrow 350 \}$ GeV for $N_{\mathrm{jet}} \geq 3$. This binning reflects the expected occupancy of signal events throughout the 2-dimensional parameter space.

6.4 Signal yield measurement

The signal yields are measured simultaneously in all bins of a differential distribution using an extended maximum likelihood fit to the measured $m_{\gamma\gamma}$ spectra. Consider that event j is measured in bin i with value $m_{\gamma\gamma}^{(i),j}$. Under the hypothesis that this bin contains ν_i^{sig} signal events and ν_i^{bkg} events, the likelihood $\mathcal{L}_i^j$ of this measurement is evaluated as

$$\mathcal{L}_i^j\left(\nu_i^{\mathrm{sig}}, \nu_i^{\mathrm{bkg}}, \vec{\theta}, \vec{\lambda}; m_{\gamma\gamma}^{(i),j}\right) = \frac{1}{\nu_i^{\mathrm{sig}} + \nu_i^{\mathrm{bkg}}}\left[\nu_i^{\mathrm{sig}}\mathcal{S}_i\left(\vec{\theta}; m_{\gamma\gamma}^{(i),j}\right) + \nu_i^{\mathrm{bkg}}\mathcal{B}_i\left(\vec{\lambda}; m_{\gamma\gamma}^{(i),j}\right)\right] \tag{6.8}$$

where $\mathcal{S}_i$ is the expected probability density function (PDF) describing the signal shape according to the variable parameters $\vec{\theta}$, and $\mathcal{B}_i$ is the expected PDF describing background events with the variable parameters $\vec{\lambda}$. The hypothesised total number of events is $\nu_i^{\mathrm{tot}} = \nu_i^{\mathrm{sig}} + \nu_i^{\mathrm{bkg}}$. Within a given model defined by the PDFs and parameters, the quantity $\mathcal{L}_i^j$ represents the probability density of a random sampling resulting in the measured value of $m_{\gamma\gamma}^{(i),j}$. Consider that N_i events were measured in this bin resulting in the set $\vec{m}_{\gamma\gamma}^{(i)}$. The probability density that N_i random samplings would result in the measured dataset is the product of $\mathcal{L}_i^j$ over all events. However, the number of measured events is itself subject to Poisson fluctuations around the hypothesised mean ν_i^{tot}. This is described by multiplying the Poisson probability function into the likelihood such that

$$\mathcal{L}_i\left(\nu_i^{\mathrm{sig}}, \nu_i^{\mathrm{bkg}}, \vec{\theta}, \vec{\lambda}, \vec{m}_{\gamma\gamma}^{(i)}\right) = \mathrm{Poiss}\left(N_i|\nu_i^{\mathrm{tot}}\right) \cdot \prod_{j=1}^{N_i} \mathcal{L}_i^j\left(\nu_i^{\mathrm{sig}}, \nu_i^{\mathrm{bkg}}, \vec{\theta}, \vec{\lambda}; m_{\gamma\gamma}^j\right) \ . \tag{6.9}$$

The quantity $\mathcal{L}_i$ then represents the probability density of obtaining the measured dataset in bin i given the model hypothesis and is called an *extended likelihood*. Neglecting the Poisson term would create a likelihood which does not describe fluctuations of the total event yield and would result in binomial uncertainties on ν_i^{sig}.

An extended likelihood function describing all measured events is constructed from the

product of $\mathcal{L}_i$ over all bins. This treatment makes it possible for model parameters to be shared between multiple bins. Furthermore, if a parameter is expected to follow a known probability distribution, $\mathcal{C}$, then this is also multiplied into the total likelihood $\mathcal{L}$ such that

$$\mathcal{L}\left(\vec{\nu}^{\text{sig}}, \vec{\nu}^{\text{bkg}}, \vec{\theta}, \vec{\lambda}, \vec{m}_{\gamma\gamma}\right) = \prod_{i \in \text{bins}} \mathcal{L}_i\left(\nu_i^{\text{sig}}, \nu_i^{\text{bkg}}, \vec{\theta}, \vec{\lambda}, \vec{m}_{\gamma\gamma}^{(i)}\right) \prod_{\theta} \mathcal{C}\left(\theta\right) \prod_{\lambda} \mathcal{C}\left(\lambda\right) \tag{6.10}$$

where $\vec{\nu}^{\text{sig}}$ and $\vec{\nu}^{\text{bkg}}$ are the sets of signal and background yields for all bins, respectively.

A likelihood fit is a numerical optimisation which determines the parameter combination which maximises the likelihood, i.e. has the highest probability of resulting in the measured dataset. The signal yields are the intended measurement and are referred to as the *parameters of interest* (PoIs). Modelling parameters which are allowed to float in the likelihood fit with no associated $\mathcal{C}$ are called *unconstrained nuisance parameters* (NPs). Those with an associated $\mathcal{C}$ are called *constrained* NPs.

The optimised value of $\mathcal{L}$ varies with dataset size and the interval over which the PDFs are normalised and is somewhat arbitrary. However, the ratio between two likelihoods can be used to derive the uncertainty on a parameter. Consider that the maximum likelihood occurs with a PoI of $\hat{\nu}_i^{\text{sig}}$ and set of other parameters, $\hat{\vec{\alpha}}$. The profile parameter $\mathcal{R}$ is defined according to

$$\mathcal{R}\left(\nu_i^{\text{sig}}\right) = \frac{\mathcal{L}\left(\nu_i^{\text{sig}}, \hat{\vec{\alpha}}^{(\nu)}\right)}{\mathcal{L}\left(\hat{\nu}_i^{\text{sig}}, \hat{\vec{\alpha}}\right)} \tag{6.11}$$

where $\hat{\vec{\alpha}}^{(\nu)}$ are the set of parameters which re-optimise the likelihood at a fixed value of ν_i^{sig}. A common re-scaling defines the parameter Λ as twice the negative logarithm of $\mathcal{R}$ such that

$$\Lambda\left(\nu_i^{\text{sig}}\right) = -2\ln\mathcal{R}\left(\nu_i^{\text{sig}}\right) \ . \tag{6.12}$$

One obtains $\Lambda(\hat{\nu}_i^{\text{sig}}) = 0$ and $\Lambda \geq 0$ by definition. By assuming that $\mathcal{L}(\nu_i^{\text{sig}}, \hat{\vec{\alpha}}^{(\nu)})$ is Gaussian distributed around $\hat{\nu}_i^{\text{sig}}$ with width $\Delta\nu_i^{\text{sig}}$, one obtains the relation

$$\Lambda\left(\hat{\nu}_i^{\text{sig}} \pm s \cdot \Delta\nu_i^{\text{sig}}\right) = s^2 \tag{6.13}$$

in which Λ is found to vary quadratically as a function of the number of standard deviations, s, one has shifted ν_i^{sig} away from the best fit point. The PoI uncertainty $\Delta\nu_i^{\text{sig}}$ is obtained by profiling Λ and evaluating the point at which $s = 1$. For any value of ν_i^{sig}, the NPs can be tuned to optimise the likelihood and decrease Λ. This causes a broadening of the likelihood curve and so increases the PoI uncertainty.

This section will discuss the signal and background modelling required to construct the likelihood function and show the resulting fits to data.

6.4.1 Signal modelling

The signal shape is driven by the photon energy resolution of ATLAS. Four parameterisations are considered. A Gaussian shape with mean μ and width σ is described by

$$s = \frac{m_{\gamma\gamma} - \mu}{\sigma} \tag{6.14}$$

$$\mathcal{S}^{\text{Gauss}}(\mu, \sigma; m_{\gamma\gamma}) = \mathcal{N} e^{-s^2/2} \tag{6.15}$$

where $\mathcal{N}$ normalises the function to unity over the interval $m_{\gamma\gamma} \in [105, 140]$ GeV. The mean is written as an offset from m_{H}, i.e. $\mu = m_{\text{H}} + \mu_{\text{offset}}$. For signal MC a value of $m_{\text{H}} = 125$ GeV is used for consistency with the mass used to generate the samples. When applied to data, a value of $m_{\text{H}} = 125.09$ GeV is assumed.

The second parameterisation is the crystal ball shape. This is described by a Gaussian core transitioning into a power law in the lower tail, and is written as

$$\mathcal{S}^{\text{CB}}(\mu, \sigma, \alpha, n; m_{\gamma\gamma}) = \mathcal{N} \begin{cases} e^{-s^2/2} & s \geq -\alpha \\ \left(\frac{n}{|\alpha|}\right)^n e^{-\alpha^2/2} \left(\frac{n}{\alpha} - \alpha - s\right)^{-n} & s < -\alpha \end{cases} \tag{6.16}$$

where the additional parameter α describes the position at which the transition occurs and n is the exponent.

The third parameterisation is the sum of crystal ball and Gaussian functions (CB+G). This is written as

$$\begin{aligned} &\mathcal{S}^{\text{CB+G}}\left(\mu, \kappa, \sigma, f^{\text{CB}}, \alpha, n; m_{\gamma\gamma}\right) \\ &\quad = \mathcal{N}[f^{\text{CB}} \mathcal{S}^{\text{CB}}(\mu, \sigma, \alpha, n; m_{\gamma\gamma}) + \left(1 - f^{\text{CB}}\right) \mathcal{S}^{\text{Gauss}}(\mu, \kappa\sigma; m_{\gamma\gamma})] \end{aligned} \tag{6.17}$$

The additional parameter κ describes the relative widths of the two Gaussian cores which are required to peak at the same value of μ. A sixth parameter f^{CB} describes the relative normalisations.

The fourth parameterisation is a double-sided crystal ball (DSCB) function. This is written as

$$\begin{aligned} &\mathcal{S}^{\text{DSCB}}(\mu, \sigma, \alpha_{\text{low}}, n_{\text{low}}, \alpha_{\text{high}}, n_{\text{high}}; m_{\gamma\gamma}) \\ &\quad = \mathcal{N} \begin{cases} e^{-s^2/2} & -\alpha_{\text{low}} \leq s \leq \alpha_{\text{high}} \\ \left(\frac{n_{\text{low}}}{|\alpha_{\text{low}}|}\right)^{n_{\text{low}}} e^{-\alpha_{\text{low}}^2/2} \left(\frac{n_{\text{low}}}{\alpha_{\text{low}}} - \alpha_{\text{low}} - s\right)^{-n_{\text{low}}} & s < -\alpha_{\text{low}} \\ \left(\frac{n_{\text{high}}}{|\alpha_{\text{high}}|}\right)^{n_{\text{high}}} e^{-\alpha_{\text{high}}^2/2} \left(\frac{n_{\text{high}}}{\alpha_{\text{high}}} - \alpha_{\text{high}} + s\right)^{-n_{\text{high}}} & s > \alpha_{\text{high}} \end{cases} \end{aligned} \tag{6.18}$$

and is illustrated in Figure 6.7. Whereas a crystall ball function describes only one tail

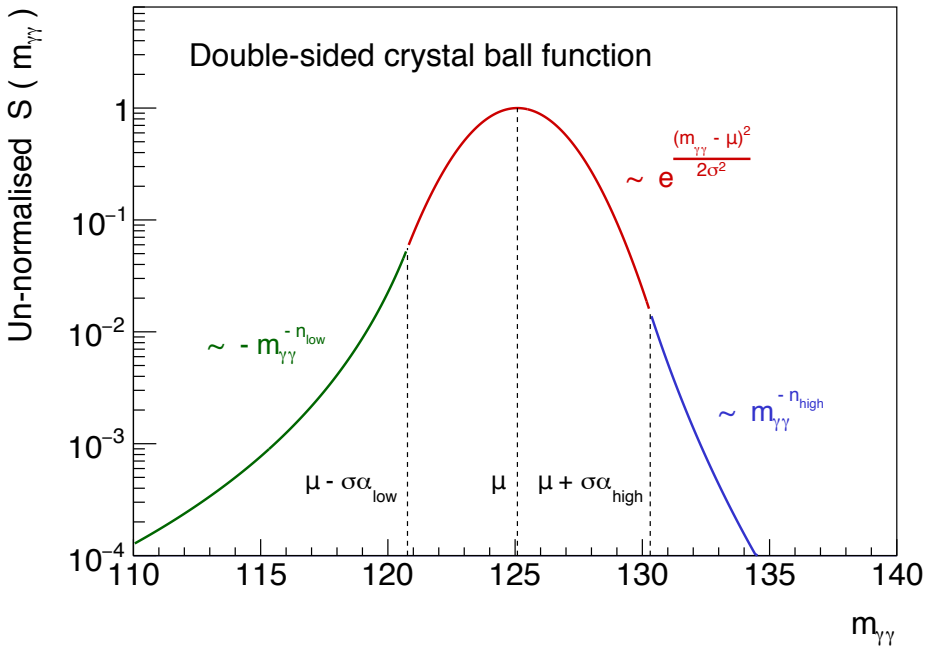

Figure 6.7: Illustration of the double-sided crystal ball parameterisation.

using a power law, a DSCB function describes both tails using two separate power laws defined by $\{\alpha_{\text{low}}, n_{\text{low}}\}$ and $\{\alpha_{\text{high}}, n_{\text{high}}\}$ respectively.

The optimum parameters are derived for each of $\mathcal{S}^{\text{Gauss}}$, $\mathcal{S}^{\text{CB}}$, $\mathcal{S}^{\text{CB+G}}$ and $\mathcal{S}^{\text{DSCB}}$ using a likelihood fit to signal MC events. Figure 6.8 shows the resulting signal shapes in each bin of $p_{\text{T}}^{\gamma\gamma}$ (excluding the overflow bin) on a logarithmic scale which is useful for evaluating the description of the tails and a linear scale for the description of the core. The Gaussian parameterisation, shown in green, is not sufficient in describing either the core or the tails. The crystal ball parameterisation, shown in purple, is sufficient in describing the lower tail. Both the CB+G and DSCB parameterisations describe the full signal peak adequately well. The DSCB parameterisation is preferred because it consistently describes both tails using a smoothly varying convex function without inflections.

Table 6.4 shows the DSCB parameters used to model the signal shape in several regions and differential distributions. The signal width is defined as half of the interval centred on μ which contains a given fraction of signal events. 67 % of the signal is contained within an interval of ± 1.89 GeV in the first bin of $p_{\text{T}}^{\gamma\gamma}$ falling to ± 1.36 GeV in the uppermost bin leading to ± 1.82 GeV overall. The signal width is typically smaller when moving to high jet multiplicity bins because jets tend to recoil from the Higgs system leading to higher $p_{\text{T}}^{\gamma\gamma}$. A narrow signal peak will typically lead to greater statistical precision because fewer background events are contained within the signal width.

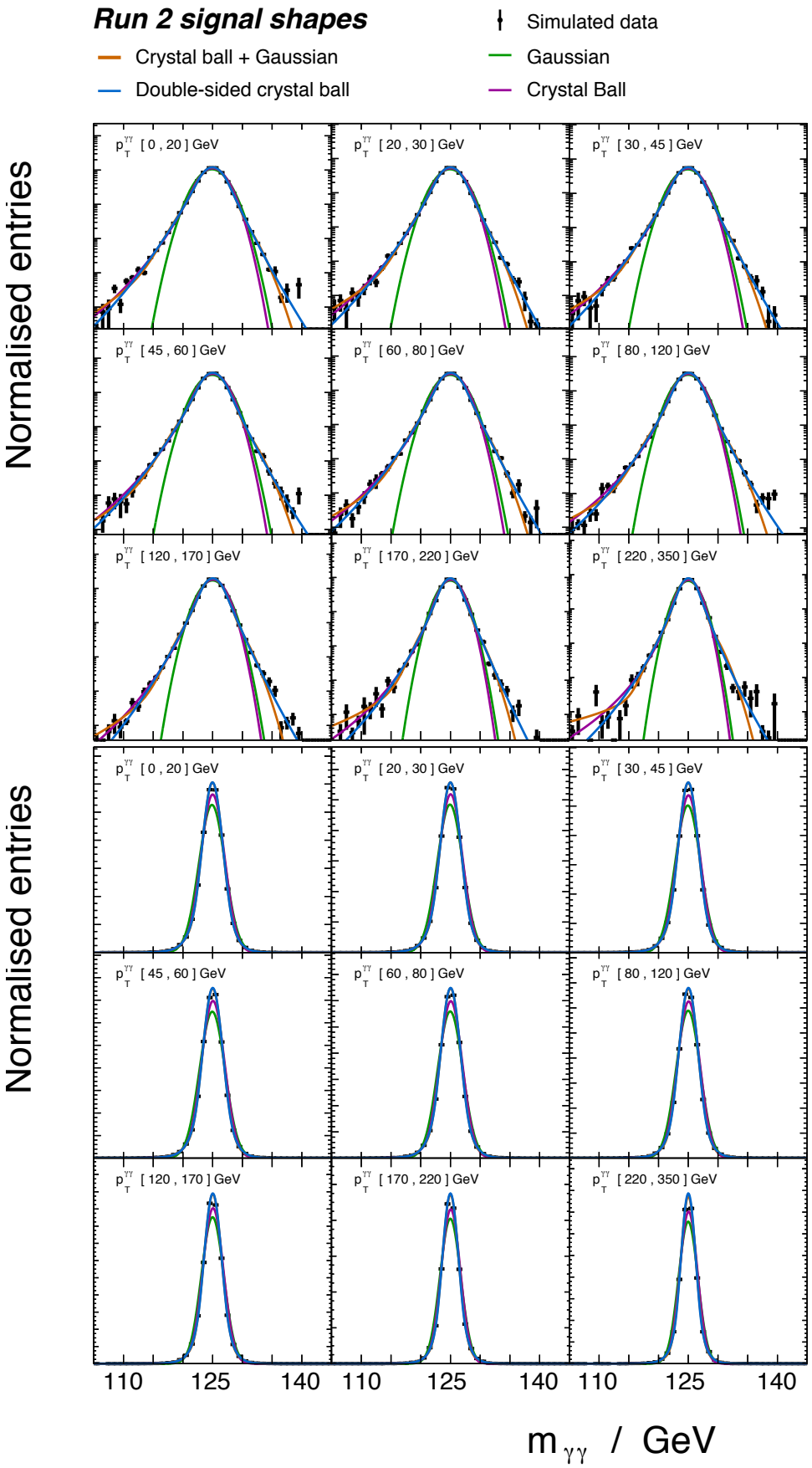

Figure 6.8: Signal model comparison in bins of $p_{\mathrm{T}}^{\gamma\gamma}$ on logarithmic and linear scales.

Bin		μ [GeV]	σ [GeV]	α_{low}	n_{low}	α_{high}	n_{high}	Signal width [GeV] 67 %	90 %	95 %
Diphoton fiducial		$m_{\text{H}} - 0.00$	1.73	1.40	13.81	1.52	35.61	1.82	3.34	4.26
VBF enhanced		$m_{\text{H}} + 0.01$	1.59	1.37	13.22	1.44	38.02	1.69	3.14	4.02
$N_{\text{lepton}} \geq 1$		$m_{\text{H}} - 0.02$	1.56	1.44	8.08	1.48	14.82	1.67	3.12	4.04
High $E_{\text{T}}^{\text{miss}}$		$m_{\text{H}} + 0.06$	1.52	1.48	9.04	1.47	10.44	1.62	3.02	3.91
ttH enhanced		$m_{\text{H}} + 0.01$	1.52	1.48	7.49	1.55	12.22	1.61	2.99	3.87
$p_{\text{T}}^{\gamma\gamma}$ [GeV]	$0 \leftrightarrow 20$	$m_{\text{H}} - 0.03$	1.81	1.39	15.82	1.58	30.26	1.89	3.46	4.40
	$20 \leftrightarrow 30$	$m_{\text{H}} - 0.00$	1.79	1.43	13.50	1.55	45.92	1.87	3.41	4.33
	$30 \leftrightarrow 45$	$m_{\text{H}} + 0.00$	1.76	1.41	13.78	1.54	32.61	1.85	3.38	4.31
	$45 \leftrightarrow 60$	$m_{\text{H}} + 0.01$	1.75	1.42	12.38	1.56	24.33	1.84	3.36	4.30
	$60 \leftrightarrow 80$	$m_{\text{H}} + 0.03$	1.72	1.43	12.37	1.52	34.14	1.81	3.31	4.22
	$80 \leftrightarrow 120$	$m_{\text{H}} + 0.03$	1.68	1.51	10.53	1.57	19.55	1.74	3.17	4.04
	$120 \leftrightarrow 170$	$m_{\text{H}} + 0.02$	1.53	1.40	16.19	1.48	29.39	1.61	2.96	3.78
	$170 \leftrightarrow 220$	$m_{\text{H}} - 0.00$	1.40	1.48	10.24	1.41	43.99	1.48	2.73	3.49
	$220 \leftrightarrow 350$	$m_{\text{H}} + 0.02$	1.28	1.45	9.47	1.45	18.33	1.36	2.52	3.25
N_{jet}	$= 0$	$m_{\text{H}} - 0.02$	1.78	1.39	15.05	1.54	37.55	1.87	3.43	4.37
	$= 1$	$m_{\text{H}} + 0.01$	1.72	1.43	13.05	1.56	27.09	1.80	3.29	4.20
	$= 2$	$m_{\text{H}} + 0.03$	1.63	1.38	12.51	1.50	23.05	1.73	3.20	4.11
	≥ 3	$m_{\text{H}} + 0.03$	1.56	1.44	10.13	1.42	37.33	1.65	3.07	3.94
$\Delta\phi_{jj}$	$-\pi \leftrightarrow -\pi/2$	$m_{\text{H}} + 0.03$	1.68	1.45	10.52	1.47	48.61	1.77	3.26	4.16
	$-\pi/2 \leftrightarrow 0$	$m_{\text{H}} + 0.01$	1.51	1.32	14.94	1.37	41.63	1.63	3.06	3.93
	$0 \leftrightarrow \pi/2$	$m_{\text{H}} + 0.04$	1.53	1.32	15.58	1.42	44.04	1.64	3.06	3.92
	$\pi/2 \leftrightarrow \pi$	$m_{\text{H}} + 0.03$	1.66	1.42	10.32	1.47	32.03	1.76	3.26	4.18

Table 6.4: Signal shape parameters in several regions and differential bins. The signal width is half of the interval centred on μ which contains a given fraction of signal events.

6.4.2 Background modelling

This section provides a summary of the background modelling used for the final publication. This work was performed by other members of the analysis team. The background PDF is parameterised using an empirical function assigned individually to each bin. First, a data-driven decomposition of the background is performed. This is used to create MC templates on which several empirical functions are tested and systematic uncertainties evaluated. As

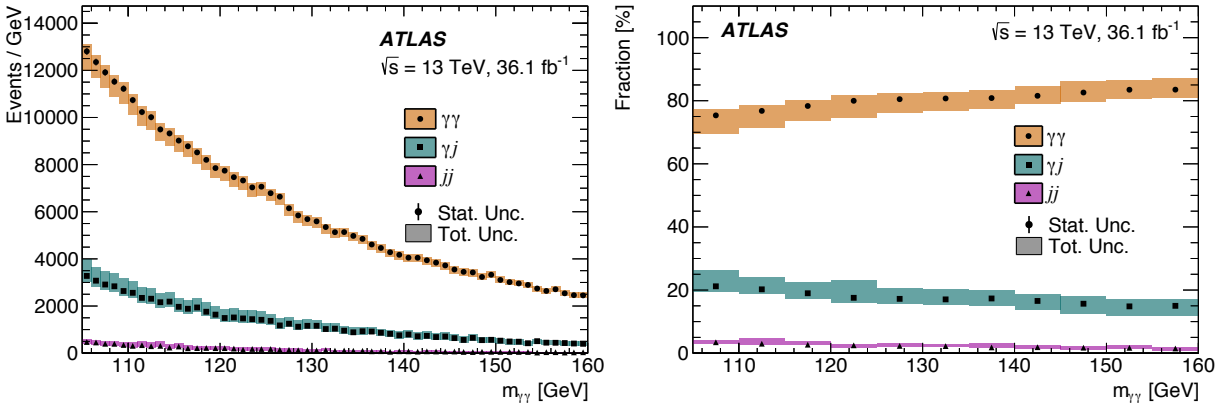

Figure 6.9: Data-driven background contributions as a function of $m_{\gamma\gamma}$ expressed as (left) an absolute rate and (right) fractional contributions. This work was performed by another member of the analysis team.

part of the analysis, the author of this thesis studied an alternative background modelling method. This is discussed in section 6.8.

Background decomposition

The dominant background contributions are from irreducible $\gamma\gamma$ and reducible γj and jj production where hadronic jets are mistakenly reconstructed as photons. The relative contributions from the different sources are determined in every fiducial region or differential bin using a double 2-dimensional sideband decomposition [242, 243]. Events in data are separated into the signal region and 15 orthogonal control regions defined by relaxed isolation and identification requirements for one or both photons. Assuming real photon reconstruction efficiencies derived from simulation, the event yields in the 16 regions are used to solve a set of linear equations to constrain the hadronic fake rate and estimate the individual $\gamma\gamma$, γj and jj yields in the signal region. Approximately 79 % of the selected background events are irreducible with an additional 19 % from γj and 3 % from jj. The background event yields and fractions are shown as a function of $m_{\gamma\gamma}$ in Figure 6.9.

Background shape

The background events in Figure 6.9 combine to form a monotonically falling background spectrum. The data sidebands are defined as $105 < m_{\gamma\gamma} < 121$ GeV and $129 < m_{\gamma\gamma} < 160$ GeV. These can be used to constrain the background PDF since they contain negligible signal contribution. However, they do not contain sufficient events to determine the functional form of the background PDF. Instead the following procedure is used.

For each bin or fiducial region, an irreducible background template is created using the $\gamma\gamma$ MC sample. Data control regions are used to derive linear parameterisations of the $\gamma j/\gamma\gamma$ and $jj/\gamma\gamma$ ratios. These functions are used to reweight events in the $\gamma\gamma$ MC

sample and so account for the reducible components which are added to the template. In the ≥ 1 *lepton* and *high* E_T^{miss} regions, an additional component from the $V\gamma\gamma$ MC sample is included. The template in the *ttH enhanced* region is created by summing events from control regions defined with relaxed b-tagging and inverted isolation or identification requirements. All templates are validated using a χ^2 compatibility comparison with the data sidebands.

Several background PDF parameterisations are tested using $\mathcal{S}+\mathcal{B}$ likelihood fits to each background-only template with m_{H} values of between 121 and 129 GeV. The maximum number of fitted signal events, $N^{\mathrm{spur}} \pm \Delta^{\mathrm{spur}}$, is interpreted as a bias caused by insufficient background modelling. This is referred to as the *spurious signal*. A function "passes" if N^{spur} is, at the 95 % confidence level, compatible with (i) less than 20 % of the expected statistical uncertainty or (ii) less than 10 % of the expected signal yield. The χ^2 probability is required to be greater than 1 % to veto bad parameterisations which achieve a small evaluated N_{spur} by chance. The uncertainty on the spurious signal is significant in low-yield bins due to limited statistical precision of the $\gamma\gamma$ MC sample. When multiple functional forms pass, that with the lowest number of free parameters is chosen. If this is also equal then that with the smallest N_{spur} is used.

Three families of parameterisations are considered. They are motivated by their smoothly falling monotonic shapes. An `ExpPolN` function of order N has N degrees of freedom and is written as

$$\mathcal{B}^{\mathrm{ExpPolN}}\left(\vec{\lambda}; m_{\gamma\gamma}\right) = \mathcal{N} \cdot e^{-\sum_{i=1}^{N} \lambda_i (m_{\gamma\gamma})^i} \ . \tag{6.19}$$

A `PolN` function of order N has N degrees of freedom and is implemented in the basis of Bernstein polynomials to improve numerical performance. This is witten as

$$\mathcal{B}^{\mathrm{PolN}}\left(\vec{\lambda}; m_{\gamma\gamma}\right) = \mathcal{N} \cdot \left(1 + \sum_{i=1}^{N} \lambda_i (m_{\gamma\gamma})^i\right) \ . \tag{6.20}$$

A `PowN` function of order N has $2N-1$ degrees of freedom and is written as

$$\mathcal{B}^{\mathrm{PowN}}\left(\vec{\lambda}; m_{\gamma\gamma}\right) = \mathcal{N} \cdot \sum_{i=1}^{N} \lambda_{i,1} (m_{\gamma\gamma})^{\lambda_{i,2}} \ . \tag{6.21}$$

After testing against the MC templates, each functional form is fit to the data sidebands allowing the parameters, $\vec{\lambda}$, to float. A χ^2 goodness-of-fit is computed. The same procedure is applied using a functional form one order higher. The higher order function is chosen if the χ^2 improvement is consistent with a probability of less than 5 % [244]. Table 6.5 shows the background PDFs chosen in several bins and fiducial regions as well as the estimated spurious signal expressed as a fraction of the expected signal yield, $\nu^{\mathrm{sig,exp}}$, and expected statistical uncertainty, $\Delta\nu^{\mathrm{sig,exp}}$.

It is notable that the background templates are constructed from the simulated $\gamma\gamma$

Bin or region	Functional form	$N^{\text{spur}}/\nu^{\text{sig,exp}}$	$N^{\text{spur}}/\Delta\nu^{\text{sig,exp}}$
Diphoton fiducial	`ExpPol2`	3.7 %	22 %
VBF enhanced	`ExpPol1`	13 %	38 %
ttH enhanced	`ExpPol1`	68 %	80 %
$0 < p_{\text{T}}^{\gamma\gamma} < 20$ GeV	`ExpPol2`	11 %	39 %
$220 < p_{\text{T}}^{\gamma\gamma} < 350$ GeV	`Pow1`	7.6 %	21 %
$N_{\text{jet}} = 0$	`ExpPol2`	7.6 %	36 %
$N_{\text{jet}} \geq 3$	`ExpPol1`	18 %	37 %
$-\pi \leq \Delta\phi_{jj} < -\pi/2$	`ExpPol2`	18 %	27 %
$-\pi/2 \leq \Delta\phi_{jj} < 0$	`ExpPol1`	9.2 %	22 %
$0 \leq \Delta\phi_{jj} < \pi/2$	`ExpPol1`	10 %	23 %
$\pi/2 \leq \Delta\phi_{jj} < \pi$	`ExpPol2`	3.9 %	5.8 %

Table 6.5: Background parameterisations and spurious signal estimates in several bins.

sample. When simulating calorimeter cell responses, a parameterisation of the expected response is used instead of the full simulation of detector interactions [218–220]. The Higgs discovery analysis [24] also used fast calorimeter parameterisations when modelling background processes. This approach significantly reduces the time taken to simulate all of the 100 million events contained within this sample, however it is expected to be less accurate. This may have two possible implications. Firstly, variations in the photon reconstruction efficiency or energy resolution may impact the expected shape of the background spectrum. Secondly, variations in observable quantities may impact the migrations into and out of a particular bin or fiducial region, also affecting the background shape.

Any such effect is not expected to cause a significant systematic uncertainty. The $m_{\gamma\gamma}$ and $p_{\text{T}}^{\gamma\gamma}$ spectra obtained using fast simulation were compared with fully simulated events. The agreement in the *diphoton fiducial* region was found to be within the $\mathcal{O}(1\ \%)$ statistical precision. Studies in Refs. [218–220] show good agreement between the fast and full simulation models for the energy scale and resolution of photons and electrons. The identification efficiencies are reproduced to within 5 %, and jet kinematics are also well described in the events studied. Furthermore, both the chosen PDFs and the background templates are validated by the comparison with the data sidebands and template fluctuations are conservatively accounted for in the definition of the spurious signal uncertainty. Finally, the background parameters and normalisations are allowed to float without external constraint in the fit to data. This flexibility reduces the reliance on the template modelling. Bias tests on the signal extraction will be presented later in the chapter.

6.4.3 Treatment of modelling uncertainties

The $\vec{\lambda}$ parameters describing the background PDFs in Eqs. 6.19 - 6.21 are treated as unconstrained NPs when performing the signal extraction. They are therefore determined

by the data instead of relying on the template modelling. If the data sidebands contained an infinite number of events then the constraint of $\vec{\lambda}$ would be exact. However, the finite dataset size leads to parameter uncertainties $\Delta\vec{\lambda}$ which transfer into statistical uncertainties on the PoIs. The absolute systematic uncertainty on the PoI due to background modelling is N^{spur}. This is not included as a NP but added in quadrature to the post-fit PoI uncertainty.

Each signal PDF is described by six DSCB parameters. The parameters $\{\alpha_{\text{low}},\ n_{\text{low}},\ \alpha_{\text{high}},\ n_{\text{high}}\}$ are fixed to the values derived from MC in section 6.4.1. The parameters $\{m_{\text{H}}, \mu, \sigma\}$ are treated as constrained NPs to account for systematic uncertainties which impact the shape of the signal peak. The evaluated Higgs mass, m_{H}, is parameterised in terms of the nominal value $m_{\text{H}}^{\text{nom}}$ (fixed), the fractional uncertainty σ^{mH} (fixed) and the NP θ_{mH} according to

$$m_{\text{H}}\left(\vec{\theta}\right) = m_{\text{H}}^{\text{nom}} \cdot \left(1 + \sigma^{\text{mH}} \cdot \theta_{\text{mH}}\right) \qquad \mathcal{C}\left(\theta_{\text{mH}}\right) = \text{Gaus}\left(0, 1; \theta_{\text{mH}}\right) \ . \tag{6.22}$$

The external constraint is a standard normal Gaussian evaluated at θ_{mH} and ensures that the likelihood curve is broadened by the correct amount assuming Gaussian uncertainties. Values of $m_{\text{H}}^{\text{nom}} = 125.09$ GeV and $\sigma^{\text{mH}} = 0.19$ % are used. The NP θ_{mH} describes the deviation of m_{H} from its nominal value in units of its uncertainty. It is constrained simultaneously by all bins of a distribution.

Thirty-nine independent NPs, $\vec{\theta}_{\text{PES}}$, are used to describe systematic uncertainties on the photon energy scale (PES). These are used to modify the DSCB mean, μ_i, in each bin i according to

$$\mu_i\left(\vec{\theta}\right) = \mu_i^{\text{nom}} \cdot \prod_{\theta_{\text{PES}}} \begin{cases} 1 + \sigma_{+,i}^{\text{PES}} \cdot \theta_{\text{PES}} & \theta_{\text{PES}} \geq 0 \\ 1 + \sigma_{-,i}^{\text{PES}} \cdot \theta_{\text{PES}} & \theta_{\text{PES}} < 0 \end{cases} \qquad \mathcal{C}\left(\theta_{\text{PES}}\right) = \text{Gaus}\left(0, 1; \theta_{\text{PES}}\right) \ . \tag{6.23}$$

Each PES source contributes an asymmetric uncertainty $\sigma_{\pm,i}^{\text{PES}}$ per-bin. Use of a single NP per source accounts for the correct systematic correlation between bins. Each μ_i^{nom} is fixed to the value derived from MC in section 6.4.1. Nine independent NPs, $\vec{\theta}_{\text{PER}}$, are used to describe the impact of photon energy resolution (PER) uncertainties on the DSCB width parameter, σ_i, in each bin according to

$$\sigma_i\left(\vec{\theta}\right) = \sigma_i^{\text{nom}} \cdot \prod_{\theta_{\text{PER}}} \begin{cases} e^{\sqrt{\ln\left(1+(\sigma_{+,i}^{\text{PER}})^2\right)} \cdot \theta_{\text{PER}}} & \theta_{\text{PER}} \geq 0 \\ e^{\sqrt{\ln\left(1+(\sigma_{-,i}^{\text{PER}})^2\right)} \cdot \theta_{\text{PER}}} & \theta_{\text{PER}} < 0 \end{cases} \qquad \mathcal{C}\left(\theta_{\text{PER}}\right) = \text{Gaus}\left(0, 1; \theta_{\text{PER}}\right) \tag{6.24}$$

where a log-normal deviation is used to disallow pulls into unphysical negative resolutions. Table 6.6 shows the fractional uncertainties in several bins. The combined impact of all PES NPs is $\lesssim 0.4$ % on μ_i. The combined impact of all PER NPs is $\lesssim 8$ % on σ_i except at high $p_{\text{T}}^{\gamma\gamma}$ where it increases to 11 %.

Bin or region	σ^{mH}	$\sigma^{\mathrm{PES}}_{+,i}$	$\sigma^{\mathrm{PES}}_{-,i}$	$\sigma^{\mathrm{PER}}_{+,i}$	$\sigma^{\mathrm{PER}}_{-,i}$
Diphoton fiducial	0.19 %	0.25 %	0.26 %	6.1 %	6.3 %
VBF enhanced	0.19 %	0.29 %	0.29 %	6.8 %	7.5 %
ttH enhanced	0.19 %	0.30 %	0.29 %	7.4 %	7.2 %
$0 < p_{\mathrm{T}}^{\gamma\gamma} < 20$ GeV	0.19 %	0.24 %	0.24 %	5.9 %	5.7 %
$220 < p_{\mathrm{T}}^{\gamma\gamma} < 350$ GeV	0.19 %	0.40 %	0.40 %	11 %	11 %
$N_{\mathrm{jet}} = 0$	0.19 %	0.24 %	0.24 %	5.8 %	5.9 %
$N_{\mathrm{jet}} \geq 3$	0.19 %	0.30 %	0.29 %	7.2 %	7.3 %
$-\pi \leq \Delta\phi_{jj} < -\pi/2$	0.19 %	0.27 %	0.27 %	6.4 %	6.6 %
$-\pi/2 \leq \Delta\phi_{jj} < 0$	0.19 %	0.30 %	0.31 %	7.4 %	7.8 %
$0 \leq \Delta\phi_{jj} < \pi/2$	0.19 %	0.30 %	0.30 %	7.5 %	7.6 %
$\pi/2 \leq \Delta\phi_{jj} < \pi$	0.19 %	0.27 %	0.27 %	6.6 %	6.7 %

Table 6.6: Uncertainty amplitudes in several bins and fiducial regions. The 39 PES and 9 PER sources are combined in quadrature in each direction.

6.4.4 Measured signal yields

The signal extraction is performed independently for each fiducial region or differential distribution using the `Minuit2` [245] program implemented within the `RooFit` package [246]. Parameter uncertainties are provided by the `Minos` program. The floated fit parameters are summarised as follows:

- the signal event yields, $\vec{\nu}^{\mathrm{sig}}$, are the PoIs
- the background event yields, $\vec{\nu}^{\mathrm{bkg}}$, are unconstrained NPs
- the background shape parameters, $\vec{\lambda}$, are unconstrained NPs
- the systematic uncertaintes on the signal shape, $\vec{\theta}$, are constrained NPs

Figure 6.10 shows the results of the signal extraction fits in several fiducial regions. Although the fits are unbinned, an appropriate binning of $m_{\gamma\gamma}$ is used to visualise the data spectra. The background and signal components of the likelihood are plotted for comparison as well as the residual compared with the fitted background-only component. The *diphoton fiducial* region is dominated by background events and the statistical uncertainty on the signal yield is driven by the number of background events in the signal region. For other fiducial regions, the anti regions are included within the fit to allow the constraint of $\vec{\theta}$ using the full dataset.

The expected and measured signal yields are shown for all fiducial regions in Table 6.7. The spurious signal uncertainty is added in quadrature with the fit uncertainty to define $\Delta\nu^{\mathrm{sig}}$. All measurements are consistent with statistical fluctuations around the expected values. The improvement in uncertainty is caused by small negative pulls on the energy resolution leading to a narrower signal peak compared with the expectation.

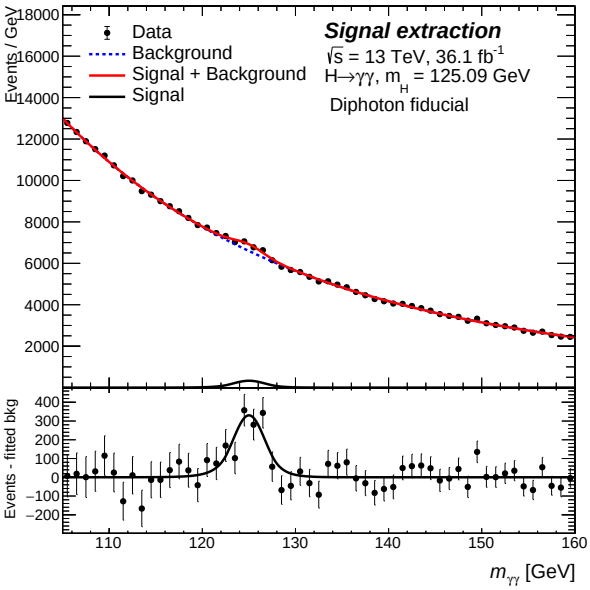

(a) Diphoton fiducial

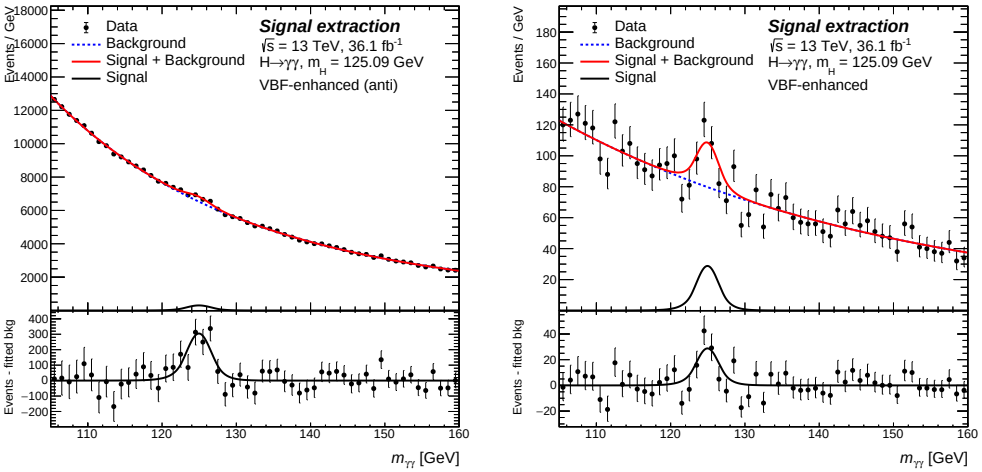

(b) VBF enhanced

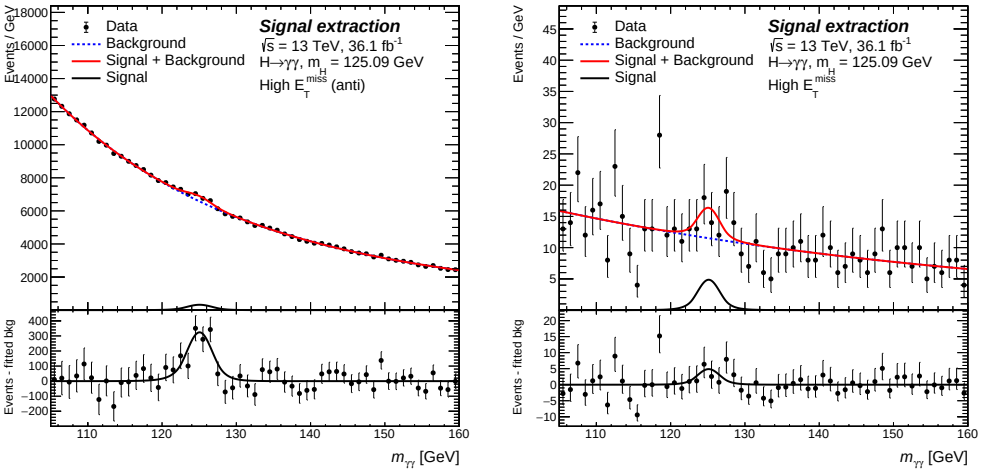

(c) High $E_{\mathrm{T}}^{\mathrm{miss}}$

Figure 6.10: Extraction of signal yields in several fiducial regions.

Region	Expected		Measured	
	ν^{sig}	$\Delta\nu^{\text{sig}}$	ν^{sig}	$\Delta\nu^{\text{sig}}$
Diphoton fiducial	1730	270	1490	263
VBF enhanced	74	28	117	28
$N_{\text{lepton}} \geq 1$	13	11	14	11
High $E_{\text{T}}^{\text{miss}}$	12	10	19	11
ttH enhanced	14	15	6	15

Table 6.7: Expected and measured signal yields in several fiducial regions.

Figure 6.11 shows the fitted $m_{\gamma\gamma}$ spectra in all published bins of $p_{\text{T}}^{\gamma\gamma}$. Low p_{T} bins are dominated by background. Higher p_{T} bins have a larger signal-to-background ratio but fewer events.

6.4.5 Impact of systematic uncertainties

Figure 6.12 shows the Λ profile of signal events in the *diphoton fiducial* region. Shown as the solid line, the profile at $\Lambda = 1$ is interpreted as the total uncertainty from the combination of statistical and systematic sources (excluding spurious signal which is not described using NPs). A statistical-only uncertainty is obtained when the same procedure is performed after fixing $\vec{\theta}$ to their best-fit values. This is shown as the dotted line. The systematic uncertainty is defined as the quadrature difference between the two.

The expected sensitivities, presented in Table 6.7, are derived using a signal extraction fit performed on a finely binned (in $m_{\gamma\gamma}$) simulated dataset. The event yield in each bin is evaluated using the background shape and normalisation obtained from data and the signal shape and normalisation expected from MC, and a statistical uncertainty is assigned assuming Poisson errors. Figure 6.13 shows the expected and observed statistical (blue) and systematic (orange) uncertainties, presented as a fraction of the total uncertainty (black), in several fiducial regions and differential bins. Statistical uncertainties dominate in all bins. Note that this plot is not stacked.

Figure 6.14 shows the expected ranking of NP contributions evaluated using a simulated dataset as described. NPs are labelled based on their type (energy scale or resolution). Red points show the pre-fit NP values and uncertainties defined as 0 ± 1 by construction because $\mathcal{C}$ were defined using standard normal Gaussian distributions. Black points show post-fit values which are centred on zero since the simulated datapoints exactly follow the model distribution. Uncertainties drop below unity because the data-points constrain the NPs. In the limit of infinite dataset size, NPs would be constrained exactly and have no post-fit uncertainty. Yellow boxes show the pre-fit impact of each NP. This is defined as the fractional change, $^{\Delta\nu}/_{\nu}$, on the PoI obtained when the NP is fixed to its pre-fit $\pm 1\sigma$ uncertainties and the likelihood is re-optimised floating all other NPs. The post-fit impact,

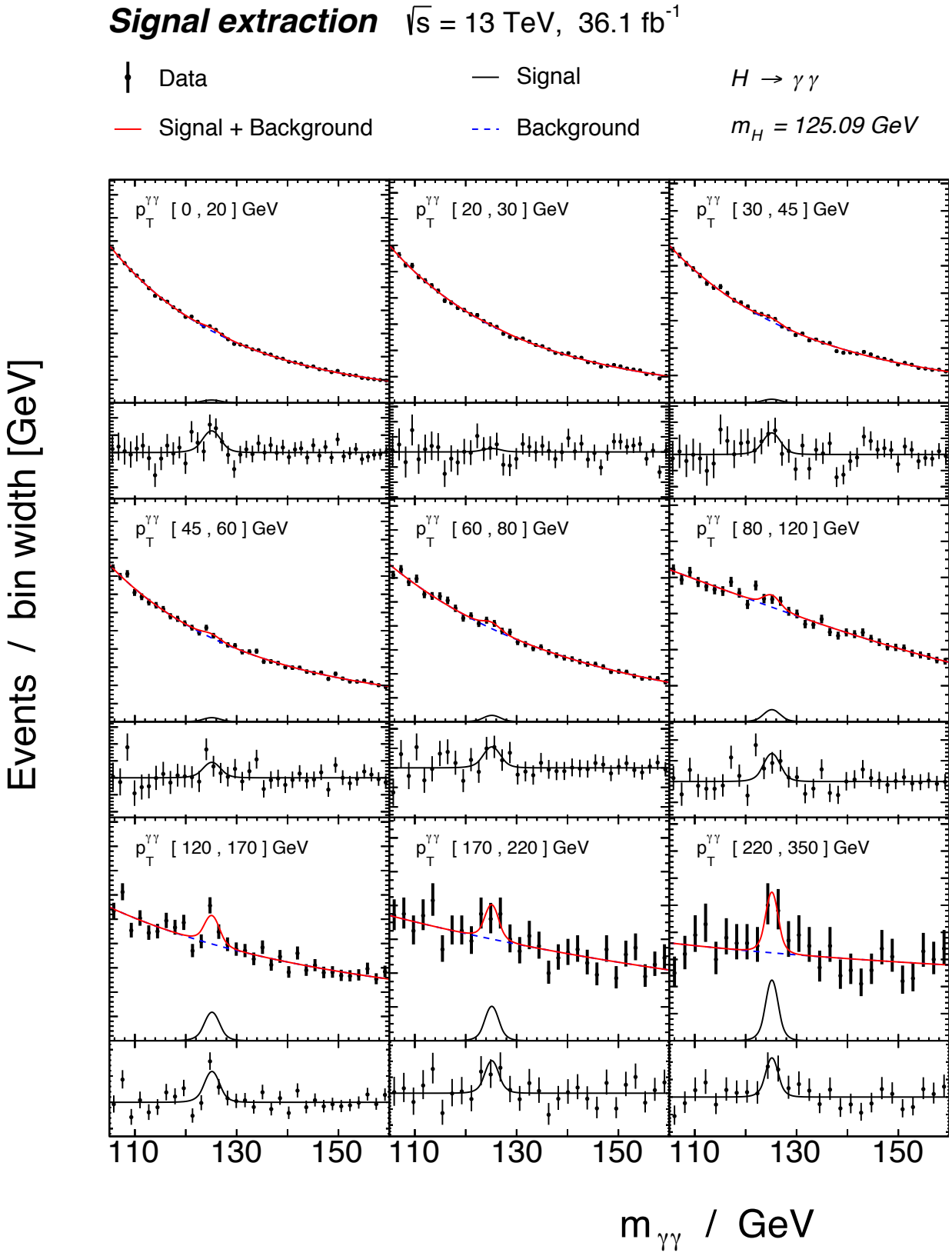

Figure 6.11: Extraction of signal yields in all published bins of the $p_{\mathrm{T}}^{\gamma\gamma}$ distribution.

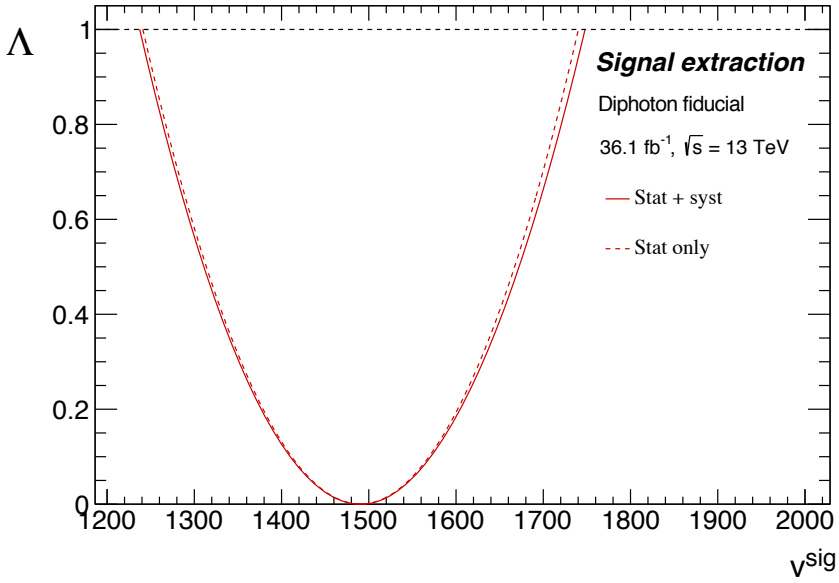

Figure 6.12: Likelihood profile of the measured signal yield in the *diphoton fiducial* region. Spurious signal is not included in the systematic uncertainty.

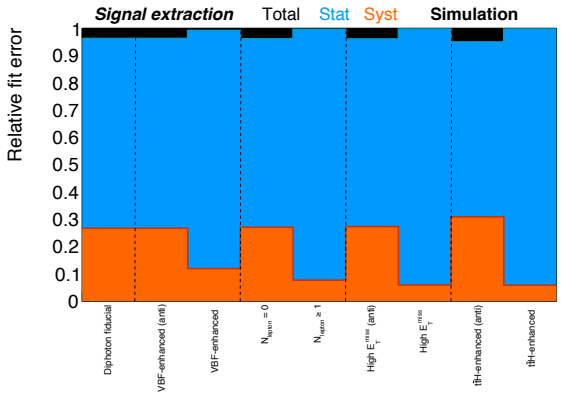

(a) Expected (fiducial regions)

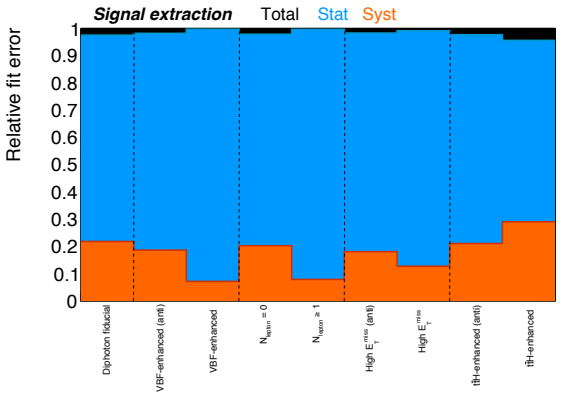

(b) Measured (fiducial regions)

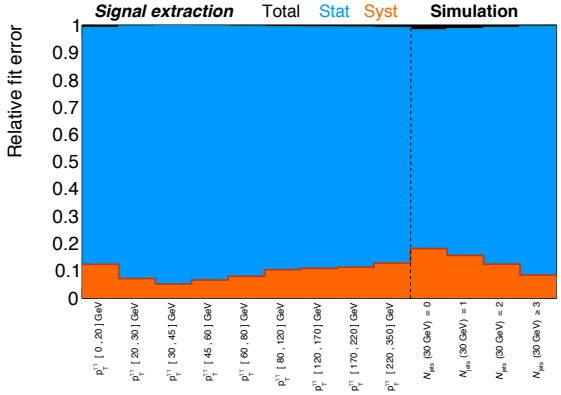

(c) Expected (differential bins)

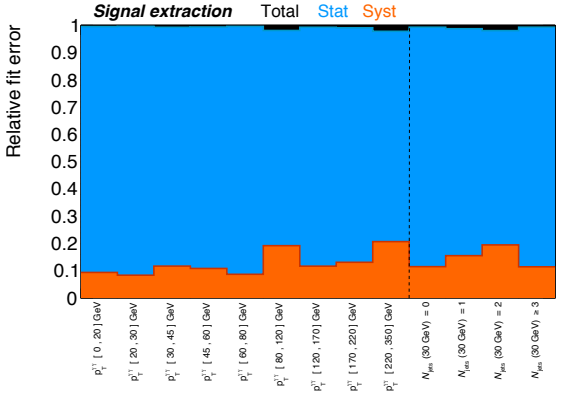

(d) Measured (differential bins)

Figure 6.13: Expected and measured breakdown of statistical and systematic uncertainties in several signal extractions. Spurious signal is not included.

Uncertainty	Diphoton fiducial	VBF enhanced	$N_{\text{jet}} = 0$	$N_{\text{jet}} = 1$	$N_{\text{jet}} = 2$	$N_{\text{jet}} \geq 3$
Fit (stat.)	17 %	22 %	31 %	29 %	34 %	31 %
Fit (syst.)	6 %	9 %	12 %	7 %	8 %	12 %
- PES $\oplus$ PER $\oplus m_H$	*4.3 %*	*3.5 %*	*3.3 %*	*4.3 %*	*4.3 %*	*3.9 %*
- Spurious signal	*4.2 %*	*7.8 %*	*11 %*	*6.1 %*	*6.5 %*	*11 %*

Table 6.8: Fractional uncertainties on the signal yields measured in several bins and fiducial regions.

shown in blue hatches, repeats this procedure when using the post-fit NP centres and uncertainties. NPs are ranked in decreasing order of their post-fit impact on the PoI (top 20 shown). Uncertainties on the energy resolution are found to dominate the systematic uncertainty on the PoI. The uncertainty on the assumed Higgs mass is found to have < 0.1 % impact on the PoI. Individual energy scale variations cause a $\lesssim 0.1$ % magnitude shift on the the PoI. This is one-sided in reflection of the symmetry of the signal peak.

Figure 6.15 shows the same procedure applied to the measured dataset in this region. Resolution NPs typically fit values of $-\lesssim 0.2$ resulting in a narrower-than-expected signal peak. Energy scale NPs are typically slightly below zero indicating a preferred peak below the expected value of μ. The pre- and post-fit PoI impacts follow the expected trend and order of magnitude with some data fluctuations observed. No NPs are pulled significantly away from zero which might have indicated insufficient modelling. NP uncertainties are not typically much smaller than unity which might have indicated over-constraint.

6.4.6 Summary of fit uncertainties

Table 6.8 summarises the fractional uncertainties associated with the extracted signal yields in several fiducial regions and bins. Statistical uncertainties dominate in all cases. The spurious signal is typically the dominant source of systematic uncertainty except in the *diphoton fiducial* region where it has an impact comparable with the systematic NPs.

6.4.7 Bias tests

Possible biases on the estimated signal yields are investigated using the bootstrapping technique. A bootstrap (or 'toy') dataset is created by assigning a random Poisson weight with a mean of 1 to each measured event. The signal extraction fit is performed on the toy dataset after fixing $\vec{\theta}$ to the best-fit values obtained from the original dataset. If ν^{data} is the original PoI measurement and $\nu^{\text{toy}} \pm \Delta\nu^{\text{toy}}$ is that obtained from the toy dataset, the *pull* is defined according to

$$\frac{\nu^{\text{toy}} - \nu^{\text{data}}}{\Delta\nu^{\text{toy}}} \,. \tag{6.25}$$

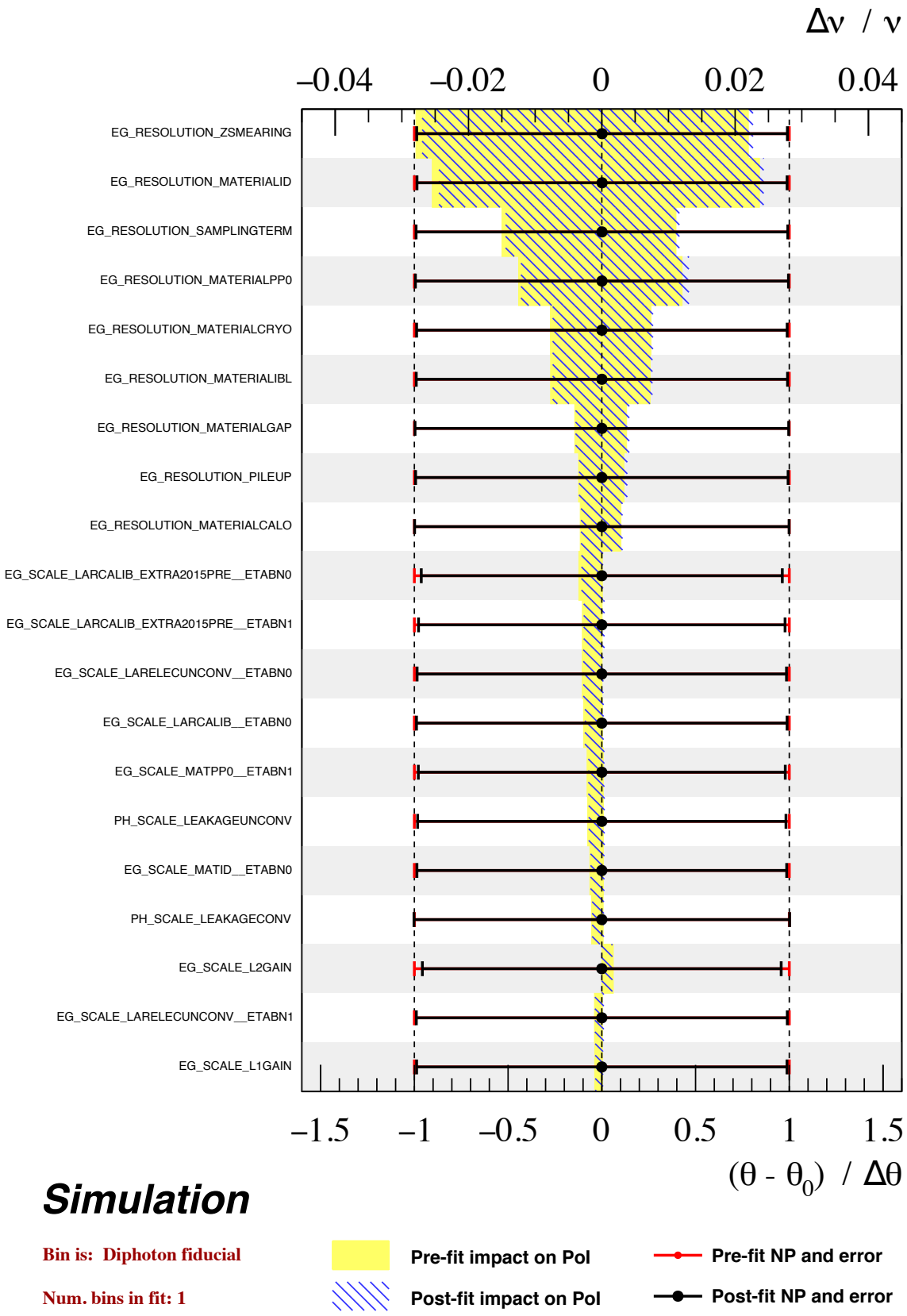

Figure 6.14: Expected impact of the dominant systematic uncertainties in the *diphoton fiducial* signal extraction.

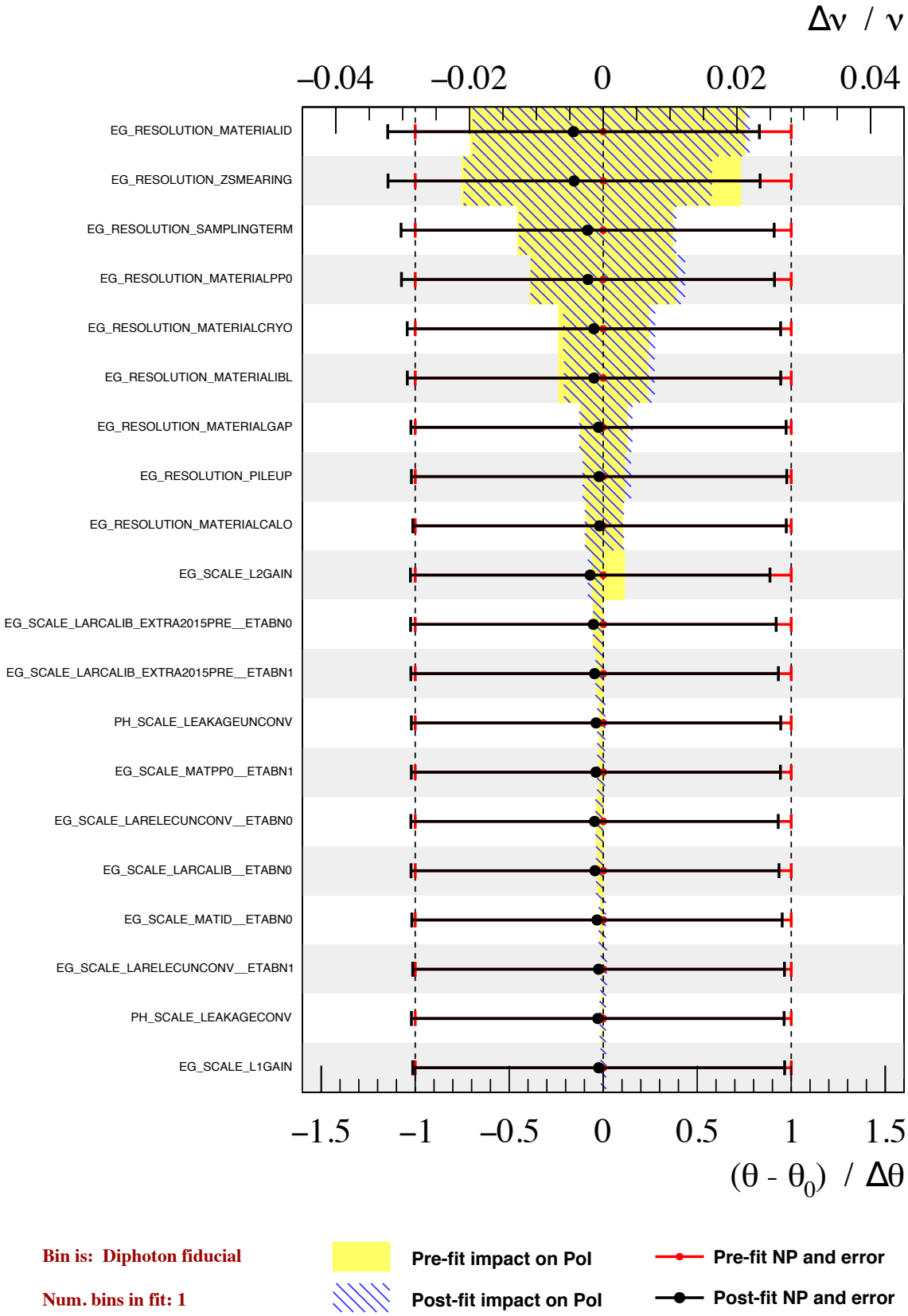

Figure 6.15: Measured impact of the dominant systematic uncertainties in the *diphoton fiducial* signal extraction.

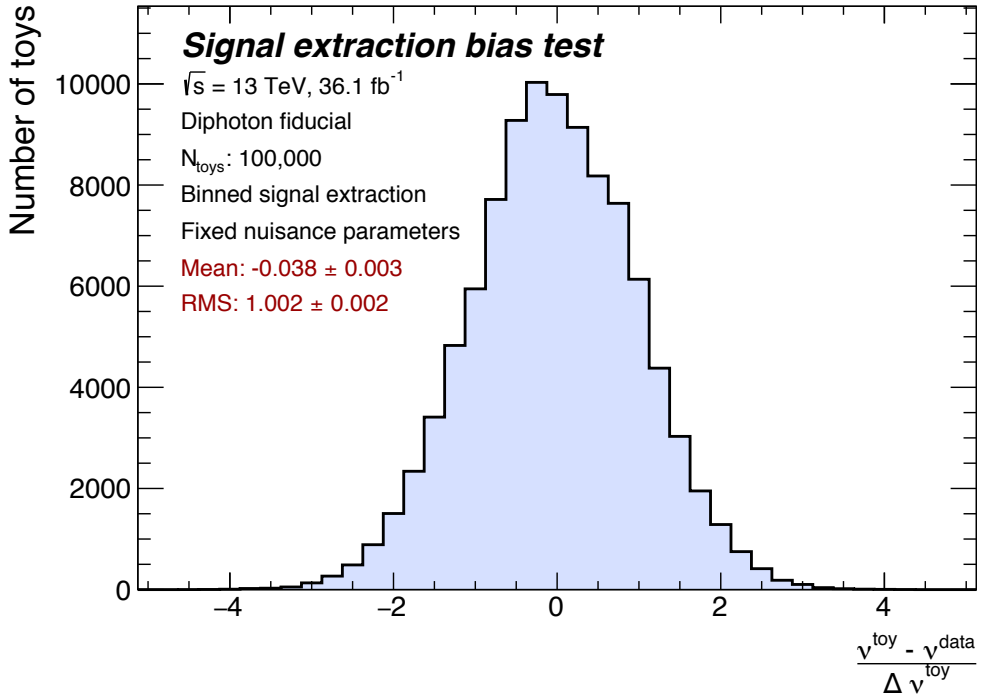

Figure 6.16: Signal yield bootstrap bias test in the *diphoton fiducial* region.

Each toy dataset represents a different statistical fluctuation. If the estimates of the PoI value and uncertainty are unbiased then the pull is a random number drawn from a standard normal distribution. This is tested by generating 100,000 toy datasets and evaluating the pull distribution as shown for the *diphoton fiducial* region in Figure 6.16. The RMS is consistent with 1 indicating a correctly estimated uncertainty. The mean shows a systematic deviation of approximately -4 % in units of $\Delta\nu^{\text{toy}}$. This means that the bias on the PoI is 25 times smaller than the statistical uncertainty and can be neglected.

The integral of a distribution is defined as the total number of signal events and is calculated by summing the measured signal yields over all bins, i.e

$$\begin{aligned} \text{Integral} &= \sum_{i \in \text{bins}} \nu_i^{\text{sig,meas}} \\ (\Delta\text{Integral})^2 &= \sum_{i,j \in \text{bins}} \text{Cov}\left(\nu_i^{\text{sig,meas}}, \nu_j^{\text{sig,meas}}\right) . \end{aligned} \tag{6.26}$$

The uncertainty accounts for the small systematic covariance between bins using the approximation of asymptotic covariance denoted Cov.

The integrals of all distributions should be comparable unless significant modelling biases are present. This is used as a cross-check. If they were 100 % correlated then we would expect the integrals to be exactly equal. However, a small statistical decorrelation occurs because each distribution separates the data into bins with unique model PDFs and parameters. The statistical correlation coefficient, ρ, between two measurements x and y

is defined according to

$$\rho_{xy} = \frac{\mathrm{Cov}\,(x,y)}{\Delta x \Delta y} = \frac{\langle xy \rangle - \langle x \rangle \langle y \rangle}{\Delta x \Delta y} \tag{6.27}$$

where Δx is the standard deviation of x and $\langle x \rangle$ is the mean. The statistical correlations are determined by evaluating Eq. 6.27 using 100,000 bootstrap datasets. The spread of bootstrapped measurements is shown for two observables in Figure 6.17. A positive correlation of 97.5 % is observed. The correlations between all pairs of distributions are shown in Figure 6.18. All distributions are strongly correlated as expected.

Figure 6.19 (orange) compares the integrals of all distributions. The uncertainties are defined according to Eq. 6.26. Blue points show the difference defined with respect to the *diphoton fiducial* region. Uncertainties account for the measured statistical correlations and small uncertainties reflect a high degree of correlation. When a quantity $y = A - B$ is defined as the difference between two correlated quantities, $A \pm \Delta A$ and $B \pm \Delta B$, then its uncertainty Δy is computed according to

$$(\Delta y)^2 = (\Delta A)^2 + (\Delta B)^2 - 2\rho_{AB} \cdot \Delta A \cdot \Delta B \tag{6.28}$$

under the approximation of asymptotic covariance. The pulls, shown in green, are defined as $y/\Delta y$.

Most distributions show a negative pull indicating that they measure fewer events than the *diphoton fiducial* region. The pulls of unbiased measurements are expected to follow a standard normal distribution when calculated with respect to the true mean. However, the *diphoton fiducial* reference is a single measurement subject to its own fluctuation with respect to the true mean. This means that Figure 6.19 (green) does not necessarily indicate a bias. The distribution of pulls is shown in Figure 6.20. This has a mean of -1.2 ± 0.2 indicating that the *diphoton fiducial* measurement lies 1.2 standard deviations above the estimated mean. The RMS is 0.9 ± 0.1 which is consistent with 1. Only one measurement lies more than 2 standard deviations away from the mean. These observations are consistent with the hypothesis of an unbiased measurement. Note that an expected bias from spurious signal has not been considered due to its nontrivial correlation between bins.

6.4.8 Statistical correlations

Bins of separate differential distributions are statistically correlated if they contain the same events. The greater the overlap in selected events, the higher the correlation. These correlations must be known for the measured distributions to be used to constrain BSM physics models. They are estimated using the bootstrap procedure described in section 6.4.7. For each toy dataset, a finely binned likelihood fit is performed using fixed $\vec{\theta}$. The statistical correlation is calculated from the scatter between any two signal yields using Eq. 6.27. Figure 6.21 shows an example using the lowest $p_{\mathrm{T}}^{\gamma\gamma}$ and N_{jet} bins.

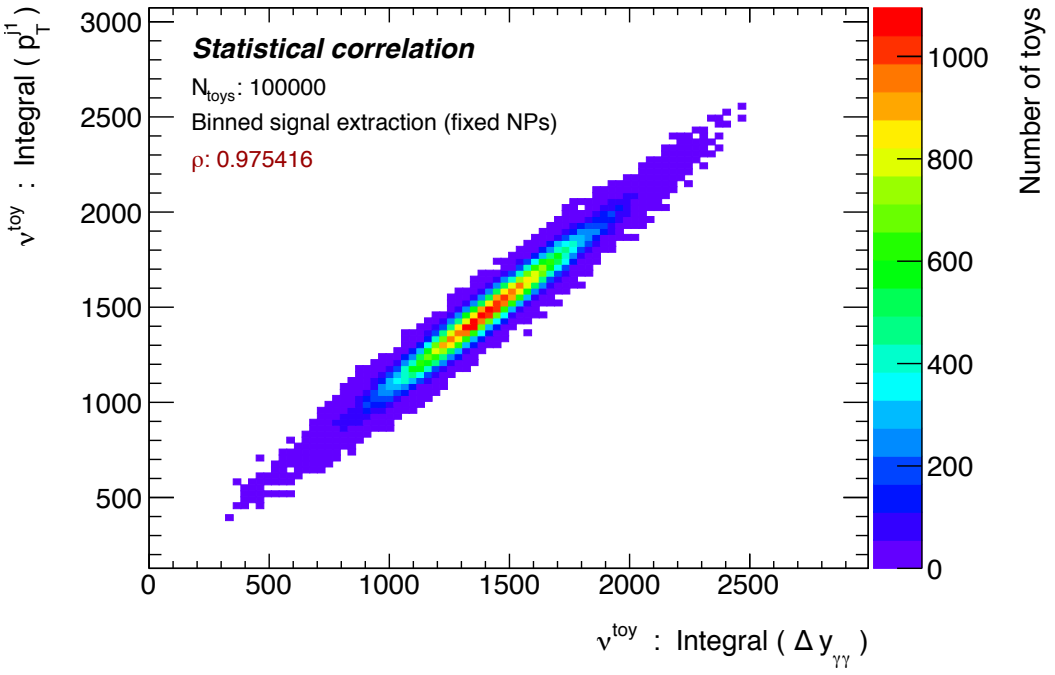

Figure 6.17: Statistical correlation between the integrals of the measured p_{T}^{j1} and $\Delta y_{\gamma\gamma}$ distributions.

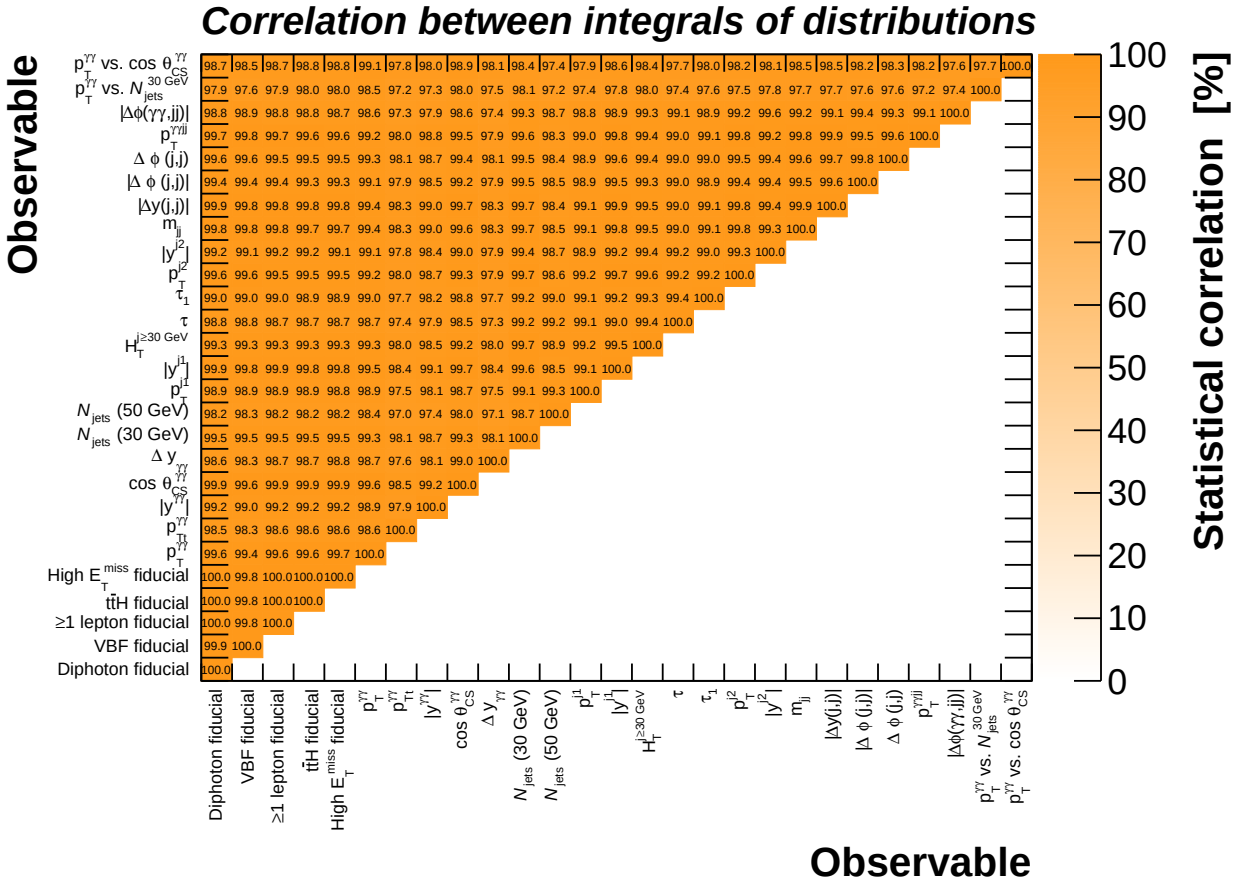

Figure 6.18: Statistical correlations between the integrals of all distributions.

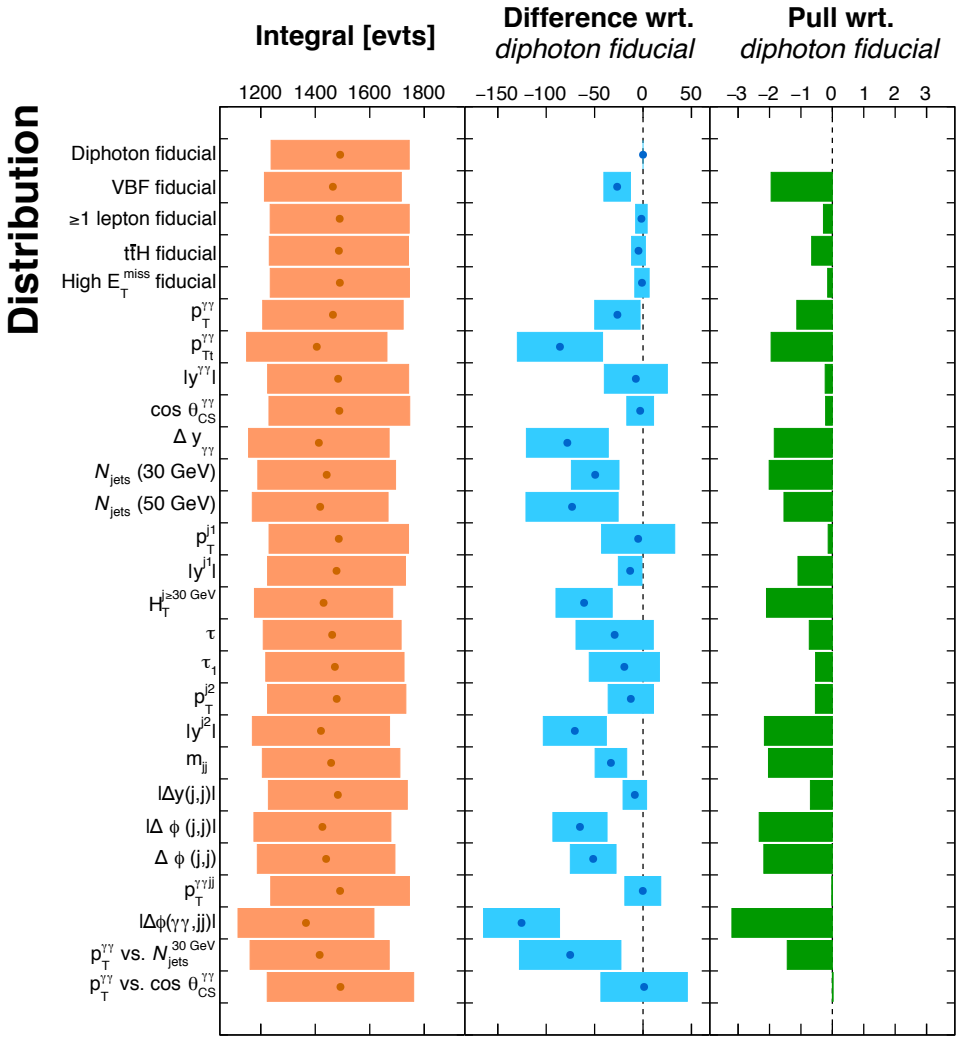

Figure 6.19: Comparison between the integrals of all measured distributions.

Consider that two bins, x and y, contain N_x and N_y events respectively and share N_{xy} of them. If t is the number of bootstrap datasets used to calculate the correlation, ρ, then its uncertainty, $\Delta\rho$, is estimated as

$$\begin{aligned} \Delta\rho^{\text{toys}} &= \tanh\left(\text{atanh}(\rho) - (t-3)^{-1/2}\right) - \rho \\ \Delta\rho^{\text{evts}} &= \rho\sqrt{(N_{xy})^{-1} + (4N_x)^{-1} + (4N_y)^{-1}} \\ \Delta\rho &= \sqrt{\left(\Delta\rho^{\text{toys}}\right)^2 + \left(\Delta\rho^{\text{evts}}\right)^2}\,. \end{aligned} \tag{6.29}$$

Two contributions account for the finite number of toys and measured events. The dataset size dominates the uncertainty when using $t = 100,000$.

Three alternative methods are used as cross-checks. The statistical correlations are calculated as follows:

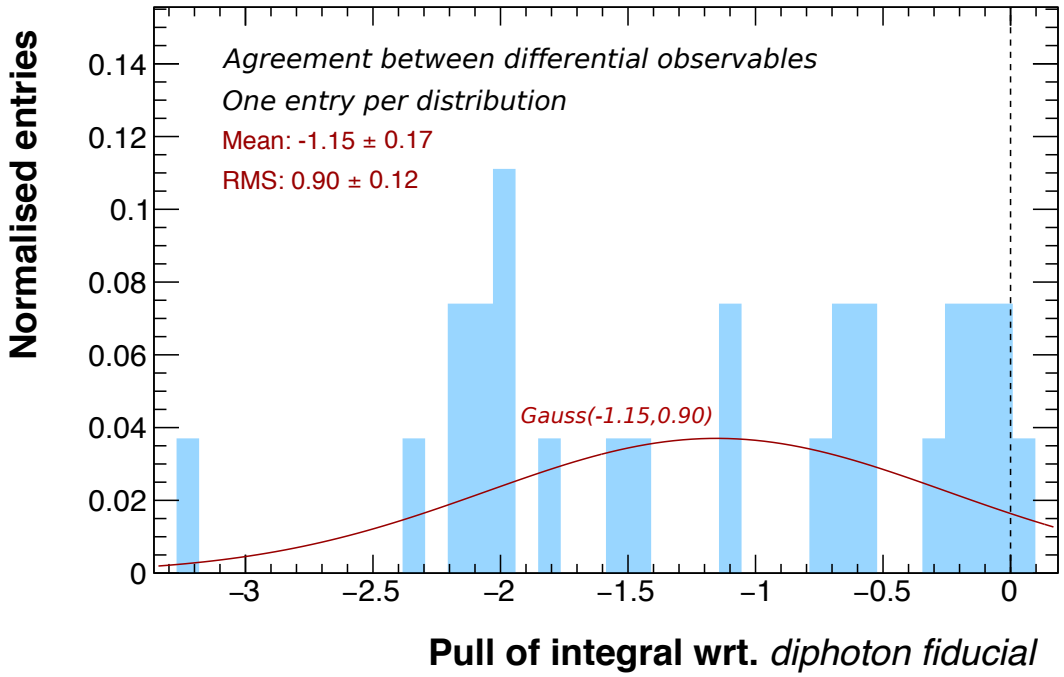

Figure 6.20: Distribution of integral pulls using *diphoton fiducial* as a reference.

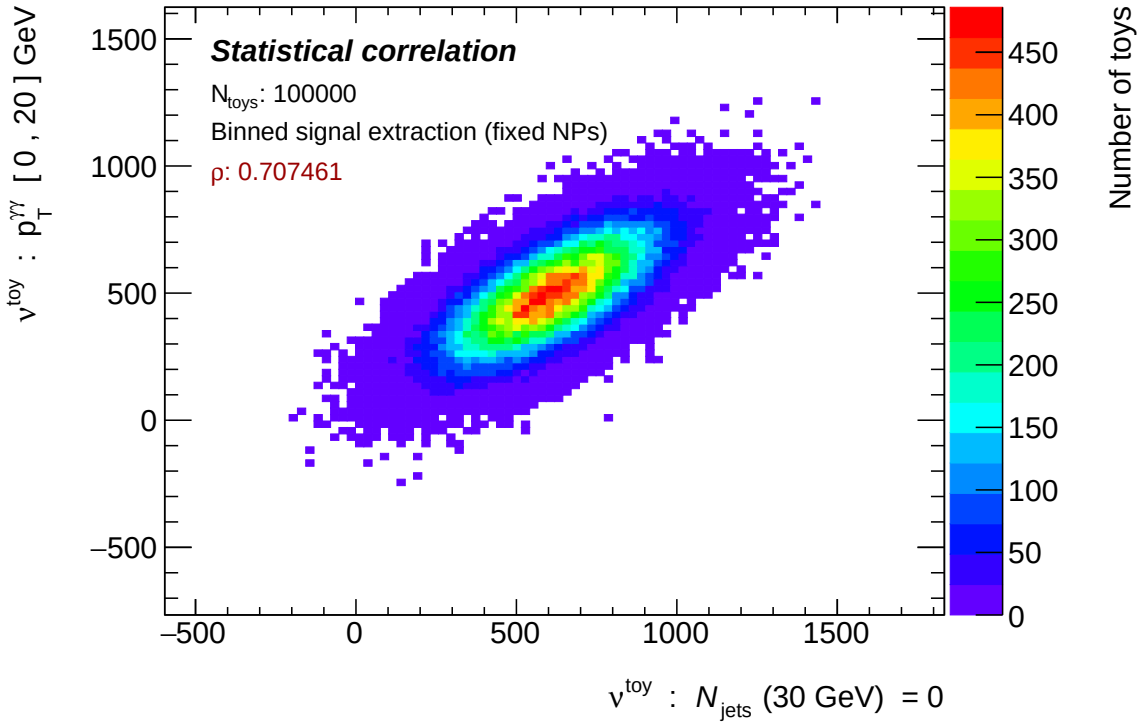

Figure 6.21: Bootstrap spread of signal yields in the $0 \leq p_{\mathrm{T}}^{\gamma\gamma} < 20$ GeV and $N_{\mathrm{jet}} = 0$ bins.

- The bootstrap method is performed with 10,000 toy datasets. Instead of using a likelihood fit in each dataset, the number of events are counted in the signal region defined as $121 < m_{\gamma\gamma} < 129$ GeV. The scatter is used to calculate the correlation using the same method as in Figure 6.21. Eq. 6.29 is used to derive $\Delta\rho$ using $t = 10,000$.

- The number of events in the signal regions, n_x and n_y, are counted in bins x and y. The statistical correlation is calculated as

$$\rho = \frac{n_{xy}}{\sqrt{n_x}\sqrt{n_y}} \tag{6.30}$$

  where n_{xy} is the number of overlapping events. No toy datasets are used and so $\Delta\rho = \Delta\rho^{\text{evts}}$. This is labelled as the "formula" approach.

- The formula approach is performed using the number of events in the sideband region. This approach is valid when (i) signal and background have approximately the same bin-to-bin correlation or (ii) the background rate is signficantly dominant compared with the signal and so statistical uncertainties are driven by fluctuations on the number of background events.

Figure 6.22 shows the measured bin-by-bin statistical correlations between the $p_{\text{T}}^{\gamma\gamma}$ and N_{jet} distributions. Bins with low p_{T} are typically correlated with small jet multiplicities because the transverse momentum of the Higgs system must be balanced with all other final states of the hard scatter. High $p_{\text{T}}^{\gamma\gamma}$ bins are therefore correlated with large jet multiplicities. All four methods are in good agreement.

Figure 6.23 shows the measured bin-to-bin statistical correlations between five differential observables. All bins are positively correlated because distributions are not required to contain the same total number of events, therefore there is no mechanism through which an upwards fluctuation of one bin can correlate with a downwards fluctuation in another. In this case the statistical correlation is solely driven by the event overlap between bins. A bin must always be 100 % correlated with itself and 0 % correlated with bins defined using orthogonal selection criteria.

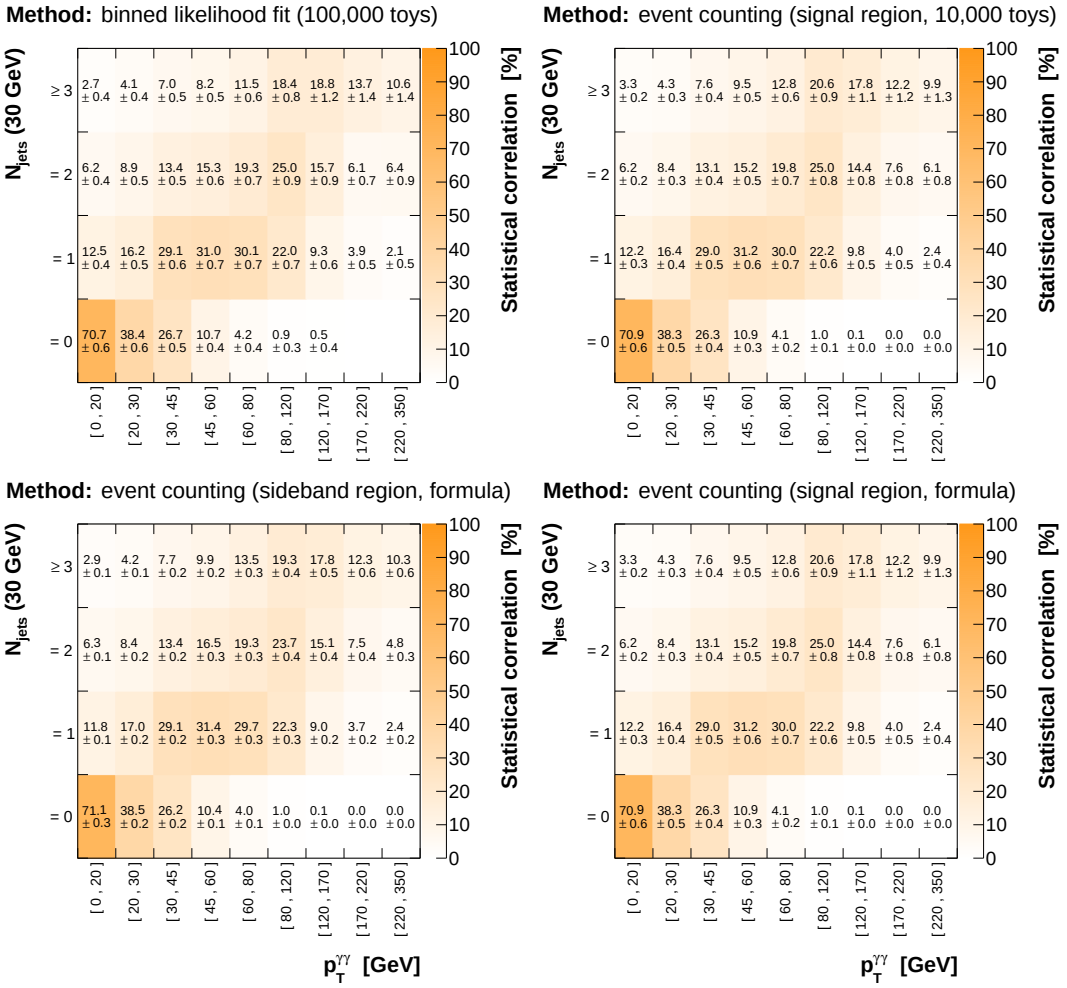

Figure 6.22: Statistical correlations in $p_{\mathrm{T}}^{\gamma\gamma}$ and N_{jet} measured using four methods.

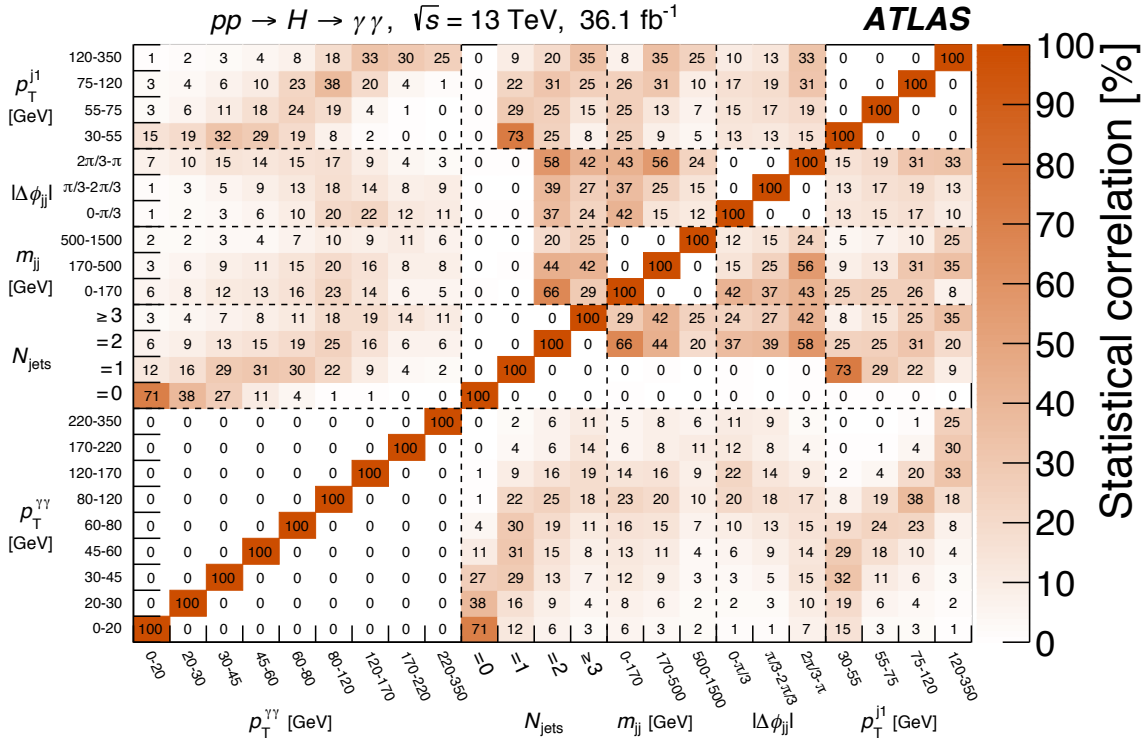

Figure 6.23: Statistical correlations between bins of several distributions.

6.5 Correction for detector effects

This analysis uses the *bin-by-bin* method to correct for detector effects. As shown in Eq. 6.3 and repeated here, the fiducial cross section in bin i is related to the corresponding signal yield and integrated luminosity according to

$$\sigma_i^{\text{fid}} = \frac{\nu_i^{\text{sig}}}{C_i \cdot L_{\text{int}}} \ . \tag{6.31}$$

The correction factor C_i accounts for detector inefficiency as well as migrations across bin boundaries and into or out-of the measurable region. It is calculated from signal MC samples according to

$$C_i = \frac{\nu_i^{\text{sig,exp}}}{n_i^{\text{fid,exp}}} \tag{6.32}$$

where $n_i^{\text{fid,exp}}$ is the expected particle level event yield. Any difference between the detector and particle level acceptances is minimised by closely matching the corresponding selection criteria.

The bin-by-bin method assumes that the number of events, expressed as a fraction of the particle level event yield, migrating into and out-of a bin follow the SM expectation. A possible systematic bias towards the expected distribution when significant migrations occur [247] is limited by assigning bin boundaries coarser than the typical resolution of each observable. An estimate of the remaining bias is accounted for through systematic uncertainties.

Alternative methods include *matrix inversion* in which the measured event yields are unfolded by inverting the detector response matrix. This can cause large negative covariances between bins of an unfolded spectrum when significant migrations and statistical uncertainties are expected [247]. This is because the fluctuation of any given detector level bin must contribute to the variance of all contributing particle level bins. The variance of an individual unfolded bin can then become large. *Regularised unfolding* methods provide an intermediate approach in which possible migrations are constrained in order to balance systematic bias and statistical covariance.

Work performed by another member of the analysis team compared the performance of the bin-by-bin method with matrix inversion and several regularised unfolding methods according to appropriate measures of bias and variance. The systematic bias induced by the bin-by-bin method was estimated to be significantly smaller than the expected statistical uncertainties in several scenarios consistent with data, and also smaller in an unrealistic "stress test" scenario. The other methods were all found to increase the variance on the unfolded cross sections as described. The bin-by-bin method is therefore considered appropriate for this analysis.

6.5.1 Fiducial selection

Particle level objects are defined from final state truth level particles with a mean lifetime of $c\tau > 10$ mm. Photons are required to satisfy $p_{\mathrm{T}} > 25$ GeV and either $0 \leq |\eta| < 1.37$ or $1.52 \leq |\eta| < 2.37$. They must not originate from the decay of a hadron, either directly or through an intermediate τ. The two highest p_{T} photons define the diphoton system. The leading (subleading) photon is required to satisfy $p_{\mathrm{T}}/m_{\gamma\gamma} > 0.35$ (0.25). Both photons are required to satisfy $E_{\mathrm{iso}}^{\mathrm{ptcl,trk}} < 0.05 \times E_{\mathrm{T}}^{\gamma}$ where $E_{\mathrm{iso}}^{\mathrm{ptcl,trk}}$ is defined as the scalar p_{T} sum of all charged particles with $p_{\mathrm{T}} > 1$ GeV within a cone of $\Delta R < 0.2$, i.e.

$$E_{\mathrm{iso}}^{\mathrm{ptcl,trk}} = \sum_{\Delta R<0.2} p_{\mathrm{T}}^{\text{charged, } p_{\mathrm{T}} > 1 \text{ GeV}} . \tag{6.33}$$

This is analogous to the detector level track isolation defined in Eq. 6.4. These selections define the *diphoton fiducial* region at particle level. The measurement of the fiducial cross section in this region is motivated as it is the most inclusive region measurable by ATLAS.

Electrons must not originate from hadron decay. Not-from-hadron photons within $\Delta R < 0.1$ are recombined with the electron in a process called *dressing*. They must satisfy $p_{\mathrm{T}} > 15$ GeV and either $0 \leq |\eta| < 1.37$ or $1.52 \leq |\eta| < 2.47$. Electrons within $\Delta R < 0.4$ of a selected photon are discarded. Muons are dressed with photons within $\Delta R < 0.1$ and required to satisfy $p_{\mathrm{T}} > 15$ GeV, $|\eta| < 2.7$ and not originate from hadron decay.

Jets are clustered from all particles except muons and neutrinos using the anti-k_{T} algorithm with a radius parameter of $r = 0.4$. They are required to satisfy $p_{\mathrm{T}} > 30$ GeV and $|y| < 4.4$ unless stated otherwise. Jets within $\Delta R < 0.4$ of a selected photon or $\Delta R < 0.2$ of a selected electron are discarded. A jet is classified as a b-jet if there exists a b-hadron with $p_{\mathrm{T}} > 5$ GeV within $\Delta R < 0.4$. The missing transverse momentum $E_{\mathrm{T}}^{\mathrm{miss}}$ is defined as the length of the vector sum of all neutrino $\vec{p}_{\mathrm{T}}$. When testing BSM models with additional invisible particles, these should be included in the $E_{\mathrm{T}}^{\mathrm{miss}}$ sum.

The additional particle level fiducial regions are defined below. The SM fractional contributions from different production processes are shown in Figure 6.24. These can be compared with the detector level compositions shown in Figure 6.5 which are typically less enhanced in VBF, VH and ttH due to migrations of ggF caused by finite jet resolution and pileup contamination. Figure 6.25 shows the particle level compositions in bins of $p_{\mathrm{T}}^{\gamma\gamma}$ and N_{jet} which can be compared with Figure 6.6.

VBF enhanced contains *diphoton fiducial* events for which a dijet system was also selected. The minimum jet p_{T} requirement is relaxed to 25 GeV. The dijet mass is required to be at least 400 GeV and the two jets must be separated by $|\Delta y| > 2.8$. The azimuthal separation between the diphoton system and the dijet system is required to be $|\Delta\phi| > 2.6$. These selections are analagous to the Run 1 measurement [113]. They were chosen heuristically based on knowledge of the characteristic sig-

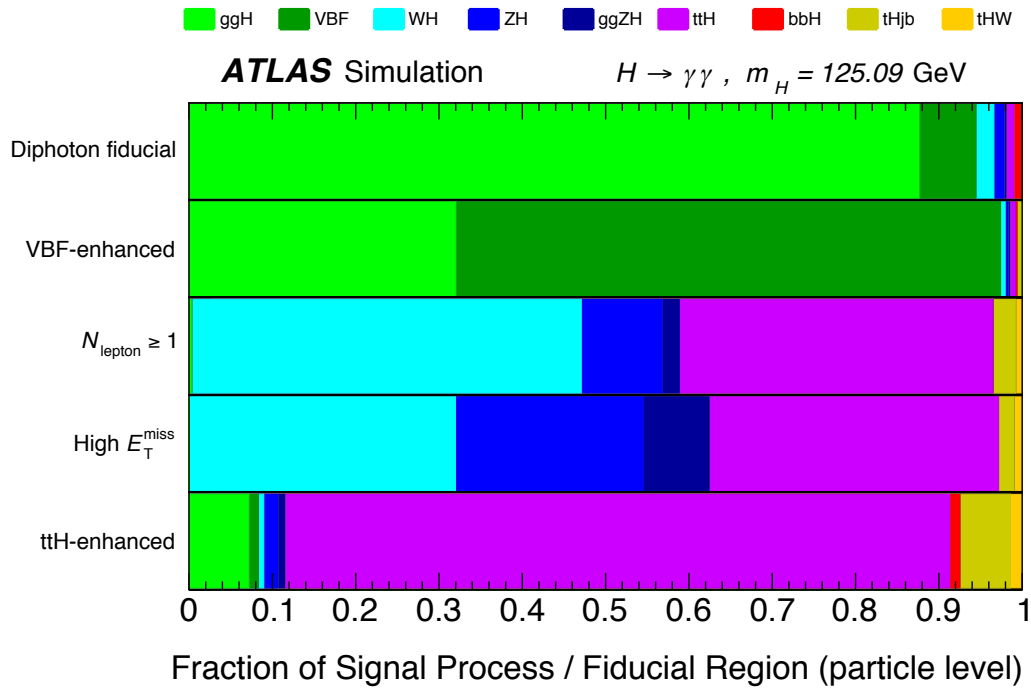

Figure 6.24: Expected production process fractions in fiducial regions at particle level.

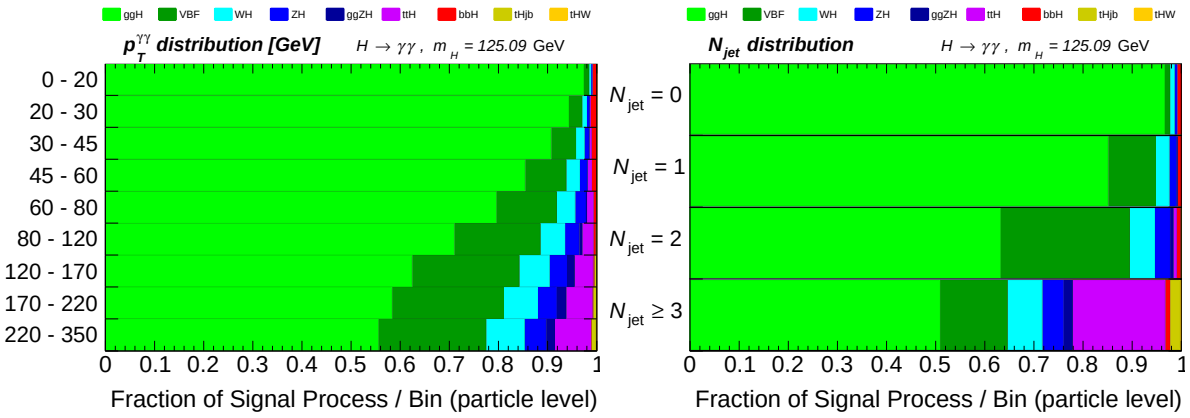

Figure 6.25: Expected production process fractions in bins of $p_{\mathrm{T}}^{\gamma\gamma}$ and N_{jet} at particle level.

natures of VBF production. Cut values were tuned to achieve a high VBF purity whilst maintaining at least a 1.5 σ expected statistical sensitivity in Run 1.

$N_{\mathrm{lepton}} \geq 1$ contains all *diphoton fiducial* events for which an electron or muon was also selected. This is the simplest region which probes Higgs production in association with charged leptons, which is dominated by the VH and ttH processes in the SM.

High $E_{\mathrm{T}}^{\mathrm{miss}}$ contains all *diphoton fiducial* events with $E_{\mathrm{T}}^{\mathrm{miss}} > 80$ GeV and $p_{\mathrm{T}}^{\gamma\gamma} > 80$ GeV. This fiducial region probes Higgs production in association with undetectable particles such as neutrinos or dark matter candidates. The cut value was chosen to achieve an expected statistical sensitivity of 2 σ.

ttH enhanced contains all *diphoton fiducial* events with (i) three selected jets and a selected electron or muon or (ii) four selected jets. In both cases at least one jet must pass the b-hadron identification. This selection was chosen heuristically based on knowledge of the characteristic signatures of ttH production. Additional kinematic constraints are not applied due to the already low expected statistical sensitivity as described in section 6.3.4.

6.5.2 Particle level isolation

The fiducial region definition is designed to balance minimal model dependence (by matching the detector level selection criteria) with computability. It is desirable that fiducial selections be simple and easily implementable in theory predictions without large uncertainties. A fixed-cone photon isolation is not an infrared and collinear (IRC) safe observable because it is sensitive to the small-angle splitting of particles which may cause energy to migrate across the cone boundary [59, 248].

Figure 6.26 shows the correction factor in the *diphoton fiducial* region evaluated independently for the various production processes. Black points show the case when no particle level isolation requirement is imposed. The WH, ZH and ttH correction factors are lower than that of ggF because the event topologies include final state objects which may overlap with the photons causing them to fail the isolation requirement and so reducing the detector level acceptance. Green points show the case when a particle level isolation requirement is applied. In this case, high multiplicity environments have similarly reduced acceptance at both particle and detector level. The numerator and denominator of Eq. 6.32 are therefore reduced by similar factors and the correction factor is less dependent on production process.

The total correction factor in each bin is calculated by combining all production processes. Use of a particle level isolation cut therefore reduces the model dependence from assuming that only SM-like production processes occur, with the fractions shown in Figures 6.24 - 6.25. This section describes how the particle level isolation selection described in section 6.5.1 was determined and presents studies of alternative methods.

Isolation studies (2015)

The particle level isolation cut is designed to mimick the detector level behaviour. Figure 6.27 shows the probability that a signal event will fail the isolation criteria at detector level, with all other cuts already having been applied, as a function of μ. Events which fail due to track isolation are shown in green, calorimeter isolation in blue and both in purple. Red points show all failing events and make up approximately $3-6$ % in ggF. The track isolation cut rejects $2-3$ % of events and is approximately flat as a function of μ. It dominates at $\mu \lesssim 15$. The calorimeter isolation cut efficiency is strongly μ-dependent

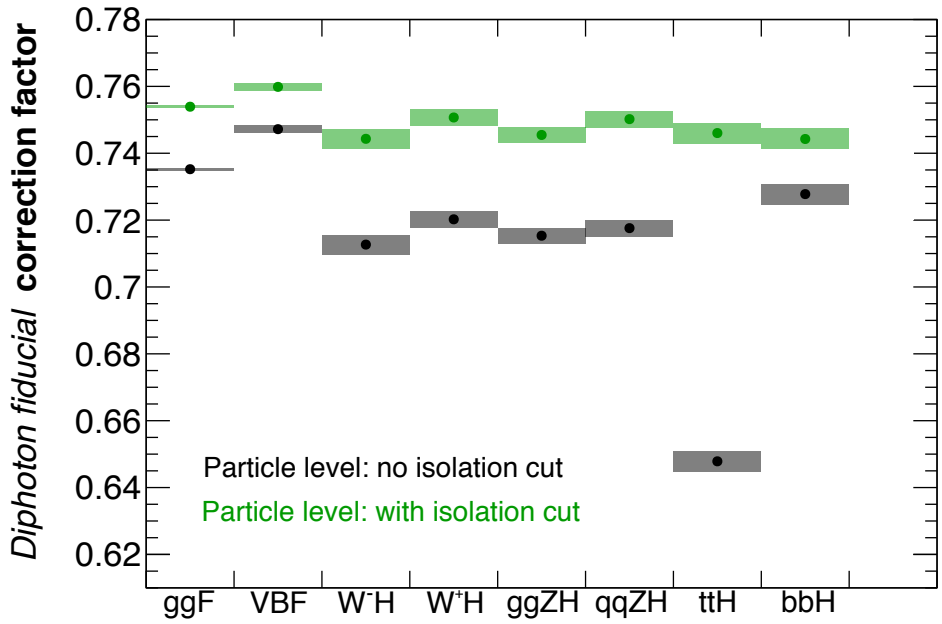

Figure 6.26: Production mode dependence of the *diphoton fiducial* correction factor.

and dominates at $\mu \gtrsim 25$. Approximately $7-9$ % of events are cut in ttH. This is higher because several jets are produced by the hard scatter process. This reduces the relative importance of the pileup dependence, although this is still visible. Pileup is not considered at particle level and so the isolation cut is expected to be comparable with the low-μ behaviour at detector level. This is dominated by track isolation.

As well as the particle level charged particle isolation defined in Eq. 6.33, several other working points were studied. The particle level calorimeter isolation, $E_{\text{iso}}^{\text{ptcl,calo}}$, is defined as the E_{T} component of the four-vector sum of all particles except for muons and neutrinos in a cone of $\Delta R < 0.2$ around the photon. Figure 6.28 shows the comparison between each particle level isolation and its detector level counterpart. These plots combine all signal MC samples and are filled for both leading and subleading photons. Black points show the median detector level isolation in each bin of particle level isolation. Uncertainties are defined as the RMS of 2000 bootstraps. The tails of the distributions are fit with a linear parameterisation as shown in red. This is used to equate the detector level quantity with the particle level one. The same treatment is applied using an alternative particle level calorimeter isolation definition, $E_{\text{iso}}^{\text{ptcl,calo,corr}}$, which uses an ambient energy subtraction analagous to that applied at detector level to remove underlying event and pileup contributions. The particle level equivalent accounts only for underlying event. Using this treatment, the three particle level isolation criteria are

$$\begin{aligned} E_{\text{iso}}^{\text{ptcl,trk}} &< 0.050 \cdot p_{\text{T}}^{\gamma} \\ E_{\text{iso}}^{\text{ptcl,calo}} &< 0.085 \cdot p_{\text{T}}^{\gamma} + 4.0 \text{ GeV} \\ E_{\text{iso}}^{\text{ptcl,calo,corr}} &< 0.090 \cdot p_{\text{T}}^{\gamma} + 3.4 \text{ GeV} \ . \end{aligned} \tag{6.34}$$

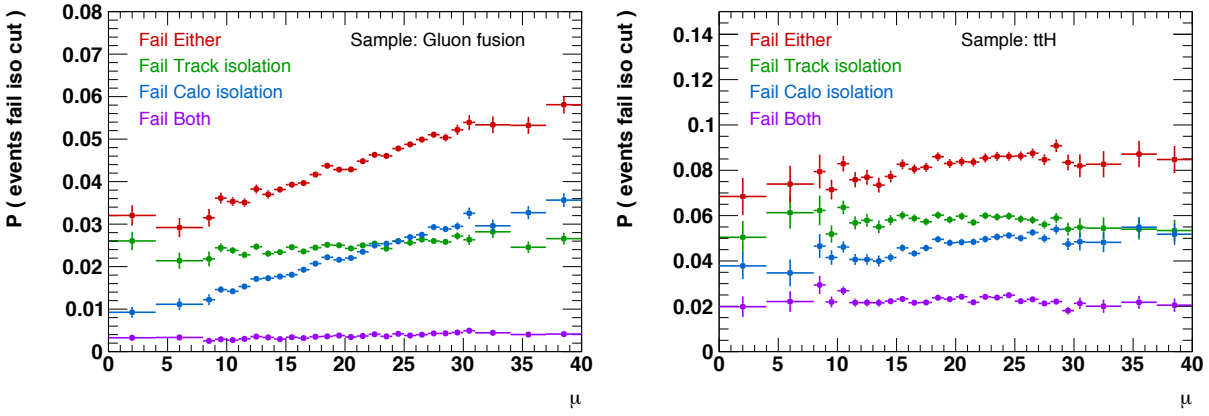

(a) ggF (b) ttH

Figure 6.27: Relative efficiency of track and calorimeter isolation cuts.

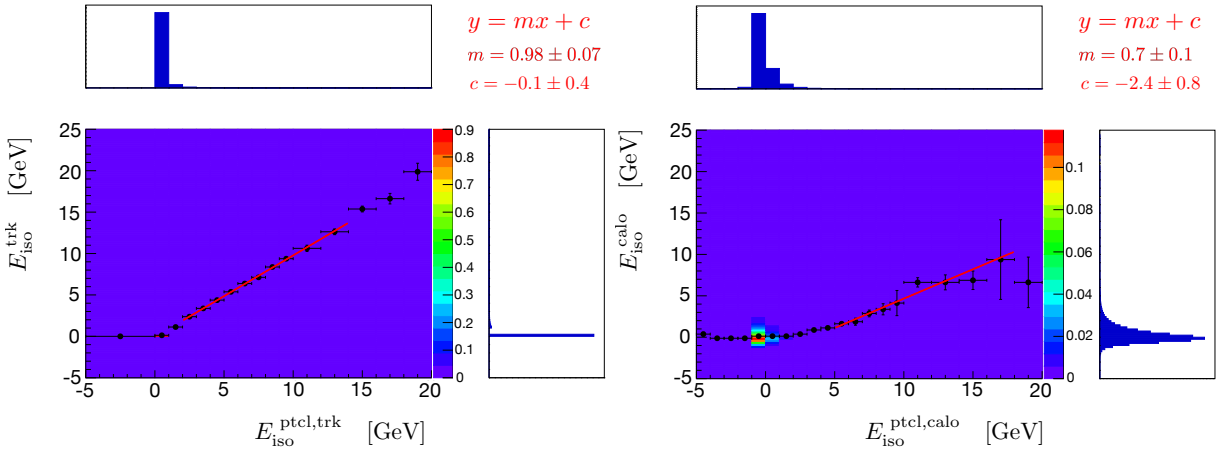

(a) Track isolation (b) Calorimeter isolation

Figure 6.28: Response in the tails of isolation distributions.

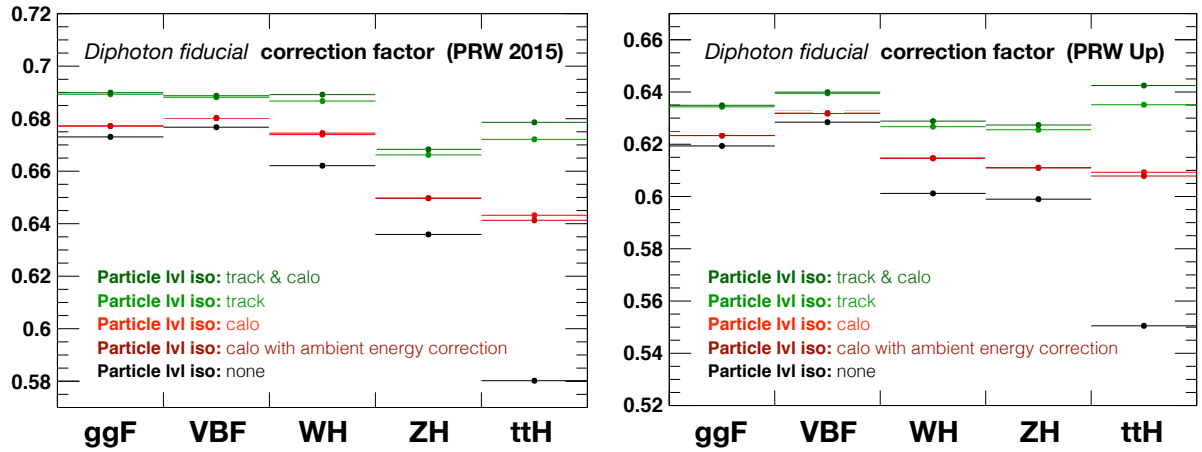

(a) PRW 2015 scenario (b) PRW Up scenario

Figure 6.29: Production process dependence of the correction factor in the *diphoton fiducial* region using various particle level isolation criteria.

Figure 6.28(a) shows that the track isolation response is consistent with $E_{\text{iso}}^{\text{trk}} = E_{\text{iso}}^{\text{ptcl,trk}}$ and so the particle level cut is identical to that applied at detector level.

Figure 6.29 shows the production process dependence achieved using these particle level isolation criteria. Two pileup scenarios are compared. PRW 2015 labels the pileup profile of 2015 with $\langle\mu\rangle = 14$ whilst PRW Up labels an arbitrary profile with $25 \lesssim \langle\mu\rangle \lesssim 30$. All working points perform better than the no-isolation case. The $E_{\text{iso}}^{\text{ptcl,trk}}$ working point is the most model independent as shown in light green. A fifth case applies both charged particle and calorimeter isolation working points as shown in dark green. This does not lead to a significant improvement and is not chosen in preference to the simpler charged particle case.

Studies of jet veto alternative

A possible alternative to particle level isolation was studied. An event is vetoed if a high-energy jet is reconstructed near to one of the two photons. High energy jets can be defined as IRC safe objects and so are expected to be less susceptible to the modelling of low-energy objects compared with a fixed-cone isolation energy. They are reconstructed using the anti-k_{T} algorithm with a radius parameter of $r = 0.2$ from all final state particles excluding neutrinos and the photons originating from the Higgs decay and required to satisfy $p_{\text{T}} > 30$ GeV.

Figure 6.30(a) shows the ΔR between the leading truth photon and the nearest such jet in ttH MC. Truth photons are matched to those at detector level using a requirement of $\Delta R < 0.4$. Photons are shown in red if their detector level counterpart failed its isolation cut or blue if it passed. The black distribution shows photons with no counterpart at detector level. Figure 6.30(b) shows the acceptance as a function of the ΔR^{min} cut value. Some discriminating power is observed.

Figure 6.30(c) shows the production process dependence of the correction factor in the *diphoton fiducial* region using the particle level jet veto method (red) at a cut value of 0.3. This is compared with the particle level isolation (green) and no-cut (black) cases. The jet veto and isolation methods achieve similar production process independence. The jet veto method is therefore a viable alternative. Currently it is not used because (i) it does not improve the model independence and (ii) no jet veto is performed at detector level and the selections are desired to be similar where possible. In the future a jet veto may be applied at both detector level and particle level, removing the need for a particle level fixed-cone isolation cut. A further consideration is that the calculation of the cross section into a region defined with a jet veto can suffer from logarithmic divergences which reduce the rate at which the perturbation series converges (see e.g. [249]). The systematic impact of such an effect remains to be studied.

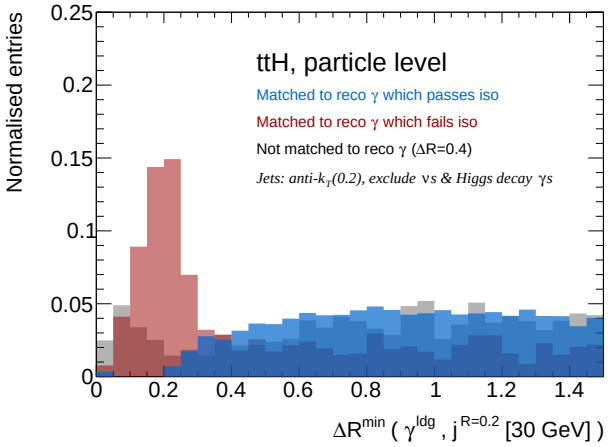

(a) $\Delta R\,(\gamma, j)$ in ttH

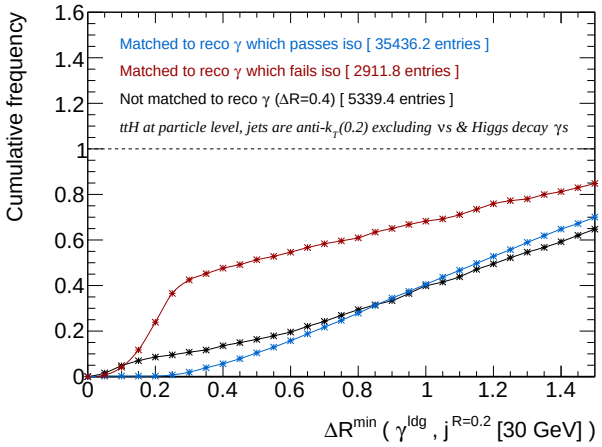

(b) Cut efficiency in ttH

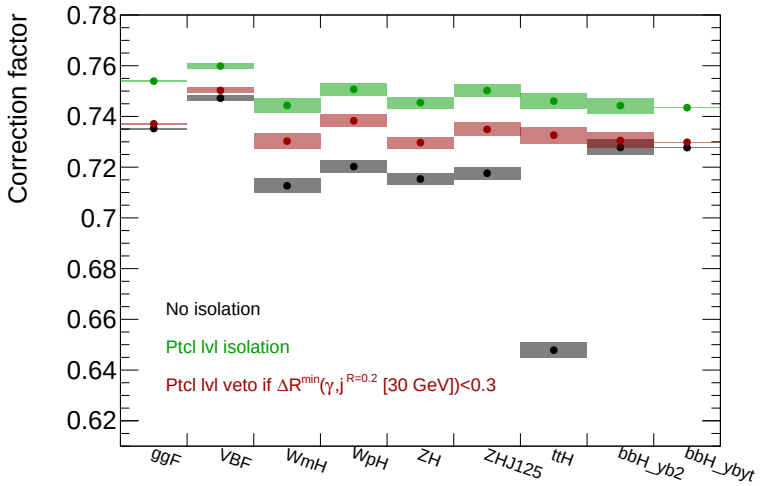

(c) Production process dependence of the *diphoton fiducial* correction factor

Figure 6.30: Study of a particle level jet veto as an alternative to photon isolation.

6.5.3 Model dependence: signal composition

A systematic uncertainty is assigned to cover possible variations in the relative fractions of different production processes. First, the *nominal* systematic uncertainty is defined. This was used for the published analysis and is applied to the results presented in the remainder of this chapter. It was subsequently found that this systematic uncertainty is likely conservative. This does not have a significant impact on the current measurement because all bins are dominated by statistical uncertainties. An *alternative* method is also presented. This will be used in chapter 7 when measuring differential cross sections using the combination of decay channels. Finally, a study into production process dependence within the N_{jet} distribution is shown.

Nominal uncertainty

This strategy was designed by another member of the analysis team. The *nominal* systematic uncertainty is calculated as follows. The ratios $\vec{s}$ between the $\{\text{VBF}, \text{WH}, \text{ZH}, \text{ttH}\}$ and ggF cross sections were measured to be

$$\frac{\vec{s}}{\vec{s}^{\,\text{SM}}} = \begin{bmatrix} (\text{VBF/ggF}) \;/\; (\text{VBF/ggF})^{\text{SM}} \\ (\text{WH/ggF}) \;/\; (\text{WH/ggF})^{\text{SM}} \\ (\text{ZH/ggF}) \;/\; (\text{ZH/ggF})^{\text{SM}} \\ (\text{ttH/ggF}) \;/\; (\text{ttH/ggF})^{\text{SM}} \end{bmatrix} = \begin{bmatrix} 1.33 \\ 0.84 \\ 3.06 \\ 3.28 \end{bmatrix} \tag{6.35}$$

using combined ATLAS and CMS data in Run 1 [109], where $\vec{s}^{\,\text{SM}}$ is the SM expectation. The eigenvectors of the four-dimensional covariance matrix define the major and minor axes of a hyper-ellipse describing the measurement uncertainties. The eigenvalues represent 1σ uncertainty amplitudes in these directions. These are used to derive $\pm 1\sigma$ shifted variations as

$$\begin{aligned} \frac{\vec{s}_i^{\,+1\sigma}}{\vec{s}^{\,\text{SM}}} &= \begin{bmatrix} 1.21 \\ 1.04 \\ 1.49 \\ 3.16 \end{bmatrix}, \begin{bmatrix} 1.66 \\ 1.21 \\ 2.82 \\ 3.42 \end{bmatrix}, \begin{bmatrix} 1.21 \\ 1.43 \\ 2.42 \\ 3.28 \end{bmatrix}, \begin{bmatrix} 1.33 \\ 0.84 \\ 3.05 \\ 4.24 \end{bmatrix} \\ \frac{\vec{s}_i^{\,-1\sigma}}{\vec{s}^{\,\text{SM}}} &= \begin{bmatrix} 1.45 \\ 0.64 \\ 4.62 \\ 3.41 \end{bmatrix}, \begin{bmatrix} 1.00 \\ 0.47 \\ 3.29 \\ 3.15 \end{bmatrix}, \begin{bmatrix} 1.45 \\ 1.24 \\ 2.69 \\ 3.29 \end{bmatrix}, \begin{bmatrix} 1.33 \\ 0.84 \\ 3.06 \\ 2.33 \end{bmatrix} \end{aligned} \tag{6.36}$$

with $i = 1, ..., 4$.

The systematic uncertainty is defined by evaluating the change in correction factor when these factors are used to reweight the production process cross sections. The four changes are combined in quadrature separately in the positive and negative directions. The largest of the two directions is taken as a symmetric uncertainty. This is conservative because the four shifts are orthogonal with respect to $\vec{s}/\vec{s}^{\,\text{SM}}$ rather than the values of $\{1, 1, 1, 1\}$ used to derive the nominal correction factors. The difference between $\vec{s}$ and $\vec{s}^{\,\text{SM}}$ is therefore quadruple counted in the quadrature combination.

Table 6.9 shows the correction factor uncertainties in fiducial regions and bins of 1-dimensional differential distributions. Diphoton observables have an estimated uncertainty of < 1 % in all bins and are not shown. Other than the *high* E_T^{miss} region which has low statistical sensitivity, the largest uncertainty (16 %) is observed in the $N_{\text{jet}} \geq 3$ bin. This is much smaller than the statistical uncertainty in this bin (31 %).

Distribution	Signal composition modelling uncertainty [%]							
	Bin 1	2	3	4	5	6	7	8
Diphoton fiducial	0.1							
VBF enhanced	0.1	4.5						
$N_{\text{lepton}} \geq 1$	0.3	4.0						
High $E_{\text{T}}^{\text{miss}}$	0.2	25						
ttH enhanced	0.6	8.1						
N_{jet} (30 GeV)	0.1	1.5	4.2	16				
N_{jet} (50 GeV)	0.2	0.9	3.5					
p_{T}^{j1}	0.1	2.3	1.7	1.2	1.4	2.9		
$\lvert y_{j1} \rvert$	0.1	1.1	1.8	2.2	1.3	1.1	2.3	4.4
H_{T}	0.1	1.8	2.6	2.7	5.1	3.1		
$\sum_j \tau_j$	0.1	1.3	0.8	1.6	2.2	3.7	2.8	
τ_{j1}	0.1	1.4	1.6	1.4	1.8	1.4		
p_{T}^{j2}	0.1	1.5	5.8	3.4	2.0			
$\lvert y_{j2} \rvert$	0.2	4.8	4.6	6.7				
m_{jj}	0.2	7.2	6.2	4.9	2.5			
$p_{\text{T}}^{\gamma\gamma jj}$	0.2	3.3	8.6	3.3				
$\lvert \Delta y_{jj} \rvert$	0.2	7.9	3.9	5.6				
$\lvert \Delta\phi(\gamma\gamma, jj) \rvert$	0.2	11	1.2	2.6				
$\lvert \Delta\phi_{jj} \rvert$	0.2	5.0	6.3	7.5				
$\Delta\phi_{jj}$	0.2	7.0	5.6	5.4	7.2			

Table 6.9: Signal composition modelling uncertainties on the correction factors using the *nominal* method.

Distribution	Signal composition modelling uncertainty [%]								
	Bin 1	2	3	4	5	6	7	8	9
Diphoton fiducial	< 0.1								
VBF enhanced	< 0.1	$^{+1.8}_{-2.1}$							
$N_{\text{lepton}} \geq 1$	< 0.1	$^{+1.4}_{-1.2}$							
High $E_{\text{T}}^{\text{miss}}$	< 0.1	$^{+6.6}_{-7.1}$							
ttH enhanced	< 0.1	$^{+2.1}_{-2.3}$							
$p_{\text{T}}^{\gamma\gamma}$	< 0.1	< 0.1	< 0.1	< 0.1	< 0.1	± 0.1	± 0.1	± 0.1	± 0.1
$\lvert y^{\gamma\gamma} \rvert$	< 0.1	< 0.1	< 0.1	< 0.1	< 0.1	< 0.1	< 0.1	< 0.1	< 0.1
N_{jet} (30 GeV)	< 0.1	$^{+0.4}_{-0.3}$	± 1.0	$^{+2.5}_{-1.8}$					
p_{T}^{j1}	< 0.1	± 0.5	± 0.3	$^{+0.2}_{-0.1}$	$^{+0.2}_{-0.1}$				

Table 6.10: Signal composition modelling uncertainties on the correction factors using the *alternative* method.

Alternative uncertainty

The *alternative* systematic uncertainty is calculated as follows. Six separate variations are defined. Each production mechanism is varied individually by a factor commensurate with the uncertainties on the signal strengths measured in Run 1 [109] with the exception of ttH for which the Run 2 constraint is used [250]. The ggF, VBF, WH, ZH, ttH and bbH cross sections are varied by ± 14.5 %, ± 20.3 %, ± 43.3 %, ± 46.8 %, $^{+50}_{-30}$ % and ± 22 % respectively. The resulting changes in correction factor are combined in quadrature.

Table 6.10 shows the correction factor uncertainties in fiducial regions and the bins of several differential distributions. It is estimated to be less than ± 0.1 % in the *diphoton fiducial* region and ≤ 0.1 % in all bins of $p_{\mathrm{T}}^{\gamma\gamma}$ and $|y^{\gamma\gamma}|$. The impact on the $N_{\mathrm{jet}} \geq 3$ bin is estimated to be $^{+2.5}_{-1.8}$ %.

Study of the $N_{\mathbf{jet}}$ distribution

The minimum jet transverse momentum is taken as 30 GeV throughout this discussion. It was observed that the signal composition uncertainty increased as a function of N_{jet} using both the *nominal* and *alternative* definitions. Figure 6.31 shows the production process dependence of the correction factors in the four separate bins. The correction factor of ttH is estimated to be 17 %, 26 % and 31 % lower than ggF in the $N_{\mathrm{jet}} = 1$, $N_{\mathrm{jet}} = 2$ and $N_{\mathrm{jet}} \geq 3$ bins respectively.

The correction factor can be written as

$$C_i = \sum_j M_{ij} \left(\frac{n_j}{n_i} \right)^{\textbf{fid, exp}} p_j^{\ \textbf{fid}} \tag{6.37}$$

where $n_j^{\mathrm{fid,\ exp}}$ is the expected yield in particle level bin j, p_j^{fid} is the probability that an event is reconstructed and M_{ij} is the probability that it is measured in detector level bin i. A small contribution from out-of-fiducial events migrating into the measured region has been neglected as it has no impact on the discussion. This will be considered in a later section. Figure 6.32 shows each of the three quantities in ggF and ttH events.

Migrations are expected to be driven by jet energy measurement uncertainties and contributions from pileup. Figure 6.32(a) shows that ggF is roughly symmetric meaning that events may migrate to both higher and lower jet multiplicities. ttH has a higher occupancy below the diagonal showing that events are more likely to migrate to higher jet multiplicities. Figure 6.32(b) shows that ggF events follow a falling spectrum from $N_{\mathrm{jet}} = 0$ whereas ttH events are most commonly in the $N_{\mathrm{jet}} \geq 3$ bin. Figure 6.32(c) shows the probability that a fiducial event is reconstructed. This also demonstrates a modest process dependence. Correction factor signal composition dependence is caused by the combination of these three quantities.

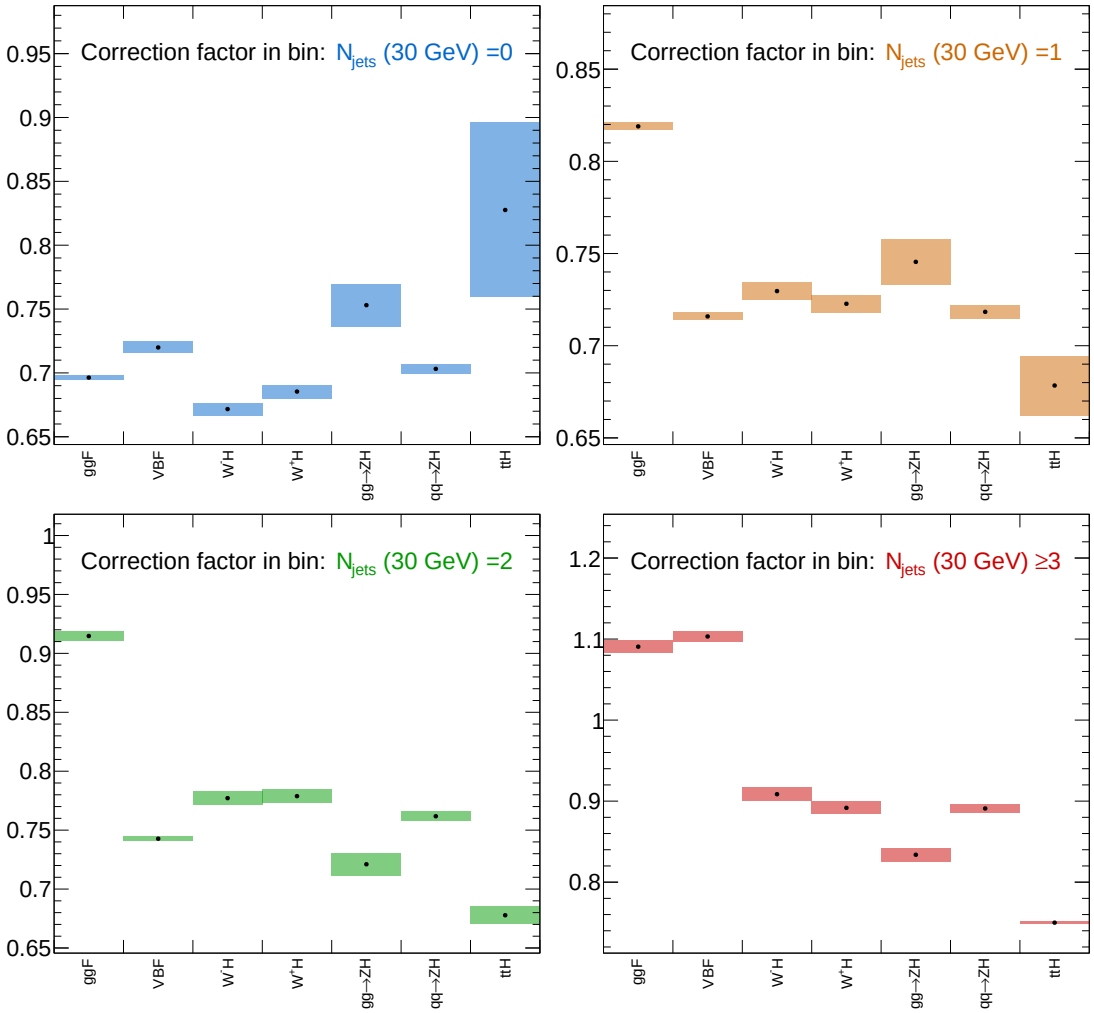

Figure 6.31: Correction factor production process dependence in bins of N_{jet}.

The conclusions of this study are as follows. The correction factor production process dependence is observed to increase in high jet multiplicity bins (Figure 6.31). This is because of differing migrations and underlying spectra in ggF and ttH (Figure 6.32). This is not a problem in the current analysis because the effect is covered by a conservative signal composition uncertainty, which still remains small compared with the statistical uncertainties. Future analyses may target smaller migrations to reduce the systematic uncertainty as the statistical precision is improved by increased dataset size. It is noted that regularised unfolding methods would also be affected by production mode variations because the migration matrices in Figure 6.32(a) differ between ggF and ttH. For completeness, Figure 6.33 shows the migration matrix combining all production processes. All measured events have at least a 73 % probability of being reconstructed in the correct bin.

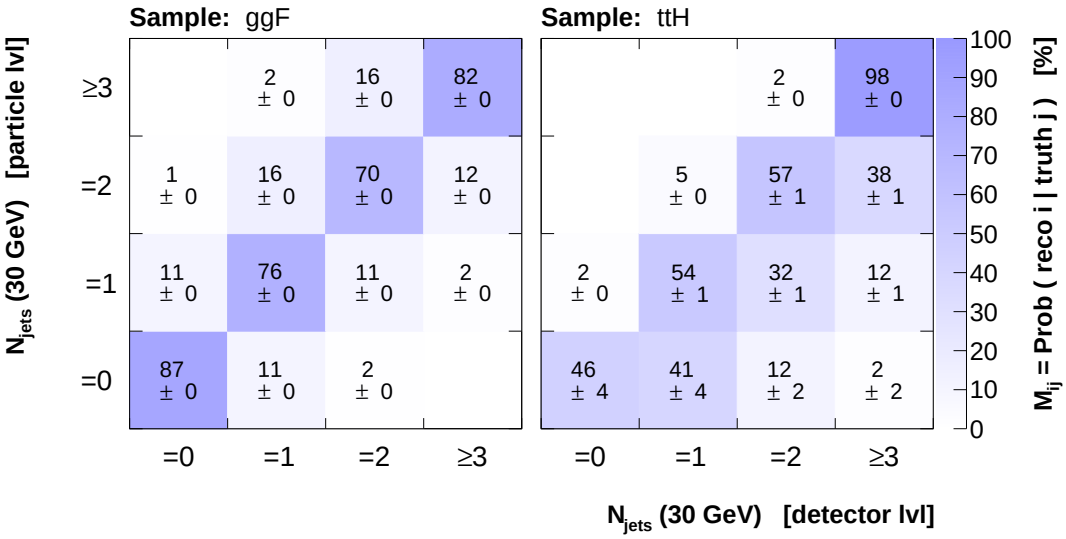

(a) M_{ij} = Prob (reco bin i|truth bin j)

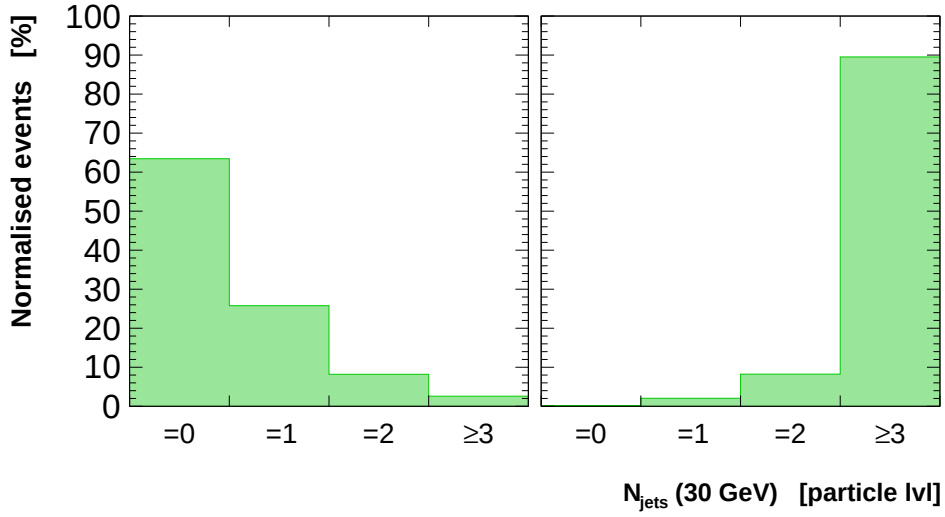

(b) $n_j^{\text{fid, exp}}$ in truth bin j

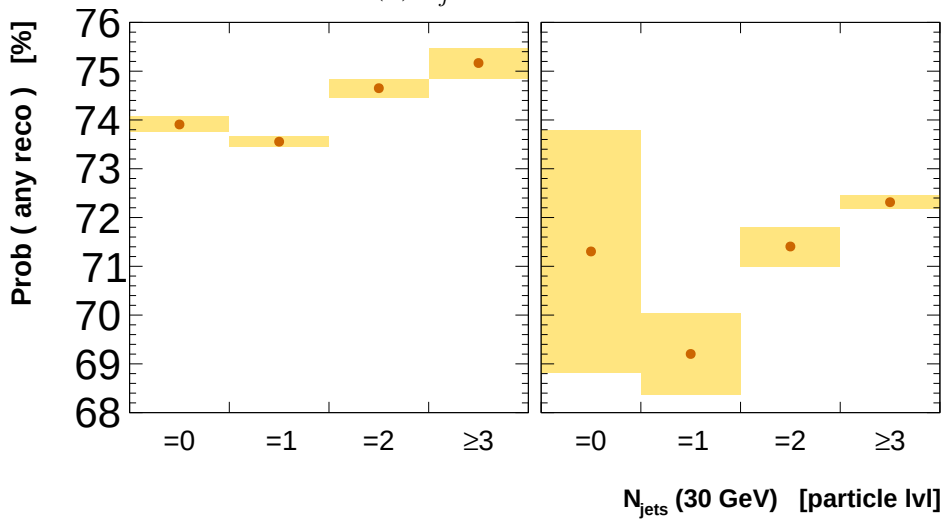

(c) p_j^{fid} = Prob (reco|truth bin j)

Figure 6.32: N_{jet} migrations, spectra and reconstruction efficiency in ggF and ttH.

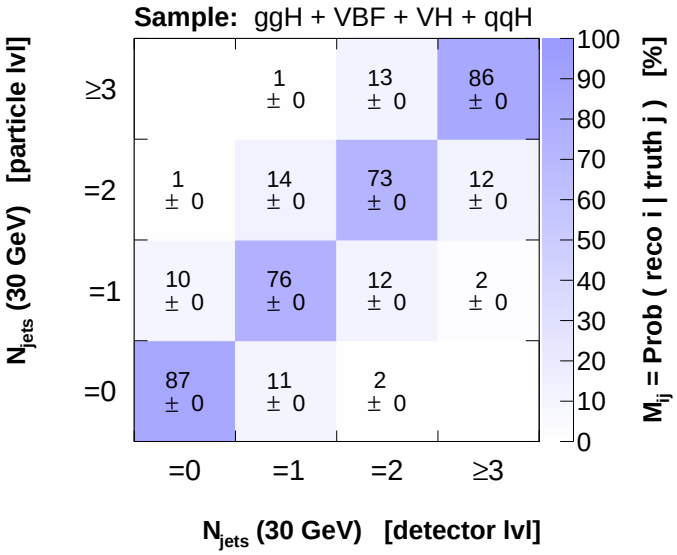

Figure 6.33: Prob (reco bin i|truth bin j) in the N_{jet} distribution combining all production processes.

6.5.4 Model dependence: pileup jets

A systematic uncertainty is assigned to the modelling of pileup jets. This is done by studying the JVT of jets in data and MC. Only jets with $p_{\text{T}} > 30$ GeV and $|y| < 2.4$ are considered as JVT cannot be calculated outside of this range.

The jet JVT distribution is validated by comparing ggF and $\gamma\gamma$ simulated events with those selected in 2015 data sideband events. The jet p_{T} and $|y|$ distributions are also validated separately at high, medium and low JVT. Figure 6.34 shows the probability that a reconstructed jet is matched with a truth-level counterpart within $\Delta R < 0.4$ in bins of JVT score. A score of ≤ 0 is shown to represent a relatively pure sample of pileup jets. Truth jets are required to satisfy $p_{\text{T}} > 15$ GeV to reduce finite resolution effects.

Figure 6.35 shows the probability that a jet will have $JVT \leq 0$ as a function of the number of reconstructed primary vertices, N_{PV}. Both MC samples are compared with the 2015 data sidebands. Data events are shown to contain approximately 20 % fewer low-JVT jets than were simulated in the ggF sample. The data and background $\gamma\gamma$ sample are in closer agreement. A 20 % uncertainty on the number of simulated pileup jets is used as a conservative estimate. Table 6.11 shows the impact on the correction factor when 20 % of all non-truth-matched reconstructed jets are discarded at random. This is taken as a symmetric systematic uncertainty. Only observables defined using jets are affected. The largest change of -5.6 % is observed in the $N_{\text{jet}} \geq 3$ bin. Conservative values of $4.9 - 6.0$ % are assumed in bins of $|\Delta y_{jj}|$, not shown.

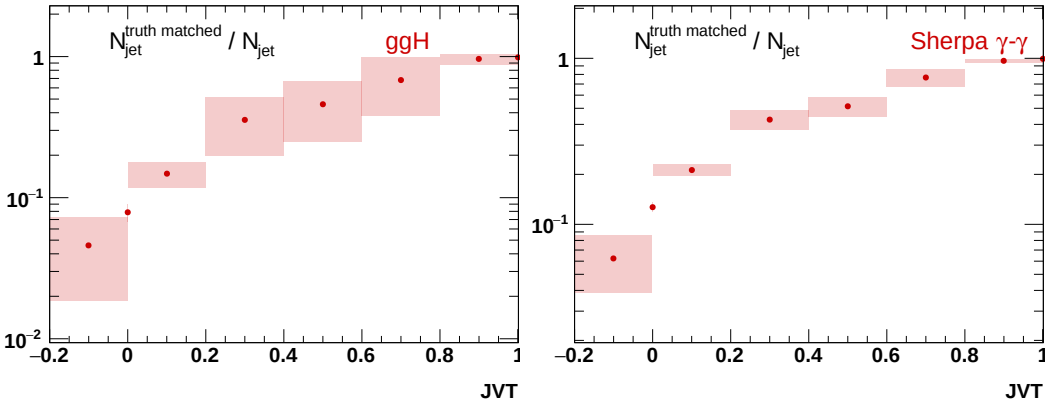

Figure 6.34: Probability that a jet is truth matched as a function of JVT.

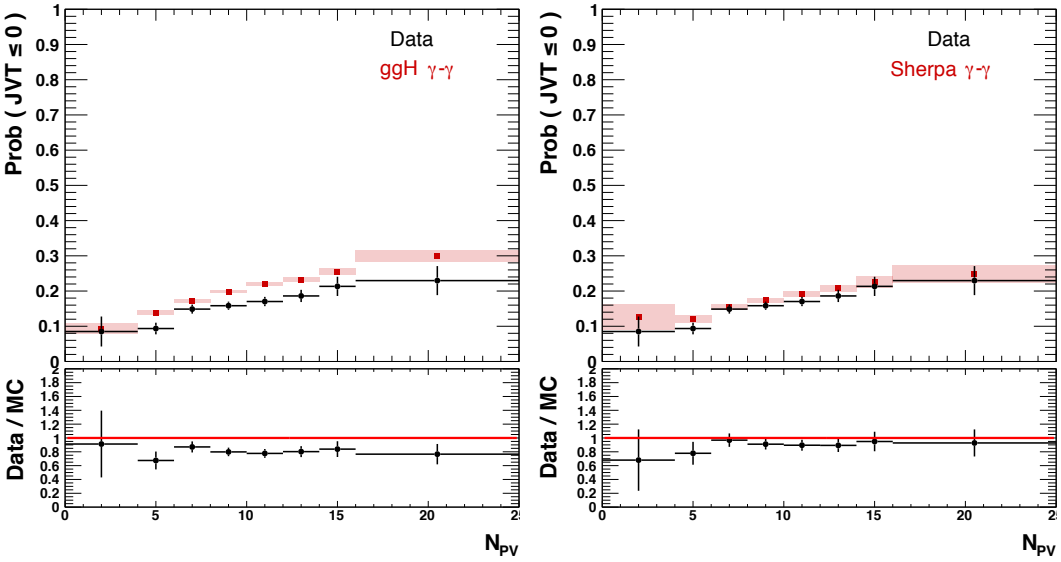

Figure 6.35: Probability that a jet has JVT ≤ 0 as a function of N_{PV}.

Distribution	Pileup modelling uncertainty [%]							
	Bin 1	2	3	4	5	6	7	8
VBF enhanced	0.1	−2.8						
ttH enhanced	0.1	−4.4						
N_{jet} (30 GeV)	1.4	−0.3	−2.4	−5.6				
N_{jet} (50 GeV)	0.2	−0.1	−1.4					
p_{T}^{j1}	1.4	−2.7	−0.6	−0.4	−0.1	0.0		
$\lvert y_{j1} \rvert$	1.4	−0.1	−0.1	−1.4	−0.1	0.0	−1.5	−3.6
H_{T}	1.4	−1.4	−1.7	−1.7	−1.4	−2.0		
$\sum_j \tau_j$	0.4	−1.1	−0.7	−1.2	−0.6	−0.7	−0.6	
τ_{j1}	1.4	−2.6	−1.3	−0.7	−0.7	−0.2		
p_{T}^{j2}	1.4	−0.3	−4.0	−1.1	−0.5			
$\lvert y_{j2} \rvert$	0.8	−2.2	−1.6	−5.5				
m_{jj}	0.8	−4.1	−3.0	−2.4	−1.8			
$p_{\mathrm{T}}^{\gamma\gamma jj}$	0.8	−1.8	−3.9	0.3				
$\lvert \Delta\phi(\gamma\gamma, jj) \rvert$	0.8	−4.7	−1.1	−1.6				
$\lvert \Delta\phi_{jj} \rvert$	0.8	−2.8	−2.5	−4.6				
$\Delta\phi_{jj}$	0.8	−4.8	−3.0	−2.2	−3.4			

Table 6.11: Correction factor uncertainties due to pileup jet modelling.

6.5.5 Model dependence: Higgs kinematic modelling

The correction factor dependence on the kinematic modelling of the Higgs is investigated by reweighting simulated events to an allowed kinematic spectrum which differs from that used to derive the correction factors. Figure 6.36 (left) compares the $p_{\mathrm{T}}^{\gamma\gamma}$ and $|y_{\gamma\gamma}|$ spectra of the original MC events (blue) with the unfolded data (black points). An additional spectrum is constructed heuristically and shown in orange. It is designed to significantly deviate from the original MC spectrum whilst still being compatible with the data. This spectrum must still respect the physical constraints of the distribution. Specifically, the $p_{\mathrm{T}}^{\gamma\gamma}$ spectrum must tend towards 0 at very small and large values and the $|y_{\gamma\gamma}|$ must tend towards 0 at $|y_{\gamma\gamma}| = 2.5$. Figure 6.36 (right) shows the function used to reweight simulated events to this spectrum. The function is intentionally extreme in the $p_{\mathrm{T}}^{\gamma\gamma}$ distribution by applying weights of up to 200 %. The shape of the simulated $|y_{\gamma\gamma}|$ spectrum is observed to be consistent with data so that a constant reweighting factor is most appropriate. This causes no change in the correction factors and so does not contribute to the systematic uncertainty.

Table 6.12 shows the impact of the $p_{\mathrm{T}}^{\gamma\gamma}$ reweighting on the correction factors in several fiducial regions and 1-dimensional differential bins. These numbers were derived by another member of the analysis team. All observables are affected due to their correlation with $p_{\mathrm{T}}^{\gamma\gamma}$. Observables with at least one jet typically suffer from the largest uncertainties due to their correlation with the tail of the $p_{\mathrm{T}}^{\gamma\gamma}$ distribution. These observables cannot be reweighted to their own observed spectra due to the limited statistical precision of data. The largest estimated uncertainty is 4.5 %. A cross check is performed by reweighting to the $p_{\mathrm{T}}^{\gamma\gamma}$ and $|y_{\gamma\gamma}|$ spectra measured in the $H \to ZZ^* \to 4l$ channel. This confirms that the estimated systematic uncertainty is significantly smaller than the statistical uncertainty.

6.5.6 Correction factors

Table 6.13 shows the correction factors calculated in several fiducial regions and differential bins. The production process dependence is also shown. The ggF and VBF correction factors are divergent in the $N_{\mathrm{lepton}} \geq 1$ and $E_{\mathrm{T}}^{\mathrm{miss}}$ regions because charged leptons and neutrinos are not present in these topologies at particle level. However, these processes still impact the total correction factor due to their contribution to the detector level event yield. Note that object scale factors, designed to match MC selection efficiencies with those measured in data, are applied at detector level but not at particle level.

The correction for detector effects includes a fractional subtraction of non-fiducial events. It is found that the `Pythia8` modelling includes so-called Dalitz decays of the form $H \to \gamma\gamma^* \to \gamma f\bar{f}$. An estimated factor $f_{\mathrm{Dalitz}}^{\text{non-fid}}$ of all measured events are Dalitz decays. A factor $f_{\mathrm{other}}^{\text{non-fid}}$ represents the fraction of all remaining measured events which are of non-fiducial origin. The subtraction of non-fiducial events is equivalent to multiplying

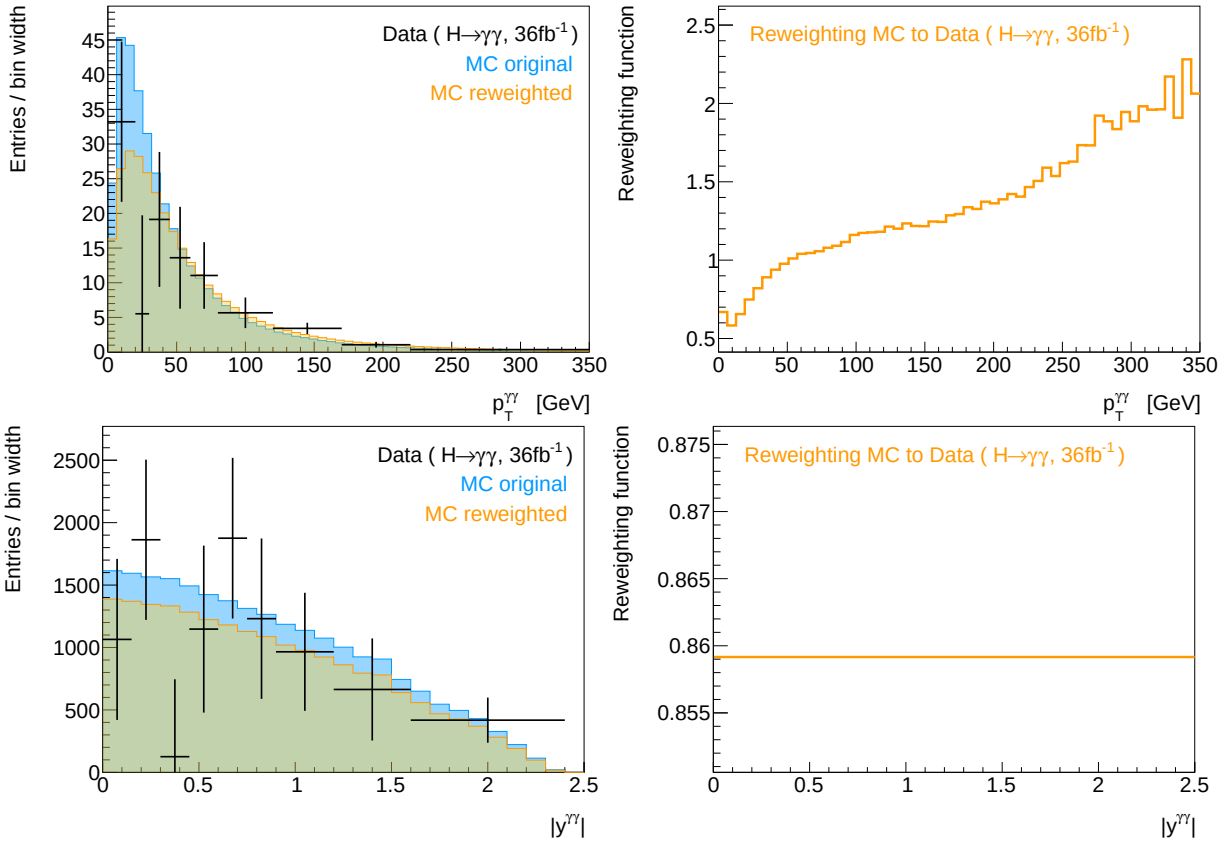

Figure 6.36: MC reweighted to observed $p_{\mathrm{T}}^{\gamma\gamma}$ and $|y_{\gamma\gamma}|$ spectra.

Distribution	$p_{\mathrm{T}}^{\gamma\gamma}$ reweighting modelling uncertainty [%]							
	Bin 1	2	3	4	5	6	7	8
Diphoton fiducial	−0.1							
VBF enhanced	0.1	0.9						
ttH enhanced	−0.1	−0.7						
N_{jet} (30 GeV)	−0.1	3.9	2.4	2.3				
N_{jet} (50 GeV)	0.1	1.1	0.5					
p_{T}^{j1}	−0.1	4.3	1.7	0.8	0.0	−0.4		
$\lvert y_{j1}\rvert$	−0.1	1.1	1.5	2.1	1.6	1.0	3.1	6.1
H_{T}	−0.1	4.5	2.1	1.3	0.8	−0.4		
$\sum_j \tau_j$	−0.1	2.5	1.3	1.0	0.6	0.1	−0.6	
τ_{j1}	0.0	2.0	0.8	0.8	0.0	0.0		
p_{T}^{j2}	−0.1	3.9	2.3	0.4	−0.1			
$\lvert y_{j2}\rvert$	0.5	1.1	1.3	3.3				
m_{jj}	0.5	2.9	1.4	1.4	1.1			
$p_{\mathrm{T}}^{\gamma\gamma jj}$	0.5	1.5	2.8	−0.6				
$\lvert\Delta y_{jj}\rvert$	0.5	2.5	1.5	2.0				
$\lvert\Delta\phi(\gamma\gamma, jj)\rvert$	0.5	2.5	−0.4	−0.4				
$\lvert\Delta\phi_{jj}\rvert$	0.5	2.8	2.3	1.6				
$\Delta\phi_{jj}$	0.5	1.7	2.8	2.7	1.7			

Table 6.12: Correction factor uncertainties due to modelling of $p_{\mathrm{T}}^{\gamma\gamma}$.

Region or bin		Correction factor, C_i									$f_{\text{Dalitz}}^{\text{non-fid}}$	$f_{\text{other}}^{\text{non-fid}}$
		ggF	VBF	W^-H	W^+H	ggZH	qqZH	ttH	bbH	**Total**		
Diphoton fiducial		0.75	0.76	0.75	0.75	0.77	0.75	0.74	0.74	**0.75**	0.4 %	1.6 %
VBF enhanced		1.08	0.77	1.17	1.20	0.83	1.20	0.79	–	**0.88**	0.4 %	1.6 %
$N_{\text{lepton}} \geq 1$		–	–	0.61	0.61	0.70	0.68	0.58	–	**0.62**	0.4 %	1.8 %
High $E_{\text{T}}^{\text{miss}}$		–	–	0.83	0.82	0.79	0.78	0.87	–	**1.07**	0.4 %	1.8 %
ttH enhanced		0.96	1.08	1.41	1.22	0.89	0.90	0.61	–	**0.66**	0.4 %	1.8 %
$p_{\text{T}}^{\gamma\gamma}$	$[0, 20]$ GeV	0.76	0.76	0.75	0.76	0.75	0.75	0.72	0.76	**0.76**	0.4 %	1.7 %
	$[20, 30]$ GeV	0.75	0.75	0.76	0.74	0.76	0.74	0.71	0.70	**0.75**	0.3 %	1.6 %
	$[30, 45]$ GeV	0.75	0.75	0.73	0.75	0.71	0.74	0.70	0.75	**0.75**	0.4 %	1.6 %
	$[45, 60]$ GeV	0.75	0.75	0.73	0.73	0.75	0.74	0.71	0.73	**0.75**	0.4 %	1.7 %
	$[60, 80]$ GeV	0.75	0.74	0.73	0.73	0.74	0.74	0.71	0.80	**0.74**	0.4 %	1.8 %
	$[80, 120]$ GeV	0.75	0.76	0.75	0.74	0.76	0.74	0.72	0.78	**0.75**	0.4 %	1.9 %
	$[120, 170]$ GeV	0.78	0.78	0.76	0.76	0.77	0.77	0.76	0.67	**0.78**	0.4 %	1.5 %
	$[170, 220]$ GeV	0.79	0.79	0.76	0.78	0.78	0.79	0.77	1.00	**0.79**	0.5 %	1.3 %
	$[220, 350]$ GeV	0.80	0.80	0.80	0.79	0.80	0.79	0.79	0.72	**0.80**	0.6 %	1.1 %
N_{jet}	$= 0$	0.70	0.72	0.67	0.69	0.75	0.70	0.83	0.66	**0.70**	0.4 %	1.7 %
	$= 1$	0.82	0.72	0.73	0.72	0.75	0.72	0.68	0.85	**0.80**	0.4 %	1.7 %
	$= 2$	0.91	0.74	0.78	0.78	0.72	0.76	0.68	0.92	**0.85**	0.4 %	1.6 %
	≥ 3	1.09	1.10	0.91	0.89	0.83	0.89	0.75	1.02	**1.00**	0.4 %	1.7 %

Table 6.13: Correction factors and out-of-fiducial contributions.

the detector level signal yield by a factor of

$$\left(1 - f^{\text{non-fid}}\right) = \left(1 - f^{\text{non-fid}}_{\text{Dalitz}}\right)\left(1 - f^{\text{non-fid}}_{\text{other}}\right) \ . \tag{6.38}$$

Table 6.13 shows that $f^{\text{non-fid}}_{\text{Dalitz}} = 0.4$ % and $f^{\text{non-fid}}_{\text{other}} = 1.6$ %. The modelling of $f^{\text{non-fid}}_{\text{Dalitz}}$ is not well known and so a conservative 100 % uncertainty is applied to this subtraction. The uncertainty on $f^{\text{non-fid}}_{\text{other}}$ is contained within the other systematic uncertainties assigned to cover the correction factor model dependence.

6.5.7 Summary of systematic uncertainties

Table 6.14 summarises the dominant systematic uncertainties arising from the correction for detector effects. The statistical and systematic uncertainties from the fit are repeated here for comparison. The statistical uncertainty dominates in all regions. The uncertainties already discussed in this chapter are marked in green. Several additional uncertainties are provided by other members of the analysis team. These are summarised as follows.

The photon reconstruction uncertainty is determined by varying the photon identification and isolation efficiency scale factors within allowed bounds determined by comparing data and MC in a variety of control regions. It also accounts for energy scale and resolution uncertainties derived through analysis of $Z \to e^+e^-$ events. Photon reconstruction contributes a 1.8 % uncertainty in the *diphoton fiducial* region and dominates the uncertainty on the correction for detector effects. It increases to 3 % in the tail of the $p^{\gamma\gamma}_{\text{T}}$ distribution.

The jet energy scale and resolution uncertainty (JES/JER) is significant in bins defined using jet selections. It also impacts the $E^{\text{miss}}_{\text{T}}$ measurement. The largest impact is in the $N_{\text{jet}} \geq 3$ bin where it contributes a 15 % uncertainty. Uncertainties on the b-tagging efficiencies have a 3.0 % impact on the ttH region which is the only measurement dependent on this observable. Charged lepton reconstruction efficiencies contribute less than 1 % in the $N_{\text{lepton}} \geq 1$ and *ttH enhanced* regions.

The pileup *scale* contribution accounts for variations in the MC μ distribution consistent with the data uncertainty. This is in addition to the *model* contribution described in section 6.5.4. The UE/PS uncertainty covers variations in the `Pythia8` AZNLO tune and the comparison with `Herwig7` when modelling the parton shower, hadronisation and underlying event. The systematic uncertainty assigned to *Modelling* is defined as the envelope of the signal composition, $p^{\gamma\gamma}_{\text{T}}$ and UE/PS uncertainties. It is typically dominated by the signal composition variation which is large in the *high* E^{miss}_{T} and *ttH enhanced* regions as well as several individual bins such as $N_{\text{jet}} \geq 3$.

Small additional contributions are included due to the Dalitz subtraction (≈ 0.4 %) and the vertex selection efficiency (less than 0.5 % in all bins) which is estimated by increasing by 11 % the weight of simulated events for which the selected vertex is not found within 3 mm of the true one. This is commensurate with the difference between data and MC.

Uncertainty	Diphoton fiducial	VBF enhanced	$N_{\text{lepton}} \geq 1$	High $E_{\text{T}}^{\text{miss}}$	ttH enhanced
Fit (stat.)	17 %	22 %	72 %	53 %	176 %
Fit (syst.)	6 %	9 %	27 %	13 %	138 %
γ reconstruction	1.8 %	1.8 %	1.8 %	1.9 %	1.8 %
JES/JER	–	8.9 %	–	6.9 %	4.5 %
b-tagging	–	–	–	–	3.0 %
e, μ reconstruction	–	–	0.7 %	–	0.2 %
Pileup	1.1 %	2.9 %	1.3 %	2.3 %	4.4 %
- Scale	*1.1 %*	*0.3 %*	*1.3 %*	*2.3 %*	*0.7 %*
- Model	–	*2.8 %*	–	–	*4.4 %*
Modelling	0.1 %	4.5 %	4.0 %	31 %	8.1 %
- Composition	*0.1 %*	*4.5 %*	*3.1 %*	*25 %*	*8.1 %*
- Shape ($p_{\text{T}}^{\gamma\gamma}$)	*0.1 %*	*0.9 %*	*0.2 %*	*0.1 %*	*0.7 %*
- UE/PS	–	*0.3 %*	*0.7 %*	*31 %*	*1.1 %*
Luminosity	3.2 %	3.2 %	3.2 %	3.2 %	3.2 %
Total	**18 %**	**26 %**	**77 %**	**63 %**	**224 %**

Table 6.14: Dominant uncertainties due to the correction for detector effects. Those shown in green are described in this chapter. Signal fit uncertainties are shown for comparison.

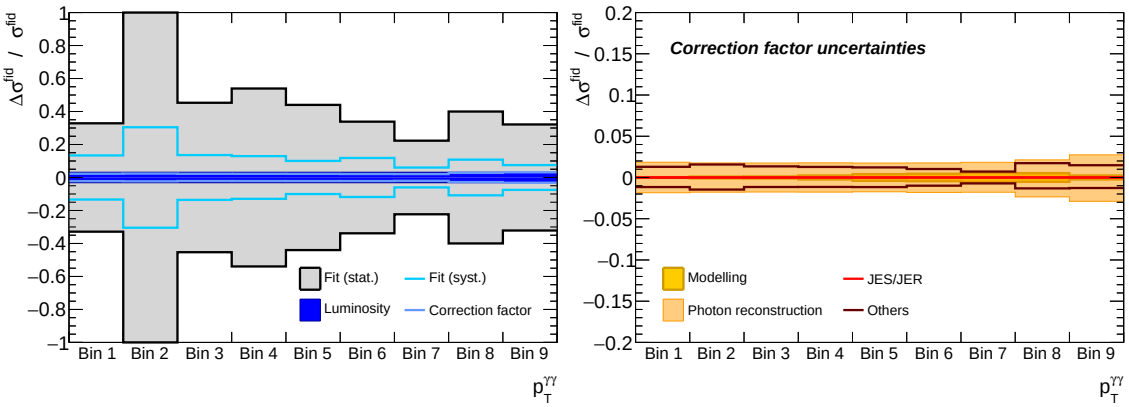

(a) $p_{\text{T}}^{\gamma\gamma}$

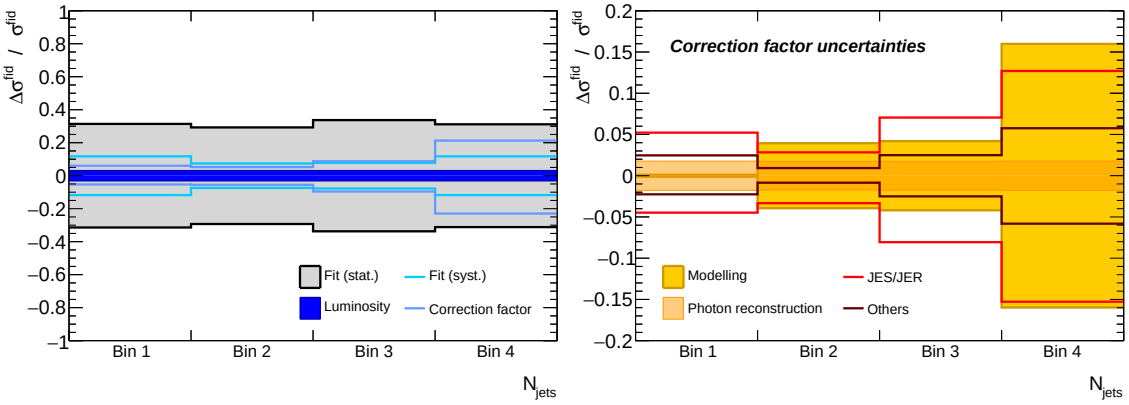

(b) N_{jet}

Figure 6.37: Summary of uncertainties from (left) all sources and (right) correction for detector effects in bins of the $p_{\text{T}}^{\gamma\gamma}$ and N_{jet} distributions.

The trigger efficiency is estimated with an uncertainty of 0.4 % in all bins. The integrated luminosity uncertainty is 3.2 %.

Figure 6.37 shows the uncertainty breakdown in bins of $p_{\mathrm{T}}^{\gamma\gamma}$ and N_{jet}. Left-hand plots show the fractional uncertainties from all sources, including the fit statistical and systematic uncertainties for comparison. Statistical fluctuations dominate in all bins. The dominant systematic uncertainty in the $p_{\mathrm{T}}^{\gamma\gamma}$ distribution is from the signal extraction fit. The low measured signal yield in bin 2 leads to divergent fractional uncertainties. The dominant systematic uncertainty in the $N_{\mathrm{jet}} \geq 3$ bin is due to the correction for detector effects. This is broken down further as shown in the right-hand plots. The $p_{\mathrm{T}}^{\gamma\gamma}$ correction factors are dominated by photon reconstruction uncertainties of $\lesssim 3$ %. The $N_{\mathrm{jet}} \geq 3$ bin has ~ 15 % contributions from both JES/JER and the signal composition uncertainty.

6.6 Results: fiducial regions

Table 6.16 shows the measured fiducial cross sections $\sigma_{\mathrm{meas}}^{\mathrm{fid}}$ and the most precise SM prediction $\sigma_{\mathrm{SM}}^{\mathrm{fid}}$ in each region. The calculation of ggF is performed at N^{3}LO QCD precision with NLO electroweak corrections in the *diphoton fiducial* region [28, 64–67, 222] and corrected for acceptance using the `Powheg NNLOPS` MC sample. All other regions use the default MC cross section for the ggF prediction. The cross section from $XH = \mathrm{VBF} + VH + ttH + bbH$ is calculated using the default MC in all regions. Due to low signal significance, 95 % confidence limits are presented in the $N_{lepton} \geq 1$, *high* E_T^{miss} and *ttH enhanced* regions assuming a Gaussian probability distribution. The *diphoton fiducial* cross section is 55 ± 10 fb and represents a 0.9 σ downwards fluctuation compared with the SM expectation of 64 ± 2 fb. This region is dominated by ggF production. The measurement in the *VBF enhanced* region is 3.7 ± 1.0 fb and represents a 1.5 σ upwards fluctuation compared with an expected 2.3 ± 0.1 fb. The three low-precision regions are consistent with the SM to within ± 1 σ.

The results are summarised in Figure 6.38 along with several alternative SM predictions. Dark blue points use the `Powheg NNLOPS` program to estimate the ggF contribution and pink points use `Sherpa` [251–262]. This is accurate to NLO (QCD) for $H+ \leq 3j$ production and includes the effects of finite top quark mass. The XH component is shown separately in green.

6.7 Results: differential distributions

The results in this section are compared with the default SM prediction as shown in blue. Several additional MC predictions of ggF are also presented for comparison [263–265]. All predictions are consistent with one another at a level much smaller than the data statistical uncertainties. Further details on the alternative MC predictions can be found in Ref. [5]. The expected XH contribution to each distribution is shown in green.

Figure 6.39 shows the measured cross section as a function of five diphoton observables. The $p_{\mathrm{T}}^{\gamma\gamma}$ and $p_{\mathrm{Tt}}^{\gamma\gamma}$ distributions are highly correlated and exhibit similar shapes in the data vs. MC comparison. The data may prefer a higher momentum distribution than the prediction, however they are generally in good agreement. Comparison with Figure 3.3 demonstrates the improvement in statistical precision compared with Run 1, especially in the tail of the distribution. The $|y_{\gamma\gamma}|$, $|\Delta y_{\gamma\gamma}|$ and $|\cos\theta^*|$ distributions are all consistent with the SM hypothesis.

Figure 6.40(a) shows the N_{jet} distribution using a minimum jet p_{T} of 30 GeV. Both exclusive and inclusive bins are shown. The shape is positively correlated with that of the $p_{\mathrm{T}}^{\gamma\gamma}$ distribution. The data favours a higher multiplicity jet distribution but is generally in good agreement with the SM prediction. Several SM estimates predict a lower yield than the default MC. Figure 6.40(b) shows the impact of increasing the minimum jet p_{T} requirement to 50 GeV. The same preference towards higher jet multiplicities is observed. Figures 6.41(a) and (b) show the two double differential distributions. All observations are consistent with the single differential measurements.

Figure 6.42 shows observables which require the presence of at least one selected jet. The first bin of of the leading jet transverse momentum, p_{T}^{j1}, represents 0-jet events. The data in this distribution favours higher momentum as observed in $p_{\mathrm{T}}^{\gamma\gamma}$. The two observables are positively correlated as shown in Figure 6.23. The leading jet rapidity, $|y_{j1}|$, is shown. The data favours jets at higher rapidities than in simulation. The scalar sum of jet transverse momenta, H_{T}, follows the same trend as p_{T}^{j1}. These observations are consistent with the upwards fluctuation in the *VBF enhanced* region and are not statistically significant. The event shape observables τ_1 and $\sum_j \tau_j$ also exhibit comparable trends.

Figures 6.43 and 6.44 show observables which require the presence of two selected jets. These are correlated with events in the tail of the $p_{\mathrm{T}}^{\gamma\gamma}$ spectrum. Statistical precision is limited in this region of phase space and so only $3-4$ bins can be measured. The first bin of of the subleading jet transverse momentum, p_{T}^{j2}, represents $\leq$ 1-jet events. The p_{T}^{j2} and m_{jj} distributions follow the same preference for high-momentum as measured in other observables. The subleading jet rapidity, $|y_{j2}|$, is consistent with fluctuations around the SM expectation. The agreement in the $p_{\mathrm{T}}^{\gamma\gamma jj}$ distribution is consistent with the observed upwards fluctuation of dijet events. The azimuthal separation of the two jets, $\Delta\phi_{jj}$, is shown as an absolute value and with a sign defined relative to the leading jet. The observation is consistent with the SM to within experimental fluctuations although data may prefer positive values. The dijet rapidity separation $|\Delta y_{jj}|$ and azimuthal spread, $\Delta\phi\,(\gamma\gamma, jj)$, are also shown.

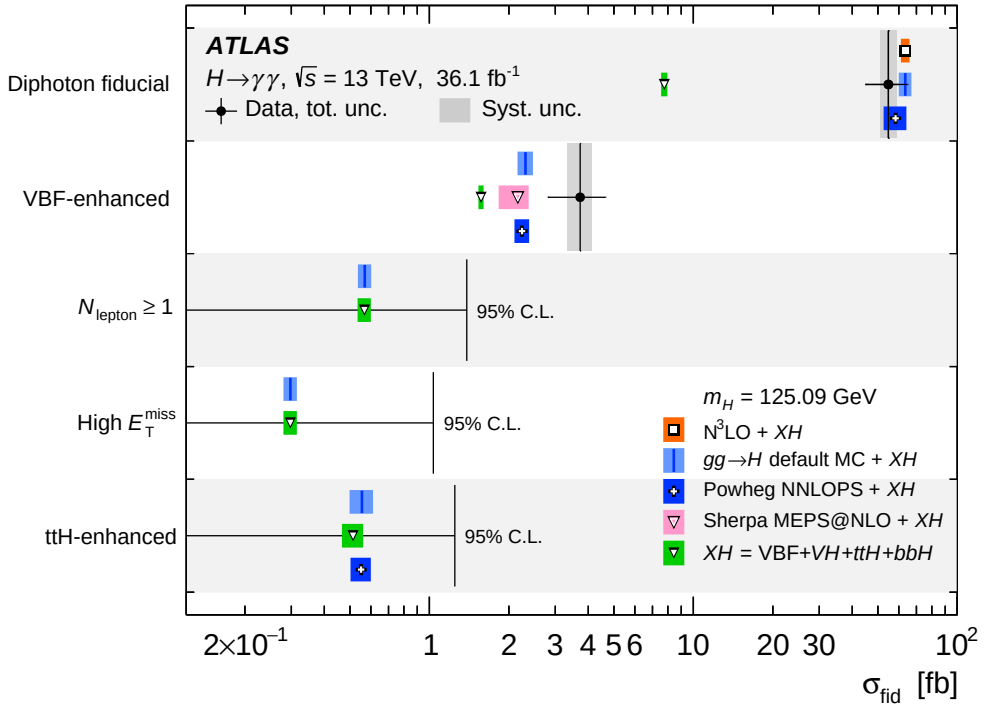

Figure 6.38: Measured fiducial cross sections in the $H \to \gamma\gamma$ channel.

Region	$\sigma^{\text{fid}}_{\text{meas}}$ [fb]	$\sigma^{\text{fid}}_{\text{SM}}$ [fb]	$\frac{\sigma^{\text{fid}}_{\text{meas}}}{\Delta\sigma^{\text{fid}}_{\text{meas}}}$	$\frac{\sigma^{\text{fid}}_{\text{meas}}-\sigma^{\text{fid}}_{\text{SM}}}{\Delta\sigma^{\text{fid}}_{\text{meas}}\oplus\Delta\sigma^{\text{fid}}_{\text{SM}}}$
Diphoton fiducial	55 ± 10	64 ± 2	5.4	-0.9
VBF enhanced	3.7 ± 1.0	2.3 ± 0.1	3.8	$+1.5$
$N_{\text{lepton}} \geq 1$	≤ 1.39 95 % CL	0.57 ± 0.03	1.3	$+0.1$
High $E_{\text{T}}^{\text{miss}}$	≤ 1.00 95 % CL	0.30 ± 0.02	1.8	$+0.7$
ttH enhanced	≤ 1.27 95 % CL	0.55 ± 0.06	0.4	-0.5

Table 6.16: Measured fiducial cross sections.

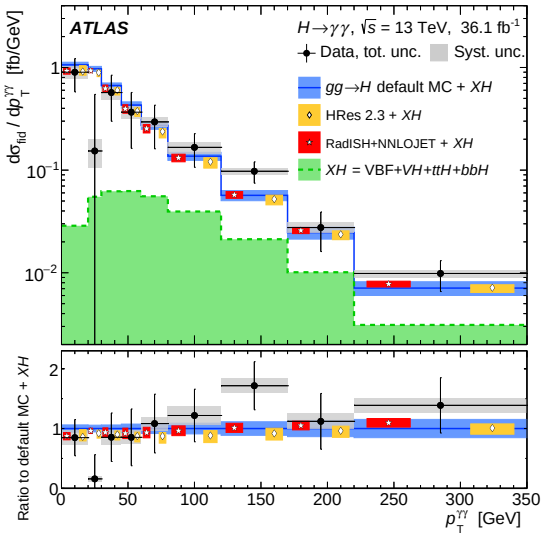

(a) $p_{\mathrm{T}}^{\gamma\gamma}$

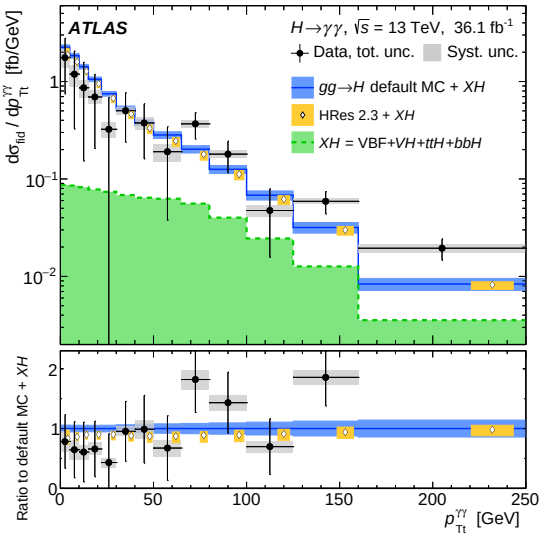

(b) $p_{\mathrm{Tt}}^{\gamma\gamma}$

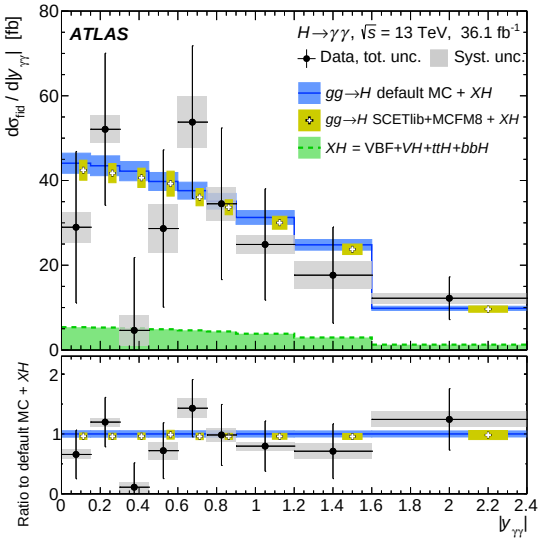

(c) $|y_{\gamma\gamma}|$

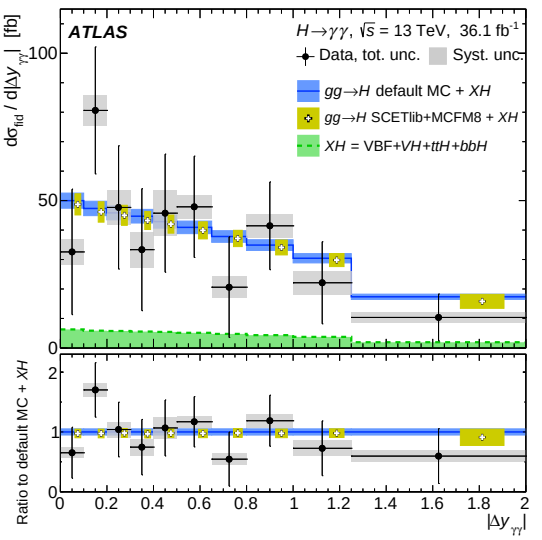

(d) $|\Delta y_{\gamma\gamma}|$

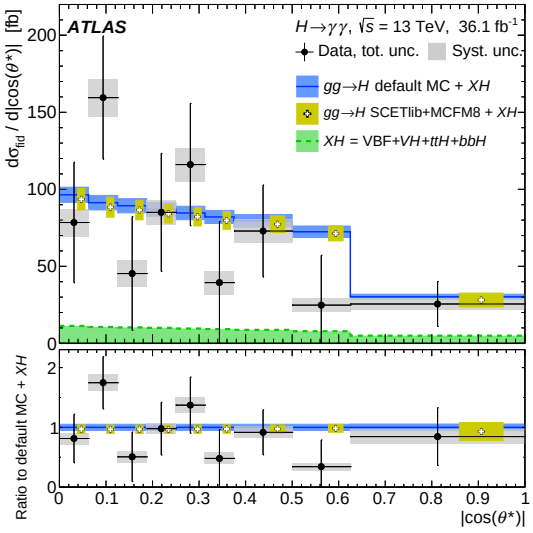

(e) $|\cos\theta^*|$

Figure 6.39: Differential measurements using diphoton observables.

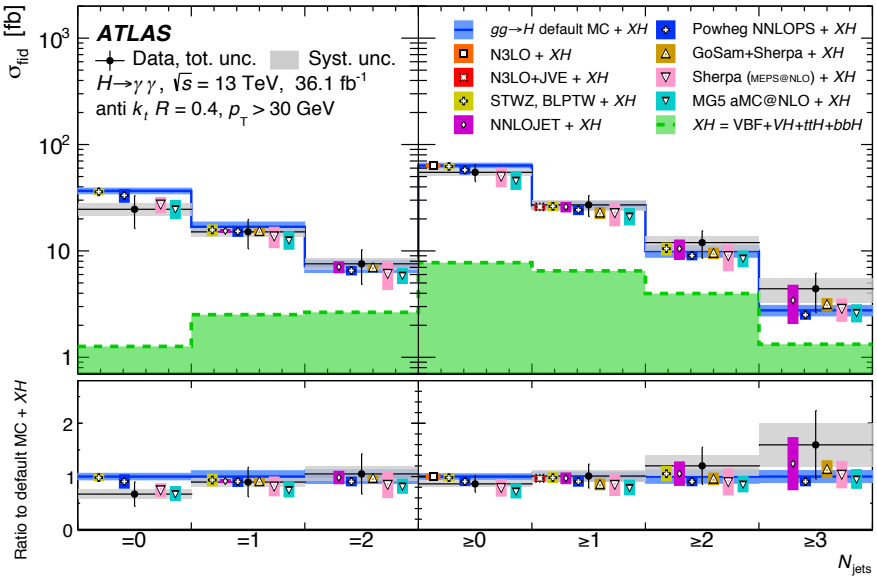

(a) N_{jet} (30 GeV)

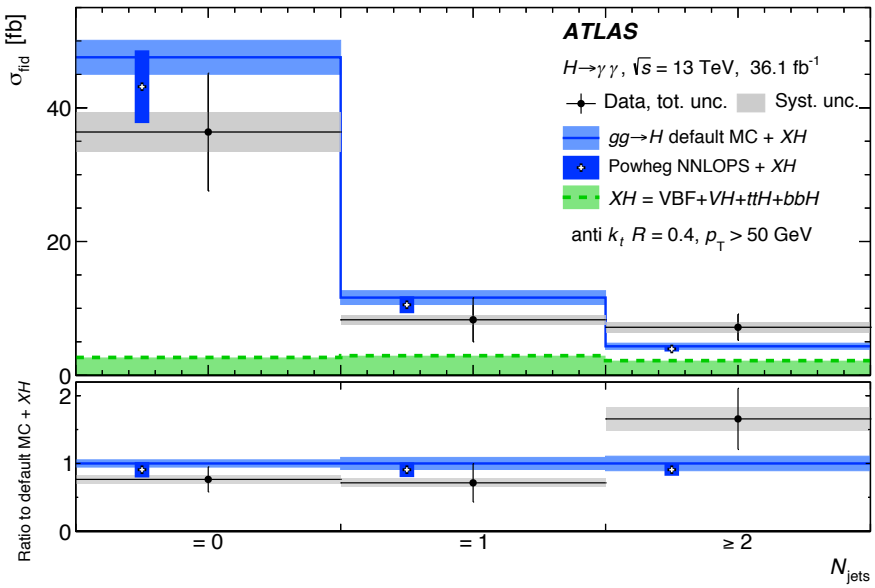

(b) N_{jet} (50 GeV)

Figure 6.40: Differential measurements of jet multiplicity.

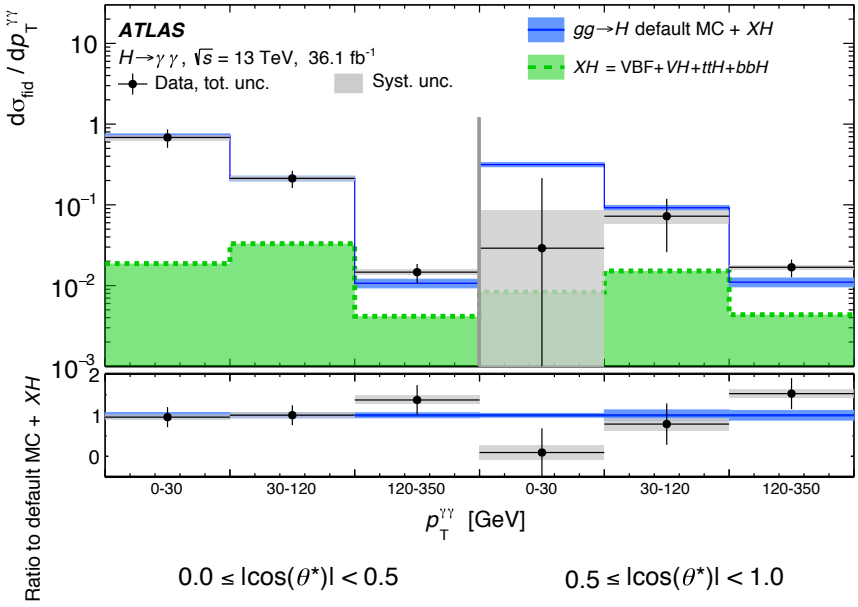

(a) $p_{\mathrm{T}}^{\gamma\gamma}$ vs. $\cos\theta^*$

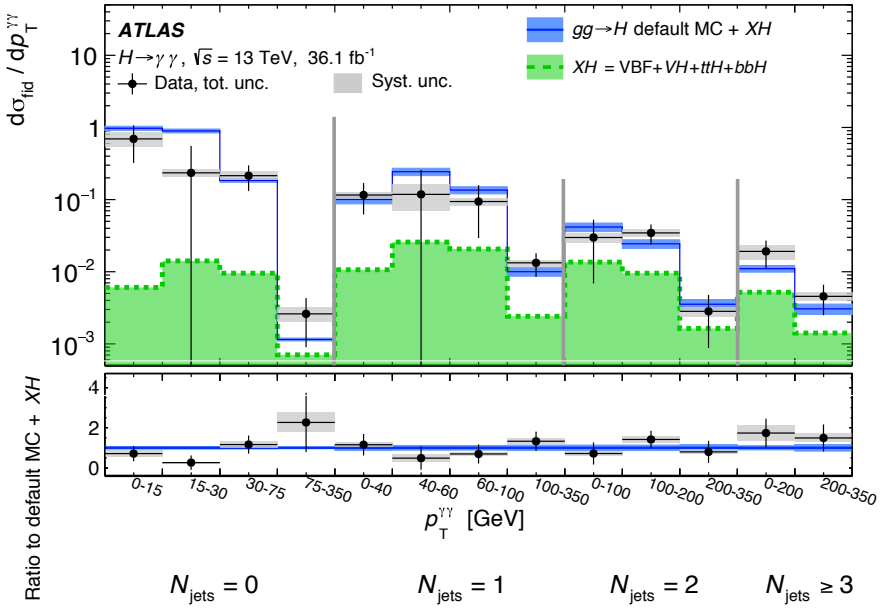

(b) $p_{\mathrm{T}}^{\gamma\gamma}$ vs. N_{jet} (30 GeV)

Figure 6.41: Double differential measurements.

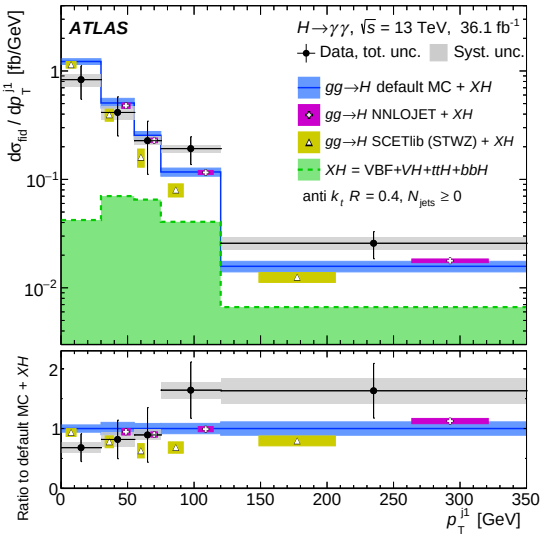

(a) p_{T}^{j1}

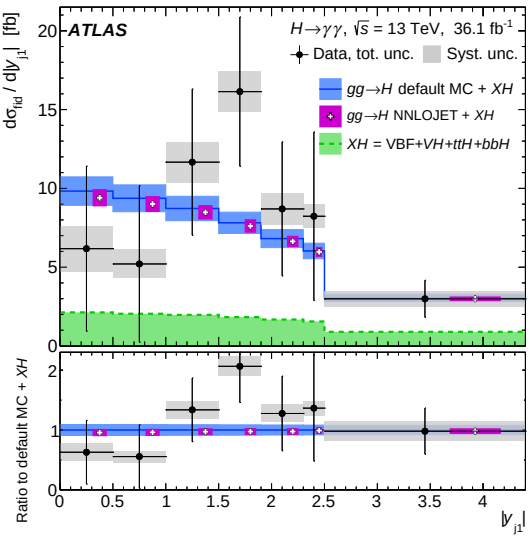

(b) $|y_{j1}|$

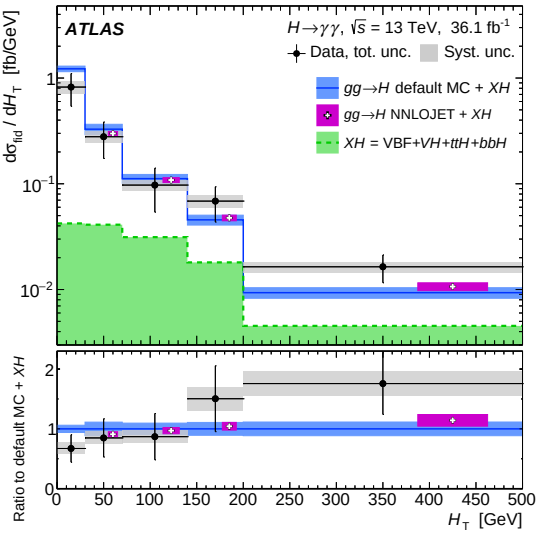

(c) H_{T}

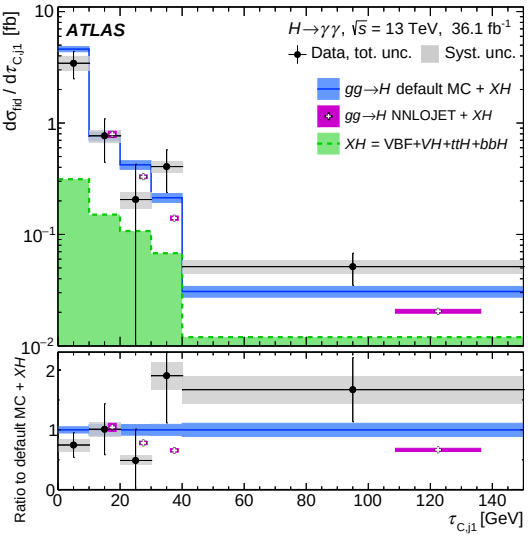

(d) τ_1

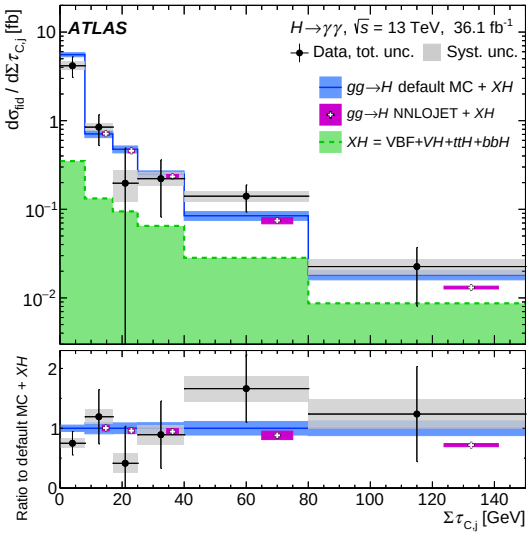

(e) $\sum_j \tau_j$

Figure 6.42: Differential measurements using ≥ 1 jet observables.

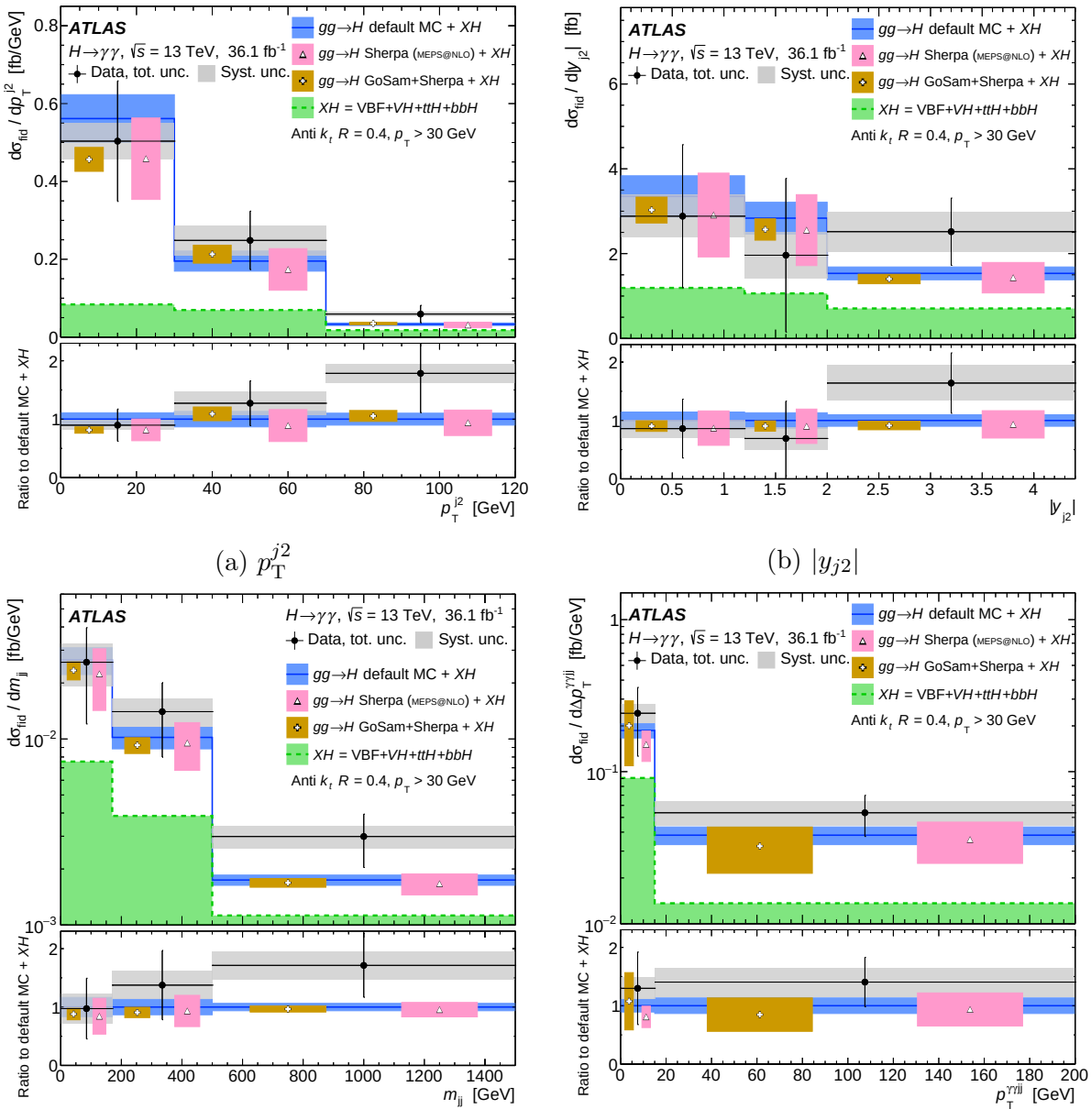

(a) p_{T}^{j2}

(b) $|y_{j2}|$

(c) m_{jj}

(d) $p_{\mathrm{T}}^{\gamma\gamma jj}$

Figure 6.43: Differential measurements using ≥ 2 jet observables.

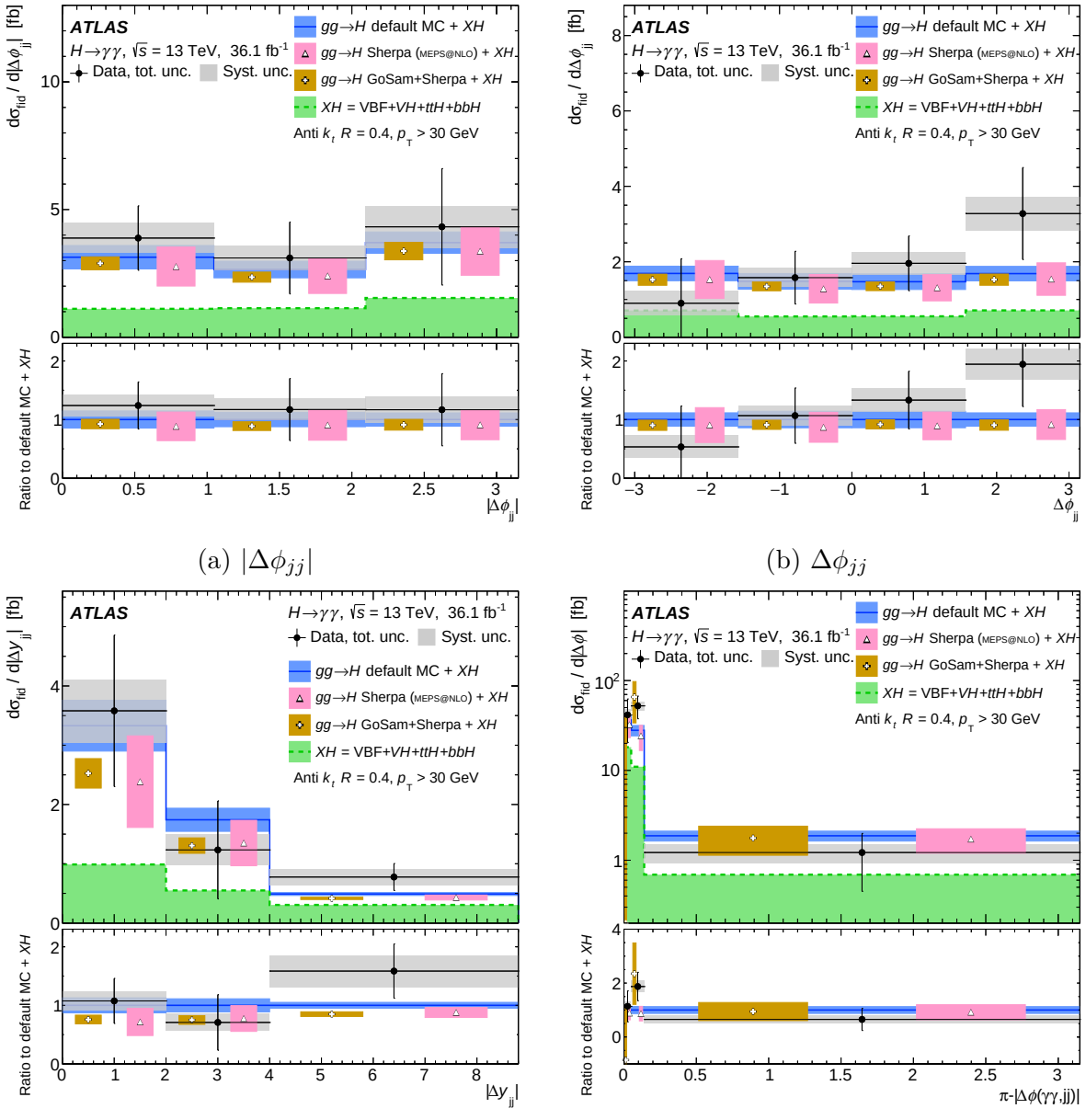

(a) $|\Delta\phi_{jj}|$

(b) $\Delta\phi_{jj}$

(c) $|\Delta y_{jj}|$

(d) $\Delta\phi\,(\gamma\gamma, jj)$

Figure 6.44: Differential measurements using ≥ 2 jet observables.

6.8 Background modelling: discrete profiling method

This section describes an alternative background modelling method which was studied as part of the measurement described in this chapter. Section 6.4.2 summarised the method through which a functional form is chosen to model the background as a function of $m_{\gamma\gamma}$. This shape is not known a priori and so several empirical function forms are tested using MC templates. A balance between the estimated systematic bias and expected statistical sensitivity is chosen. The bias is referred to as *spurious signal*. The function degrees of freedom impact the statistical uncertainty on the PoIs because the background shape parameters are not fixed to their expected values but allowed to float in the signal extraction fit. This is because the MC templates are not considered to be sufficiently precise, statistically or systematically, to constrain them. The background modelling is of significant importance in $H \to \gamma\gamma$ measurements because the background rate is much larger than the signal in many bins, therefore variations in the estimated background contribution may be small on the scale of the background but large on the scale of the signal.

The following drawbacks of this method are identified. The MC templates are used because they can be generated with greater statistical precision than is available in the data sidebands. For a given m_{H}, the template must have at least a factor 5 greater statistical sensitivity than the measured dataset in order to impose the criterion that the spurious signal be no more than 20 % of the expected statistical uncertainty. Assuming that the precision varies as $\sim 1/\sqrt{n}$ where n is the event yield in the signal region, this means that it must contain at least 25 times as many events. The required event simulation therefore becomes prohibitively large as the dataset size increases. At 36 fb^{-1} it is already observed that the spurious signal estimates are sensitive to statistical fluctuations of the MC templates. This will pose a significant challenge in the analysis of $\gtrsim 120$ fb^{-1} data expected at the end of Run 2. Furthermore, this method treats the MC template as a "true" underlying distribution. In reality, the true distribution cannot be known with greater precision than is available from the data. A background modelling method with less dependence on the assumed templates is therefore desirable.

The discrete profiling method [4] has been used by the CMS experiment in several $H \to \gamma\gamma$ measurements [26, 109, 266–270]. This treats the functional form used to model the background shape as a discrete nuisance parameter in the signal fit. When Λ is profiled using a PoI, ν, the function which maximises the likelihood is chosen at each point. For a fit to a single bin, the resulting Λ profile is the envelope of all allowed functions. This is illustrated in Figure 6.45. The estimated PoI, $\hat{\nu}$, and its asymmetric uncertainties, $\Delta\nu^{\pm}$, are defined using this curve[2]. This naturally resolves the ambiguity in function choice by defining the central value of the PoI using the function most likely to reproduce the observed

[2]Here we resolve the profile at a value of 1 to define uncertainties. This assumes that the likelihood is Gaussian as a function of ν, and so Λ is quadratic. A 68 % confidence interval could instead be used.

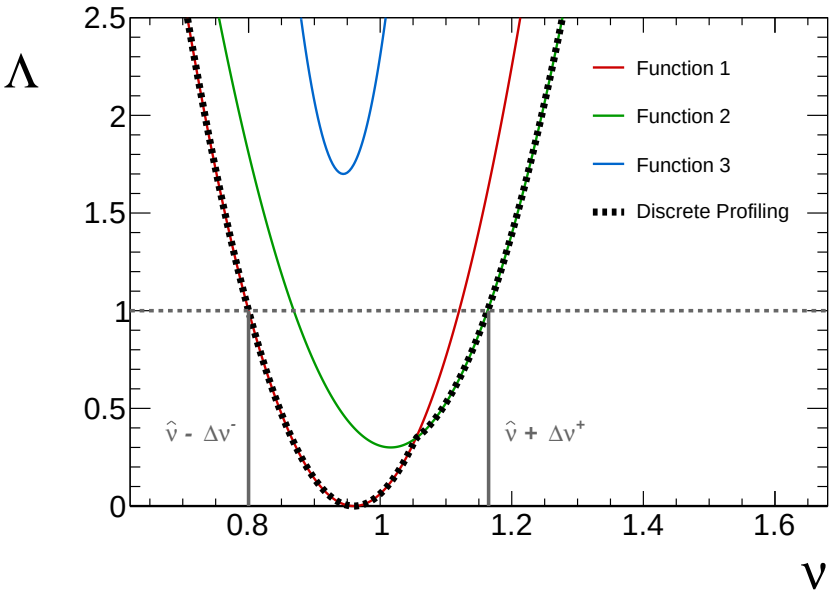

Figure 6.45: Diagram showing the principle behind the discrete profiling method based on Figures 1, 3 and 4 of Ref. [4].

dataset, whilst broadening its uncertainty when competing choices exist. Functional forms which do not well describe the data have a lower optimised likelihood and do not contribute to the envelope. This section describes the implementation of the discrete profiling method in the ATLAS $H \to \gamma\gamma$ cross section measurement and studies the perfomance.

6.8.1 Considerations

Consider a familiy of functions, such as `ExpPolN`, for which the $(N+n)^{\text{th}}$ function nests the N^{th} for all $n > 0$. This means that one can make a higher order function equal to any lower order one with an appropriate choice of parameters. The higher order function will always result in an optimised likelihood equal to or greater than that of the lower order function. The discrete profiling method will therefore always pick out the highest order function allowed in any given family. However, the highest order function will also cause the largest statistical uncertainty. This method may therefore degrade the statistical sensitivity by choosing functions with more degrees of freedom than are necessary. A penalty term is included in the profile parameter Λ to mitigate this effect. The form and magnitude of this penalty is somewhat arbitrary and can be tuned in order to balance statistical and systematic uncertainties. The aim is that a higher order function will only be chosen if it cause a sufficiently large increase in p-value. The chosen parameterisation is

$$\Lambda_{\text{corr}} = \Lambda + N_{\text{par}} \tag{6.39}$$

where Λ_{corr} is the penalised profile parameter and N_{par} is the number of free parameters in the function.

This penalty term is chosen because it is demonstrated to perform well in the case studies presented in Ref. [4] and is adopted by the CMS analyses [26, 109, 266–270]. The quantity Λ is equal to the χ^2 in the asymptotic limit of binned fits. The Λ difference between two functions is therefore a $\Delta\chi^2$. This is expected to increase by approximately 1 unit per degree of freedom for nested functions with similar p-values. This interpretation motivates the form of Eq. 6.39 when comparing functions within a family. However, this does not motivate the comparison between different function families for which the expected $\Delta\chi^2$ is not necessarily similar to the difference in free parameters, and so equal Λ_{corr} do not imply similar p-values. There are therefore two degrees of arbitrariness: the strength with which higher orders are penalised, and the equivalence between the Λ_{corr} of different function families. These two effects should be optimised in analyses where the discrete profiling method is used.

The envelope interpretation of Figure 6.45 is not valid when a fit is performed with common nuisance parameters shared between multiple bins. When a given PoI is profiled, these NPs must be re-optimised simultaneously in all bins. If N_f is the number of functions profiled per bin, and N_b is the number of bins, then the number of permutations which must be evaluated is $N_f^{N_b}$. This presents a computational challenge. Furthermore, the NPs associated with the shapes of background functions which are not selected are so-called *flat directions*. This means that varying them has no impact on the evaluated likelihood. The lack of a likelihood gradient with respect to a parameter causes numerical problems in many common minimisation routines because an optimum point (likelihood maximum, Λ minimum) cannot be found. These numerical challenges must be overcome if the discrete profiling method is to be used.

6.8.2 Technical implementation

It is desirable to use the `RooFit` package where possible due to its optimisation, reliability and integration with the `Minos` program for efficient computation of parameter uncertainties. A possible implementation treats the function choice as a NP in the fit. Several parameterisations are considered as visualised in Figure 6.46. Each case is tested and found to be unreliable for the reasons described below, therefore the use of such a NP is disfavoured.

A indexes the function using a discrete NP. The Λ_{corr} profile does not vary continuously with with NP and so its gradient cannot be estimated at any point. This form is incompatible with many optimisation routines.

B indexes the function using a continuous parameter. Although a valid Λ_{corr} gradient is

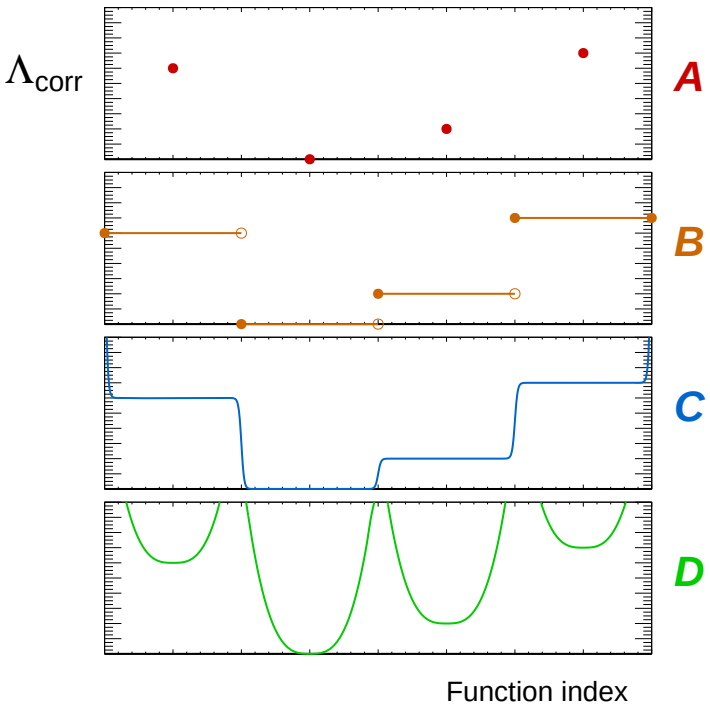

Figure 6.46: Diagram showing several methods through which a NP can be parameterised to describe the profiling of functions.

estimated, this gradient is zero and the profile is discontinuous. This causes a fit failure using the optimisation routines tested.

C allows a continuous transition between Λ_{corr} minima. Points along the transition region represent a linear combination of two different functions. These may be chosen in multi-bin fits if they correspond to $\vec{\theta}$ values which are favoured by other bins. This is not a desired outcome.

D uses external constraints to penalise NP values not centred on the desired index values. The height and shape of the Λ_{corr} wells are tailored for performance. This was not found to reliably result in the global Λ_{corr} minimum.

It is found that performance is improved when such a NP is not explicitly defined. Instead, the Λ_{corr} evaluated in a given bin using a given set of parameters is defined as the smallest of all allowed functions. Note that this causes discontinuities in the gradient of Λ_{corr} with respect to other parameters as visualised in Figure 6.45. A nested optimisation method is also preferred. The `RooFit` package is used to optimise the PoIs and evaluate their uncertainties using the `Minos` program. For each PoI set, a second minimiser is configured to find the optimum set of NPs and perform the function choice. Data is binned in $m_{\gamma\gamma}$ using a width of 0.2 GeV to improve numerical performance. This is estimated to have little impact on the expected statistical precision. Flat directions in the background shape parameters are prevented by the use of external constraints. These are parameterised

as the sum of a two-sided Fermi-Dirac function with a Gaussian centred on the best-fit values obtained using a sideband-only fit. This approach is optimised for numerical performance. The Gaussian contribution is small to prevent a bias towards the chosen value when the direction is not flat.

The numerical performance is tested using the following approach. Data and MC events are separated into differential bins defined using selection criteria applied to arbitrary observables. The sidebands of an 18 fb^{-1} dataset are fit with an arbitrary background function to parameterise the background shapes and normalisations. The MC events are used to derive the expected signal shapes and normalisations. The resulting signal-plus-background model is used to generate pseudo-datasets with a target luminosity of 36.5 fb^{-1}. Each pseudo-dataset is subject to unique fluctuations which may be best described by different function choices, therefore providing multiple scenarios in which to test the Λ_{corr} profile. Several functions are chosen to profile in each bin. The ExpPolN and PolN functions are considered as defined in Eq. 6.19 - 6.20. Since `PolN` are implemented in the basis of Bernstein polynomials, these are referred to as `BernsteinN` in this section.

Figure 6.47 shows the Λ_{corr} profiles of a variety of functions in three different pseudo-datasets generated for the *diphoton fiducial* region using an `ExpPol3` background shape. Black dots show the central value of the PoI as well as its upper and lower uncertainties estimated using the implementation of the discrete profiling method. Vertical black lines show the uncertainties estimated from the envelope of the individual curves. Three constrained NPs are used to describe PES, PER and m_{H} uncertainties with arbitrary magnitudes. The discrete profiling method implementation agrees with the envelope method in all cases. Two examples are shown in which competitive functions are found. Minimisation occurs in $2 - 10$ minutes depending on the complexity of the Λ_{corr} profile.

Figure 6.48 shows the same comparison in all four bins of a four-bin fit. The $\vec{\theta}$ NPs are fixed in order to make a valid comparison between the discrete profiling and envelope methods. All bins are generated using an `ExpPol3` background model. The discrete profiling implementation is shown to estimate the correct PoI value and uncertainties in all bins. The uncertainty in one bin is expanded by a competing function choice. The total fit time is 30 minutes of which 20 minutes was spent evaluating the four PoI uncertainties.

Figure 6.49 shows the same comparison in the first twelve bins of a fourteen-bin fit. The remaining two bins trivially contain only one function. The $\vec{\theta}$ NPs are fixed. A variety of `ExpPolN` background models are used to generate the pseudo-data. The discrete profiling implementation is shown to estimate the correct PoI value and uncertainties in all bins. The uncertainties in three bins are expanded by competing function choices. The total fit time is approximately 6.5 hours of which 4.5 hours were spent evaluating the fourteen PoI uncertainties. These results show that a technical implementation of the discrete profiling method has been performed in the context of ATLAS $H \to \gamma\gamma$ measurements. However, the performance is limited in high-multiplicity bin fits.

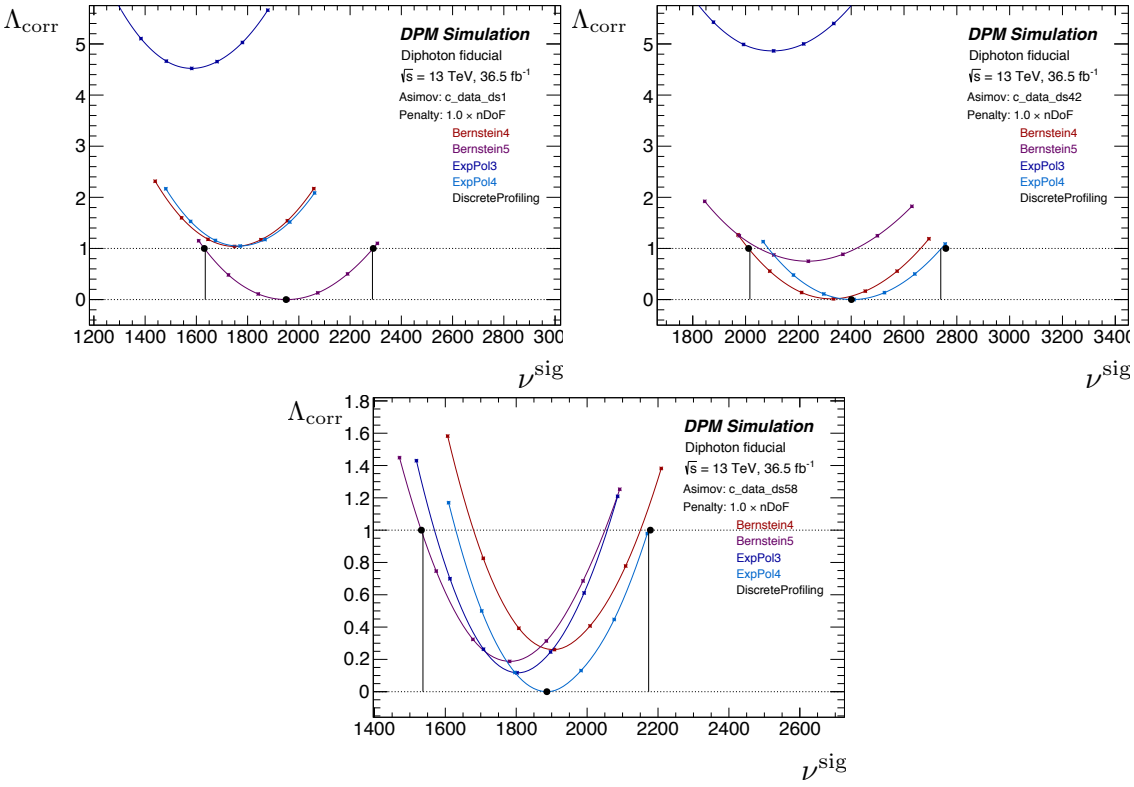

Figure 6.47: Comparison between the implemented discrete profiling method (black points) and the envelope of the individual profiled functions (black lines) in three pseudo-datasets.

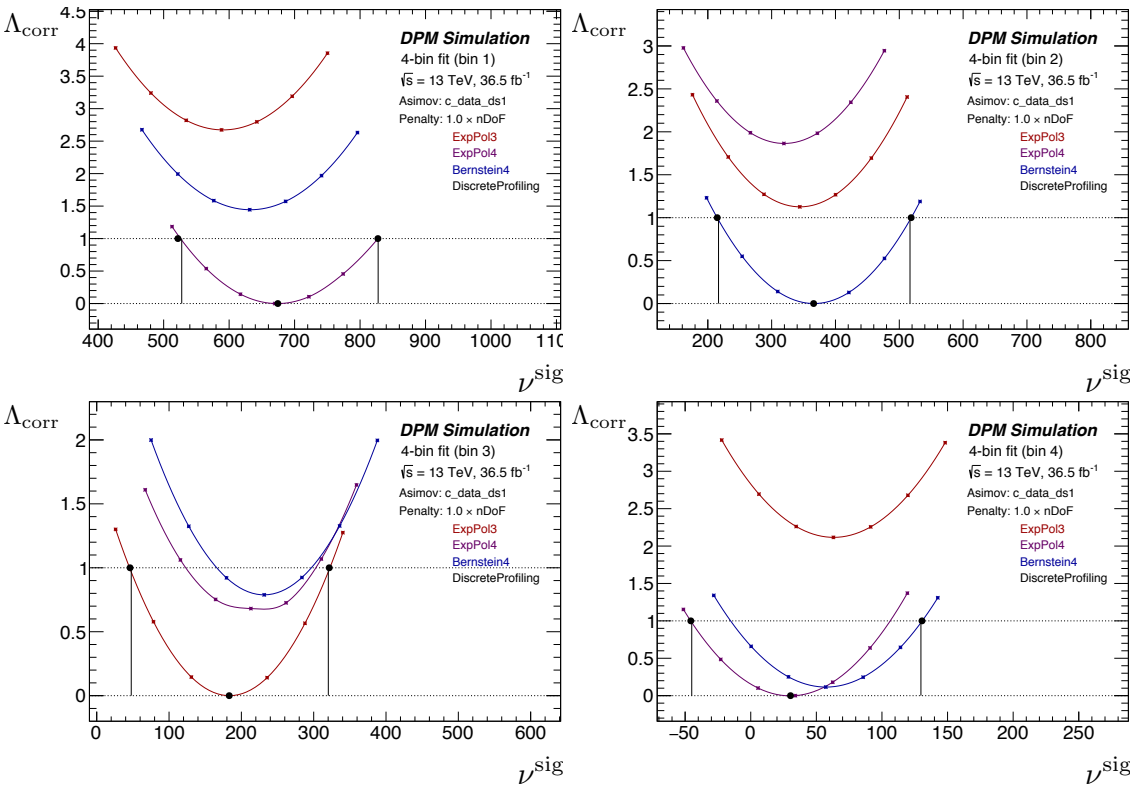

Figure 6.48: Comparison between the implemented discrete profiling method (black points) and the envelope of the individual profiled functions (black lines) in all bins of a 4-bin fit.

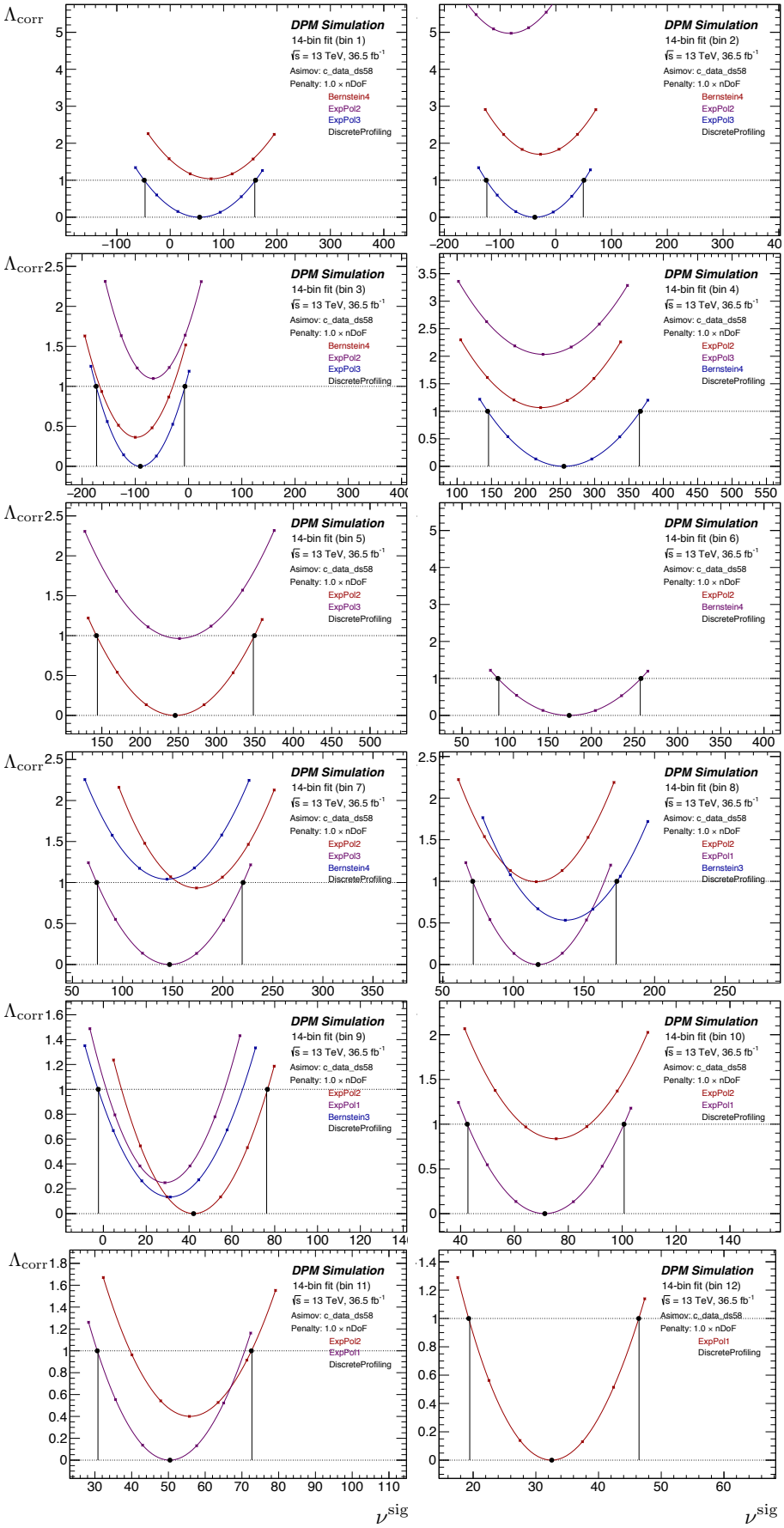

Figure 6.49: Discrete profiling method implementation in the first 12 bins of a 14-bin fit.

6.8.3 Statistical properties

This section considers the statistical properties of the discrete profiling method. When fitting to data, each function represents a possible approximation of an unknown underlying distribution. The discrete profiling method aims to naturally include a data-driven modelling uncertainty. However, the pseudo-datasets used to test the method are generated under the assumption of a known background model. One of the profiled functions is therefore equivalent to the true underlying distribution rather than an approximation of it. Whilst conceptually different, this method allows a true mean signal yield to be defined. This is required when studying the potential bias of a PoI estimate.

1000 pseudo-datasets are created in the *diphoton fiducial* region using an `ExpPol3` background model as described in section 6.8.2. Figure 6.50 shows the pull on the extracted signal yield where ν^{sig} is the toy measurement and $\nu^{\text{exp,sig}}$ is the true mean. The PoI uncertainty $\Delta\nu^{\text{sig}}$ is taken in the direction of the true mean. Unbiased estimates with correct coverage are expected to follow a standard normal distribution. This is overlayed in black for comparison.

When an `ExpPol2` model is used, the bias is estimated to be 104 % compared with the expected statistical uncertainty showing that this function does not have enough degrees of freedom to correctly describe the background shape. The `ExpPol3` distribution has small estimated bias and well estimated uncertainties as expected. This is also true of the `ExpPol4` function because it is able to reproduce the `ExpPol3` shape exactly with the extra degree of freedom serving to increase the statistical uncertainty. Several instabilities were observed in the `ExpPol5` fits which cause outliers in the pull distribution. Use of the `Bernstein4` function leads to a bias of 37 % of the statistical uncertainty. This bias is somewhat reduced when an extra degree of freedom is included (`Bernstein5`), although the low RMS may indicate overestimated uncertainties.

The sensitivity is defined as the average of the upper and lower error estimates, $\Delta\nu^{\text{sig}}_{\pm}$, divided by the true mean of the PoI. This is shown in Figure 6.51(a) using the `ExpPol3`, `Bernstein4` and `Bernstein5` background models. The mean sensitivities are 16.0 %, 16.8 % and 18.5 % respectively. The RMS is also shown. Figure 6.51(b) shows the sensitivity distribution obtained when profiling these three functions. The mean sensitivity is 17.7 % and there is a large occupancy above 20 %. This is not observed when any individual function is used independently. It is due to the expansion of uncertainties caused by competing functions as shown in Figure 6.52. This suggests that significant degradation in sensitivity can occur when two function minima have similar Λ_{corr} but different estimated PoIs. The PoI central value corresponds to the choice of `ExpPol3`, `Bernstein4` and `Bernstein5` in 53 %, 28 % and 20 % of fits respectively.

Figure 6.51(c) shows the pull distribution. The bias is estimated to be 8 % of the expected statistical uncertainty and the RMS indicates a moderate overestimate of uncertain-

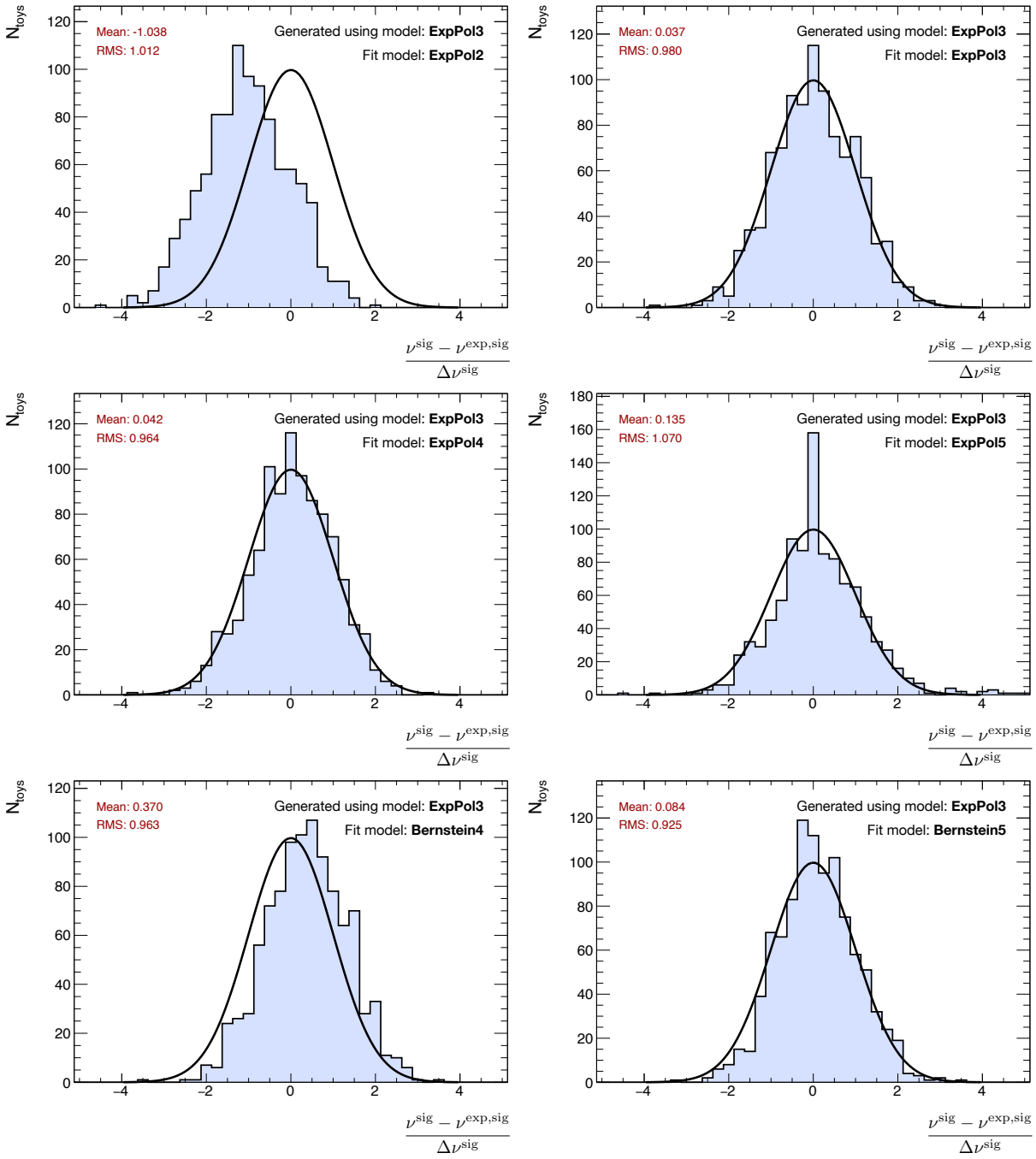

Figure 6.50: Pulls when fitting to pseudo-datasets generated using an `ExpPol3` background model under the hypothesis of various models. The black curve is a standard normal distribution, shown for comparison.

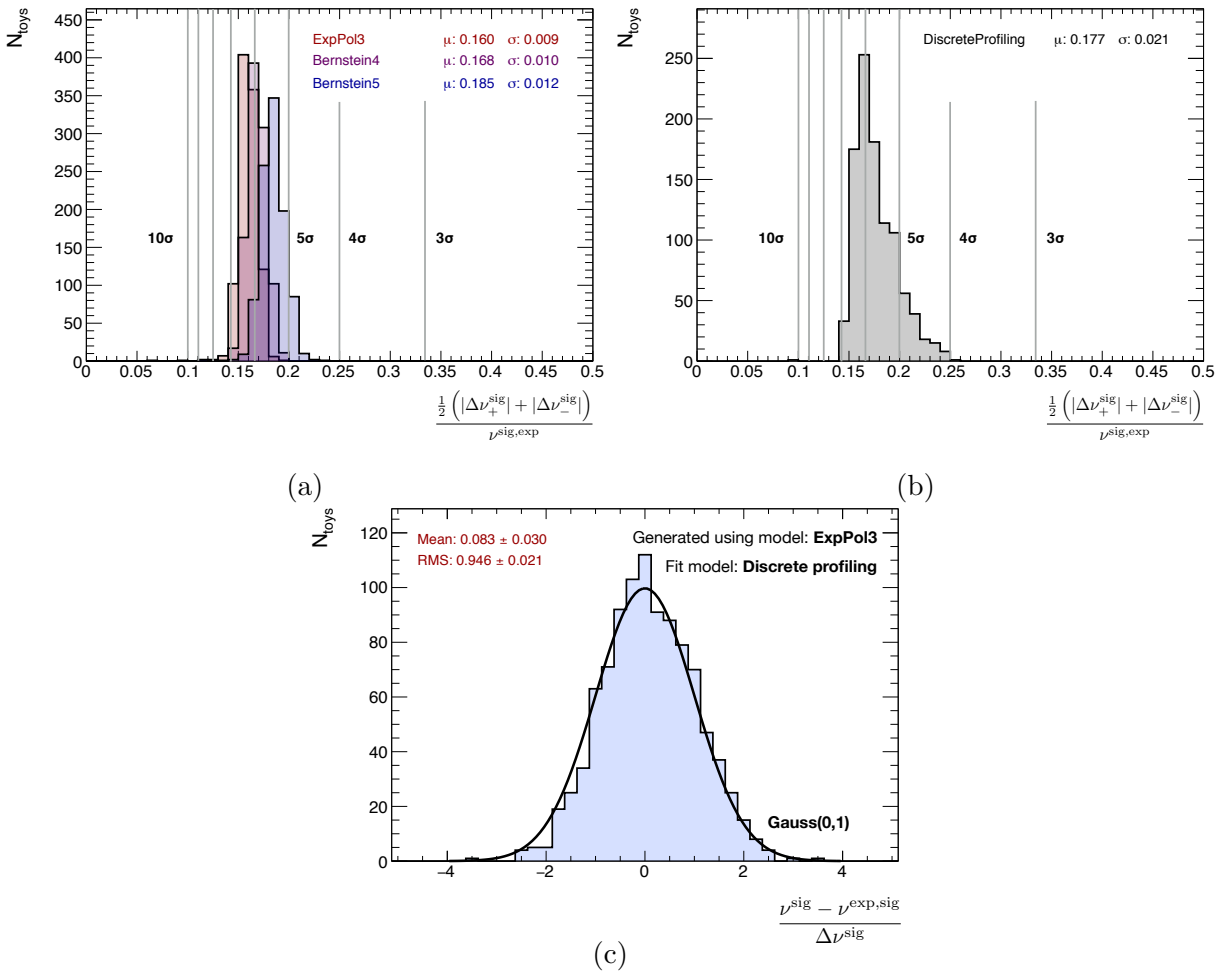

Figure 6.51: Sensitivity, bias and coverage when profiling `ExpPol3`, `Bernstein4` and `Bernstein5`.

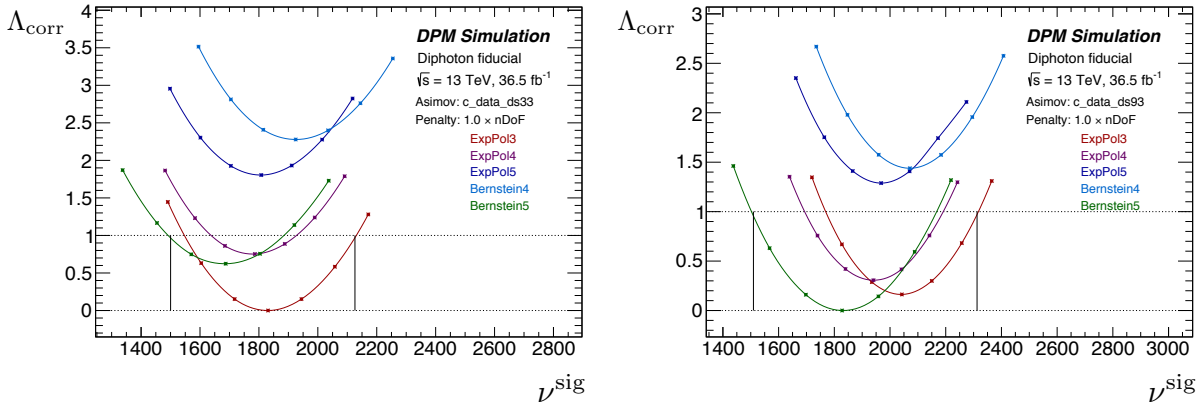

Figure 6.52: Examples of uncertainties defined by competitive functions.

ties. This performance is worse than when fitting using the "correct" function (`ExpPol3`) but better than incorrectly using either `Bernstein4` or `Bernstein5`. Such intermediate behaviour is consistent with the observations of Ref [4].

Figure 6.53 shows the same treatment using `ExpPol3`, `ExpPol4` and `ExpPol5` functions. The mean sensitivities are 16.0 %, 16.9 % and 17.3 % respectively with an intermediate value of 16.6 % when using discrete profiling. Numerical instabilities in several `ExpPol5` fits are visible as outliers. The pull distribution mean and RMS demonstrate limited bias and sufficient coverage respectively.

The sensitivity distribution of Figure 6.53(b) appears to demonstrate a smaller tail than observed in Figure 6.51(b). This may be due to statistical decorrelation. Bootstrap analysis of a partial 18 fb^{-1} dataset shows that the signal yields obtained using an `ExpPol3` background model are approximately 95 % correlated with those obtained using `ExpPol4`, `ExpPol5` and `Bernstein4`. However, they are only 86 % correlated with the `Bernstein5` case. This means that PoIs measured using `ExpPol3` are often subject to different statistical fluctuations than those using `Bernstein5`. If their Λ_{corr} are similar, as demonstrated in Figure 6.52(right), then this difference is added approximately linearly onto the estimated uncertainty.

6.8.4 Discussion

The discrete profiling method is implemented in the signal extraction fit. It is shown to provide good uncertainty coverage, and the bias is smaller than when enforcing an "incorrect" function, when applied to the simulated pseudo-datasets considered. The sensitivity is found to be intermediate within the range of functions profiled. These observations are consistent with the studies presented in Ref. [4]. It is therefore considered to be a viable method for background modelling within ATLAS measurements.

The method was not chosen to model the background in the measurement presented in this chapter. This is due to two reasons:

- The method is computationally challenging and current implementations are limited in performance. It is not possible to perform multi-bin fits to 100,000 bootstrap datasets with fit times of $\mathcal{O}$ (hours) per dataset. Future improvements could mitigate this problem.

- An individual measurement may be impacted by a degradation in sensitivity if, by chance, two functions compete as shown Fig. 6.52 (right). If a significant statistical decorrelation is present then such a case may be due to differing statistical fluctuations. There is concern that this degradation in sensitivity would therefore represent an over-counting of statistical fluctuations.

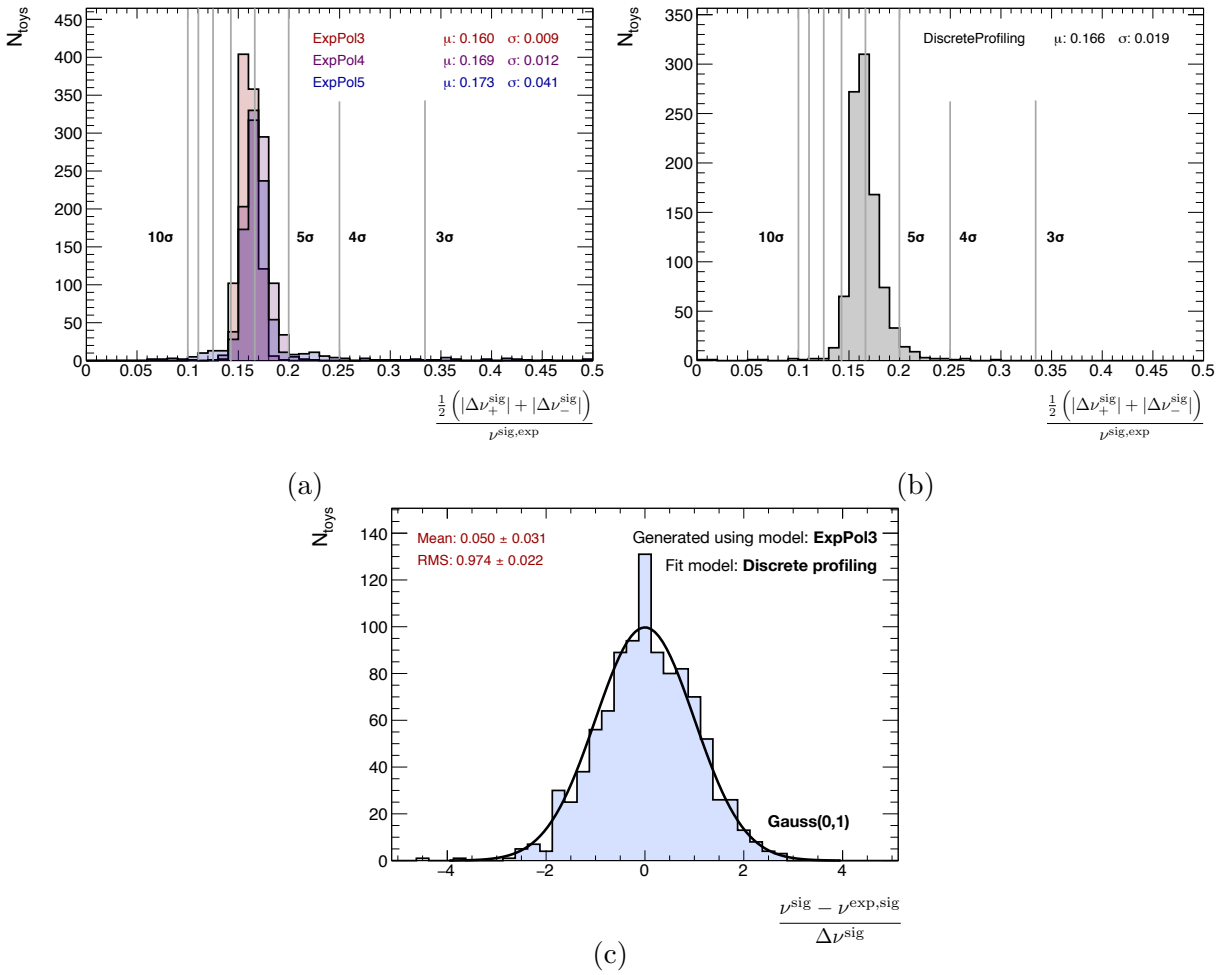

Figure 6.53: Sensitivity, bias and coverage when profiling `ExpPol3`, `ExpPol4` and `ExpPol5`.

In the measurement presented in this chapter, the MC templates are considered sufficiently precise to estimate an upper limit on the systematic bias (spurious signal) induced by approximating the true background shape in each bin with the empirical function chosen. Note that both the templates and functions were tested in the data sidebands to ensure their compatibility. Future measurements may wish to adopt the discrete profiling method, or a similar purely data-driven approach, as the increased dataset size prohibits the generation of templates. If so, further work is recommended in equating the Λ_{corr} of different function families.

Combined $H \to \gamma\gamma$ and $H \to 4l$ cross sections at $\sqrt{s} = 13$ TeV

This chapter describes the measurement of the total cross section of $pp \to H$ production, both inclusively and differentially, using the combination of the $H \to \gamma\gamma$ and $H \to ZZ^* \to 4l$ channels [7, 8]. The main focus is the preparation and validation of the $H \to \gamma\gamma$ contribution to this analysis. Details of the $H \to ZZ^* \to 4l$ measurement are provided where appropriate. The chapter is laid out as follows. Section 7.1 introduces the measurement. Section 7.2 describes the dataset and MC samples studied. Section 7.3 defines the observables and their binning and highlights minor differences compared with the fiducial analyses. The preparation of the $H \to \gamma\gamma$ measurement is described in section 7.4 followed by details of the combination in section 7.5. The results are presented in section 7.6.

7.1 Introduction

Fiducial cross sections were measured in the $H \to \gamma\gamma$ and $H \to ZZ^* \to 4l$ channels using 36.1 fb^{-1} data collected by the ATLAS detector in 2015 and 2016. The results of

$$\begin{aligned} \sigma^{\text{fid}}(H \to \gamma\gamma) &= 55 \pm 9\,(\text{stat.}) \pm 4\,(\text{syst.})\ \text{fb} \\ \sigma^{\text{fid}}(H \to 4l) &= 3.62 \pm 0.50\,(\text{stat.})^{+0.25}_{-0.20}\,(\text{syst.})\ \text{fb} \end{aligned} \tag{7.1}$$

[5, 63] provide comparable sensitivity and are both dominated by statistical uncertainties. The precision of a measured $pp \to H$ cross section will therefore benefit from the combination of channels. Such a combination is justified as both measurements are consistent with the quoted SM expectations of

$$\begin{aligned} \sigma^{\text{fid}}(H \to \gamma\gamma) &= 64 \pm 2\ \text{fb} \\ \sigma^{\text{fid}}(H \to 4l) &= 2.91 \pm 0.13\ \text{fb}. \end{aligned} \tag{7.2}$$

The fiducial phase space regions were defined using requirements on the final state objects. Fiducial cross sections cannot be directly combined because the final states differ in each channel. In this analysis, no selection requirements are applied to the Higgs bo-

son and so the total production cross section is measured. The combination is performed assuming that the fiducial acceptance and branching ratio follow the SM expectation in both channels. This means that one assumes knowledge of (i) what fraction of events are produced outside of the detector acceptance and (ii) how often the Higgs decays through each channel. The measurement of a total cross section with combined statistical sensitivity is therefore complementary to the fiducial cross section measurements in individual channels which are performed with minimal SM assumptions. The total Higgs production cross section is a well-defined theoretical quantity which can be compared with a variety of predictions without imposing fiducial selection criteria.

The total cross section is measured in the full phase space as well as differentially with respect to the following four observables defined at particle level.

- The transverse momentum of the Higgs, p_{T}^{H}, is sensitive to perturbative QCD modelling particularly in the ggF process. The Higgs rapidity, $|y^{\mathrm{H}}|$, is sensitive to parton distribution functions (PDFs).
- The jet multiplicity, N_{jets}, and transverse momentum of the jet with the highest p_{T}, p_{T}^{j1}, are sensitive to the modelling of QCD radiation, the relative contributions of different production processes and possible BSM production of hadronic objects.

7.1.1 Statistical method

The total cross section is measured using an extended maximum likelihood fit. The parameters of interest (PoIs) are the measured total cross sections, $\vec{\sigma}^{\,\mathrm{tot}}$. The likelihood function is defined using the product of the likelihoods of the individual channels, $\mathcal{L}^{\gamma\gamma}$ and $\mathcal{L}^{4l}$, which include the extended Poisson terms. The $H \to \gamma\gamma$ channel constrains $\vec{\sigma}^{\,\mathrm{tot}}$ using the $m_{\gamma\gamma}$ distribution as described in chapter 6. This is binned in intervals of 0.1 GeV to improve numerical performance with negligible degradation in statistical precision. The PoIs in the fiducial analysis were defined as the signal yields, $\vec{\nu}^{\,\mathrm{sig}}$. These are related to the total cross sections via

$$\nu_i^{\,\mathrm{sig}} = \frac{C_i^{\gamma\gamma} \cdot \mathcal{A}_i^{\gamma\gamma} \cdot L^{\mathrm{int}} \cdot \mathcal{B}\left(H \to \gamma\gamma\right) \cdot \sigma_i^{\,\mathrm{tot}}}{1 - f_i^{\mathrm{Dalitz}}} \tag{7.3}$$

where i labels the bin of a differential distribution, $\mathcal{B}$ denotes the branching ratio of the specified channel, $\mathcal{A}_i^X$ is the fiducial acceptance factor in channel X, C_i^X is the correction factor introduced in section 6.5, L^{int} is the integrated luminosity and f_i^{Dalitz} is the fraction of measured events which originate from Dalitz decays. The $H \to 4l$ measurement is based on the binned m_{4l} distributions using $4l \in \{4e, 4\mu, 2e2\mu, 2\mu2e\}$ final states. The PoIs are defined identically to Eq. 7.3 except that no Dalitz subtraction is required in this channel. Details of the likelihood parameterisation can be found in Ref. [63] and references therein. Nuisance parameters (NPs), $\vec{\theta}$, describing systematic uncertainties are externally

constrained by probability distributions, $\mathcal{C}$. NPs can be separated into $\vec{\theta}^{\gamma\gamma}$, $\vec{\theta}^{4l}$ and $\vec{\theta}^{\text{both}}$ depending on which channel they modify the likelihood of. The total likelihood function, $\mathcal{L}$ is then written as

$$\mathcal{L}\left(\vec{m}_{\gamma\gamma}, \vec{m}_{4l}; \vec{\sigma}^{\text{ tot}}, \vec{\theta}^{\gamma\gamma}, \vec{\theta}^{4l}, \vec{\theta}^{\text{both}}\right) = \mathcal{L}^{\gamma\gamma}\left(\vec{m}_{\gamma\gamma}; \vec{\sigma}^{\text{ tot}}, \vec{\theta}^{\gamma\gamma}, \vec{\theta}^{\text{both}}\right) \cdot \mathcal{L}^{4l}\left(\vec{m}_{4l}; \vec{\sigma}^{\text{ tot}}, \vec{\theta}^{4l}, \vec{\theta}^{\text{both}}\right) \cdot \prod_{\theta} \mathcal{C}(\theta). \tag{7.4}$$

The fiducial measurements used likelihood fits to determine the signal yields. These were corrected for detector effects, Dalitz contribution and luminosity after-the-fact, at which point associated systematic uncertainties were introduced. The total cross section measurement applies these corrections, as well as those for acceptance and branching ratio, inside the fit. All associated uncertainties must therefore be implemented using constrained NPs and the PoIs are re-parameterised according to Eq. 7.3. The following steps must be completed in each channel:

- Derivation of the acceptance factors and their uncertainties.
- Implementation of Eq. 7.3, or the $H \to 4l$ equivalent, with all associated systematic uncertainty NPs in the likelihood function.

The likelihood is calculated from the raw dataset in order to profile the precise shape of the likelihood contour without approximating it as exactly Gaussian or Poisson with respect to each PoI or NP. The acceptance factor in bin i of channel X is derived from simulated signal MC samples as

$$A_i^X = \frac{n_i^{X,\text{fid}}}{n_i^{X,\text{tot}}} \tag{7.5}$$

where $n_i^{X,\text{fid}}$ is the particle level signal yield in that bin after applying the fiducial selection criteria and $n_i^{X,\text{tot}}$ is the particle level signal yield in that bin with no selection criteria applied to the Higgs boson.

7.2 Data and Monte Carlo samples

The measured dataset is the same as that described in chapter 6. It comprises of 36 fb^{-1} data collected at $\sqrt{s} = 13$ TeV in 2015 and 2016. The $H \to \gamma\gamma$ channel uses a diphoton trigger with loose identification and E_{T} thresholds of 35 and 25 GeV for the highest two E_{T} photon candidates. This is more than 99 % efficient for selected signal events. The $H \to ZZ^* \to 4l$ channel uses a combination of single, di- and tri-lepton triggers with decreasing thresholds and is 98 % efficient for selected signal events.

Signal MC samples are used to model ggF, VBF, WH, ZH, ttH and bbH production of the Higgs. For the $H \to \gamma\gamma$ channel these samples are described in section 6.2 including

the event generators, PDF sets, `Pythia8` tunes and the total cross section calculations used to determine the overall normalisations. The branching ratio is calculated to be 0.227 % using `HDecay` [214] and `Prophecy4F` [215–217].

The same generated events are used for the $H \to ZZ^* \to 4l$ channel. In this case the branching ratio is calculated to be 0.0124 % including the effect of interference between the $2e2\mu$ and $2\mu2e$ final states which reduces their combined cross section by approximately 10 %. The decay of the Higgs is simulated along with the parton shower by the `Pythia8` program using the `AZNLO` parameter set in both channels, with the exception of the $H \to ZZ^* \to 4l$ ttH sample which uses `Herwig++` with the `UEEE5` parameter set.

7.3 Observable definitions

The fiducial selection criteria are described in section 6.5.1 for the $H \to \gamma\gamma$ channel. The $H \to ZZ^* \to 4l$ channel uses the following fiducial selection criteria applied to stable final state particles with a lifetime τ satisfying $c\tau > 10$ mm. Electrons and muons are required to be not-from-hadron, either directly or through an intermediate τ, and are dressed with not-from-hadron photons within a cone of $\Delta R < 0.1$. Muons (electrons) are required to satisfy $p_{\mathrm{T}} > 5$ (7) GeV and $|\eta| < 2.7$ (2.47). Jets are clustered from all particles excluding not-from-hadron muons, electrons, neutrinos and dressing photons using the anti-k_{T} algorithm with a radius parameter of 0.4. Jets within $\Delta R < 0.1$ (0.2) of a selected muon (electron) are removed. Events are required to have either four muons, four electrons, or two muons and two electrons. The three highest p_{T} leptons must satisfy $p_{\mathrm{T}} > 20$, 15 and 10 GeV respectively. The leading lepton pair with mass m_{12} is defined as the same flavour opposite sign (SFOS) pair with mass closest to m_{Z}. The subleading pair with mass m_{34} is the second-closest SFOS pair. Mass window selections of $50 < m_{12} < 106$ GeV, $12 < m_{34} < 115$ GeV and $115 < m_{4l} < 130$ GeV are applied. All leptons must be separated by $\Delta R > 0.1$ (0.2) if they are the same (different) flavour. All SFOS lepton pairs are required to have an invariant mass greater than 5 GeV.

Observables in the total phase space are defined as follows. The Higgs kinematic quantities $p_{\mathrm{T}}^{\mathrm{H}}$ and $|y^{\mathrm{H}}|$ are calculated from the Higgs four-momentum which is stored in the event record. Jets are clustered from all stable final state particles excluding not-from-hadron muons, electrons and neutrinos, photons used to dress leptons originating from the Higgs decay, or photons originating from the Higgs decay. Jets are defined using the anti-k_{T} algorithm with a radius parameter of 0.4 and must satisfy $p_{\mathrm{T}} > 30$ GeV. No rapidity requirement is applied. This is motivated in order to define a maximally inclusive jet selection, whilst a minimum jet transverse momentum is applied to reduce sensitivity to the production and modelling of low energy radiation. The jet definition is designed to be independent of the Higgs decay products and reflect the hadronic activity of the event. These are used to define the observables p_{T}^{j1} and N_{jets}.

Bin boundaries of differential distribution														
$p_{\mathrm{T}}^{\mathrm{H}}$	$H \to \gamma\gamma$ (old)	0			20	30	45	60	80	120	170	220	350	GeV
	$H \to \gamma\gamma$ (new)	0	10		20	30	45	60	80	120	200		350	
	$H \to ZZ^* \to 4l$	0	10	15	20	30	45	60	80	120	200		350	
	Combination	0	10		20	30	45	60	80	120	200		350	
$\lvert y^{\mathrm{H}} \rvert$	$H \to \gamma\gamma$	0	.15	.3	.45	.6	.75	.9	1.2	1.6			2.4	
	$H \to ZZ^* \to 4l$	0		.3		.6		.9	1.2	1.6	2.0		2.5	
	Combination	0		.3		.6		.9	1.2	1.6			2.5	
$p_{\mathrm{T}}^{\mathrm{j1}}$	$H \to \gamma\gamma$	0 jet	30		55	75	120	350						
	$H \to ZZ^* \to 4l$	0 jet	30	40	55	75	120	350	GeV					
	Combination	0 jet	30		55	75	120	350						
N_{jets}	$H \to \gamma\gamma$	$= 0$	$= 1$		$= 2$	≥ 3								
	$H \to ZZ^* \to 4l$	$= 0$	$= 1$		$= 2$	≥ 3								
	Combination	$= 0$	$= 1$		$= 2$	≥ 3								

Table 7.1: Differential cross section bin boundaries compared with the individual channels.

Where possible, differential distributions in the two channels were measured using common bin boundaries in order to facilitate the combination. These boundaries define the binning used for the combined distribution. When one channel has two fine granularity bins with boundaries at $\{ A , B , C \}$ and the other has a single coarse bin with boundaries at $\{ A , C \}$, the coarser boundaries are used for the combination. This is achieved by writing the cross section as

$$\sigma_{AC}^{\mathrm{tot}} = \sigma_{AB}^{\mathrm{tot}} + \sigma_{BC}^{\mathrm{tot}} \tag{7.6}$$

where subscripts denote bin boundaries. The PoI $\sigma_{AC}^{\mathrm{tot}}$ is then constrained using two measured bins in the first channel and a single bin in the second channel. In the case of the $|y^{\mathrm{H}}|$ observable, the uppermost limit of the $H \to \gamma\gamma$ measurement was defined at 2.4 because this channel has no acceptance at higher values. The combination extends the uppermost limit to 2.5, identical to that used for $H \to ZZ^* \to 4l$. The difference is accounted for by the acceptance correction, i.e. the denominator of $A_i^{\gamma\gamma}$ is defined with a bin extending to 2.5 whilst the numerator remains unchanged. The impact on the acceptance factor of this bin is 8 %.

In the $p_{\mathrm{T}}^{\mathrm{H}}$ observable, the binnings of the individual $H \to \gamma\gamma$ and $H \to ZZ^* \to 4l$ measurements were found to be inconsistent. For the combination, the binning of the $H \to \gamma\gamma$ measurement is modified in order to achieve common boundaries with the $H \to ZZ^* \to 4l$ channel. This means that the boundaries at $\{ 120 , 170 , 220 , 350 \}$ GeV are changed to $\{ 120 , 200 , 350 \}$ GeV. In addition, the granularity at low p_{T} is improved by dividing the first bin into two. The boundaries at $\{ 0 , 20 \}$ GeV are replaced by $\{ 0 , 10 , 20 \}$ GeV. This is found to satisfy the binning criteria described in section 6.3.4. Table 7.1 compares the bin boundaries of the $H \to \gamma\gamma$, $H \to ZZ^* \to 4l$ and combined measurements. The remainder of this section describes the impact of the jet rapidity and binning modifications in the $H \to \gamma\gamma$ channel.

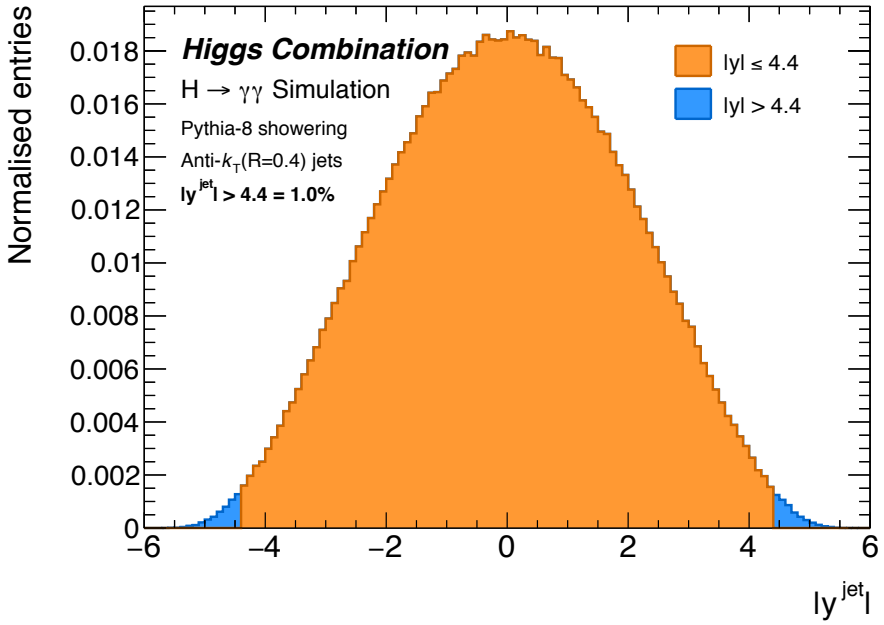

Figure 7.1: Jet rapidity distribution in the total phase space.

Impact of removing the jet rapidity cut

In the fiducial analyses, both channels required the jet rapidity to satisfy $|y| < 4.4$. In the combination, no rapidity cut is applied. This is done to define jet observables with the fewest selection criteria possible. Figure 7.1 shows the jet rapidity distribution summed over all production processes. Orange bins satisfy $|y| < 4.4$ whereas blue bins have $|y| > 4.4$ and make up 1 % of all measured jets. Removing this cut causes events to migrate between bins of N_{jets} and p_{T}^{j1}. The expected yield does not change by more than 2 % in any bin. When breaking down into individual production processes, the largest change is 15 % observed in the VBF, $N_{\text{jets}} = 0$ bin. This is because VBF production tends to create a dijet system at very forward rapidities. No other change is greater than 5 %.

Modification to the binning of p_{T}^{H}

The signal model parameters, background function choice, correction factors and all associated systematic uncertainties are re-evaluated using the modified binning of the p_{T}^{H} distribution in the $H \to \gamma\gamma$ channel. None of these quantities are found to deviate significantly from those derived using the original binning and no significant change in the total systematic uncertainty is observed. Figure 7.2 shows a comparison of the measured signal yields obtained using the original and updated binnings. Error bars represent the total fit uncertainty and include the spurious signal. The binning is modified both at low and high p_{T} as shown in Table 7.1. The updated binning is not found to cause significant fluctuations compared with the original $H \to \gamma\gamma$ analysis. This binning will be used throughout the remainder of this chapter.

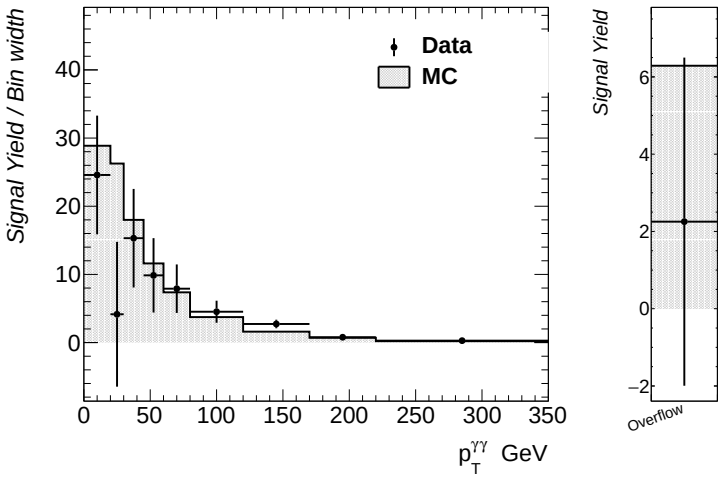

(a) Original binning

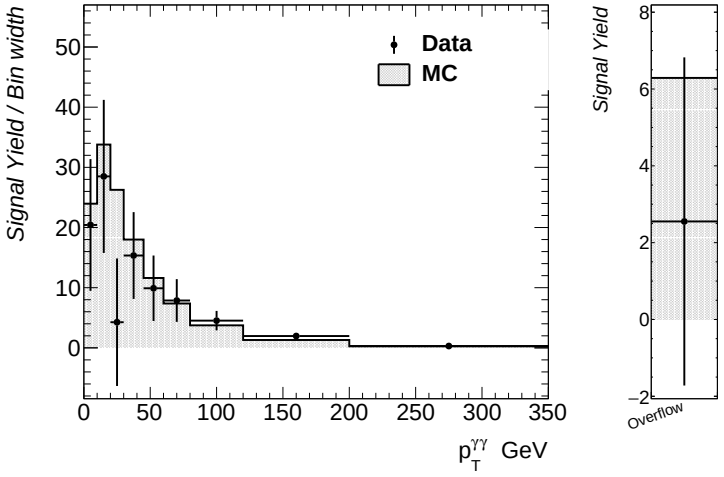

(b) Updated binning

Figure 7.2: Comparison between the $p_{\mathrm{T}}^{\gamma\gamma}$ signal yields measured using the original binning and that defined for the combination with $H \to ZZ^* \to 4l$.

7.4 Preparation of the $H \to \gamma\gamma$ measurement

This section discusses the total cross section measurement in the $H \to \gamma\gamma$ channel. This is performed using a statistical workspace describing the likelihood function of the $H \to \gamma\gamma$ channel. The creation and validation of the workspace is described. This includes the derivation of acceptance factors and their uncertainties. The combination is later performed by simultaneously constraining the workspaces of the two channels.

7.4.1 Acceptance factors

Figure 7.3 shows the acceptance factors in the $H \to \gamma\gamma$ channel split into individual production processes. The combined factors are labelled *total* and shown in black. Coloured boxes display the statistical uncertainty caused by the finite size of the MC samples. Some

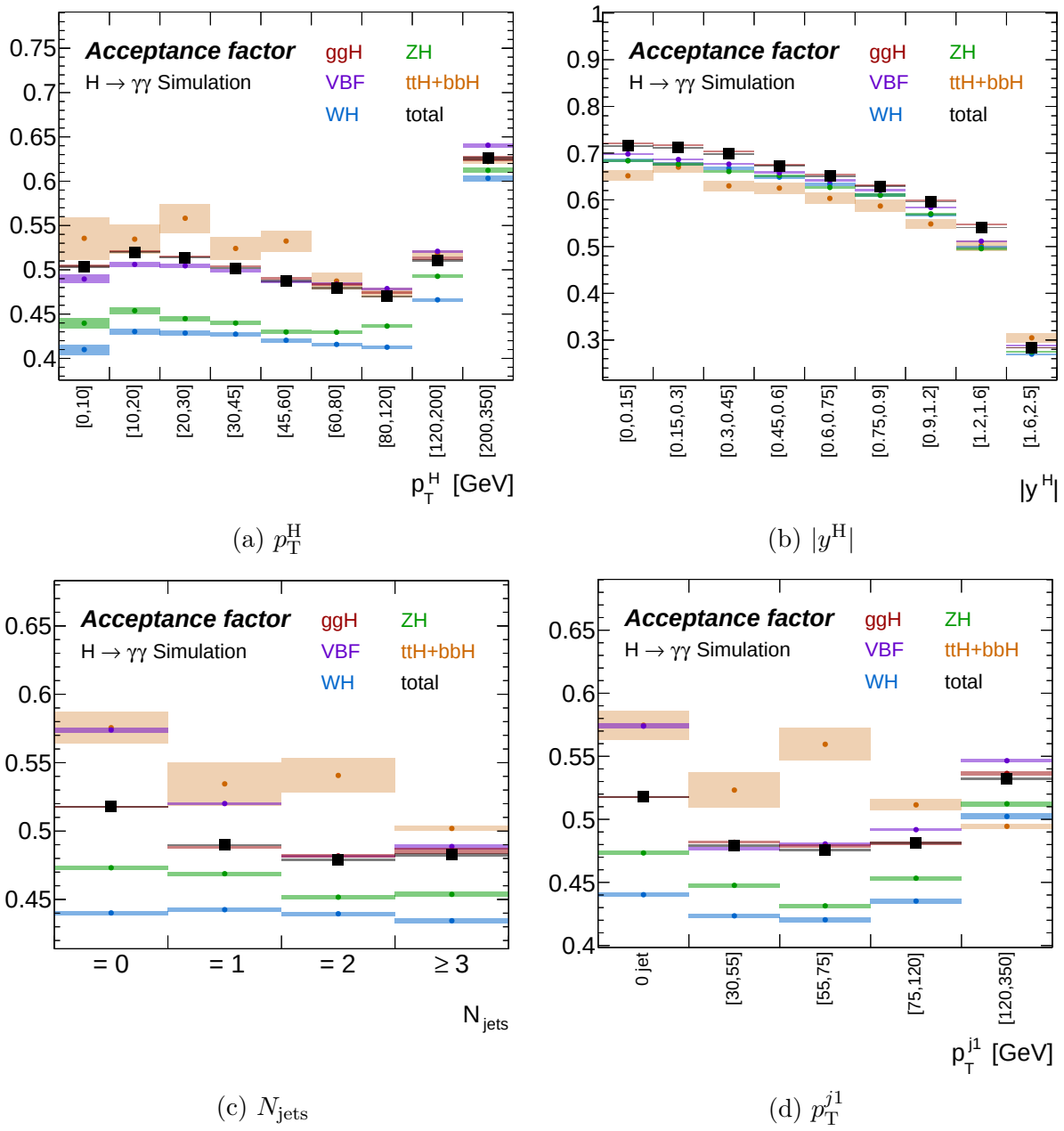

(a) $p_{\mathrm{T}}^{\mathrm{H}}$ (b) $|y^{\mathrm{H}}|$

(c) N_{jets} (d) p_{T}^{j1}

Figure 7.3: Acceptance factors in the $H \to \gamma\gamma$ channel with statistical uncertainties.

production process dependence is observed in all distributions. This is expected because topologies are differently affected by the momentum, rapidity and isolation requirements of the *diphoton fiducial* region as well as the acceptance of particle level jets. Note that the fiducial volume requires that both photons satisfy $|y| < 2.37$. This causes the steep decline in fiducial acceptance at high $|y^{\mathrm{H}}|$. The acceptance of low-$|y^{\mathrm{H}}|$ bins is approximately 70 % whereas other distributions are typicaly $\sim$ 50 %. This is because the other distributions integrate over all values of $|y^{\mathrm{H}}|$, including those above the detector acceptance. Since production processes follow a different spread of $|y^{\mathrm{H}}|$, this likely causes the $ttH + bbH$ component (orange) to appear below the *total* in the first 8 bins of $|y^{\mathrm{H}}|$ but generally be above it in all other distributions. The *diphoton fiducial* acceptance factor is

50.4 % resulting from the combination of *ggF* (50.6 %), *VBF* (50.4 %), *WH* (44.0 %), *ZH* (46.2 %) and $ttH + bbH$ (52.9 %).

Model dependence: signal composition uncertainty

The signal composition uncertainty is evaluated by separately varying the cross sections of the different production processes by factors commensurate with the uncertainties on the signal strengths measured in Run 1 [109] with the exception of ttH for which the Run 2 contraint is used [250]. These variations are identical to the *alternative* variations presented in section 6.5.3. For each production process, a single NP describes the up- and down-wards variations. The ggF, VBF, WH, ZH, ttH and bbH cross sections are varied by ±14.5 %, ±20.3 %, ±43.3 %, ±46.8 %, $^{+50}_{-30}$ % and ±22 % respectively. The combination of all six variations has a maximum impact of $^{+0.4}_{-0.2}$ % on the acceptance factors in bins of $p_{\mathrm{T}}^{\mathrm{H}}$, ±0.2 % in bins of $|y^{\mathrm{H}}|$, $^{+0.3}_{-0.4}$ % in bins of $p_{\mathrm{T}}^{\mathrm{j1}}$, ±0.5 % in bins of N_{jets} and ±0.2 % in the *diphoton fiducial* region.

Understanding the shape of $A^{\gamma\gamma}\left(p_{\mathrm{T}}^{\mathrm{H}}\right)$

Two turning points are observed when the acceptance factors are plotted in bins of $p_{\mathrm{T}}^{\mathrm{H}}$ as shown in Figure 7.3(a). By contrast, the acceptance factors in the $H \to ZZ^* \to 4l$ channel are observed to monotonically increase as a function of $p_{\mathrm{T}}^{\mathrm{H}}$. This is explained as follows. The *diphoton fiducial* volume is defined by the presence of two photons passing η, isolation and $p_{\mathrm{T}}/m_{\gamma\gamma}$ requirements. Figure 7.4(a) shows the acceptance in bins of $p_{\mathrm{T}}^{\mathrm{H}}$ when no $p_{\mathrm{T}}/m_{\gamma\gamma}$ requirements are imposed[1]. No turning points are observed. Figure 7.4(b) shows the case when only $p_{\mathrm{T}}/m_{\gamma\gamma}$ requirements are imposed. This demonstrates that the dip in acceptance at intermediate $p_{\mathrm{T}}^{\mathrm{H}}$ is caused by the $p_{\mathrm{T}}/m_{\gamma\gamma}$ requirement.

The Higgs boson is modelled with a mass of $m_{\mathrm{H}} = m_{\gamma\gamma} = 125$ GeV and a width of 4 MeV. The effective minimum p_{T} requirement is therefore 43.8 (31.3) GeV for the leading (subleading) photon. Figure 7.4(c) shows the distribution of the subleading p_{T} in three slices of $p_{\mathrm{T}}^{\mathrm{H}}$ corresponding to before, during and after the acceptance drop. Figure 7.4(d) shows the $\Delta\phi$ between the two decay photons. In the rest frame of the Higgs, the photons are produced back-to-back with $m_{\mathrm{H}}/2 \sim 63$ GeV of momentum. If $p_{\mathrm{T}}^{\mathrm{H}}$ is below 40 GeV then 17 % of events fail the subleading photon p_{T} cut and the diphoton $\Delta\phi$ is steeply distributed towards π. This is shown by the black points. As $p_{\mathrm{T}}^{\mathrm{H}}$ increases there is often a cancellation between the vector $\vec{p}_{\mathrm{T}}$ of a photon (in the Higgs rest frame) and the transverse boost of the Higgs. The magnitude of the resulting subleading photon p_{T} is reduced on average, and more events fail the cut. This is shown in red. At high $p_{\mathrm{T}}^{\mathrm{H}}$, the transverse boost forces both photons to have high p_{T} in the same hemisphere of ϕ. The acceptance therefore increases again, and $\Delta\phi$ typially takes value of $< \pi/2$. This is shown in blue.

[1] A subset of ggF events are used for this study.

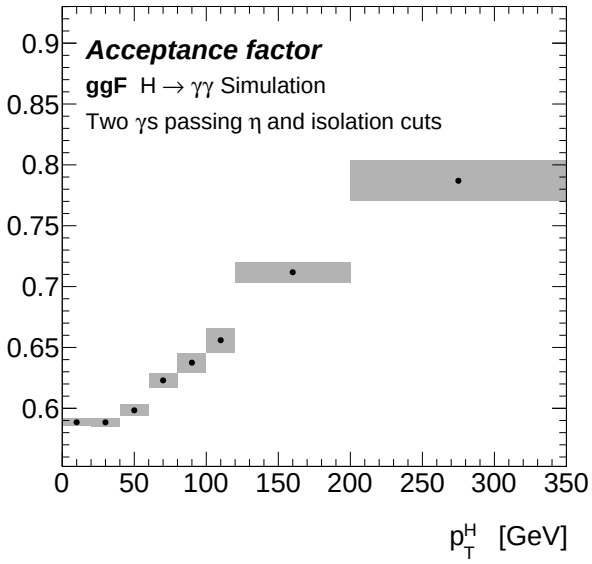

(a) Acceptance factors (no p_{T}^{γ} cuts).

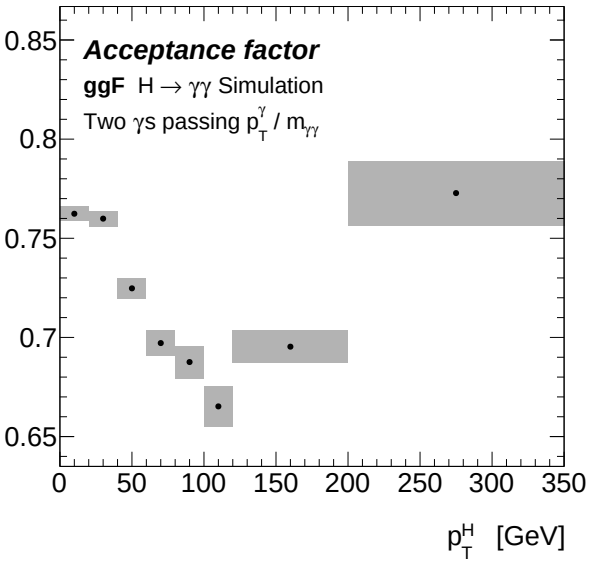

(b) Acceptance factors (only p_{T}^{γ} cuts).

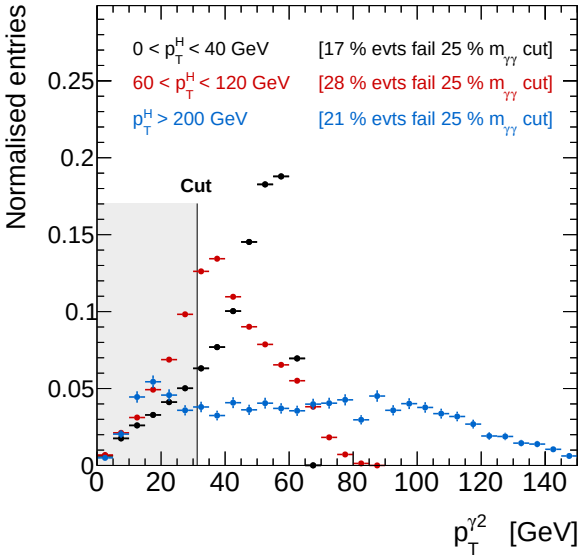

(c) Distribution of $p_{\mathrm{T}}^{\gamma 2}$.

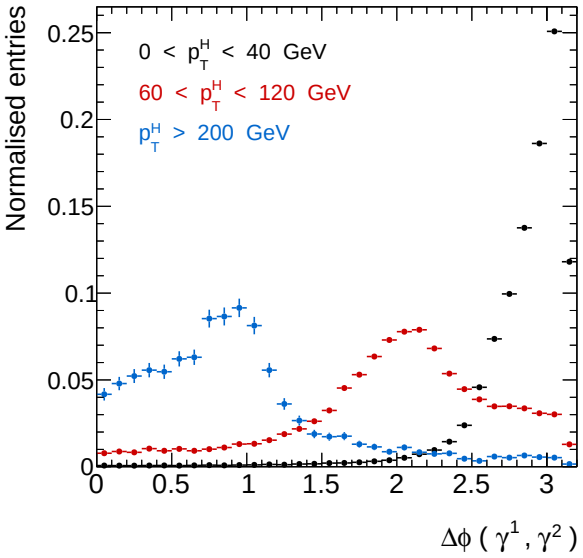

(d) Distribution of $\Delta\phi\left(\gamma^1, \gamma^2\right)$.

Figure 7.4: Plots summarising the acceptance factor dependence on $p_{\mathrm{T}}^{\mathrm{H}}$.

Model dependence: parton shower and hadronisation uncertainty

An uncertainty due to the modelling of parton shower and hadronisation is evaluated. The nominal acceptance factors, for which parton shower, hadronisation and underlying event were simulated using the `Pythia8` program, are compared with those using `Herwig7`. These are shown in Figure 7.5. Coloured boxes represent statistical uncertainties which are likely overestimated due to the correlated event generation of the two samples. The difference between `Pythia8` and `Herwig7` is assigned as a symmetric systematic uncertainty as shown in Table 7.2. The amplitude is ±0.7 % on the *diphoton fiducial* acceptance factor. The maximum amplitude is ±1.4 % observed at low $p_{\mathrm{T}}^{\mathrm{H}}$.

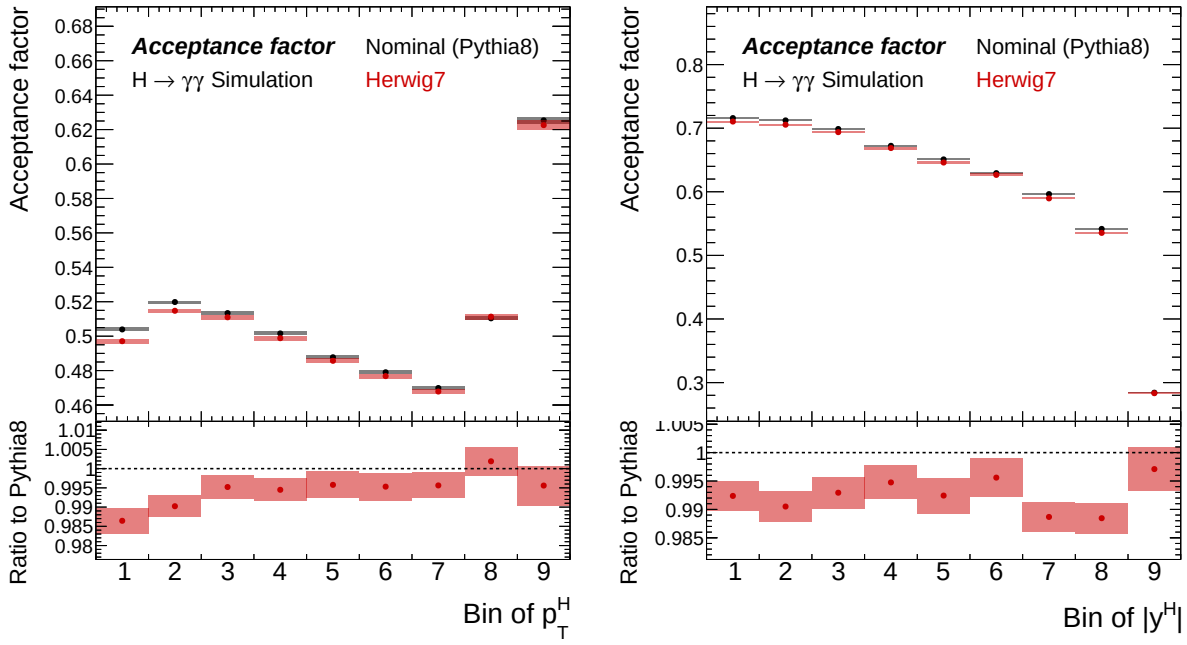

(a) $p_{\mathrm{T}}^{\mathrm{H}}$ (b) $|y^{\mathrm{H}}|$

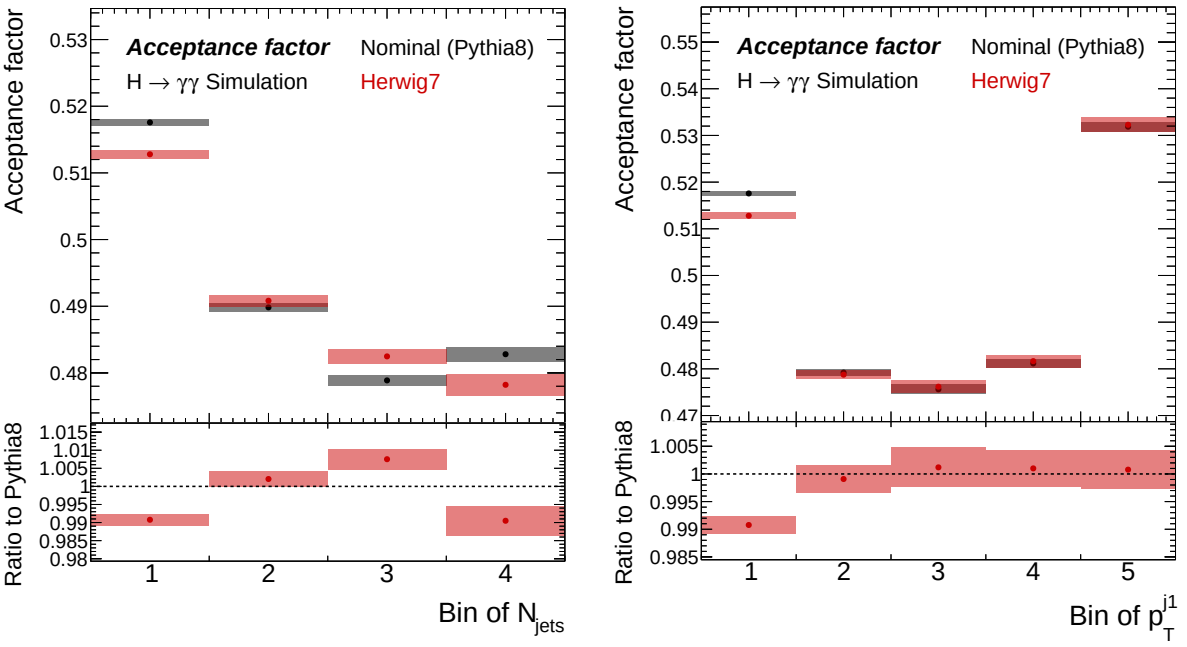

(c) N_{jets} (d) p_{T}^{j1}

Figure 7.5: Parton shower dependence of acceptance factors in the $H \to \gamma\gamma$ channel.

	|Herwig7 - Pythia8| [%]								
	Bin 1	2	3	4	5	6	7	8	9
Diphoton fiducial	0.7								
$p_{\mathrm{T}}^{\mathrm{H}}$	1.4	1.0	0.5	0.6	0.4	0.5	0.4	0.2	0.4
$\lvert y^{\mathrm{H}}\rvert$	0.8	0.9	0.7	0.5	0.8	0.4	1.1	1.2	0.3
N_{jets}	0.9	0.2	0.8	1.0					
p_{T}^{j1}	0.9	0.1	0.1	0.1	0.1				

Table 7.2: Parton shower uncertainties on the $H \to \gamma\gamma$ acceptance factors.

$p_{\mathrm{T}}^{\mathrm{H}}$	Systematic uncertainty [%]								
	Bin 1	2	3	4	5	6	7	8	9
ggF: MC stat.	0.2	0.2	0.2	0.2	0.2	0.2	0.2	0.2	0.3
ggF: PDF	1.0	0.9	0.8	0.7	0.6	0.5	0.5	0.3	0.3
ggF: α_s	0.3	0.3	0.2	0.2	0.2	0.1	0.1	0.1	-
ggF: QCD	-	-	-	-	-	-	-	-	0.1
VBF: QCD	-	-	-	-	-	-	-	-	0.1

Table 7.3: Systematic uncertainties on the acceptance factors from other sources.

Other modelling uncertainties

As well as the signal composition and parton shower, several other systematic uncertainties are assigned. These were evaluated by another member of the analysis team. 30 variations in PDF are considered following the PDF4LHC recommendations [222]. A single uncertainty represents the quadrature sum. PDF modelling in the ggF process has a 0.7 % impact on the *diphoton fiducial* acceptance factor. Varying the strong coupling constant α_s according to the same recommendations has a 0.2 % impact from ggF. The impact of possible QCD mismodelling is estimated as the envelope produced when the renormalisation and factorisation scales are varied by factors of 0.5, 1.0 and 2.0 in all 8 possible permutations. In the ggF NNLOPS sample, the QCD modelling is instead estimated as the quadrature sum of 9 variations which impact the jet multiplicity, kinematics and Higgs p_{T} [5]. The impact due to ggF is 0.1 %. PDF, α_s and QCD variations of all other production processes have an impact of < 0.1 % on the *diphoton fiducial* acceptance factor. Table 7.3 shows the dominant uncertainties in bins of $p_{\mathrm{T}}^{\mathrm{H}}$ requiring that the impact is at least 0.1 %. An additional component due to finite MC dataset size is included and labelled *MC stat.* PDF modelling of ggF is dominant at low $p_{\mathrm{T}}^{\mathrm{H}}$ and comparable with *MC stat* in the final bins. The only ≥ 0.1 % contribution from any other production process is the QCD modelling of VBF which remains small.

7.4.2 Constructing the likelihood function

This section describes how the likelihood function used to extract signal yields in the fiducial cross section measurement is modified to extract total cross sections. The original function contains unconstrained NPs describing the background shape and constrained NPs describing the impact of photon energy scale (39 NPs), photon energy resolution (9 NPs) and Higgs mass (1 NP) uncertainties on the signal shape. These are also used in the total cross section measurement. In each bin i of a differential distribution, the signal yield ν_i^{sig} is related to the total cross section σ_i^{tot} through the factors $C_i^{\gamma\gamma}$, $\mathcal{A}_i^{\gamma\gamma}$, L^{int}, $\mathcal{B}(H \to \gamma\gamma)$ and f_i^{Dalitz} as introduced in Eq. 7.3. These quantities are profiled within their systematic

uncertainties. The evaluated quantity Q_i is related to its nominal value Q_i^{nom} as

$$Q_i\left(\vec{\theta}\right) = Q_i^{\text{nom}} \cdot \prod_{\theta_Q} \begin{cases} 1 + \sigma^Q_{+,i} \cdot \theta_Q & \theta_Q \geq 0 \\ 1 + \sigma^Q_{-,i} \cdot \theta_Q & \theta_Q < 0 \end{cases} \tag{7.7}$$

where θ_Q labels a NP describing a systematic uncertainty and $\sigma^Q_{\pm,i}$ is the corresponding fractional uncertainty amplitude which is allowed to be asymmetric. All NPs introduced for the total cross section are profiled using external standard normal constraint terms. These uncertainties could instead be written as pulls on the PoIs themselves, however this approximates them as having individually Gaussian shapes. Writing uncertainties on the quantity they impact means that the likelihood will have a more precise shape when profiled as a function of the PoIs.

Uncertainties on the correction factors are described in section 6.5. In the fiducial analysis, the physics modelling uncertainty was taken as the envelope of the signal composition, underlying event / parton shower (UE/PS) and Higgs kinematic sources. A conservative signal composition uncertainty was used. This approach is modified in two ways:

- The signal composition, UE/PS and kinematic sources are accounted for using separate systematic NPs. Their impacts are effectively combined in each bin rather than taking the envelope. This has small impact on the measurement precision in every bin and is motivated because the envelope method does not allow bin correlations to be taken into account.

- The signal composition uncertainty is evaluated using the *alternative* method presented in section 6.5.3. Six NPs correspond to variations in the ggF, VBF, WH, ZH, ttH and bbH cross sections. This is consistent with the approach used to evaluate the equivalent uncertainties in the acceptance factor and $H \to ZZ^* \to 4l$ channel.

With this updated approach, a total of eight NPs are used to describe the impact of physics modelling assumptions on the correction factors in each distribution. The largest per-bin impact due to signal composition is 2.5 %, due to UE/PS is 1.8 % and due to Higgs kinematic reweighting is 4.3 %. A further three NPs describe the impact of trigger, vertex selection and Dalitz contribution respectively. Their combined impact is less than 0.8 % in all bins. One NP describes the impact of pileup jet modelling which is 0 for the p_{T}^{H} and $|y^{\text{H}}|$ observables and has a maximum of 5.6 %. Five NPs describe the impact of photon energy scale, photon energy resolution, photon identification, track isolation and pileup reweighting respectively. These have a maximum combined impact of 4.1 % at high p_{T}^{H}. An additional 19 NPs describe jet energy scale and resolution uncertainties. The maximum impact is 16 % in the $N_{\text{jets}} \geq 3$ bin.

Uncertainties on the acceptance factors are described in section 7.4.1. Three NPs are used to describe ggF PDF, α_s and QCD modelling respectively. Uncertainties on the

NP		Number	Constraint
Sig/bkg modelling	Background shape	variable-per-bin	None
	PES	39	Gaus
	PER	9	Log-norm
	m_H	1	Gaus
	Spurious signal	1-per-bin	Gaus
Correction factor (measurement)	Trigger efficiency	1	Gaus
	Vertex ID	1	Gaus
	Dalitz subtraction	1	Gaus
Correction factor (modelling)	PES	1	Gaus
	PER	1	Gaus
	Photon ID	1	Gaus
	Track Isolation	1	Gaus
	PRW	1	Gaus
	Pileup	1	Gaus
	UE/PS	1	Gaus
	Kinematic reweighting	1	Gaus
	JES/JER	19	Gaus
Acceptance factor	ggF PDF	1	Gaus
	ggF α_s	1	Gaus
	ggF QCD	1	Gaus
	Parton shower	1	Gaus
Correction & Acceptance	Signal composition	6	Gaus
Other	Luminosity	1	Gaus
	Branching ratio	1	Gaus

Table 7.4: Summary of the NPs in the $H \to \gamma\gamma$ total cross section measurements.

modelling of other production processes are neglected due to their < 0.2 % impact. One NP is used to describe parton shower modelling. Signal composition variations are described using the same six NPs used to describe the equivalent correction factor uncertainties. This ensures that the anticorrelation between the two quantities is correctly taken into account.

The luminosity and branching ratio uncertainties are 3.2 % and 2.1 % [28] respectively and described by a single NP each. The spurious signal is treated as an absolute uncertainty on the signal yield. This means that the signal PDF is normalised according to ${\nu_i}^{\text{sig,corr}}$ which is defined as

$${\nu_i}^{\text{sig,corr}} = {\nu_i}^{\text{sig}} + \theta_i^{SS} \cdot {\nu_i}^{\text{SS}} \tag{7.8}$$

where ${\nu_i}^{\text{SS}}$ is the expected spurious signal contribution and θ_i^{SS} is the corresponding NP in that bin. The number of spurious signal NPs per distribution is equal to the number of bins. The spurious signal contribution is evaluated proportionately to the integrated luminosity. This means that when L^{int} is pulled downwards, the expected spurious signal contribution is reduced accordingly (and vice versa). Table 7.4 summarises all NPs profiled in the $H \to \gamma\gamma$ total cross section measurement.

7.4.3 Closure tests

Several closure tests are performed in order to validate the central values and uncertainties evaluated when using the total cross section workspace. These are as follows:

1. The acceptance factors and branching ratio are fixed to 1. A workspace fit therefore returns the fiducial cross sections. These are compared with the results of the fiducial cross section analysis as shown in Table 7.5 in bins of N_{jets}. The agreement is better than 0.2 % in all distributions.

2. When fitting for the fiducial cross sections, the statistical uncertainties are evaluated by fixing the constrained NPs to their best-fit values and profiling the likelihood as a function of the PoIs. These are compared with the published values as shown in Table 7.6 in bins of N_{jets}. Relative fluctuations are $\lesssim 2$ % in all distributions and are considered to be numerical in nature. Note that this test uses the Hessian matrix to evaluate PoI uncertainties by numerically estimating the covariance at the point of maximum likelihood. This leads to symmetric uncertainties. The fiducial analysis used the `Minos` program which scans the likelihood curve and so allows asymmetric uncertainties. The total uncertainties are subject to relative fluctuations of up to several percent. This is assumed to be because the fiducial analysis applied systematic shifts and combined the resulting uncertainties on the cross section instead of implementing them as pulls on the correction factors.

3. A toy dataset, finely binned in $m_{\gamma\gamma}$, is generated using (i) the expected background shapes and normalisations obtained using a fit to the data sidebands and (ii) the expected signal shapes and normalisations from MC. The workspace is used to extract the total cross sections from this dataset. These are compared with the expected values as shown in Table 7.7 in bins of N_{jets}. The agreement is better than 0.1 % in all distributions.

7.4.4 $H \to \gamma\gamma$ total cross section result

Using the $H \to \gamma\gamma$ channel, the total cross section is measured to be $47.9^{+9.1}_{-8.6}$ pb using a workspace built from the *diphoton fiducial* cross section measurement. The total systematic uncertainty on the acceptance factor is 0.9 %. The correction factor, luminosity and branching ratio uncertainties are 2.4 %, 3.2 % and 2.1 % respectively. The systematic uncertainty from signal and background modelling is 7.1 %. The total systematic uncertainty is 8.7 %. The measurement precision is dominated by a 16.6 % statistical uncertainty. The result is consistent with the SM expectation of 55.6 ± 2.5 pb [28] to within 1 standard deviation. The differential results will be presented along with the combination in section 7.6.

σ^{fid} [fb]	N_{jets} = 0	= 1	= 2	≥ 3
Target result	24.6	15.1	7.6	4.4
Workspace result	24.6	15.1	7.6	4.4
SM expectation	36.4	16.9	7.2	2.8
$\frac{\text{Workspace}-\text{Target}}{\text{SM}}$	-0.1 %	< 0.1 %	< 0.1 %	-0.1 %

Table 7.5: Fiducial cross sections measured using the workspace approach.

$\Delta\sigma^{\text{fid}}$ (stat.) [fb]		N_{jets} = 0	= 1	= 2	≥ 3
Target result	up	7.70	4.43	2.52	1.38
	down	7.68	4.40	2.50	1.36
Workspace result	up	7.68	4.39	2.51	1.37
	down	7.68	4.39	2.51	1.37
$\frac{\text{Workspace}-\text{Target}}{\text{Target}}$	up	-0.3 %	-0.8 %	-0.4 %	-0.8 %
	down	0.1 %	-0.2 %	0.4 %	0.7 %

Table 7.6: Fiducial cross section statistical uncertainties using the workspace approach.

σ^{tot} [fb]	N_{jets} = 0	= 1	= 2	≥ 3
SM expectation	31.2	15.1	6.63	2.52
Workspace closure test	31.2	15.1	6.62	2.52
$\frac{\text{Closure}-\text{SM}}{\text{SM}}$	< 0.1 %	< 0.1 %	< 0.1 %	< 0.1 %

Table 7.7: Closure test of total cross sections using the workspace approach.

7.5 Summary of combined measurement

The $H \to ZZ^* \to 4l$ channel has an acceptance of 42 % and a fiducial correction factor of 53 %. The non-fiducial contribution is 2 %. This section provides a short summary of the full details provided in Ref. [63] before discussing the statistical framework of the combination. Templates describe the signal and background contributions in bins of m_{4l}. The background is dominated by an irreducible component of non-resonant ZZ^* production from $q\bar{q}$ annihilation and gluon fusion. Several sub-dominant reducible components from Z + jets, $t\bar{t}$, WZ, $t\bar{t} + Z$ and triboson events are also accounted for. The dominant background contributions are constrained using a combination of data-driven control regions and efficiency determinations which are combined with modelling from large simulated samples. Pure simulation is used to model small backgrounds. In most cases the background templates are derived from simulation and fixed for a given luminosity in the likelihood fit. The total cross section is then related to the normalisation of the signal templates.

Using the $H \to ZZ^* \to 4l$ channel, the total cross section is measured to be 68^{+11}_{-10} pb.

This consistent with a SM expectation of 55.6 ± 2.5 pb to approximately 1.2 standard deviations. Statistical uncertainty dominates with a contribution of 14 % compared with a systematic uncertainty of 7 %. This is dominated by 3 % contributions from the identification and energy scale and resolution measurements of both electrons and muons as well as 4 % from luminosity. Whilst the nominal luminosity uncertainty is 3.2 %, the impact on the cross section is larger due to its effect on the background normalisation. In the fiducial spectra relevant for the combination, individual bins of differential distributions are impacted by $1-5$ % from lepton measurements, $0-30$ % from jet energy scale and resolution and $0-22$ % from the modelling of correction factors. The latter is driven by the signal composition uncertainty which is larger in the $H \to ZZ^* \to 4l$ channel due to the use of lepton isolation requirements at detector but not particle level. Acceptance factor uncertainties are derived using the same methodology as in the $H \to \gamma\gamma$ channel. An additional component is included to account for the modelling of m_{H} with an impact of ≤ 0.7 %. The largest uncertainty is ≤ 4.2 % due to parton shower modelling.

In the combined fit, several NPs are constrained simultaneously using both channels. Correlations in the branching ratios are accounted for. The branching ratios are also correlated with m_{H} causing a maximum relative impact of 2 % on $\mathcal{B}(H \to ZZ^* \to 4l)$. Acceptance factor PDF, scale, QCD and parton shower uncertainties are treated as 100 % correlated between channels. The dominant sources of correction factor systematic uncertainties in jet-related distributions, i.e. the 6 NPs describing signal composition and 19 NPs describing jet energy scale and resolution variations, are also 100 % correlated. The signal composition NPs also impact the acceptance factors in both channels to properly account for this (anti-)correlation. The luminosity uncertainty is also 100 % correlated between channels.

7.6 Results

The total cross section is measured to be $57.0\ ^{+6.0}_{-5.9}\,(\mathrm{stat.})\ ^{+4.0}_{-3.3}\,(\mathrm{syst.})$ pb. This is consistent with the SM expectation of 55.6 ± 2.5 pb. The agreement between the two channels is estimated by profiling $-2\ln\mathcal{L}/\mathcal{L}^{\max}$ as a function of $\sigma^{\mathrm{tot}}(H \to \gamma\gamma) - \sigma^{\mathrm{tot}}(H \to ZZ^* \to 4l)$ where $\mathcal{L}^{\max}$ is the unconditional likelihood maximum and $\mathcal{L}$ is the optimised likelihood at a fixed profile point. This is expected to follow a χ^2 distribution where the number of bins is equal to the number of degrees of freedom. The resulting p-value is 14 %.

The measured differential cross sections are shown as black points in in Figure 7.6. All bins are dominated by statistical uncertainties. Red and blue points show the results using the $H \to \gamma\gamma$ and $H \to ZZ^* \to 4l$ channels respectively. These are compatible in all bins. The measurements are compared with several SM predictions. For every prediction, the contribution from associated production (XH) is modelled using the MC samples described in section 6.2. The ggF component is modelled using a variety of simulations described in

more detail in Ref. [5]. The NNLOPS prediction is the nominal MC sample where 1.1 is the k-factor used to set the total normalisation with N^{3}LO precision. The MadGraph5_aMC@NLO sample is also normalised with N^{3}LO precision using a k-factor of 1.47. All other ggF predictions use their respective normalisations. All predictions agree at a level finer than the measurement uncertainties in all bins.

The measured $p_{\mathrm{T}}^{\mathrm{H}}$ distribution is shown in Figure 7.6(a). The bottom panel shows the ratio with respect to data. The data appear to favour Higgs production with higher $p_{\mathrm{T}}^{\mathrm{H}}$ compared with all predictions. The compatibility with NNLOPS is estimated to be $p = 29$ % ignoring uncertainties on the prediction. The two channels are estimated to be consistent at the level of $p = 58$ %. The measured $|y^{\mathrm{H}}|$ distribution is shown in Figure 7.6(b). No clear systematic trend is observed in the comparison between data and predictions. The consistency of data with NNLOPS is $p = 0.92$ and between the two channels is $p = 0.20$.

The measured N_{jets} distribution is shown in Figure 7.6(c). Inclusive bins are measured by summing the measured cross sections of exclusive $N_{\mathrm{jets}} = 0$, $= 1$, $= 2$ and ≥ 3 bins as appropriate. The data distribution may favour higher jet multiplicities compared with the predictions. The consistency with NNLOPS is estimated to be $p = 43$ %. The two channels are consistent with $p = 53$ %. The measured $p_{\mathrm{T}}^{\mathrm{j1}}$ distribution is shown in Figure 7.6(d). The data measure more events than predicted by the SM in the two highest bins of p_{T}^{j1}. The comparison with NNLOPS (SCETlib) has an estimated $p = 6$ % (23 %). The measurements in both channels trend above the preditions in both bins. The consistency between channels is estimated to be $p = 67$ %. The data and SM prediction locally agree to better than 3 standard deviations in all bins. The $p_{\mathrm{T}}^{\mathrm{H}}$, N_{jets} and $p_{\mathrm{T}}^{\mathrm{j1}}$ observables are known to be positively correlated.

In summary, the total and differential cross sections are measured to be consistent with the SM expectation within the available statistical precision. Some shape differences are noted in the comparison between data and the SM. Some deviations may be expected given the number of bins measured. A global significance, taking this look-elsewhere-effect into account, is not computed. The combination of channels leads to significantly improved statistical precision which remains the dominant source of uncertainty in all bins as well as on the total cross section. Future measurements will therefore benefit from an increase in dataset size.

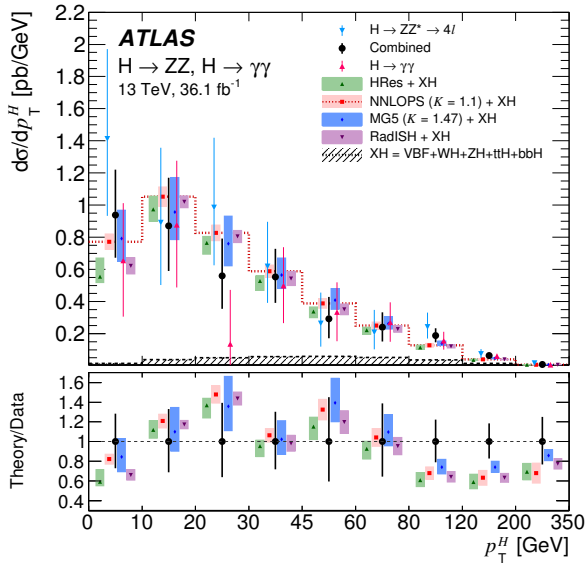

(a) $p_{\mathrm{T}}^{\mathrm{H}}$

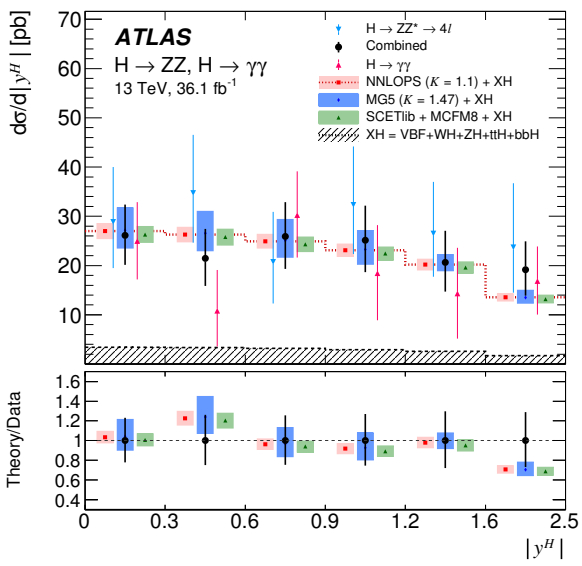

(b) $|y^{\mathrm{H}}|$

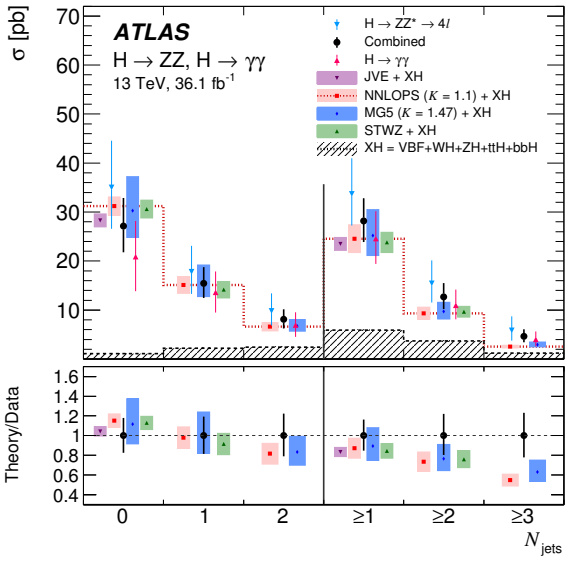

(c) N_{jets}

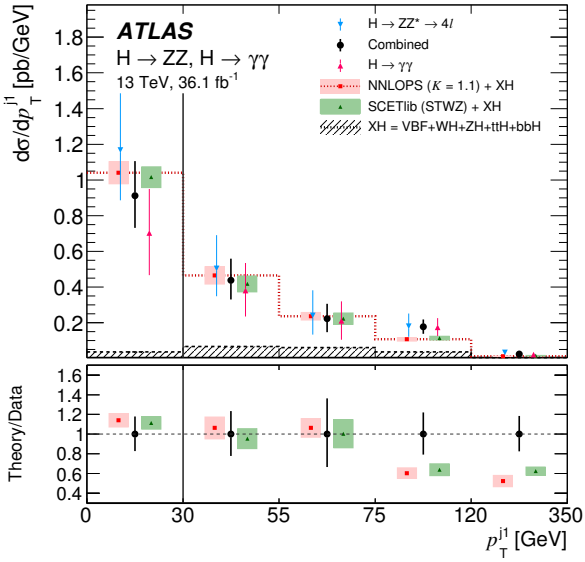

(d) p_{T}^{j1}

Figure 7.6: Differential cross sections measured using the combination of $H \to \gamma\gamma$ and $H \to ZZ^* \to 4l$ channels.

Expected sensitivity of $H \to \gamma\gamma$ cross sections at HL-LHC

The High Luminosity LHC (HL-LHC) is an upgrade of the LHC and its experiments proposed for installation during Long Shutdown 3 in $2024 - 2026$. It is designed for increased beam intensities allowing data to be collected at a centre-of-mass energy of $\sqrt{s} = 14$ TeV with 200 inelastic proton collisions per bunch crossing. An estimated 3 ab^{-1} data is expected to be collected by 2035. The primary goal is to improve measurements of rare processes which are limited by statistical precision. In the Higgs sector this will improve sensitivity in the tails of energy spectra which are kinematically suppressed due to the requirement of high partonic centre-of-mass energy.

The increased collision rate will lead to a greater particle flux within all ATLAS systems. Of most relevance for photon identification and energy measurement, the LAr calorimeters are planned to be upgraded to provide sufficient resolution and acceptable radiation tolerance [271]. In this chapter, the expected sensitivity of a p_{T}^{H} differential cross section measurement using the $H \to \gamma\gamma$ channel at HL-LHC is estimated using the expected performance of the upgraded calorimeters [6].

8.1 Outline

The statistical sensitivity is estimated using the following method. A template is simulated using the expected signal and background yields, ν_i^{sig} and ν_i^{bkg}, and probability density functions, $\mathcal{S}_i(m_{\gamma\gamma})$ and $\mathcal{B}_i(m_{\gamma\gamma})$, as a function of the diphoton invariant mass. This is done for all bins i of p_{T}^{H} and expressed as

$$\frac{\mathrm{d}N_i}{\mathrm{d}m_{\gamma\gamma}} = \nu_i^{\text{sig}} \cdot \mathcal{S}_i\left(m_{\gamma\gamma}\right) + \nu_i^{\text{bkg}} \cdot \mathcal{B}_i\left(m_{\gamma\gamma}\right) \tag{8.1}$$

where $\mathrm{d}N_i$ is the event yield over an interval $\mathrm{d}m_{\gamma\gamma}$. Signal yields are extracted from this dataset with an extended maximum likelihood fit using the `Minuit2` program. Parameter uncertainties are derived using the `Minos` program. Background yields and shape parameters are treated as unconstrained NPs. Three constrained NPs describe the impact of photon energy scale, photon energy resolution and Higgs mass uncertainties.

The statistical uncertainty is driven by the number of signal and background events contained within the signal region. The analysis is therefore driven by the estimation of signal and background rates and the resolution of the invariant mass peak, since a wider peak is affected by the statistical fluctuation of a larger background contribution. Values of $\sqrt{s} = 14$ TeV, $\mu = 200$ and $\int \mathcal{L}\mathrm{dt} = 3\ \mathrm{ab}^{-1}$ are assumed and object kinematic selections are taken as unchanged from Run 2. The trigger is assumed to maintain its Run 2 efficiency of over 99 % for selected events and remain unprescaled. This is consistent with the target performance of HL-LHC. A trigger prescale of P would be expected to increase the statistical uncertainty by a factor of $\sqrt{P}$.

Systematic uncertainties, including those affecting the likelihood fit, are assumed to be unchanged from Run 2. This is a benchmark for future improvements. The fiducial phase space definition is arbitrary at this stage. The Run 2 definition is used for simplicity.

The chapter is organised as follows. Monte Carlo samples are described in section 8.2 followed by the estimation of HL-LHC photon reconstruction efficiencies and fake rates in section 8.3. Section 8.4 shows the derivation of expected signal and background spectra and the resulting toy dataset. The systematic uncertainty benchmarks are presented in section 8.5 followed by the results in Section 8.6. Section 8.7 summarises the conclusions.

8.2 Monte Carlo samples

Simulated datasets are used for the dominant signal and background processes. The Monte Carlo samples described in section 6.2 are used to describe Higgs boson production via ggF, VBF, VH, ttH, tH and bbH, as well as the irreducible $\gamma\gamma$ background, at $\sqrt{s} = 13$ TeV with the Run 2 detector and pileup of $\mu \sim 10 - 40$, $\langle\mu\rangle = 24$. The γj background is simulated using Sherpa [92–94] with merged parton shower. In addition, ggF and VBF samples with 50k events each are simulated with $\sqrt{s} = 14$ TeV, $\mu = 200$ and early working versions of the HL-LHC inner detector and calorimeter geometries and photon reconstruction (pileup corrections not applied). Events are generated using the `Powheg-Box` program [83–87] (NLO accuracy in QCD) interfaced with `Pythia8` [53] for parton shower, hadronisation and underlying event using the `AU2` tune of the `CT10` PDF set [226].

8.3 Photon efficiency and fake rate at HL-LHC

The real and fake photon reconstruction efficiencies are estimated at HL-LHC. This is required in order to estimate both the signal and background rates. The real photon reconstruction efficiency, $\epsilon_\gamma^{\mathrm{reco}}$, is defined as the probability that a truth level photon is reconstructed at detector level. The fake reconstruction efficiency, $\epsilon_{\mathrm{j}}^{\mathrm{reco}}$, is defined as the probability that a truth jet is reconstructed as a photon. Tight identification and isolation criteria are applied. These are shown in Figure 8.1 as a function of the transverse

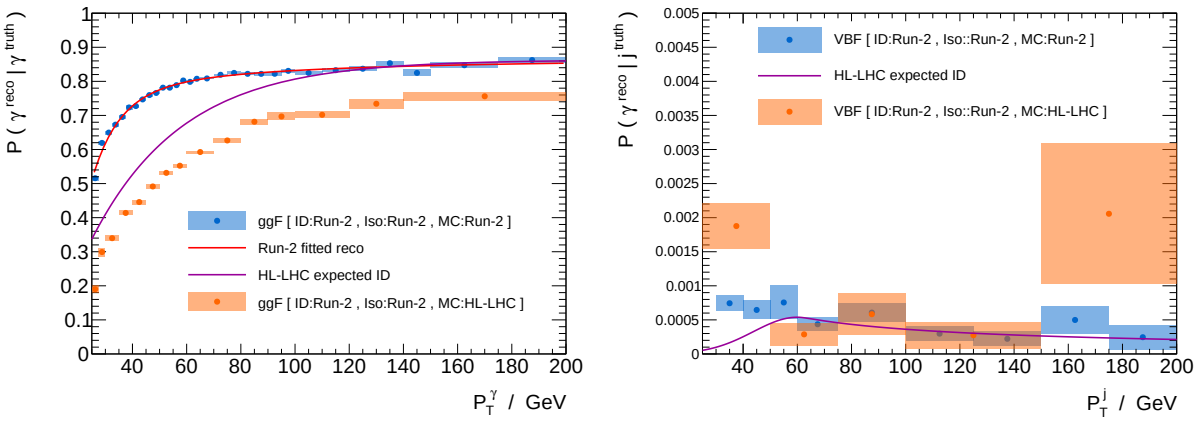

(a) $\epsilon_\gamma^{\text{reco}} \equiv \text{P}\left(\gamma^{\text{reco}}|\gamma^{\text{truth}}\right)$ (b) $\epsilon_{\text{j}}^{\text{reco}} \equiv \text{P}\left(\gamma^{\text{reco}}|\text{j}^{\text{truth}}\right)$

Figure 8.1: Probability that a true (a) photon or (b) jet will be reconstucted as a photon in Run 2 and HL-LHC conditions.

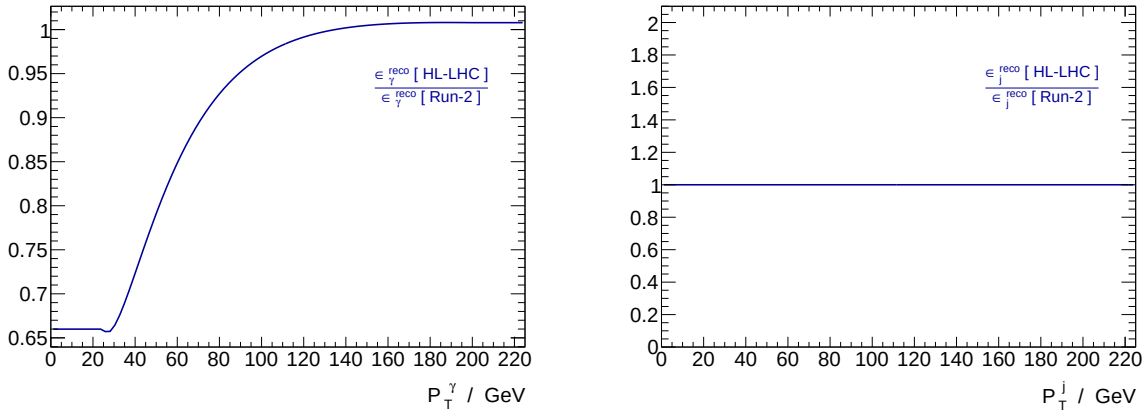

(a) ω_γ (b) ω_{j}

Figure 8.2: Ratio of the (a) real and (b) fake photon reconstruction efficiencies between HL-LHC and Run-2, conservatively assumed to be 1 for fake photons.

momentum of the truth object. The following quantities are presented:

- Blue points show values obtained using the Run 2 ggF and VBF samples.
- Red line (left plot only) shows a smooth parameterisation of the Run 2 $\epsilon_\gamma^{\text{reco}}$.
- Orange points show values obtained using the HL-LHC samples.
- Purple lines show an optimised HL-LHC photon reconstruction algorithm. This is provided by other members of the collaboration and supersedes the MC samples.

The ratio between the HL-LHC and Run 2 real (fake) photon reconstruction efficiencies is labelled ω_γ (ω_{j}) according to

$$\omega_\gamma = \frac{\epsilon_\gamma^{\text{reco}}\ [\text{HL-LHC}]}{\epsilon_\gamma^{\text{reco}}\ [\text{Run 2}]} \qquad \omega_{\text{j}} = \frac{\epsilon_{\text{j}}^{\text{reco}}\ [\text{HL-LHC}]}{\epsilon_{\text{j}}^{\text{reco}}\ [\text{Run 2}]}\ . \tag{8.2}$$

These are shown in Figure 8.2. In the following sections, these numbers will be used to extrapolate the expected event rates from Run 2 to HL-LHC conditions. For real photons, this is taken as the ratio between the purple and red lines in Figure 8.1(a) and assumed to be constant for $p_{\mathrm{T}} < 25$ GeV. The HL-LHC real photon efficiency is approximately 65 % of the Run 2 value at low p_{T}. This rises to 100 % for photons with $p_{\mathrm{T}} \gtrsim 150$ GeV. The MC statistical precision is not high enough to evaluate a precise ratio for ω_j and so a value of $\omega_j = 1$ is assumed. This is consistent with the ratio between the purple line and blue points in the tail of the distribution presented in Figure 8.1(b).

In Figure 8.1(b), it is notable that the HL-LHC parameterisation increases monotonically from $\epsilon_j^{\mathrm{reco}} \approx 0$ to $\epsilon_j^{\mathrm{reco}} \approx 0.05$ % in the interval $25 \leq p_{\mathrm{T}}^{\mathrm{j}} \lesssim 60$ GeV whereas the simulated trend in Run 2 is a monotonic decrease from an initial value of $\epsilon_j^{\mathrm{reco}} \approx 0.07$ %. It is suspected that this discrepency is caused by a truth level jet p_{T} cut applied when deriving the HL-LHC parameterisation, and so this artefact does not represent a true change in performance.

8.4 Expected signal and background spectra

This section describes how the expected signal and background yields and probability density functions (PDFs) are derived for HL-LHC. The toy dataset is then generated.

8.4.1 Binning of $p_{\mathrm{T}}^{\mathrm{H}}$

The binning of $p_{\mathrm{T}}^{\mathrm{H}}$ is chosen to mimick the Run 2 analysis below 220 GeV. This enables easy comparison between current and future sensitivity and allows use of the existing background decomposition measurements. An additional bin was measured in the range $220 \leq p_{\mathrm{T}}^{\mathrm{H}} < 350$ GeV in the Run 2 analysis. Since an important goal of HL-LHC is the measurement of the tail of the energy spectrum, finer granularity is desired in this region, therefore this bin is split with an intermediate boundary at 280 GeV. Furthermore, an additional bin is introduced at $350 \leq p_{\mathrm{T}}^{\mathrm{H}} < 600$ GeV. The resulting bin boundaries are

$$p_{\mathrm{T}}^{\mathrm{H}} \in [0, 20, 30, 45, 60, 80, 120, 170, 220, 280, 350, 600] \text{ GeV}. \tag{8.3}$$

8.4.2 Signal shape

The expected signal PDF is obtained, in each bin of $p_{\mathrm{T}}^{\mathrm{H}}$, using the following method. Detector level photon energy measurements are simulated by smearing the p_{T} of the truth level photons in simulated ggF events using a parameterisation of the expected HL-LHC photon energy resolution. Event selections are applied, and the diphoton invariant mass is reconstructed. This is fit with a double-sided Crystal Ball (DSCB) function. Two scenarios are considered which correspond to *optimistic* and *pessimistic* performance benchmarks.

Process	ggF	VBF	WH	ZH	ttH	bbH	tH
ρ^{sig}	1.126	1.131	1.103	1.115	1.210	1.136	1.214

Table 8.1: Ratio, ρ^{sig}, between the expected Higgs production cross sections at $\sqrt{s} = 14$ TeV and 13 TeV [28].

Figure 8.3 shows the reconstructed signal shape when this process is applied to 50 k events at $\sqrt{s} = 14$ TeV. The DSCB parameter σ which describes the width of the Gaussian core is shown in units of GeV. The optimistic resolution of $\sigma = 1.85 \pm 0.03$ GeV is similar to the Run 2 performance whereas the pessimistic $\sigma = 2.53 \pm 0.07$ GeV is considered a worst-case scenario. This MC sample is not large enough to determine the signal shape in each bin of p_{T}^{H} with sufficient statistical precision. Instead the larger sample of 1.98 M events at $\sqrt{s} = 13$ TeV is used. This is sufficient because the change of centre-of-mass energy is not expected to significantly alter the event kinematics within individual bins of p_{T}^{H}. The final signal shapes are shown in Figure 8.4.

8.4.3 Signal yield

The expected signal yields $\nu^{\text{sig}}_{\text{2015-16}}$ are derived for 36.1 fb^{-1} data in Run 2 conditions from signal MC. The expected signal yield at HL-LHC is calculated as $\nu^{\text{sig}}_{\text{HL-LHC}} = \lambda \cdot \rho^{\text{sig}} \cdot \omega^{\text{sig}}_{\gamma\gamma} \cdot \nu^{\text{sig}}_{\text{2015-16}}$ using the following definitions:

ρ^{sig} is the expected factor increase in production cross section when transferring from $\sqrt{s} = 13$ TeV to 14 TeV. This is evaluated independently for each Higgs production mechanism as shown in Table 8.1.

λ is the factor increase in integrated luminosity, equal to $3000/36.1 = 83.1$.

$\omega^{\text{sig}}_{\gamma\gamma}$ is the expected change in diphoton reconstruction efficiency. This is evaluated in each bin of p_{T}^{H} by reweighting every event in $\sqrt{s} = 13$ TeV MC by a factor of ω_γ for each of the signal photons.

The factor ρ^{sig} has a weak evolution with p_{T}^{H} due to the evolving production process fractions. Furthermore, the p_{T}^{H} spectrum is expected to be enhanced at high momentum due to the preferential increase in initial states with high partonic centre-of-mass energy. A comparison between the ggF MC samples at $\sqrt{s} = 13$ and 14 TeV showed that the effect is smaller than the MC statistical precision in every bin, therefore this effect is neglected. The expected signal yields are shown in Table 8.2.

8.4.4 Background shape and yield

The background probability density functions are modelled using the empirical functional forms chosen in the Run 2 analysis. The three modified bins at $p_{\text{T}}^{\text{H}} \in [220, 280, 350, 600]$

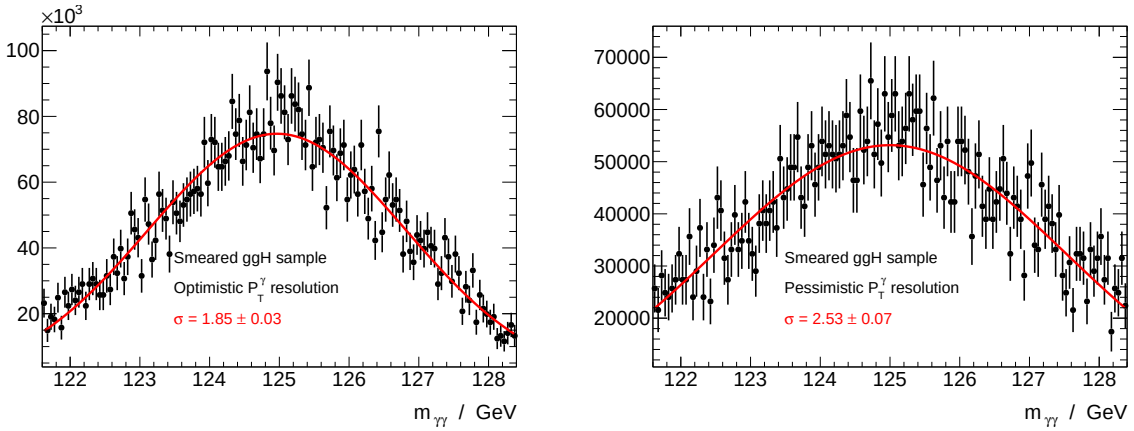

(a) Optimistic (b) Pessimistic

Figure 8.3: Simulated $H \to \gamma\gamma$ invariant mass resolution using two performance benchmarks at HL-LHC.

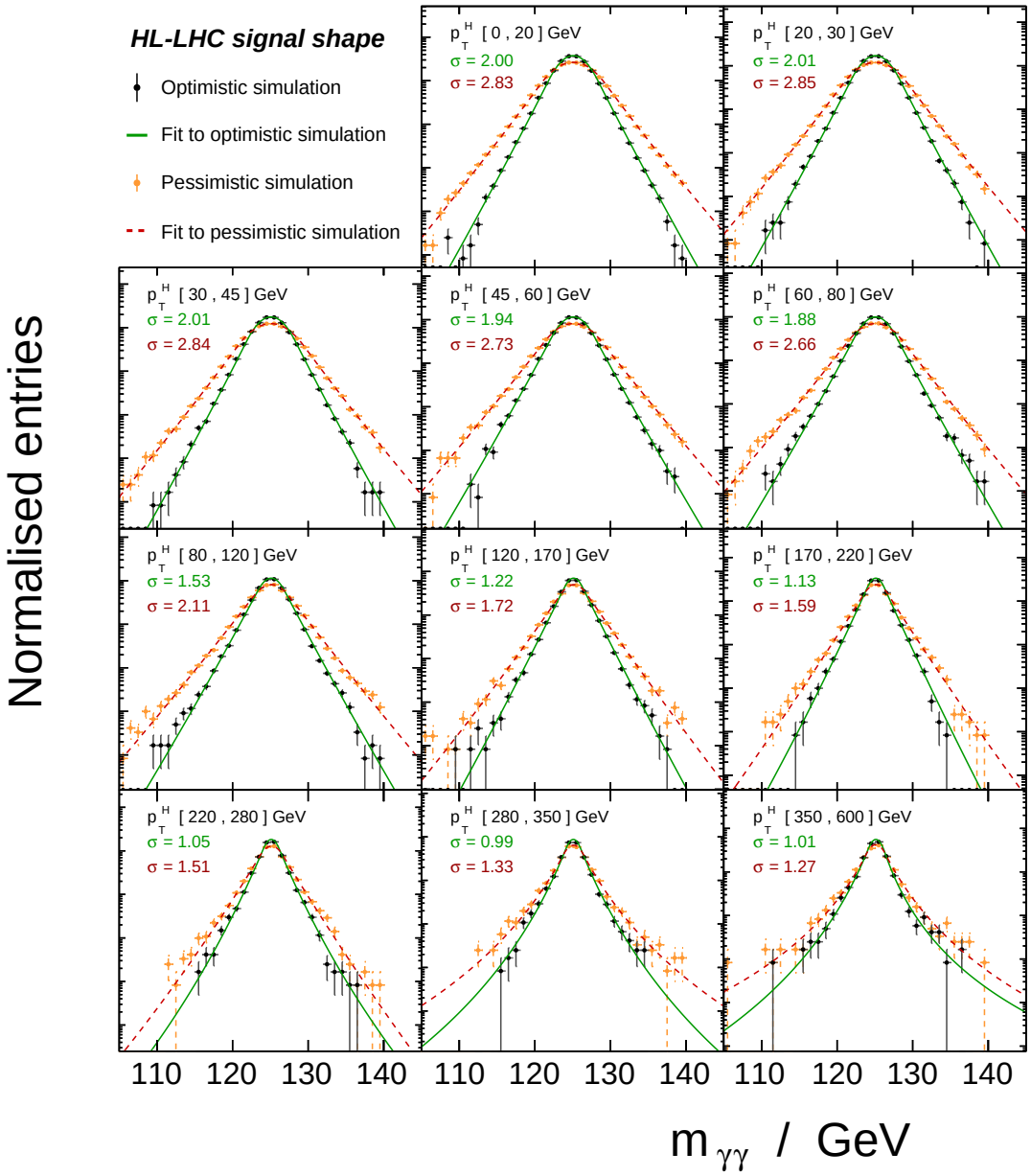

Figure 8.4: Simulated double-sided crystal ball signal shapes in bins of $p_{\mathrm{T}}^{\mathrm{H}}$.

Bin of $p_{\mathrm{T}}^{\mathrm{H}}$	$\nu_{\text{2015-16}}^{\text{sig}}$	ρ^{sig}	$\omega_{\gamma\gamma}^{\text{sig}}$	λ	$\nu_{HL-LHC}^{\text{sig}}$
$\in$ [0,20] GeV	578	1.126	0.688	83.1	37.2 k
$\in$ [20,30] GeV	263	1.126	0.689	83.1	16.9 k
$\in$ [30,45] GeV	270	1.126	0.694	83.1	17.5 k
$\in$ [45,60] GeV	174	1.126	0.703	83.1	11.5 k
$\in$ [60,80] GeV	147	1.126	0.714	83.1	9.9 k
$\in$ [80,120] GeV	150	1.127	0.743	83.1	10.4 k
$\in$ [120,170] GeV	80	1.129	0.809	83.1	6.1 k
$\in$ [170,220] GeV	35	1.130	0.864	83.1	2.9 k
$\in$ [220,280] GeV	18	1.131	0.904	83.1	1.6 k
$\in$ [280,350] GeV	9	1.133	0.937	83.1	750
$\in$ [350,600] GeV	6	1.135	0.989	83.1	540

Table 8.2: Expected signal yields in 2015-16, $\nu_{\text{2015-16}}^{\text{sig}}$, and the factors through which they are scaled in order to determine $\nu_{\text{HL-LHC}}^{\text{sig}}$.

are assumed to to follow the `Pow1` parameterisation assigned to the $p_{\mathrm{T}}^{\mathrm{H}} \in [220, 350]$ bin in Run 2. The final list of functional forms is

$$\begin{aligned} p_{\mathrm{T}}^{\mathrm{H}} \in [\ &\texttt{ExpPol2}\ ,\ \texttt{ExpPol2}\ ,\ \texttt{ExpPol2}\ ,\ \texttt{ExpPol2}\ ,\ \texttt{ExpPol2}\ , \\ &\texttt{ExpPol2}\ ,\ \texttt{Pow1}\ ,\ \texttt{ExpPol1}\ ,\ \texttt{Pow1}\ ,\ \texttt{Pow1}\ ,\ \texttt{Pow1}\ ] \end{aligned} \tag{8.4}$$

$$\begin{aligned} \texttt{ExpPol1} &= \mathcal{N}(\theta_1) \cdot e^{\theta_1 m_{\gamma\gamma}} \\ \texttt{ExpPol2} &= \mathcal{N}\left(\vec{\theta}\right) \cdot e^{\theta_1 m_{\gamma\gamma} + \theta_2 m_{\gamma\gamma}^2} \\ \texttt{Pow1} &= \mathcal{N}(\theta_1) \cdot m_{\gamma\gamma}^{\theta_1} \end{aligned} \tag{8.5}$$

with the corresponding bin boundaries shown in Eq. 8.3. They are normalised to unity by the factor $\mathcal{N}$ and contain the bin dependent nuisance parameters $\theta_{1,2}$. Expected values of $\theta_{1,2}$ must be determined to generate the toy dataset. The assumption of simple functional forms is justified because the functional forms are arbitrary when the data sidebands contain sufficient events to constrain the background contribution in the signal region. This means that the signal yield uncertainties are not significantly impacted by uncertainties on the background shape parameters. This assumption is valid for a dataset size of 3 ab^{-1} given the bin boundaries used.

Background in bins with $p_{\mathrm{T}}^{\mathrm{H}} < 350$ GeV

For each bin in the range $p_{\mathrm{T}}^{\mathrm{H}} \in [0, ..., 350]$ GeV, the background shape parameters are evaluated using a maximum likelihood fit to a sideband-only template. The template is constructed by reweighting the events measured in the 2015-16 data sidebands according to the change in reconstruction efficiency when transferring between Run 2 and HL-LHC

conditions. In each bin of $p_{\mathrm{T}}^{\mathrm{H}}$, the reweighting function is written as

$$\frac{n^{\text{HL-LHC}}}{n^{\text{2015-16}}}(m_{\gamma\gamma}) \;=\; f_{\gamma\gamma}\cdot\omega_{\gamma\gamma}^{\text{bkg}}(m_{\gamma\gamma}) \;+\; f_{\gamma\mathrm{j}}\cdot\omega_{\gamma\mathrm{j}}^{\text{bkg}}(m_{\gamma\gamma}) \;+\; f_{\mathrm{jj}}\cdot\omega_{\mathrm{jj}}^{\text{bkg}} \tag{8.6}$$

where n is the event yield per luminosity in a bin of $m_{\gamma\gamma}$, $\{f_{\gamma\gamma}, f_{\gamma\mathrm{j}}, f_{\mathrm{jj}}\}$ are the fractions of the reducible $\gamma\gamma$ and irreducible $\gamma\mathrm{j}, \mathrm{jj}$ backgrounds in Run 2 conditions and $\omega_{\gamma\gamma}^{\text{bkg}}, \omega_{\gamma\mathrm{j}}^{\text{bkg}}, \omega_{\mathrm{jj}}^{\text{bkg}}$ are the expected changes in reconstruction efficiency.

The values of $f_{\gamma\gamma/\gamma\mathrm{j}/\mathrm{jj}}$ are taken as measured in the Run 2 analysis and described in Section 6.4. The background purities in the final bin are assumed to be constant across the new intermediate boundary. The three ω^{bkg} functions are modelled as follows.

The $\omega_{\gamma\gamma/\gamma\mathrm{j}}^{\text{bkg}}$ functions are evaluated in each bin of $p_{\mathrm{T}}^{\mathrm{H}}$ by reweighting simulated $\gamma\gamma$ and $\gamma\mathrm{j}$ events by a factor of

- $\omega_{\gamma}(p_{\mathrm{T}}^{\gamma})$ for each selected photon when ΔR-matched to a truth-level photon,
- $\omega_{\mathrm{j}}(p_{\mathrm{T}}^{\mathrm{j}})$ when matched to a truth-level jet, and
- ω_{PU} otherwise.

The factor ω_{PU} accounts for contributions from pileup objects. The probability that a selected event contains at least one reconstruced photon which is *not* matched to a truth-level photon or jet is found to be less than 0.01 % (18 %) in $\gamma\gamma$ ($\gamma\mathrm{j}$) events. Two benchmarks are considered:

$\omega_{\mathbf{PU}} = 1$ is an *optimistic* scenario in which the fake photon contribution from pileup objects does not change between Run 2 and HL-LHC

$\omega_{\mathbf{PU}} = {}^{200}/_{\mu} \approx 10$ is a *pessimistic* scenario in which it scales linearly with pileup and μ is evaluated on an event-by-event basis

The resulting $\omega_{\gamma\gamma/\gamma\mathrm{j}}^{\text{bkg}}$ fluctuate as a function of $m_{\gamma\gamma}$. They are smoothed out using constant, linear or quadratic functions as shown in Figures 8.5 and 8.6. The quantity $\omega_{\mathrm{jj}}^{\text{bkg}}$ cannot be predicted using simulation as no MC sample exists. However, coarse estimates are sufficient as this background accounts for only $0.2 - 3.4$ % of events in Run 2. Since $\omega_{\mathrm{j}} = 1$ and $\omega_{\mathrm{PU}} = 1$, it follows that $\omega_{\mathrm{jj}}^{\text{bkg}} = 1$ in all $p_{\mathrm{T}}^{\mathrm{H}}$ bins under the optimistic pileup scenario. The pessimistic scenario is modelled by assuming

$$\frac{\omega_{\mathrm{jj}}^{\text{bkg}}(\text{pessimistic pileup})}{\omega_{\mathrm{jj}}^{\text{bkg}}(\text{optimistic pileup}) = 1} = \frac{\omega_{\gamma\mathrm{j}}^{\text{bkg}}(\text{pessimistic pileup})}{\omega_{\gamma\mathrm{j}}^{\text{bkg}}(\text{optimistic pileup})} \tag{8.7}$$

resulting in a range of $\omega_{\mathrm{jj}}^{\text{bkg}} = 1.51 - 4.04$. This assumes that the probability of a hard-scatter object being repaced by pileup is similar in $\gamma\mathrm{j}$ and jj events and neglects di-pileup background.

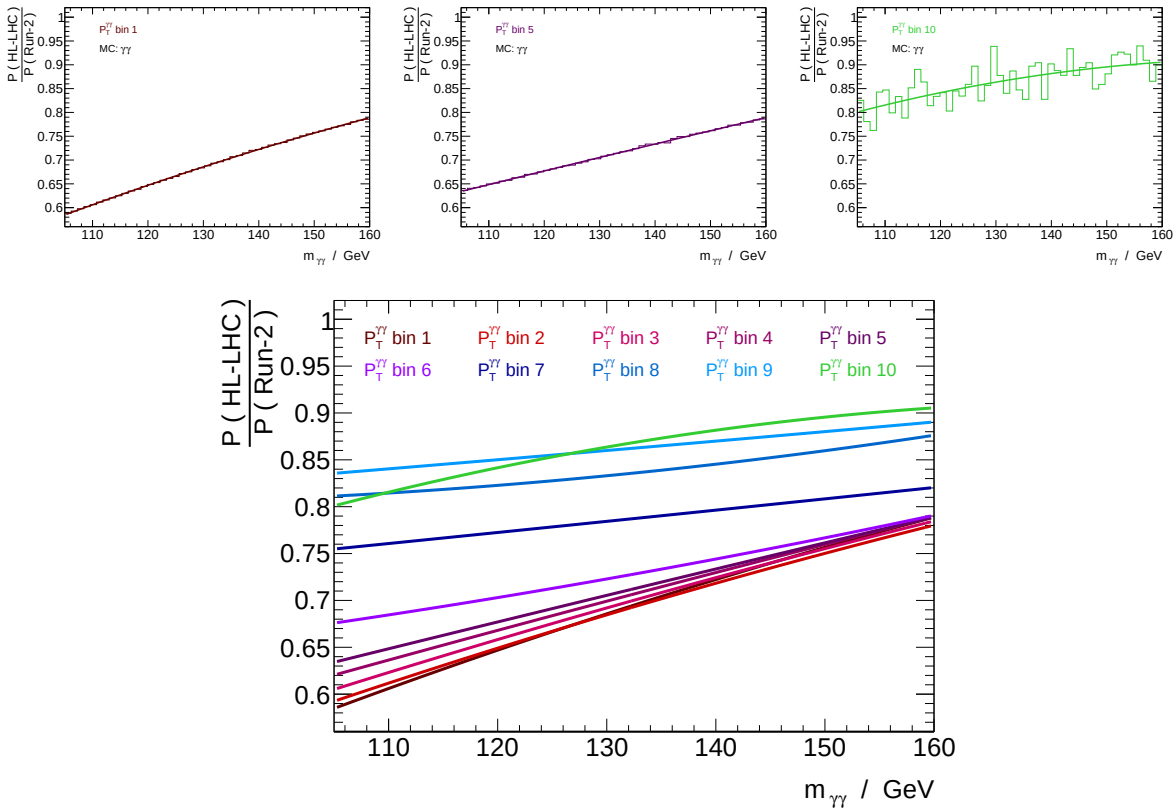

Figure 8.5: Parameterisation of $\omega_{\gamma\gamma}^{\text{bkg}} \equiv \frac{\text{P (HL-LHC)}}{\text{P (Run-2)}}$ from reweighted simulation in (top) three individual bins of $p_{\text{T}}^{\text{H}} \equiv p_{\text{T}}^{\gamma\gamma}$ and (bottom) in all bins.

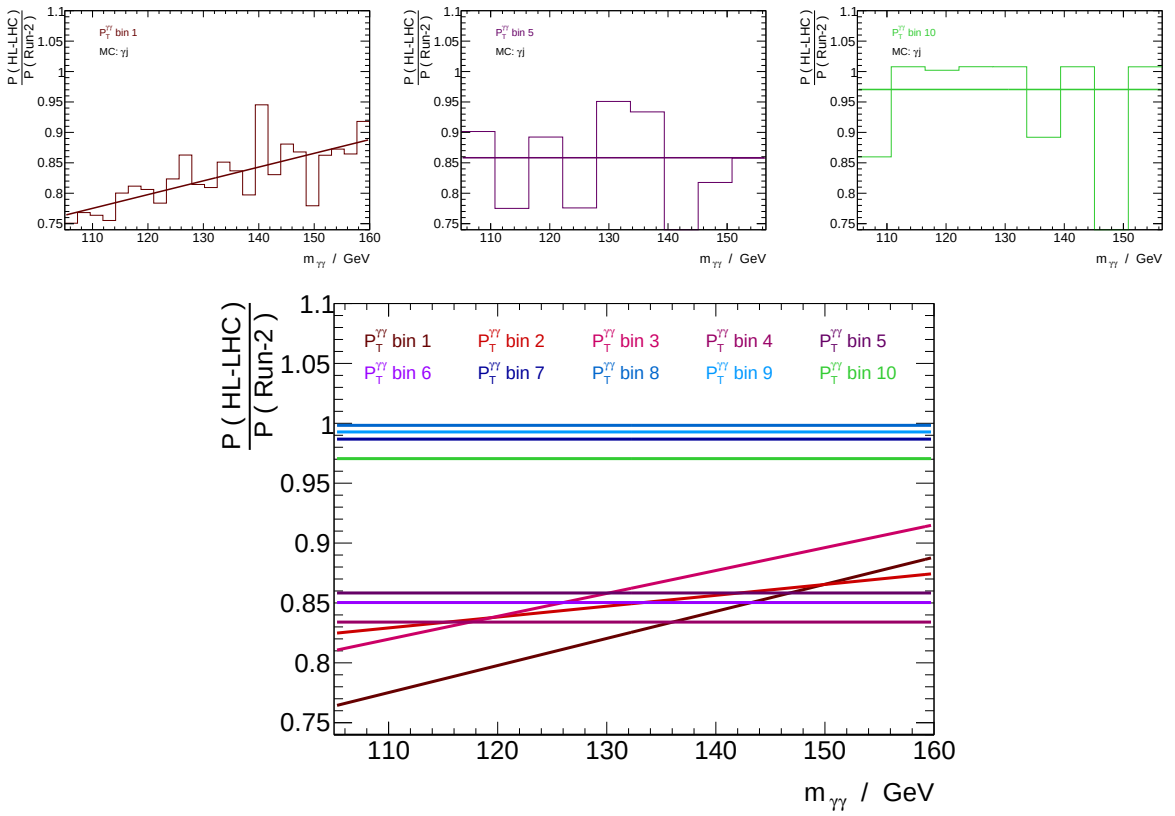

Figure 8.6: Parameterisation of $\omega_{\gamma\text{j}}^{\text{bkg}} \equiv \frac{\text{P (HL-LHC)}}{\text{P (Run-2)}}$ from reweighted simulation in (top) three individual bins of $p_{\text{T}}^{\text{H}} \equiv p_{\text{T}}^{\gamma\gamma}$ and (bottom) in all bins.

Figure 8.7 shows the resulting HL-LHC templates in purple, normalised to unit integrated luminosity. They are compared with the Run 2 data sidebands, shown in blue. The background yields are obtained by scaling these templates by the expected luminosity of 3 ab^{-1} and a factor, ρ^{bkg}, to account for the change in cross section when transferring from $\sqrt{s} = 13$ TeV to 14 TeV. This is assumed to be equal to the gluon fusion value of 1.126 because of the similar initial state kinematics probed.

Table 8.7 shows the expected background purities in both the optimistic and pessimistic pileup scenarios. The downward trend of $f_{\gamma\gamma}$ in the final two p_{T}^{H} bins is consistent with a statistical fluctuation in the 2015-16 measurement. Fluctuations in the pessimistic pileup scenario are caused by large weights assigned to individual events.

Background in $p_{\text{T}}^{\text{H}} \in [350, 600]$ GeV bin

The 2015-16 data sidebands do not contain sufficient events to reliably fit a background shape in the $p_{\text{T}}^{\text{H}} \in [350, 600]$ GeV bin. Instead, the following method is used:

- In the Run 2 $\gamma\gamma$ simulation, event yields in the upper and lower sidebands are counted after scaling the real and fake photon efficiencies to HL-LHC conditions. These are parameterised using empirical functional forms as a function of p_{T}^{H}. This is shown in Figure 8.8(a).
- The function normalisations are fixed to match the expected HL-LHC yields in the interval $p_{\text{T}}^{\text{H}} \in [220, 350]$ GeV. This is shown in Figures 8.8(b) and (c). Integrating these functions over the interval $p_{\text{T}}^{\text{H}} \in [350, 600]$ GeV estimates the expected upper and lower sideband yields in this bin.
- The template from the $p_{\text{T}}^{\text{H}} \in [220, 280]$ GeV bin is reweighted to match these expected yields. This creates a template in $p_{\text{T}}^{\text{H}} \in [350, 600]$ GeV bin, which is used to fit the background shape.

This approach models the p_{T}^{H}-evolution of the γj and jj background yields as being identical to that of the $\gamma\gamma$ background. This is conservative because they are expected to be more steeply falling as demonstrated by their decreasing purities in Table 8.3.

8.4.5 Toy dataset

Figure 8.9 shows the toy dataset generated using the optimistic pileup and resolution scenarios. A bin width of 1 GeV is used for visualisation whereas finer 0.2 GeV bins are used to perform the likelihood fit. The sideband events are sufficient to constrain the background shape in all bins. The $p_{\text{T}}^{\text{H}} \in [280, 350]$ GeV bin does not exhibit a monotonically falling background. This is likely due to a statistical fluctuation of the background template in this bin. This unphysical behaviour is not considered to be important because the background contribution in the signal region is well estimated regardless of its gradient.

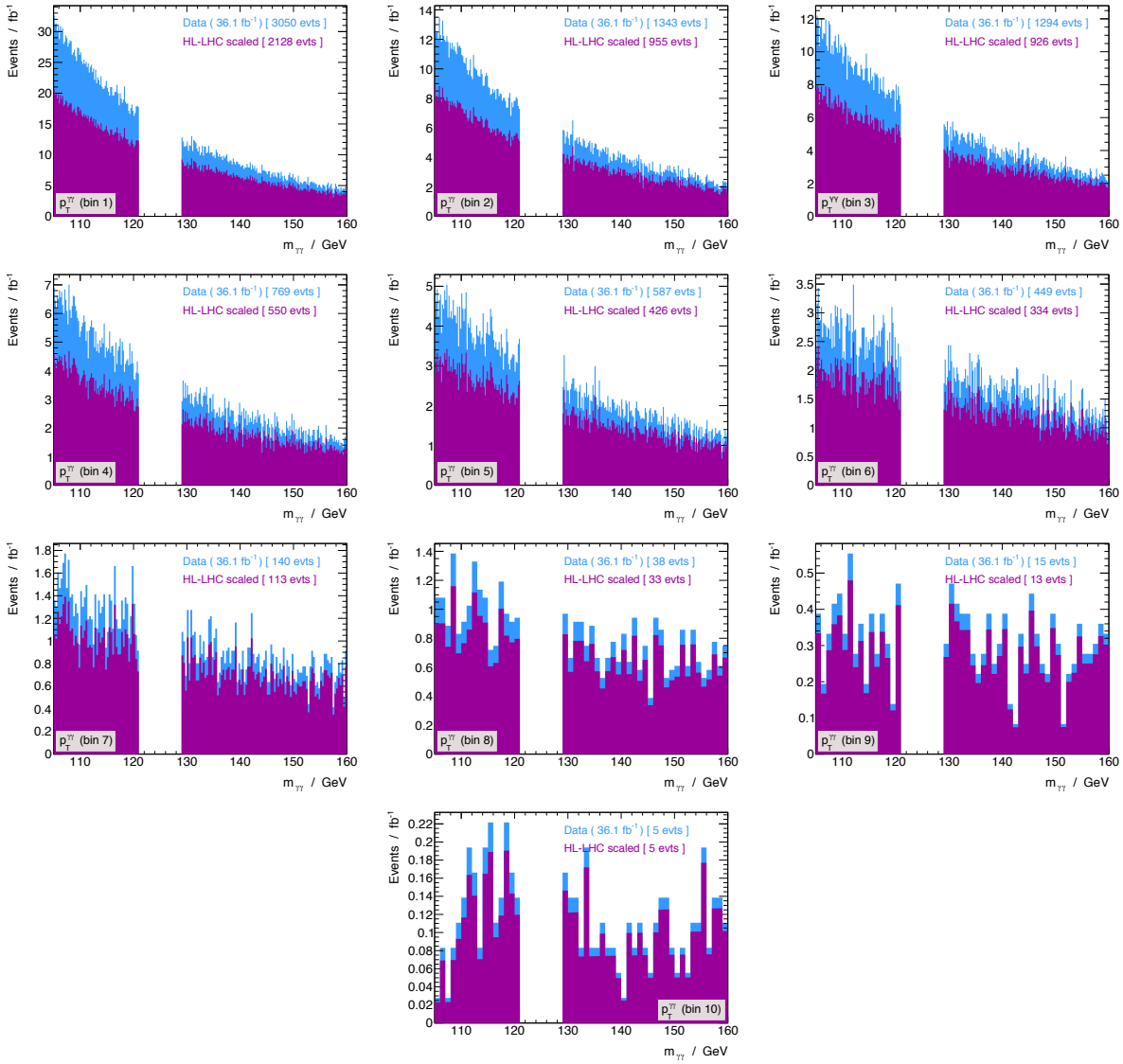

Figure 8.7: 2015-16 data sidebands (blue) and the result of scaling to HL-LHC reconstruction efficiencies (purple) using the optimistic pileup scenario for bins with $p_{\mathrm{T}}^{H} < 350$ GeV.

$p_{\mathrm{T}}^{\mathrm{H}}$	*2015-16*			*HL-LHC (optimistic)*			*HL-LHC (pessimistic)*		
[GeV]	$\gamma\gamma$	γj	jj	$\gamma\gamma$	γj	jj	$\gamma\gamma$	γj	jj
$[0, 20]$	78 %	19 %	3.4 %	74 %	22 %	4.9 %	68 %	25 %	6.8 %
$[20, 30]$	76 %	21 %	2.9 %	71 %	25 %	4.1 %	67 %	27 %	6.6 %
$[30, 45]$	79 %	19 %	2.4 %	74 %	23 %	3.4 %	63 %	31 %	6.4 %
$[45, 60]$	82 %	16 %	1.7 %	79 %	19 %	2.4 %	71 %	24 %	5.1 %
$[60, 80]$	83 %	15 %	1.5 %	80 %	18 %	2.1 %	65 %	31 %	4.7 %
$[80, 120]$	85 %	14 %	1.2 %	83 %	16 %	1.6 %	68 %	27 %	5.3 %
$[120, 170]$	88 %	11 %	0.6 %	86 %	14 %	0.7 %	63 %	35 %	2.0 %
$[170, 220]$	87 %	12 %	0.3 %	85 %	14 %	0.3 %	59 %	40 %	1.0 %
$[220, 280]$	84 %	16 %	0.2 %	82 %	18 %	0.2 %	76 %	24 %	0.6 %
$[280, 350]$				82 %	18 %	0.2 %	73 %	26 %	0.7 %

Table 8.3: Background process purities in 2015-16 data and projected for HL-LHC in the optimistic and pessimistic pileup scenarios.

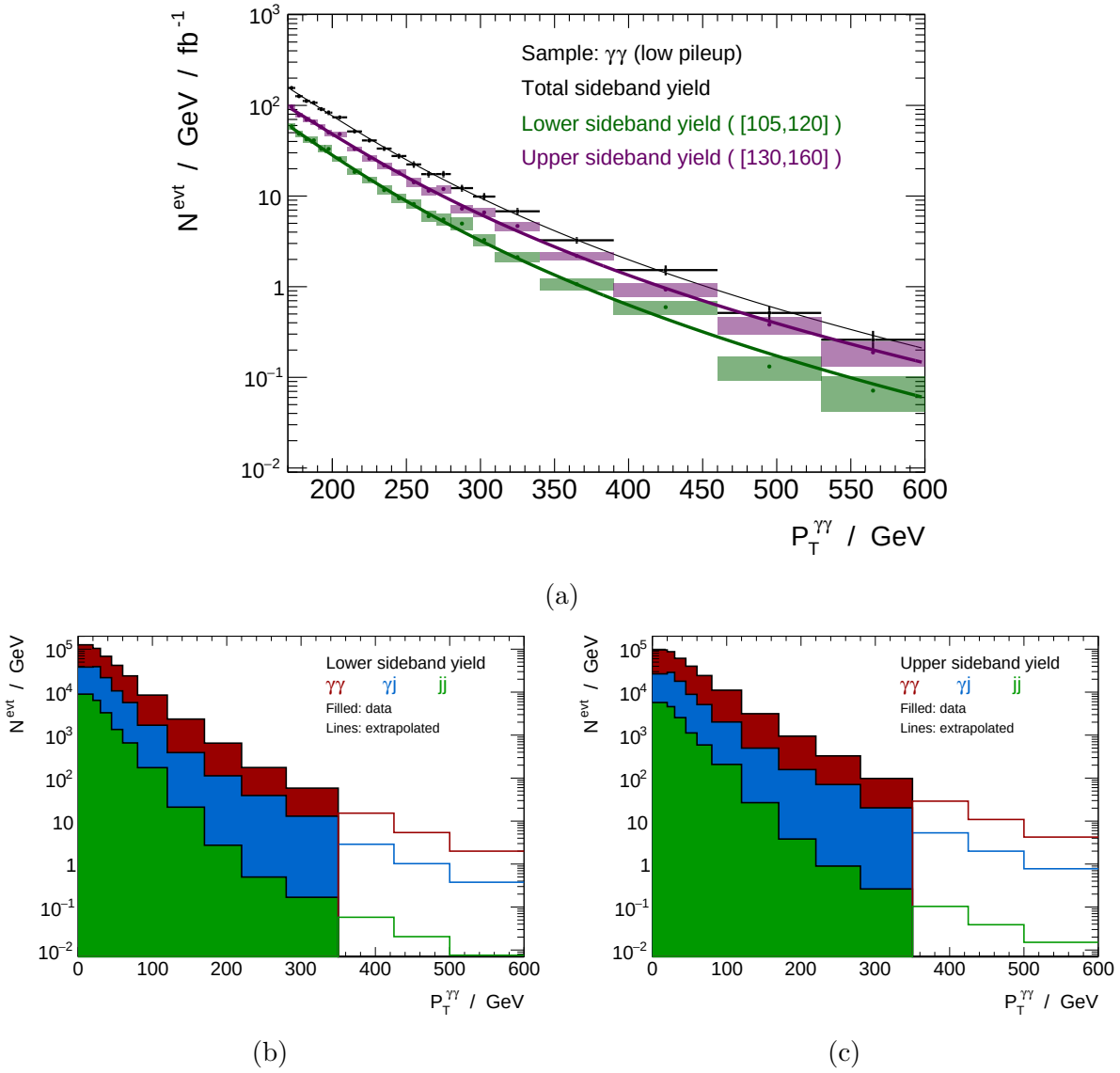

Figure 8.8: Sideband yields in $\gamma\gamma$ MC shown in (a). Extrapolation of template sideband yields into $p_{\mathrm{T}}^{\mathrm{H}} > 350$ GeV using the optimistic pileup scenario shown in (b) and (c).

8.5 Systematic uncertainties

The benchmark systematic uncertainties are summarised as follows. They are derived from the Run 2 *diphoton fiducial* cross section measurement. Many are likely to be reduced over time due to analysis improvements. They are assumed to be constant as a function of $p_{\mathrm{T}}^{\mathrm{H}}$ as experimental uncertainties are approximately uniform with respect to this observable. The systematic uncertainties have a combined impact of **7.0 %** in each bin.

Fit systematics due to the photon energy scale, resolution and Higgs mass are described by three individual NPs in the likelihood fit. External Gaussian, log-normal and Gaussian constraints are used, respectively. Their combined impact is **1-2 %**. This

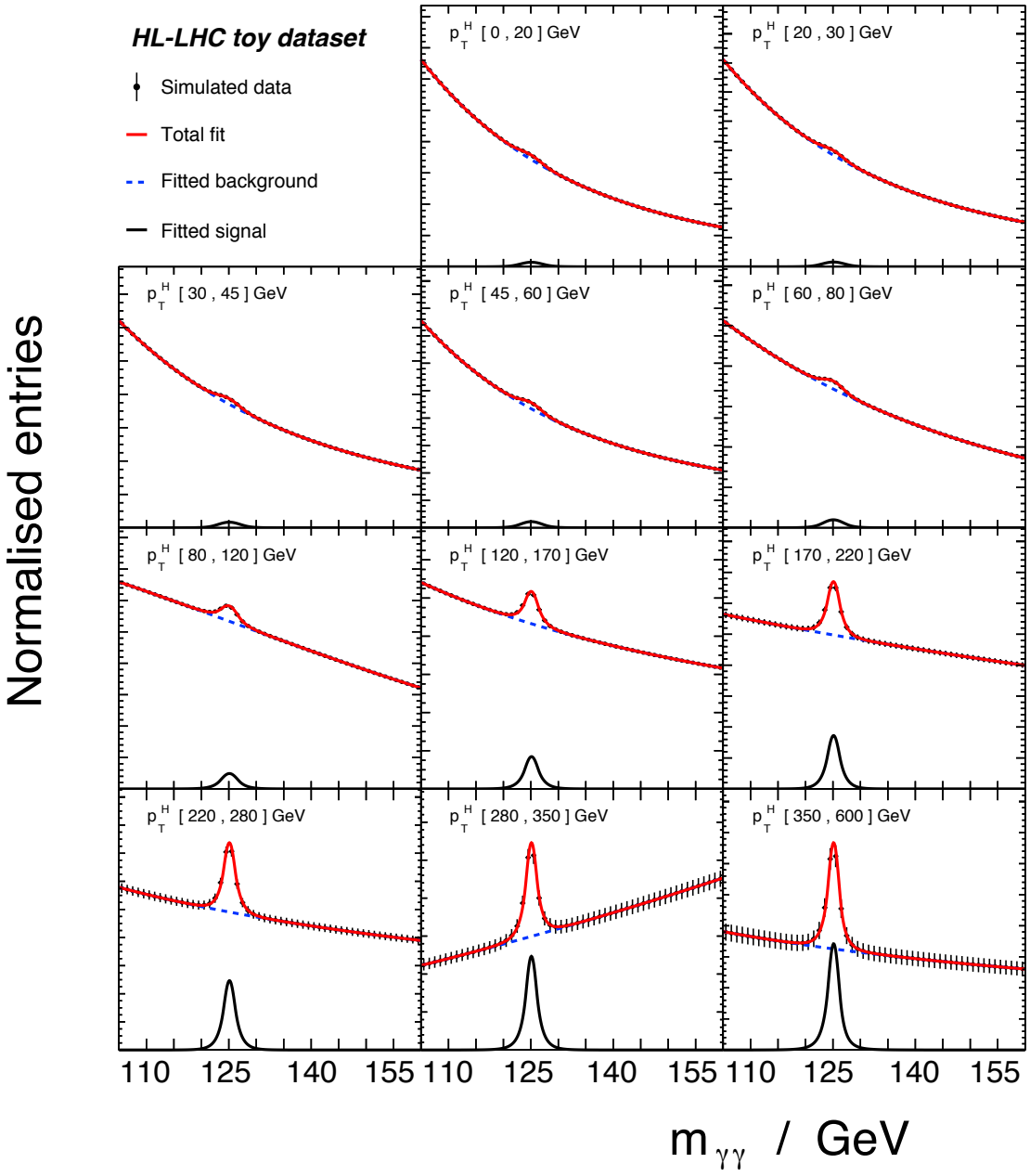

Figure 8.9: Toy dataset using the optimistic resolution and pileup scenarios.

is smaller than the 4.3 % impact measured in Run 2 because the toy dataset is large enough to constrain the NPs. The total systematic uncertainty benchmark increases from 7.0 % to 8.0 % when a NP impact of 4.3 % is assumed. This has little impact on the conclusions of the analysis.

Modelling of signal composition, p_T^H and parton shower when deriving unfolding matrices or factors. An uncertainty of **4.2 %** is assigned. It is likely that improved modelling and knowledge of the signal composition will reduce this uncertainty.

Photon reconstruction results in a **1.8 %** uncertainty.

Pileup modelling results in a **1.1 %** uncertainty.

Background modelling is taken as the **3.7 %** spurious signal bias estimated for the *diphoton fiducial* measurement in Run 2. This is likely to be reduced in high $p_{\mathrm{T}}^{\mathrm{H}}$ bins for which the signal purity is higher, but for which the current modelling is limited by simulation statistical fluctuations. It may also be reduced by narrowing the sideband regions as dataset size increases, and due to analysis improvements.

Luminosity results in a **3.2 %** uncertainty.

8.6 Results

Table 8.4 summarises the expected sensitivity at HL-LHC using four scenarios labelled as QR, where $Q \in \{O, P\}$ represent the optimistic and pessimistic pileup benchmarks and $R \in \{O, P\}$ label those for resolution. The limiting cases are OO and PP for which the expected spectra are shown in Figure 8.10. The impact of fit systematics is evaluated as the quadrature difference between the uncertainties obtained using fixed and floating systematic NPs when fitting the toy datasets. Statistical sensitivity exceeds the systematic benchmark at low $p_{\mathrm{T}}^{\mathrm{H}}$ with the current binning. High $p_{\mathrm{T}}^{\mathrm{H}}$ bins have an expected $\mathcal{O}(10\sigma)$ sensitivity and so considerably finer binning is possible.

$p_{\mathrm{T}}^{\mathrm{H}}$	*Fit stat.*				*Fit*	*Other*	Total	
$[GeV]$	OO	PO	OP	PP	*syst.*	*syst.*	OO	PP
$[0, 20]$	3.7 %	3.9 %	4.8 %	5.1 %	1.1 %	6.8 %	7.8 %	8.6 %
$[20, 30]$	5.5 %	5.6 %	7.2 %	7.4 %	1.1 %	6.8 %	8.8 %	10.1 %
$[30, 45]$	5.2 %	5.6 %	6.8 %	7.3 %	1.2 %	6.8 %	8.6 %	10.1 %
$[45, 60]$	6.1 %	6.4 %	7.8 %	8.3 %	1.0 %	6.8 %	9.2 %	10.8 %
$[60, 80]$	6.2 %	6.8 %	8.0 %	8.8 %	1.1 %	6.8 %	9.2 %	11.2 %
$[80, 120]$	4.8 %	5.2 %	6.0 %	6.6 %	1.3 %	6.8 %	8.4 %	9.6 %
$[120, 170]$	4.1 %	4.7 %	5.0 %	5.7 %	1.2 %	6.8 %	8.1 %	9.0 %
$[170, 220]$	4.8 %	5.6 %	5.6 %	6.6 %	1.3 %	6.8 %	8.4 %	9.6 %
$[220, 280]$	5.6 %	5.8 %	6.5 %	6.7 %	1.5 %	6.8 %	8.9 %	9.7 %
$[280, 350]$	6.9 %	7.1 %	7.8 %	8.1 %	1.4 %	6.8 %	9.8 %	10.7 %
$[350, 600]$	7.6 %	8.3 %	8.5 %	9.4 %	1.4 %	6.8 %	10.3 %	11.7 %

Table 8.4: Summary of expected uncertainties at HL-LHC.

8.7 Conclusions

The HL-LHC reconstruction efficiency for real photons is expected to be 65 % of the Run 2 performance at $p_{\mathrm{T}} = 25$ GeV rising to $\gtrsim 100$ % at high energy. The fake reconstruction efficiency is not well modelled with the current benchmark being comparable between Run

2 and HL-LHC. The optimistic diphoton resolution is comparable with the current Run 2 performance, whilst a pessimistic approach leads to an $\mathcal{O}(1-2\,\%)$ absolute increase in statistical uncertainty. HL-LHC will have significant sensitivity to high $p_{\mathrm{T}}^{\mathrm{H}}$ events as quantified in Table 8.4. Improved systematic uncertainties, particularly due to theoretical and background modelling, will likely be beneficial.

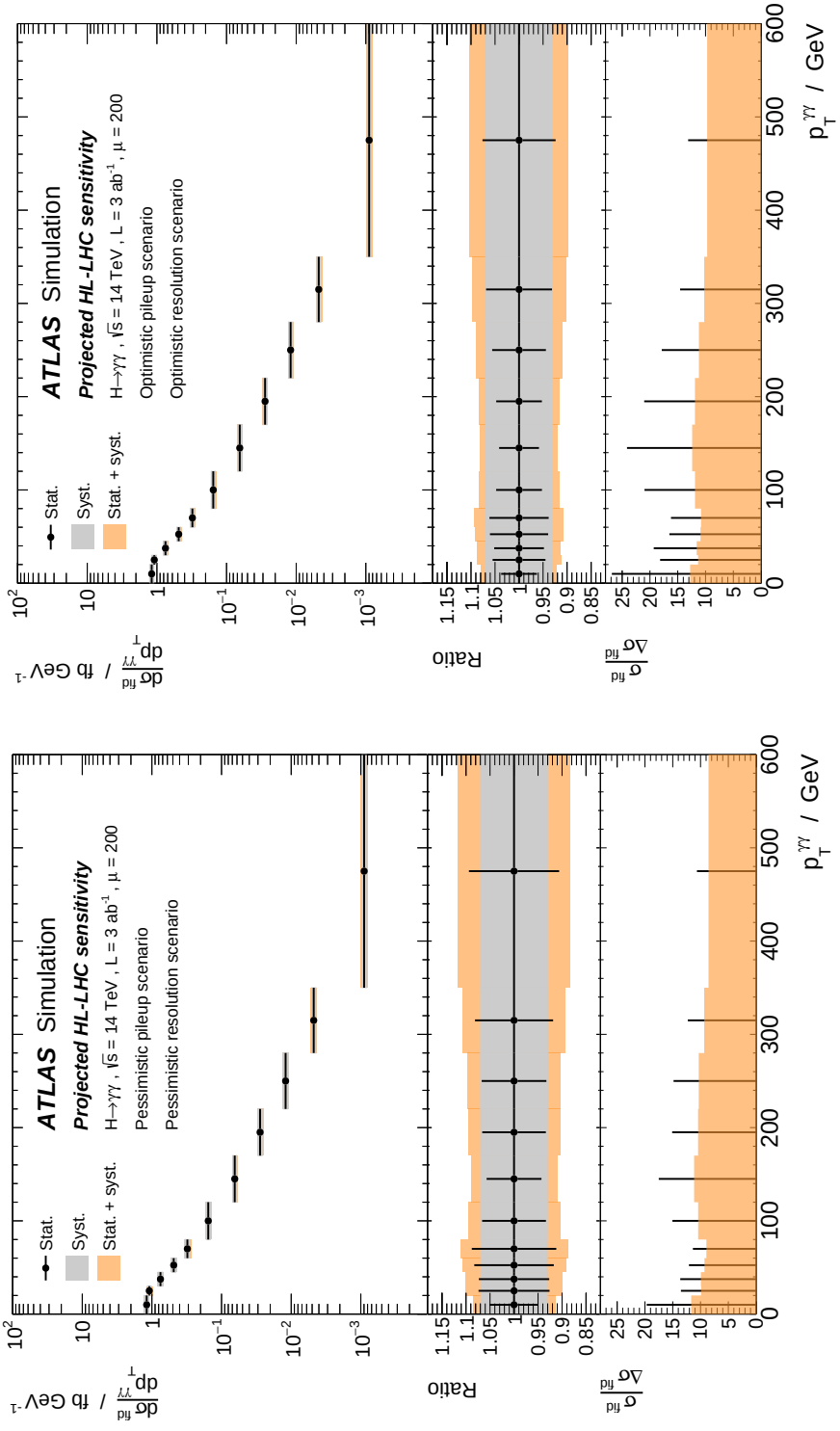

(a) Optimistic benchmarks

(b) Pessimistic benchmarks

Figure 8.10: Expected $p_{\mathrm{T}}^{\mathrm{H}}$ differential cross section measurement at HL-LHC.

Conclusions

The offline luminosity measurement is performed using data collected by the ATLAS detector at $\sqrt{s} = 8$ TeV in 2012 and $\sqrt{s} = 13$ TeV in 2015 and 2016 using the track counting method. In 2012 data, the run-integrated luminosity is shown to be stable with respect to `TileCal` at the level of $\lesssim 0.5$ %. This justifies the use of these offline luminometers in performing calibration transfer (2.5 %) and long-term stability ($\lesssim 1.4$ %) corrections to the online luminosity with a total uncertainty of ± 1.5 %. In 2015 and 2016 data, a significant relative μ-dependence is observed between the online and track counting luminosity measurements. This is shown to be driven by in-train bunch collisions. The track counting measurement is again found to be relatively stable both internally and with respect to `TileCal`. Calibration transfer corrections of -1.3 ± 0.8 % (50 ns bunch spacing) and -2.6 ± 0.9 % (25 ns bunch spacing) are derived for the preliminary measurement of 2015 data, and the long-term stability is constrained to ± 1.0 %. The online luminosity in 2016 data is corrected using a time and μ-dependent function with an uncertainty of ± 3.0 %. These contributions provide important constraints on the total luminosity uncertainties of ± 1.9 %, ± 2.1 % and ± 3.4 % in 2012, 2015 (preliminary) and 2016 (preliminary) respectively.

The fiducial cross section of the process $pp \to H \to \gamma\gamma$ is measured to be $55 \pm 9\,(\text{stat.}) \pm 4\,(\text{syst.})$ fb compared with the Standard Model expectation of 64 ± 2 fb using 36.1 fb^{-1} data collected at $\sqrt{s} = 13$ TeV. The cross section in a fiducial phase space region with an expected VBF contribution of 65 % is measured to be $3.7 \pm 0.8\,(\text{stat.}) \pm 0.5\,(\text{syst.})$ fb compared with the Standard Model expectation of 2.3 ± 0.1 fb. Limits on three additional fiducial cross sections are presented. Several differential cross sections are measured in the most inclusive fiducial phase space region with sensitivity to the properties and modelling of the Higgs boson and its interactions with different particles. Whilst some shape differences are noted, all observations are consistent with the Standard Model.

The total cross section of the process $pp \to H$ is measured to be $57.0\ ^{+6.0}_{-5.9}\ (\text{stat.})\ ^{+4.0}_{-3.3}\,(\text{syst.})$ pb compared with the Standard Model expectation of 55.6 ± 2.5 pb using the combination of diphoton and four-lepton channels. The fiducial acceptances and branching ratios are assumed to follow the Standard Model expectations. Four differential cross sections are measured in the full phase space with improved statistical precision compared with the individual channels. All observations are consistent with the Standard Model.

The expected statistical sensitivity of a differential cross section measurement in the diphoton channel is estimated using the expected performance of the proposed phase 2 calorimeter upgrade. Several performance benchmarks of photon energy resolution and pileup rejection are tested with an assumed integrated luminosity of 3 ab^{-1} and a centre-of-mass energy of $\sqrt{s} = 14$ TeV. The high energy tail of the Higgs transverse momentum distribution is expected to be measured with significantly improved sensitivity.

Bibliography

[1] ATLAS Collaboration,
"Measurement of the Higgs boson production cross section at 7, 8 and 13 TeV center-of-mass energies in the $H \to \gamma\gamma$ channel with the ATLAS detector",
tech. rep. ATLAS-CONF-2015-060, 2015,
URL: https://cds.cern.ch/record/2114826.

[2] ATLAS Collaboration, "Measurement of fiducial, differential and production cross sections in the $H \to \gamma\gamma$ decay channel with 13.3 fb^{-1} of 13 TeV proton-proton collision data with the ATLAS detector", tech. rep. ATLAS-CONF-2016-067, 2016, URL: https://cds.cern.ch/record/2206210.

[3] ATLAS Collaboration, "Measurements of Higgs boson properties in the diphoton decay channel with 36.1 fb^{-1} *pp* collision data at the center-of-mass energy of 13 TeV with the ATLAS detector", tech. rep. ATLAS-CONF-2017-045, 2017,
URL: http://cds.cern.ch/record/2273852.

[4] P.D. Dauncey et al,
Handling uncertainties in background shapes: the discrete profiling method,
Journal of Instrumentation **10** (2015) P04015,
URL: http://stacks.iop.org/1748-0221/10/i=04/a=P04015.

[5] ATLAS Collaboration,
Measurements of Higgs boson properties in the diphoton decay channel with 36 fb^{-1} of pp collision data at $\sqrt{s} = 13$ TeV with the ATLAS detector,
Phys. Rev. D **98** (052005 2018),
URL: https://link.aps.org/doi/10.1103/PhysRevD.98.052005.

[6] ATLAS Collaboration, "Technical Design Report for the Phase-II Upgrade of the ATLAS LAr Calorimeter", tech. rep. CERN-LHCC-2017-018. ATLAS-TDR-027, CERN, 2017, URL: http://cds.cern.ch/record/2285582.

[7] ATLAS Collaboration, "Combined measurement of differential and inclusive total cross sections in the $H \to \gamma\gamma$ and the $H \to ZZ^* \to 4\ell$ decay channels at $\sqrt{s} = 13$ TeV with the ATLAS detector", tech. rep. ATLAS-CONF-2018-002, 2018,
URL: https://cds.cern.ch/record/2308390.

[8] ATLAS collaboration,
Combined measurement of differential and total cross sections in the $H \to \gamma\gamma$ and the $H \to ZZ^* \to 4\ell$ decay channels at $\sqrt{s} = 13$ TeV with the ATLAS detector,
Submitted to Phys. Lett. B (2018), arXiv: 1805.10197 [hep-ex].

[9] S.L. Glashow, *A model of leptons*, Nucl. Phys. **22** (1961).

[10] A. Salam, *A model of leptons*, Conf. Proc. **C680519** (1968) p. 367.

[11] S. Weinberg, *A model of leptons*, Phys. Rev. Lett. **19** (1967).

[12] P.W. Higgs, *Spontaneous Symmetry Breakdown without Massless Bosons*,
Phys. Rev. **145** (4 1966).

[13] P.W. Higgs, *Broken symmetries, massless particles and gauge fields*,
Physics Letters **12** (1964).

[14] P.W. Higgs, *Broken Symmetries and the Masses of Gauge Bosons*,
Phys. Rev. Lett. **13** (16 1964).

[15] F. Englert and R. Brout,
Broken Symmetry and the Mass of Gauge Vector Mesons,
Phys. Rev. Lett. **13** (9 1964).

[16] C. R. Hagen G. S. Guralnik and T. W. B. Kibble,
Global Conservation Laws and Massless Particles, Phys. Rev. Lett. **13** (20 1964).

[17] T. W. B. Kibble, *Symmetry Breaking in Non-Abelian Gauge Theories*,
Phys. Rev. **155** (5 1967).

[18] Y. Nambu and G. Jona-Lasinio, *Dynamical Model of Elementary Particles Based on an Analogy with Superconductivity. I*, Phys. Rev. **122** (1961).

[19] ATLAS Collaboration,
ATLAS detector and physics performance: Technical Design Report, 1,
Technical Design Report ATLAS, CERN, 1999,
URL: https://cds.cern.ch/record/391176.

[20] CMS Collaboration, *CMS Physics: Technical Design Report Volume 1: Detector Performance and Software*, CERN, 2006,
URL: https://cds.cern.ch/record/922757.

[21] Oliver Sim Bruening et al., *LHC Design Report*,
CERN Yellow Reports: Monographs, CERN, 2004,
URL: http://cds.cern.ch/record/782076.

[22] Oliver Sim Bruening et al., *LHC Design Report*,
CERN Yellow Reports: Monographs, CERN, 2004,
URL: http://cds.cern.ch/record/815187.

[23] Michael Benedikt, Paul Collier, V Mertens, John Poole, and Karlheinz Schindl, *LHC Design Report*, CERN Yellow Reports: Monographs, CERN, 2004, URL: http://cds.cern.ch/record/823808.

[24] ATLAS Collaboration, *Observation of a new particle in the search for the Standard Model Higgs boson with the ATLAS detector at the LHC*, Phys. Lett. B **716** (2012).

[25] CMS Collaboration, *Observation of a new boson at a mass of 125 GeV with the CMS experiment at the LHC*, Phys. Lett. B **716** (2012).

[26] ATLAS and CMS Collaborations, *Evidence for the spin-0 nature of the Higgs boson using ATLAS data*, Phys. Rev. Lett. **114** (2015).

[27] ATLAS Collaboration, *Study of the spin and parity of the Higgs boson in diboson decays with the ATLAS detector*, Eur. Phys. J **476** (2015).

[28] D. de Florian et al, *Handbook of LHC Higgs Cross Sections: 4. Deciphering the Nature of the Higgs Sector*, CERN-2017-002-M (2017).

[29] ATLAS Collaboration, *Constraints on non-Standard Model Higgs boson interactions in an effective Lagrangian using differential cross sections measured in the $H \to \gamma\gamma$ decay channel at $\sqrt{s}$=8 TeV with the ATLAS detector*, Physics Letters B **753** (2016) p. 69 , ISSN: 0370-2693, URL: http://www.sciencedirect.com/science/article/pii/S0370269315009272.

[30] ATLAS Collaboration, *Test of CP Invariance in vector-boson fusion production of the Higgs boson using the Optimal Observable method in the ditau decay channel with the ATLAS detector*, Eur. Phys. J. **C76** (2016), arXiv: 1602.04516 [hep-ex].

[31] G. Klaemke and D. Zeppenfeld, *Higgs plus two jet production via gluon fusion as a signal at the CERN LHC*, Journal of High Energy Physics **2007** (2007), URL: http://stacks.iop.org/1126-6708/2007/i=04/a=052.

[32] K. Arnold J.R. Andersen and D. Zeppenfeld, *Azimuthal angle correlations for Higgs boson plus multi-jet events*, Journal of High Energy Physics **2010** (2010), ISSN: 1029-8479, URL: https://doi.org/10.1007/JHEP06(2010)091.

[33] M. J. Dolan, P. Harris, M. Jankowiak and M. Spannowsky, *Constraining CP-violating Higgs Sectors at the LHC using gluon fusion*, Phys. Rev. **D90** (2014), arXiv: 1406.3322 [hep-ph].

[34] A. Banerjee et al., *Constraining Composite Higgs Models using LHC data*, JHEP **03** (2018) p. 062, arXiv: 1712.07494 [hep-ph].

[35] C. Englert, T. Plehn, D. Zerwas and P.M. Zerwas, *Exploring the Higgs portal*, Phys. Lett. **B703** (2011) p. 298, arXiv: 1106.3097 [hep-ph].

[36] G. Degrassi, P.P Giardino, F. Maltoni and D. Pagani, *Probing the Higgs self coupling via single Higgs production at the LHC*, JHEP **12** (2016), arXiv: 1607.04251 [hep-ph].

[37] F. Maltoni, D. Pagani, A. Shivaji, and X. Zhao, *Trilinear Higgs coupling determination via single-Higgs differential measurements at the LHC*, Eur. Phys. J. **C77** (2017) p. 887, arXiv: 1709.08649 [hep-ph].

[38] F. Mandl and G. Shaw, *Quantum Field Theory*, 2nd ed., Wiley, 2010.

[39] A. Pilaftsis, "Quantum Field Theory", Lecture course at *The University of Manchester*, 2014.

[40] M. Dasgupta, "Gauge Theories", Lecture course at *The University of Manchester*, 2014.

[41] B. Pecjak P. Dauncey, C. Englert A. Banfi and D. Maître, "Quantum Field Theory", Lecture course at *HEP School for Experimental High Energy Physics*, 2015.

[42] P.F. Loverre U. Dore and L. Ludovici, *Measurement of the Weinberg angle in neutrino interactions*, The European Physical Journal H **41** (2016) p. 137, ISSN: 2102-6467, URL: https://doi.org/10.1140/epjh/e2016-70006-y.

[43] D0 Collaboration, *Measurement of the effective weak mixing angle in $p\bar{p} \to Z/\gamma^* \to e^+e^-$ events*, Phys. Rev. Lett. **115** (2015) p. 041801, arXiv: 1408.5016 [hep-ex].

[44] N. Cabibbo, *Unitary Symmetry and Leptonic Decays*, Phys. Rev. Lett. **10** (12 1963) p. 531, URL: https://link.aps.org/doi/10.1103/PhysRevLett.10.531.

[45] M. Kobayashi and T. Maskawa, *CP Violation in the Renormalizable Theory of Weak Interaction*, Prog. Theor. Phys. **49** (1973) p. 652.

[46] B. Pontecorvo, *Mesonium and anti-mesonium*, Sov. Phys. JETP **6** (1957) p. 429, [Zh. Eksp. Teor. Fiz.33,549(1957)].

[47] Z. Maki, M. Nakagawa and S. Sakata,
Remarks on the Unified Model of Elementary Particles,
Progress of Theoretical Physics **28** (1962) p. 870, eprint: /oup/backfile/content_public/journal/ptp/28/5/10.1143/ptp.28.870/2/28-5-870.pdf,
URL: http://dx.doi.org/10.1143/PTP.28.870.

[48] C. Patrignani et al. (Particle Data Group), *2017 Review of Particle Physics*,
Chin. Phys. C **40** (2016 (2017 update)).

[49] S. Dulat et al, *New parton distribution functions from a global analysis of quantum chromodynamics*, Phys. Rev. D **93** (2016).

[50] A. Buckley et al, *General-purpose event generators for LHC physics*,
CERN-PH-TH-2010-298 (2010).

[51] R.D. Field and R.P. Feynman,
Quark elastic scattering as a source of high-transverse-momentum mesons,
Phys. Rev. D **15** (9 1977) p. 2590,
URL: https://link.aps.org/doi/10.1103/PhysRevD.15.2590.

[52] Bo Andersson, "THE LUND STRING MODEL",
7th European Symposium on Antiproton Interactions: From LEAR to the Collider and Beyond Durham, England, July 9-13, 1984, 1986 p. 447.

[53] S. Mrenna T. Sjostrand and Peter Skands, *A Brief Introduction to PYTHIA 8.1*,
Comput. Phys. Commun. **178** (2008).

[54] S. Gieseke et al., *Herwig++ 1.0: an event generator for e^+e^- annihilation*,
Journal of High Energy Physics **2004** (2004),
URL: http://stacks.iop.org/1126-6708/2004/i=02/a=005.

[55] J. Bellm et al., *Herwig++ 2.7 Release Note*, (2013), arXiv: 1310.6877 [hep-ph].

[56] M. Bähr et al., *Herwig++ physics and manual*,
The European Physical Journal C **58** (2008), ISSN: 1434-6052,
URL: https://doi.org/10.1140/epjc/s10052-008-0798-9.

[57] M. Bahr et al, *Herwig++ Physics and Manual*, Eur. Phys. J. **C58** (2008).

[58] J. Bellm et al, *Herwig 7.0 / Herwig++ 3.0 Release Note*,
Eur. Phys. J. **C76** (2016).

[59] G.P. Salam M. Cacciari and G. Soyez, *The anti-kt jet clustering algorithm*,
Journal of High Energy Physics **2008** (2008),
URL: http://stacks.iop.org/1126-6708/2008/i=04/a=063.

[60] ATLAS Collaboration,
Measurement of Higgs boson production in the diphoton decay channel in pp collisions at center-of-mass energies of 7 and 8 TeV with the ATLAS detector,
Phys. Rev. **D90** (2014) p. 112015, arXiv: 1408.7084 [hep-ex].

[61] L. Dixon and M.S. Siu,
Resonance-Continuum Interference in the Diphoton Higgs Signal at the LHC,
Phys. Rev. Lett. **90** (25 2003) p. 252001,
URL: https://link.aps.org/doi/10.1103/PhysRevLett.90.252001.

[62] L. Dixon and Y. Li, *Bounding the Higgs Boson Width through Interferometry*,
Phys. Rev. Lett. **111** (11 2013) p. 111802,
URL: https://link.aps.org/doi/10.1103/PhysRevLett.111.111802.

[63] ATLAS Collaboration,
Measurement of inclusive and differential cross sections in the $H \to ZZ^* \to 4l$ decay channel in pp collisions at $\sqrt{s}$ = 13 TeV with the ATLAS detector,
J. High Energ. Phys. **132** (2017).

[64] C. Anastasiou et al.,
Higgs Boson Gluon-Fusion Production in QCD at Three Loops,
Phys. Rev. Lett. **114** (21 2015),
URL: https://link.aps.org/doi/10.1103/PhysRevLett.114.212001.

[65] C. Anastasiou et al., *High precision determination of the gluon fusion Higgs boson cross-section at the LHC*, Journal of High Energy Physics **2016** (2016),
ISSN: 1029-8479, URL: https://doi.org/10.1007/JHEP05(2016)058.

[66] A. Stefano Actis et al.,
NLO electroweak corrections to Higgs boson production at hadron colliders,
Physics Letters B **670** (2008), ISSN: 0370-2693, URL:
http://www.sciencedirect.com/science/article/pii/S0370269308012689.

[67] R. Boughezal C. Anastasiou and F. Petriello,
Mixed QCD-electroweak corrections to Higgs boson production in gluon fusion,
Journal of High Energy Physics **2009** (2009),
URL: http://stacks.iop.org/1126-6708/2009/i=04/a=003.

[68] M. Ciccolini, A. Denner, and S. Dittmaier,
Strong and Electroweak Corrections to the Production of a Higgs Boson + 2 Jets via Weak Interactions at the Large Hadron Collider,
Phys. Rev. Lett. **99** (16 2007),
URL: https://link.aps.org/doi/10.1103/PhysRevLett.99.161803.

[69] M. Ciccolini, Denner A., and Dittmaier S., *Electroweak and QCD corrections to Higgs production via vector-boson fusion at the CERN LHC*, Phys. Rev. D **77** (1 2008), URL: https://link.aps.org/doi/10.1103/PhysRevD.77.013002.

[70] Paolo Bolzoni, Fabio Maltoni, Sven-Olaf Moch, and Marco Zaro, *Higgs Boson Production via Vector-Boson Fusion at Next-to-Next-to-Leading Order in QCD*, Phys. Rev. Lett. **105** (1 2010), URL: https://link.aps.org/doi/10.1103/PhysRevLett.105.011801.

[71] Oliver Brein, Abdelhak Djouadi, and Robert Harlander, *NNLO QCD corrections to the Higgs-strahlung processes at hadron colliders*, Physics Letters B **579** (2004), URL: http://www.sciencedirect.com/science/article/pii/S0370269303017234.

[72] L. Altenkamp et al., *Gluon-induced Higgs-strahlung at next-to-leading order QCD*, Journal of High Energy Physics **2013** (2013), URL: https://doi.org/10.1007/JHEP02(2013)078.

[73] A. Denner et al., *Electroweak corrections to Higgs-strahlung off W/Z bosons at the Tevatron and the LHC with Hawk*, Journal of High Energy Physics **2012** (2012), URL: https://doi.org/10.1007/JHEP03(2012)075.

[74] W. Beenakker et al., *NLO QCD corrections to $t\bar{t}H$ production in hadron collisions*, Nuclear Physics B **653** (2003), ISSN: 0550-3213, URL: http://www.sciencedirect.com/science/article/pii/S0550321303000440.

[75] S. Dawson, C. Jackson, L. H. Orr, L. Reina, and D. Wackeroth, *Associated Higgs boson production with top quarks at the CERN Large Hadron Collider: NLO QCD corrections*, Phys. Rev. D **68** (3 2003), URL: https://link.aps.org/doi/10.1103/PhysRevD.68.034022.

[76] Yu Zhang, Wen-Gan Ma, Ren-You Zhang, Chong Chen, and Lei Guo, *QCD NLO and EW NLO corrections to $t\bar{t}H$ production with top quark decays at hadron collider*, Physics Letters B **738** (2014), ISSN: 0370-2693, URL: http://www.sciencedirect.com/science/article/pii/S0370269314006728.

[77] S. Frixione et al., *Electroweak and QCD corrections to top-pair hadroproduction in association with heavy bosons*, Journal of High Energy Physics **2015** (2015), ISSN: 1029-8479, URL: https://doi.org/10.1007/JHEP06(2015)184.

[78] S. Dawson et al., *Exclusive Higgs boson production with bottom quarks at hadron colliders*, Phys. Rev. D **69** (7 2004), URL: https://link.aps.org/doi/10.1103/PhysRevD.69.074027.

[79] S. Dittmaier et al.,
Higgs radiation off bottom quarks at the Fermilab Tevatron and the CERN LHC,
Phys. Rev. D **70** (7 2004),
URL: https://link.aps.org/doi/10.1103/PhysRevD.70.074010.

[80] M. Kramer R. Harlander and M. Schumacher, *Bottom-quark associated Higgs-boson production: reconciling the four- and five-flavour scheme approach*, (2011), arXiv: 1112.3478 [hep-ph].

[81] ATLAS Collaboration, *Measurements of gluon-gluon fusion and vector-boson fusion Higgs boson production cross-sections in the $H \to WW^* \to e\nu\mu\nu$ decay channel in pp collisions at $\sqrt{s} = 13$ TeV with the ATLAS detector*,
Phys. Lett. **B789** (2019), arXiv: 1808.09054 [hep-ex].

[82] ATLAS Collaboration,
Cross-section measurements of the Higgs boson decaying into a pair of τ-leptons in proton-proton collisions at $\sqrt{s} = 13$ TeV with the ATLAS detector,
Submitted to: Phys. Rev. (2018), arXiv: 1811.08856 [hep-ex].

[83] P. Nason,
A new method for combining NLO QCD with shower Monte Carlo algorithms,
Journal of High Energy Physics **2004** (2004),
URL: http://stacks.iop.org/1126-6708/2004/i=11/a=040.

[84] P. Nason S. Frixione and C. Oleari, *Matching NLO QCD computations with parton shower simulations: the POWHEG method*,
Journal of High Energy Physics **2007** (2007),
URL: http://stacks.iop.org/1126-6708/2007/i=11/a=070.

[85] S. Alioli et al., *A general framework for implementing NLO calculations in shower Monte Carlo programs: the POWHEG BOX*,
Journal of High Energy Physics **2010** (2010), ISSN: 1029-8479,
URL: https://doi.org/10.1007/JHEP06(2010)043.

[86] P. Nason and C. Oleari, *NLO Higgs boson production via vector-boson fusion matched with shower in POWHEG*, Journal of High Energy Physics **2010** (2010), ISSN: 1029-8479, URL: https://doi.org/10.1007/JHEP02(2010)037.

[87] V. Sanz K. Mimasu and C. Williams, *Higher order QCD predictions for associated Higgs production with anomalous couplings to gauge bosons*,
Journal of High Energy Physics **2016** (2016) p. 39, ISSN: 1029-8479,
URL: https://doi.org/10.1007/JHEP08(2016)039.

[88] P. Nason,
A New method for combining NLO QCD with shower Monte Carlo algorithms,
JHEP **11** (2004) p. 040, arXiv: hep-ph/0409146 [hep-ph].

[89] J. Alwall et al., *The automated computation of tree-level and next-to-leading order differential cross sections, and their matching to parton shower simulations*, Journal of High Energy Physics **2014** (2014), ISSN: 1029-8479, URL: https://doi.org/10.1007/JHEP07(2014)079.

[90] S. Frixione and B.R. Webber, *Matching NLO QCD computations and parton shower simulations*, JHEP **06** (2002) p. 029, arXiv: hep-ph/0204244 [hep-ph].

[91] R. Frederix and S. Frixione, *Merging meets matching in MC@NLO*, JHEP **12** (2012) p. 061, arXiv: 1209.6215 [hep-ph].

[92] T. Gleisberg et al., *Event generation with SHERPA 1.1*, Journal of High Energy Physics **2009** (2009), URL: http://stacks.iop.org/1126-6708/2009/i=02/a=007.

[93] S. Schumann and F. Krauss, *A parton shower algorithm based on Catani-Seymour dipole factorisation*, Journal of High Energy Physics **2008** (2008), URL: http://stacks.iop.org/1126-6708/2008/i=03/a=038.

[94] Stefan Hoeche, Frank Krauss, Steffen Schumann, and Frank Siegert, *QCD matrix elements and truncated showers*, Journal of High Energy Physics **2009** (2009), URL: http://stacks.iop.org/1126-6708/2009/i=05/a=053.

[95] K. Hamilton et al., *NNLOPS simulation of Higgs boson production*, Journal of High Energy Physics **2013** (2013) p. 222, ISSN: 1029-8479, URL: https://doi.org/10.1007/JHEP10(2013)222.

[96] Stefano Catani and Massimiliano Grazzini, *Next-to-Next-to-Leading-Order Subtraction Formalism in Hadron Collisions and its Application to Higgs-Boson Production at the Large Hadron Collider*, Phys. Rev. Lett. **98** (22), URL: https://link.aps.org/doi/10.1103/PhysRevLett.98.222002.

[97] CMS Collaboration, *Observation of the diphoton decay of the Higgs boson and measurement of its properties*, Eur. Phys. J. **C74** (2014) p. 3076, arXiv: 1407.0558 [hep-ex].

[98] *Measurements of Higgs boson production and couplings in the four-lepton channel in pp collisions at center-of-mass energies of 7 and 8 TeV with the ATLAS detector*, Phys. Rev. **D91** (2015) p. 012006, arXiv: 1408.5191 [hep-ex].

[99] *Measurement of the properties of a Higgs boson in the four-lepton final state*, Phys. Rev. **D89** (2014) p. 092007, arXiv: 1312.5353 [hep-ex].

[100] *Observation and measurement of Higgs boson decays to WW* with the ATLAS detector*, Phys. Rev. **D92** (2015) p. 012006, arXiv: 1412.2641 [hep-ex].

[101] *Study of (W/Z)H production and Higgs boson couplings using $H \to WW^*$ decays with the ATLAS detector*, JHEP **08** (2015) p. 137, arXiv: 1506.06641 [hep-ex].

[102] *Measurement of Higgs boson production and properties in the WW decay channel with leptonic final states*, JHEP **01** (2014) p. 096, arXiv: 1312.1129 [hep-ex].

[103] *Evidence for the Higgs-boson Yukawa coupling to tau leptons with the ATLAS detector*, JHEP **04** (2015) p. 117, arXiv: 1501.04943 [hep-ex].

[104] *Evidence for the 125 GeV Higgs boson decaying to a pair of τ leptons*, JHEP **05** (2014) p. 104, arXiv: 1401.5041 [hep-ex].

[105] *Search for the $b\bar{b}$ decay of the Standard Model Higgs boson in associated $(W/Z)H$ production with the ATLAS detector*, JHEP **01** (2015) p. 069, arXiv: 1409.6212 [hep-ex].

[106] *Search for the standard model Higgs boson produced in association with a W or a Z boson and decaying to bottom quarks*, Phys. Rev. **D89** (2014) p. 012003, arXiv: 1310.3687 [hep-ex].

[107] *Search for the Standard Model Higgs boson decay to $\mu^+\mu^-$ with the ATLAS detector*, Phys. Lett. **B738** (2014) p. 68, arXiv: 1406.7663 [hep-ex].

[108] *Search for a standard model-like Higgs boson in the $?^+?^?$ and $e^+e^?$ decay channels at the LHC*, Phys. Lett. **B744** (2015) p. 184, arXiv: 1410.6679 [hep-ex].

[109] ATLAS and CMS Collaborations, *Measurements of the Higgs boson production and decay rates and constraints on its couplings from a combined ATLAS and CMS analysis of the LHC pp collision data at $\sqrt{s} = 7$ and 8 TeV*, J. High Energ. Phys. **08** (2016).

[110] CMS Collaboration, *Constraints on the spin-parity and anomalous HVV couplings of the Higgs boson in proton collisions at 7 and 8 TeV*, Phys. Rev. D **92** (2015).

[111] J. C. Collins and D. E. Soper, *Angular distribution of dileptons in high-energy hadron collisions*, Phys. Rev. D **2219** (1977).

[112] ATLAS Collaboration, *Evidence for the spin-0 nature of the Higgs boson using ATLAS data*, Phys. Lett. B **726** (2013).

[113] ATLAS Collaboration, *Measurements of fiducial and differential cross sections for Higgs boson production in the diphoton decay channel at $\sqrt{s} = 8$ TeV with ATLAS*, J. High Energ. Phys. **09** (2014).

[114] ATLAS Collaboration,
Fiducial and differential cross sections of Higgs boson production measured in the four-lepton decay channel in pp collisions at $\sqrt{s}$ = 8 TeV with the ATLAS detector,
Phys. Lett. B. **738** (2014).

[115] CMS Collaboration, *Measurement of differential cross sections for Higgs boson production in the diphoton decay channel in pp collisions at $\sqrt{s}$ = 8 TeV*,
Eur. Phys. J. **C76** (2016).

[116] CMS Collaboration,
Measurement of differential and integrated fiducial cross sections for Higgs boson production in the four-lepton decay channel in pp collisions at $\sqrt{s}$ =7 and 8 TeV,
J. High Energ. Phys. **04** (2016).

[117] The ATLAS collaboration,
Cross-section measurements of the Higgs boson decaying to a pair of tau leptons in proton–proton collisions at $\sqrt{s} = 13$ TeV with the ATLAS detector,
ATLAS-CONF-2018-021 (2018).

[118] *Observation of the Higgs boson decay to a pair of τ leptons with the CMS detector*,
Phys. Lett. **B779** (2018) p. 283, arXiv: 1708.00373 [hep-ex].

[119] *Measurements of gluon-gluon fusion and vector-boson fusion Higgs boson production cross-sections in the $H \to WW^* \to e\nu\mu\nu$ decay channel in pp collisions at $\sqrt{s} = 13$ TeV with the ATLAS detector*, (2018), arXiv: 1808.09054 [hep-ex].

[120] *Measurements of properties of the Higgs boson decaying to a W boson pair in pp collisions at $\sqrt{s}$ = 13 TeV*, Submitted to: Phys. Lett. (2018),
arXiv: 1806.05246 [hep-ex].

[121] *Measurement of the Higgs boson mass in the $H \to ZZ^* \to 4\ell$ and $H \to \gamma\gamma$ channels with $\sqrt{s} = 13$ TeV pp collisions using the ATLAS detector*,
Phys. Lett. **B784** (2018) p. 345, arXiv: 1806.00242 [hep-ex].

[122] *Measurements of properties of the Higgs boson decaying into the four-lepton final state in pp collisions at $\sqrt{s} = 13$ TeV*, JHEP **11** (2017) p. 047,
arXiv: 1706.09936 [hep-ex].

[123] ATLAS Collaboration, *Observation of Higgs boson production in association with a top quark pair at the LHC with the ATLAS detector*,
Physics Letters B **784** (2018) p. 173 , ISSN: 0370-2693, URL:
http://www.sciencedirect.com/science/article/pii/S0370269318305732.

[124] ATLAS Collaboration, *Evidence for the associated production of the Higgs boson and a top quark pair with the ATLAS detector*, Phys. Rev. D **97** (2018).

[125] *Observation of $t\bar{t}H$ production*, Phys. Rev. Lett. **120** (2018) p. 231801, arXiv: 1804.02610 [hep-ex].

[126] CMS Collaboration, *Evidence for associated production of a Higgs boson with a top quark pair in final states with electrons, muons, and hadronically decaying τ leptons at $\sqrt{s}$= 13 TeV*, CMS-HIG-17-018 (2018), URL: arXiv:1803.054853.

[127] CMS Collaboration, *Search for $t\bar{t}H$ production in the $H \to b\bar{b}$ decay channel with leptonic $t\bar{t}$ decays in proton-proton collisions at $\sqrt{s} = 13$ TeV*, CMS-HIG-17-026 (2018), URL: arXiv:1804.03682.

[128] CMS Collaboration, *Search for $t\bar{t}H$ production in the all-jet final state in proton-proton collisions at $\sqrt{s} = 13$ TeV*, CMS-HIG-17-022 (2018), URL: arXiv:1803.06986.

[129] CMS Collaboration, *Measurements of Higgs boson properties in the diphoton decay channel in proton-proton collisions at $\sqrt{s} = 13$ TeV*, CMS-HIG-16-040 (2017), URL: arXiv:1804.02716.

[130] CMS Collaboration, *Measurements of properties of the Higgs boson decaying into the four-lepton final state in pp collisions at $\sqrt{s} = 13$ TeV*, J. High Energ. Phys. **11** (2017).

[131] F. Bezrukov and M. Shaposhnikov, *Why should we care about the top quark Yukawa coupling?*, J. Exp. Theor. Phys. **120** (2015).

[132] *Observation of $H \to b\bar{b}$ decays and VH production with the ATLAS detector*, (2018), arXiv: 1808.08238 [hep-ex].

[133] *Observation of Higgs boson decay to bottom quarks*, Submitted to: Phys. Rev. Lett. (2018), arXiv: 1808.08242 [hep-ex].

[134] L. Evans and P. Bryant, *LHC Machine*, J. Inst. **3** (2008).

[135] M. Lamont R. Assmann and S. Myers, *A brief history of the LEP collider*, Nucl. Phys. B - Proceedings Supplements **109** (2002), URL: http://www.sciencedirect.com/science/article/pii/S0920563202900058.

[136] *LEP Design Report Vol.1*, (1983), URL: https://cds.cern.ch/record/98881.

[137] *LEP Design Report: Vol.2. The LEP Main Ring*, 1984, URL: https://cds.cern.ch/record/102083.

[138] Carlo Wyss, *LEP Design Report: Vol.3*, 1996, URL: https://cds.cern.ch/record/314187.

[139] "Design Report Tevatron 1 project", tech. rep., 1984, URL: https://cds.cern.ch/record/1478620.

[140] Schindl and Karlheinz, *The injector chain for the LHC*, (1999), URL: https://cds.cern.ch/record/397574.

[141] L. Arnaudon et al, "Linac4 Technical Design Report", tech. rep., 2006, URL: https://cds.cern.ch/record/1004186.

[142] *Linear accelerator 4*, (2012), URL: https://cds.cern.ch/record/1997425.

[143] A. Rao, *The 2018 data-taking run at the LHC has begun*, (2018), URL: http://cds.cern.ch/record/2315786.

[144] ATLAS Collaboration *et al*, *The ATLAS Experiment at the CERN Large Hadron Collider*, J. Inst. **3** (2008).

[145] LHCb Collaboration, "Road map for selected key measurements from LHCb. Roadmap for selected key measurements of LHCb", tech. rep. arXiv:0912.4179. CERN-LHCb-PUB-2009-029, CERN, 2010, URL: https://cds.cern.ch/record/1224241.

[146] ALICE Collaboration *et al*, *ALICE: Physics Performance Report, Volume II*, J. Phys. G: Nucl. Part. Phys. **32** (2006).

[147] TOTEM Collaboration, *Total cross-section, elastic scattering and diffraction dissociation at the Large Hadron Collider at CERN: TOTEM Technical Design Report*, Technical Design Report TOTEM, CERN, 2004, URL: https://cds.cern.ch/record/704349.

[148] LHCf Collaboration, *LHCf experiment: Technical Design Report*, CERN, 2006, URL: https://cds.cern.ch/record/926196.

[149] D. d?Enterria, *Physics at the LHC: a short overview*, J. Phys. Conf. Ser. **270** (2011).

[150] MoEDAL Collaboration, tech. rep., 2009, URL: https://cds.cern.ch/record/1181486.

[151] *ATLAS inner detector: Technical Design Report, 1*, Technical Design Report ATLAS, 1997, URL: https://cds.cern.ch/record/331063.

[152] ATLAS Collaboration, *ATLAS pixel detector: Technical design report*, CERN-LHCC-98-13 (1998).

[153] ATLAS Collaboration, "ATLAS Insertable B-Layer Technical Design Report", tech. rep. CERN-LHCC-2010-013. ATLAS-TDR-19, 2010, URL: https://cds.cern.ch/record/1291633.

[154] ATLAS Collaboration,
Operation and performance of the ATLAS semiconductor tracker, JINST **9** (2014),
arXiv: 1404.7473 [hep-ex].

[155] ATLAS Collaboration,
Study of the material of the ATLAS inner detector for Run 2 of the LHC,
J. Inst. **12** (2017) P12009.

[156] ATLAS Collaboration, *The ATLAS Transition Radiation Tracker (TRT) proportional drift tube: Design and performance*, JINST **3** (2008).

[157] *ATLAS liquid argon calorimeter: Technical design report*,
CERN-LHCC-96-41 (1996).

[158] *ATLAS tile calorimeter: Technical design report*, CERN-LHCC-96-42 (1996).

[159] *ATLAS muon spectrometer: Technical design report*,
CERN-LHCC-97-22, ATLAS-TDR-10 (1997).

[160] ATLAS TDAQ Collaboration,
The ATLAS Data Acquisition and High Level Trigger system,
Journal of Instrumentation **11** (2016),
URL: http://stacks.iop.org/1748-0221/11/i=06/a=P06008.

[161] "Trigger Menu in 2016", tech. rep. ATL-DAQ-PUB-2017-001, CERN, 2017,
URL: http://cds.cern.ch/record/2242069.

[162] Oleksandr Viazlo and ATLAS LUCID Collaboration,
"ATLAS LUCID detector upgrade for LHC Run 2",
tech. rep. ATL-FWD-PROC-2015-004, CERN, 2015,
URL: https://cds.cern.ch/record/2062038.

[163] V. Cindro et al, *The ATLAS Beam Conditions Monitor*,
Journal of Instrumentation **3** (2008),
URL: https://doi.org/10.1088%2F1748-0221%2F3%2F02%2Fp02004.

[164] T. Cornelissen et al, *The new ATLAS track reconstruction (NEWT)*,
Journal of Physics: Conference Series **119** (2008),
URL: http://stacks.iop.org/1742-6596/119/i=3/a=032014.

[165] D. Wicke, *A New algorithm for solving tracking ambiguities*, (1999).

[166] *Performance of the ATLAS track reconstruction algorithms in dense environments in LHC Run 2*, The European Physical Journal C **77** (2017),
URL: https://doi.org/10.1140/epjc/s10052-017-5225-7.

[167] A. Salzburger,
"HCPSS 2014: Fermilab-CERN Hadron Collider Physics Summer School 2014",
Lecture course.

[168] R. Fruehwirth, *Application of Kalman filtering to track and vertex fitting*, Nuclear Instruments and Methods in Physics Research Section A: Accelerators, Spectrometers, Detectors and Associated Equipment **262** (1987), URL: http://www.sciencedirect.com/science/article/pii/0168900287908874.

[169] ATLAS Collaboration, "Improved electron reconstruction in ATLAS using the Gaussian Sum Filter-based model for bremsstrahlung", tech. rep., 2012, URL: http://cds.cern.ch/record/1449796.

[170] ATLAS Collaboration, *Reconstruction of primary vertices at the ATLAS experiment in Run 1 proton–proton collisions at the LHC*, The European Physical Journal C **77** (2017), URL: https://doi.org/10.1140/epjc/s10052-017-4887-5.

[171] J. Jimenez Peña, *Alignment of the ATLAS Inner Detector Upgraded for the LHC Run II*, Journal of Physics: Conference Series **664** (2015) p. 072025, URL: http://stacks.iop.org/1742-6596/664/i=7/a=072025.

[172] ATLAS Colaboration, "Early Inner Detector Tracking Performance in the 2015 data at $\sqrt{s} = 13$ TeV", tech. rep. ATL-PHYS-PUB-2015-051, 2015, URL: https://cds.cern.ch/record/2110140.

[173] "Early Inner Detector Tracking Performance in the 2015 data at $\sqrt{s} = 13$ TeV", tech. rep. ATL-PHYS-PUB-2015-051, CERN, 2015, URL: https://cds.cern.ch/record/2110140.

[174] "Track Reconstruction Performance of the ATLAS Inner Detector at $\sqrt{s} = 13$ TeV", tech. rep. ATL-PHYS-PUB-2015-018, CERN, 2015, URL: http://cds.cern.ch/record/2037683.

[175] ATLAS Collaboration, *Measurement of the photon identification efficiencies with the ATLAS detector using LHC Run-1 data*, The European Physical Journal C **76** (2016), URL: https://doi.org/10.1140/epjc/s10052-016-4507-9.

[176] ATLAS Collaboration, *Electron and photon energy calibration with the ATLAS detector using LHC Run 1 data*, The European Physical Journal C **74** (2014), URL: https://doi.org/10.1140/epjc/s10052-014-3071-4.

[177] ATLAS Collaboration, "Electron and photon energy calibration with the ATLAS detector using data collected in 2015 at $\sqrt{s} = 13$ TeV", tech. rep., 2016, URL: https://cds.cern.ch/record/2203514.

[178] W. Lampl et al,
"Calorimeter Clustering Algorithms: Description and Performance",
tech. rep. ATL-LARG-PUB-2008-002. ATL-COM-LARG-2008-003, 2008,
URL: https://cds.cern.ch/record/1099735.

[179] ATLAS Collaboration, *Measurement of the photon identification efficiencies with the ATLAS detector using LHC Run 2 data collected in 2015 and 2016*,
Submitted to: Eur. Phys. J. (2018), arXiv: 1810.05087 [hep-ex].

[180] ATLAS Collaboration, "Photon identification in 2015 ATLAS data", tech. rep.,
2016, URL: https://cds.cern.ch/record/2203125.

[181] H. Herde, "Muon reconstruction performance in ATLAS at Run-II", tech. rep.,
2015, URL: https://cds.cern.ch/record/2059849.

[182] ATLAS Collaboration, "Muon reconstruction performance of the ATLAS detector in proton–proton collision data at $\sqrt{s}$ =13 TeV", tech. rep. 5, 2016,
arXiv: 1603.05598 [hep-ex].

[183] J. Illingworth and J. Kittler, *A survey of the hough transform*,
Computer Vision, Graphics, and Image Processing **44** (1988), URL:
http://www.sciencedirect.com/science/article/pii/S0734189X88800331.

[184] Atlas Collaboration, *Muon reconstruction performance of the ATLAS detector in proton–proton collision data at* $\sqrt{s} = 13$ *TeV*,
The European Physical Journal C **76** (2016) p. 292, ISSN: 1434-6052,
URL: https://doi.org/10.1140/epjc/s10052-016-4120-y.

[185] ATLAS Collaboration, *Topological cell clustering in the ATLAS calorimeters and its performance in LHC Run 1*, The European Physical Journal C **77** (2017),
URL: https://doi.org/10.1140/epjc/s10052-017-5004-5.

[186] A. Hrynevich, *ATLAS jet and missing energy reconstruction, calibration and performance in LHC Run-2*, Journal of Instrumentation **12** (2017),
URL: http://stacks.iop.org/1748-0221/12/i=06/a=C06038.

[187] ATLAS Collaboration, "Jet Calibration and Systematic Uncertainties for Jets Reconstructed in the ATLAS Detector at $\sqrt{s} = 13$ TeV", tech. rep., 2015,
URL: https://cds.cern.ch/record/2037613.

[188] ATLAS Collaboration, *Performance of pile-up mitigation techniques for jets in pp collisions at* $\sqrt{s} = 8$ *TeV using the ATLAS detector*, Eur. Phys. Jour. C **76** (2016),
URL: https://doi.org/10.1140/epjc/s10052-016-4395-z.

[189] ATLAS Collaboration, "Jet Calibration and Systematic Uncertainties for Jets Reconstructed in the ATLAS Detector at $\sqrt{s} = 13$ TeV", tech. rep., 2015,
URL: https://cds.cern.ch/record/2037613.

[190] ATLAS collaboration, "Jet energy resolution in proton-proton collisions at $\sqrt{s} = 7$ TeV recorded in 2010 with the ATLAS detector", tech. rep. 3, 2013, arXiv: 1210.6210 [hep-ex].

[191] ATLAS collaboration, "Data-driven determination of the energy scale and resolution of jets reconstructed in the ATLAS calorimeters using dijet and multijet events at $\sqrt{s} = 8\ TeV$", tech. rep. ATLAS-CONF-2015-017, CERN, 2015, URL: http://cds.cern.ch/record/2008678.

[192] ATLAS collaboration, "Jet Calibration and Systematic Uncertainties for Jets Reconstructed in the ATLAS Detector at $\sqrt{s} = 13$ TeV", tech. rep. ATL-PHYS-PUB-2015-015, CERN, 2015, URL: https://cds.cern.ch/record/2037613.

[193] ATLAS Collaboration, "Tagging and suppression of pileup jets with the ATLAS detector", tech. rep., 2014, URL: https://cds.cern.ch/record/1700870.

[194] ATLAS Collaboration, "Expected performance of the ATLAS b-tagging algorithms in Run-2", tech. rep., 2015, URL: https://cds.cern.ch/record/2037697.

[195] ATLAS Collaboration, "Optimisation of the ATLAS b-tagging performance for the 2016 LHC Run", tech. rep., 2016, URL: https://cds.cern.ch/record/2160731.

[196] ATLAS Collaboration, "Measurements of b-jet tagging efficiency with the ATLAS detector using $t\bar{t}$ events at $\sqrt{s} = 13$ TeV", tech. rep., 2018, URL: https://cds.cern.ch/record/2316380.

[197] ATLAS collaboration, "Performance of missing transverse momentum reconstruction for the ATLAS detector in the first proton-proton collisions at at $\sqrt{s}$= 13 TeV", tech. rep. ATL-PHYS-PUB-2015-027, 2015, URL: https://cds.cern.ch/record/2037904.

[198] ATLAS collaboration, "Performance of missing transverse momentum reconstruction with the ATLAS detector using proton-proton collisions at $\sqrt{s} = 13$ TeV", tech. rep. 11, 2018, arXiv: 1802.08168 [hep-ex].

[199] *Geant4– simulation toolkit*, Nuclear Instruments and Methods in Physics Research Section A: Accelerators, Spectrometers, Detectors and Associated Equipment **506** (2003), URL: http://www.sciencedirect.com/science/article/pii/S0168900203013688.

[200] ATLAS Collaboration, *Luminosity determination in pp collisions at $\sqrt{s}$ = 8 TeV using the ATLAS detector at the LHC*, Eur. Phys. J. **C76** (2016) p. 653, arXiv: 1608.03953 [hep-ex].

[201] P. Grafstroem and W. Kozanecki, *Luminosity determination at proton colliders*, Progress in Particle and Nuclear Physics **81** (2015) p. 97 , ISSN: 0146-6410, URL: http://www.sciencedirect.com/science/article/pii/S0146641014000878.

[202] The ATLAS Collaboration, *Measurements of top-quark pair to Z-boson cross-section ratios at $\sqrt{s}$ =13, 8, 7 TeV with the ATLAS detector*, J. High Energ. Phys. **02** (2017), URL: https://doi.org/10.1007/JHEP02(2017)117.

[203] S. van der Meer, "Calibration of the effective beam height in the ISR", tech. rep. CERN-ISR-PO-68-31. ISR-PO-68-31, CERN, 1968, URL: http://cds.cern.ch/record/296752.

[204] The TOTEM Collaboration, *Measurement of proton-proton inelastic scattering cross-section at $\sqrt{s}$ =7 TeV*, Europhysics Letters **101** (2013), URL: http://stacks.iop.org/0295-5075/101/i=2/a=21003.

[205] TOTEM Collaboration, *Luminosity-Independent Measurement of the Proton-Proton Total Cross Section at $\sqrt{s} = 8$ TeV*, Phys. Rev. Lett. **111** (1 2013), URL: https://link.aps.org/doi/10.1103/PhysRevLett.111.012001.

[206] ATLAS Collaboration, *Measurement of the Inelastic Proton-Proton Cross Section at $\sqrt{s} = 13$ TeV with the ATLAS Detector at the LHC*, Phys. Rev. Lett. **117** (18 2016), URL: https://link.aps.org/doi/10.1103/PhysRevLett.117.182002.

[207] A. Sidoti, *Minimum Bias Trigger Scintillators in ATLAS Run II*, Journal of Instrumentation **9** (2014), URL: https://doi.org/10.1088%2F1748-0221%2F9%2F10%2Fc10020.

[208] K. Fuchsberger M. Hostettler and G. Papotti, "Operational experience with luminosity scans for beam size estimation in 2016 LHC proton physics operation", *Proceedings of IPAC2017, Copenhagen, Denmark*, 2017.

[209] LHCf Collaboration, *Measurement of forward photon production cross-section in proton-proton collisions at $\sqrt{s}$ = 13 TeV with the LHCf detector. Measurement of forward photon-energy spectra for $\sqrt{s}$ = 13 TeV proton-proton collisions with the LHCf detector*, Phys. Lett. B **780** (2017) p. 233, URL: https://cds.cern.ch/record/2255884.

[210] "Measurement of W and Z Boson Production Cross Sections in pp Collisions at root s = 13 TeV in the ATLAS Detector", tech. rep. ATLAS-CONF-2015-039, CERN, 2015, URL: https://cds.cern.ch/record/2045487.

[211] "Measurements of the $t\bar{t}$ production cross-section in the dilepton and lepton-plus-jets channels and of the ratio of the $t\bar{t}$ and Z boson cross-sections in pp collisions at $\sqrt{s} = 13$ TeV with the ATLAS detector", tech. rep. ATLAS-CONF-2015-049, CERN, 2015, URL: https://cds.cern.ch/record/2052605.

[212] "Track Reconstruction Performance of the ATLAS Inner Detector at $\sqrt{s} = 13$ TeV", tech. rep. ATL-PHYS-PUB-2015-018, CERN, 2015, URL: https://cds.cern.ch/record/2037683.

[213] J. R. Andersen et al., "Les Houches 2015: Physics at TeV Colliders Standard Model Working Group Report", *9th Les Houches Workshop on Physics at TeV Colliders (PhysTeV 2015) Les Houches, France, June 1-19, 2015*, 2016, arXiv: 1605.04692 [hep-ph], URL: http://lss.fnal.gov/archive/2016/conf/fermilab-conf-16-175-ppd-t.pdf.

[214] J. Kalinowski A. Djouadi and M. Spira, *HDECAY: a program for Higgs boson decays in the Standard Model and its supersymmetric extension*, Computer Physics Communications **108** (1998), URL: http://www.sciencedirect.com/science/article/pii/S0010465597001239.

[215] A. Bredenstein et al., *Radiative corrections to the semileptonic and hadronic Higgs-boson decays $H \to WW/ZZ \to 4$ fermions*, Journal of High Energy Physics **2007** (2007), URL: http://stacks.iop.org/1126-6708/2007/i=02/a=080.

[216] A. Bredenstein et al., *Precise predictions for the Higgs-boson decay $H \to WW/ZZ \to 4$ leptons*, Phys. Rev. D **74** (1 2006), URL: https://link.aps.org/doi/10.1103/PhysRevD.74.013004.

[217] A. Bredenstein, A. Denner, S. Dittmaier, and M.M. Weber, *Precision calculations for the Higgs decays $H \to ZZ/WW \to 4$ leptons*, Nuclear Physics B - Proceedings Supplements **160** (2006), Proceedings of the 8th DESY Workshop on Elementary Particle Theory, ISSN: 0920-5632, URL: http://www.sciencedirect.com/science/article/pii/S0920563206006372.

[218] The ATLAS Collaboration, *The ATLAS Simulation Infrastructure*, European Physical Journal C **70** (2010).

[219] T. Yamanaka, *The ATLAS calorimeter simulation FastCaloSim*,
Journal of Physics: Conference Series **331** (2011),
URL: https://doi.org/10.1088%2F1742-6596%2F331%2F3%2F032053.

[220] W. Lukas, *Fast Simulation for ATLAS: Atlfast-II and ISF*,
J. Phys. Conf. Ser. **396** (2012).

[221] K. Hamilton et al., *Merging H/W/Z + 0 and 1 jet at NLO with no merging scale: a path to parton shower + NNLO matching*,
Journal of High Energy Physics **2013** (2013), ISSN: 1029-8479,
URL: https://doi.org/10.1007/JHEP05(2013)082.

[222] J. Butterworth et al., *PDF4LHC recommendations for LHC Run II*,
Journal of Physics G: Nuclear and Particle Physics **43** (2016),
URL: http://stacks.iop.org/0954-3899/43/i=2/a=023001.

[223] The ATLAS Collaboration, *Measurement of the Z/γ^* boson transverse momentum distribution in pp collisions at $s = \sqrt{s} = 7$ TeV with the ATLAS detector*,
Journal of High Energy Physics **2014** (2014).

[224] R.D. Ball et al., *Parton distributions for the LHC run II*,
Journal of High Energy Physics **2015** (2015), ISSN: 1029-8479,
URL: https://doi.org/10.1007/JHEP04(2015)040.

[225] "ATLAS Run 1 Pythia8 tunes", tech. rep. ATL-PHYS-PUB-2014-021,
CERN, 2014, URL: https://cds.cern.ch/record/1966419.

[226] Hung-Liang et al. Lai, *New parton distributions for collider physics*,
Phys. Rev. D **82** (7 2010),
URL: https://link.aps.org/doi/10.1103/PhysRevD.82.074024.

[227] C. Röhr S. Gieseke and A. Siódmok, *Colour reconnections in Herwig++*,
The European Physical Journal C **72** (2012) p. 2225, ISSN: 1434-6052,
URL: https://doi.org/10.1140/epjc/s10052-012-2225-5.

[228] F. Demartin et al.,
Higgs production in association with a single top quark at the LHC,
The European Physical Journal C **75** (2015).

[229] "Summary of ATLAS Pythia 8 tunes", tech. rep. ATL-PHYS-PUB-2012-003,
CERN, 2012, URL: https://cds.cern.ch/record/1474107.

[230] A.D. Martin et al., *Parton distributions for the LHC*,
The European Physical Journal C **63** (2009), ISSN: 1434-6052,
URL: https://doi.org/10.1140/epjc/s10052-009-1072-5.

[231] The ATLAS Collaboration, *Measurement of the photon identification efficiencies with the ATLAS detector using LHC Run-1 data*, Eur. Phys. J. **C76** (2016), arXiv: 1606.01813 [hep-ex].

[232] "Electron efficiency measurements with the ATLAS detector using the 2015 LHC proton-proton collision data", tech. rep. ATLAS-CONF-2016-024, CERN, 2016, URL: https://cds.cern.ch/record/2157687.

[233] Matteo Cacciari and Gavin P. Salam, *Dispelling the N3 myth for the kt jet-finder*, Physics Letters B **641** (2006), ISSN: 0370-2693, URL: http://www.sciencedirect.com/science/article/pii/S0370269306010094.

[234] G. P. Salam M. Cacciar and G. Soyez, *FastJet user manual*, The European Physical Journal C **72** (2012) p. 1896, ISSN: 1434-6052, URL: https://doi.org/10.1140/epjc/s10052-012-1896-2.

[235] The ATLAS Collaboration, *Performance of pile-up mitigation techniques for jets in pp collisions at $\sqrt{s} = 8$ TeV using the ATLAS detector*, Eur. Phys. J. **C76** (2016), arXiv: 1510.03823 [hep-ex].

[236] F. Bishara et al., *Constraining Light-Quark Yukawa Couplings from Higgs Distributions*, Phys. Rev. Lett. **118** (2017), arXiv: 1606.09253 [hep-ph].

[237] ATLAS Collaboration, "Study of the spin of the Higgs-like boson in the two photon decay channel using 20.7 fb-1 of pp collisions collected at $\sqrt{s} = 8$ TeV with the ATLAS detector", tech. rep. ATLAS-CONF-2013-029, CERN, 2013, URL: https://cds.cern.ch/record/1527124.

[238] J. R. Andersen et al, *Handbook of LHC Higgs Cross Sections: 3. Higgs Properties*, (2013), arXiv: 1307.1347 [hep-ph].

[239] M. Vesterinen and T.R. Wyatt, *A novel technique for studying the Z boson transverse momentum distribution at hadron colliders*, Nuclear Instruments and Methods in Physics Research Section A: Accelerators, Spectrometers, Detectors and Associated Equipment **602** (2009), ISSN: 0168-9002, URL: http://www.sciencedirect.com/science/article/pii/S0168900209003040.

[240] OPAL Collaboration, *Search for anomalous production of dilepton events with missing transverse momentum in e^+e^- collisions at $\sqrt{s} = =$ 161-GeV and 172-GeV*, Eur. Phys. J. **C4** (1998), arXiv: hep-ex/9710010 [hep-ex].

[241] F.J. Tackmann I.W. Stewar and W.J. Waalewijn,
Factorization at the LHC: From parton distribution functions to initial state jets,
Phys. Rev. D **81** (9 2010) p. 094035,
URL: https://link.aps.org/doi/10.1103/PhysRevD.81.094035.

[242] The ATLAS Collaboration, *Measurement of the inclusive isolated prompt photon cross section in pp collisions at $\sqrt{s} = 7$ TeV with the ATLAS detector*,
Phys. Rev. **D83** (2011), arXiv: 1012.4389 [hep-ex].

[243] The ATLAS Collaboration, *Measurement of the isolated di-photon cross-section in pp collisions at $\sqrt{s} = 7$ TeV with the ATLAS detector*, Phys. Rev. **D85** (2012), arXiv: 1107.0581 [hep-ex].

[244] R. A. Fisher,
On the interpretation of χ^2 from contingency tables, and the calculation of p,
Journal of the Royal Statistical Society **85** (1922) p. 87.

[245] F. James and M. Roos, *Minuit: A System for Function Minimization and Analysis of the Parameter Errors and Correlations*, Comput. Phys. Commun. **10** (1975).

[246] Wouter Verkerke and David P. Kirkby, *The RooFit toolkit for data modeling*,
eConf **C0303241** (2003), [,186(2003)], arXiv: physics/0306116 [physics].

[247] G. Cowan, *A survey of unfolding methods for particle physics*,
Conf. Proc. **C0203181** (2002) p. 248.

[248] G.P. Salam, *Towards Jetography*, Eur. Phys. J. **C67** (2010) p. 637,
arXiv: 0906.1833 [hep-ph].

[249] F.C. Berger et al, *Higgs Production with a Central Jet Veto at NNLL+NNLO*,
JHEP **04** (2011), arXiv: 1012.4480 [hep-ph].

[250] ATLAS Collaboration, *Evidence for the associated production of the Higgs boson and a top quark pair with the ATLAS detector*, Phys. Rev. **D97** (2018),
arXiv: 1712.08891 [hep-ex].

[251] T. Gleisberg et al., *Event generation with SHERPA 1.1*,
Journal of High Energy Physics **2009** (2009) p. 007,
URL: http://stacks.iop.org/1126-6708/2009/i=02/a=007.

[252] S. Schumann and F. Krauss,
A parton shower algorithm based on Catani-Seymour dipole factorisation,
Journal of High Energy Physics **2008** (2008) p. 038,
URL: http://stacks.iop.org/1126-6708/2008/i=03/a=038.

[253] N. Greiner et al., *Phenomenological analysis of Higgs boson production through gluon fusion in association with jets*, Journal of High Energy Physics **2016** (2016),
ISSN: 1029-8479, URL: https://doi.org/10.1007/JHEP01(2016)169.

[254] S. Höche et al, *A critical appraisal of NLO+PS matching methods*, Journal of High Energy Physics **2012** (2012), ISSN: 1029-8479, URL: https://doi.org/10.1007/JHEP09(2012)049.

[255] S. Höche et al, *QCD matrix elements + parton showers. The NLO case*, Journal of High Energy Physics **2013** (2013), ISSN: 1029-8479, URL: https://doi.org/10.1007/JHEP04(2013)027.

[256] M. Buschmann et al, *Mass effects in the Higgs-gluon coupling: boosted vs. off-shell production*, Journal of High Energy Physics **2015** (2015), ISSN: 1029-8479, URL: https://doi.org/10.1007/JHEP02(2015)038.

[257] M. Schönherr E. Bothmann and S. Schumann, *Reweighting QCD matrix-element and parton-shower calculations*, The European Physical Journal C **76** (2016), ISSN: 1434-6052, URL: https://doi.org/10.1140/epjc/s10052-016-4430-0.

[258] T. Gleisberg and S. Höche, *Comix, a new matrix element generator*, Journal of High Energy Physics **2008** (2008) p. 039, URL: http://stacks.iop.org/1126-6708/2008/i=12/a=039.

[259] R. Kuhn F. Krauss and G. Soff, *AMEGIC++ 1.0, A Matrix Element Generator In C++*, Journal of High Energy Physics **2002** (2002), URL: http://stacks.iop.org/1126-6708/2002/i=02/a=044.

[260] G. Cullen et al, *GoSam-2.0: a tool for automated one-loop calculations within the Standard Model and beyond*, The European Physical Journal C **74** (2014), ISSN: 1434-6052, URL: https://doi.org/10.1140/epjc/s10052-014-3001-5.

[261] S. Höche and M. Schönherr, *Uncertainties in next-to-leading order plus parton shower matched simulations of inclusive jet and dijet production*, Phys. Rev. D **86** (9 2012) p. 094042, URL: https://link.aps.org/doi/10.1103/PhysRevD.86.094042.

[262] G. Cullen et al, *Automated one-loop calculations with GoSam*, The European Physical Journal C **72** (2012), ISSN: 1434-6052, URL: https://doi.org/10.1140/epjc/s10052-012-1889-1.

[263] A. Banfi et al, *Jet-vetoed Higgs cross section in gluon fusion at N3LO+NNLL with small-R resummation*, Journal of High Energy Physics **2016** (2016), ISSN: 1029-8479, URL: https://doi.org/10.1007/JHEP04(2016)049.

[264] X. Chen et al,
Precise QCD predictions for the production of Higgs + jet final states,
Physics Letters B **740** (2015), ISSN: 0370-2693, URL:
http://www.sciencedirect.com/science/article/pii/S0370269314008235.

[265] X. Chen et al,
NNLO QCD corrections to Higgs boson production at large transverse momentum,
Journal of High Energy Physics **2016** (2016), ISSN: 1029-8479,
URL: https://doi.org/10.1007/JHEP10(2016)066.

[266] CMS Collaboration, *Observation of the diphoton decay of the Higgs boson and measurement of its properties*, Eur. Phys. J. C **74** (2014).

[267] CMS Collaboration, *Precise determination of the mass of the Higgs boson and tests of compatibility of its couplings with the standard model predictions using proton collisions at 7 and 8 TeV*, Eur. Phys. J. C **75** (2015).

[268] CMS Collaboration, *Measurement of differential cross sections for Higgs boson production in the diphoton decay channel in pp collisions at* $\sqrt{s} = 8$ *TeV*,
Eur. Phys. J. C **76** (2016).

[269] CMS Collaboration,
Measurement of inclusive and differential Higgs boson production cross sections in the diphoton decay channel in proton-proton collisions at $\sqrt{s} = 13$ *TeV*, (2018),
arXiv: 1807.03825 [hep-ex].

[270] CMS Collaboration, *Measurements of Higgs boson properties in the diphoton decay channel in proton-proton collisions at* $\sqrt{s} = 13$ *TeV*, (2018),
arXiv: 1804.02716 [hep-ex].

[271] Thomas G. McCarthy, "Upgrade of the ATLAS Liquid Argon Calorimeters for the High-Luminosity LHC", *Proceedings, 2016 IEEE Nuclear Science Symposium and Medical Imaging Conference: NSS/MIC 2016: Strasbourg, France*, 2016,
arXiv: 1612.07102 [physics.ins-det], URL:
https://inspirehep.net/record/1505424/files/arXiv:1612.07102.pdf.